Oscillatory processes during the aggregation and the fragmentation of the amyloid fibrils.

Mathieu Mezache

Inria
Laboratoire Jacques Louis Lions

Doctoral School **Sciences Mathématiques de Paris Centre**
University Department **Équipe Mamba**

Thesis defended by **Mathieu Mezache**

Defended on **17th December, 2019**

In order to become Doctor from Inria and from Laboratoire Jacques Louis Lions

Academic Field **Applied mathematics**

Thesis Title

Oscillatory processes during the aggregation and the fragmentation of amyloid fibrils.

Thesis supervised by Marie Doumic Supervisor
Human Rezaei Co-Supervisor

Committee members

Referees	Thierry Goudon	Senior Researcher at Inria
	José A. Cañizo	Professor at University of Granada
Examiners	Florence Hubert	Professor at Aix-Marseille Université
	Klemens Fellner	Professor at University of Graz
	Delphine Salort	Professor at Sorbonne Université
	Juan J.L. Velàzquez	Professor
Supervisors	Marie Doumic	Senior Researcher at Inria Paris
	Human Rezaei	Senior Researcher at Inra

This thesis has been prepared at

Équipe Mamba
Inria Paris
2, rue Simone Iff
CS 42112
75589 Paris Cedex 12

Web Site `https://team.inria.fr/mamba/fr/`

Oscillatory processes during the aggregation and the fragmentation of amyloid fibrils.

Abstract

The objective of this thesis is to study the physical process of protein aggregation and fragmentation. More specifically, oscillatory kinetic phenomena are identified during this process and are the subject of an in-depth analysis. The process of protein aggregation and fragmentation is intimately linked to the contraction and development of a vast class of incurable neurodegenerative diseases, amyloid diseases. Our work focuses on prion diseases, a subcategory of amyloid diseases, caused by the misfolding of protein conformation and the aggregation of these misfolded proteins into fibrils.

First, our study focuses on experimental static light scattering data (SLS). The signals obtained correspond approximately to the second moment of the size distribution of amyloid fibrils in vitro and therefore provide information on the evolution of the size distribution over time. We note damped oscillations at specific locations on the signals. These oscillations highlight the presence of complex, underlying kinetic phenomena during protein aggregation/fragmentation processes.

The analysis of SLS signals leads us to build a parametric characterization of oscillations in the frequency domain (Fourier domain). We propose a numerical procedure to obtain these parameters. Then, we build a statistical test of hypotheses. We thus obtain a p-value that allows us to quantitatively assert the presence of oscillations in the experimental signals.

In a second step, we introduce and mathematically analyze a kinetic model of proteins capable of generating oscillations. The model is a variant of the polymerization/depolymerization system and considers two species of monomers: a pathological monomer that polymerizes and a healthy monomer that depolymerizes. Unlike traditional models, depolymerization is catalytic and non-linear and an exchange phenomenon occurs between the two species of monomers and polymers. The model combines a Lotka-Volterra system for monomers with a growth/fragmentation system: Becker-Döring in the discrete size setting, Lifshitz-Slyozov in the continuous size setting. In the discrete size model, the oscillations are damped and under certain conditions we prove the exponential convergence towards a stationary state. While in the continuous model, the system oscillates perpetually or converges to a Dirac depending on the shape of the reaction coefficients.

By complexifying the model, in particular by integrating other species of polymers and kinetic reactions, it is possible to achieve a realistic modelling of protein kinetic processes. The mathematical study of these models leads to new interesting problems, improves and clarifies the understanding of the underlying physical phenomena.

Keywords: prion diseases, amyloids, hypothesis testing, spectral analysis, signal detection and filtering, prion modelling, lifshitz-slyozov, becker-döring, asymptotic behaviour, entropy inequality, stability analysis

Équipe Mamba
Inria Paris – 2, rue Simone Iff – CS 42112 – 75589 Paris Cedex 12 –

Résumé

Cette thèse a pour objectif l'étude du processus physique de l'agrégation et la fragmentation des protéines. Plus particulièrement, des phénomènes cinétiques oscillatoires sont identifiés durant ce processus et font l'objet d'une analyse approfondie. Le processus d'agrégation et de fragmentation de protéines est intimement lié à la contraction et au développement d'une vaste classe de maladies neurodégénratives incurables, les maladies amyloïdes. Notre travail se focalise sur les maladies à prions, une sous-catégorie des maladies amyloïdes. Les maladies à prions ont pour cause le changement de conformation de protéines et l'agrégation de ces protéines sous forme de fibres.
Dans un premier temps, notre étude porte sur les données expérimentales de diffusion statique de la lumière (SLS). Les signaux obtenus correspondent approximativement au moment d'ordre 2 de la distribution de taille des fibres amyloïdes in vitro. Ils renseignent sur l'évolution en temps de la distribution de taille. Des oscillations atténuées et localisées à des endroits spécifiques sur les signaux sont observables. Ces oscillations mettent en avant la présence de phénomènes cinétiques complexes, sous-jacent, lors des processus d'agrégation/fragmentation de protéines.
L'analyse des signaux SLS nous mène à construire une caractérisation paramétrique des oscillations dans le domaine fréquentiel. Nous proposons ensuite une procédure numérique pour obtenir ces paramètres. Puis, nous construisons un test statistique d'hypothèses. Nous obtenons ainsi une p-valeur renseignant de manière quantitative sur la présence d'oscillations dans les signaux expérimentaux.
Dans un second temps, nous introduisons et analysons mathématiquement un modèle cinétique de protéines capables d'engendrer des oscillations. Le modèle est une variante du système de polymérisation/dépolymérisation et considère deux espèces de monomères : un monomère pathologique qui polymérise et un monomère sain qui dépolymérise. Contrairement aux modèles traditionnels, la dépolymérisation est catalytique et non-linéaire. Un phénomène d'échange opère entre les deux espèces de monomères et les polymères. Le modèle couple un système Lotka-Volterra pour les monomères à un système de croissance/fragmentation : Becker-Döring dans le cas discret en taille, Lifshitz-Slyozov dans le cas continu. Nous étudions le comportement en temps long de ces deux systèmes. Dans le modèle discret en taille, les oscillations sont atténuées et sous certaines conditions il y a convergence vers un état stationnaire. Alors que dans le modèle continu, le système oscille de manière soutenue ou converge vers un Dirac en fonction de la forme des coefficients de réactions. En complexifiant le modèle, en particulier en intégrant d'autres espèces de polymères et de réactions cinétiques, il est possible d'aboutir à une modélisation réaliste des processus cinétiques de protéines. L'étude mathématique de ces modèles conduit à de nouveaux problèmes intéressants, améliore et précise la compréhension des phénomènes physiques sous-jacents.

Mots clés : les maladies à prions, amyloïde,test d'hypothèses, analyse spectrale, traitement du signal, modélisation des prions, lifshitz-slyozov, becker-döring, comportement asymptotique, inégalités d'entropie, analyse de stabilité

À Cherif M.

Remerciements

Je tiens tout d'abord à remercier mes directeurs de thèses, Marie Doumic et Human Rezaei, de m'avoir proposé un sujet d'étude passionnant et de m'avoir encadré durant ces trois années. Ils m'ont fait découvrir l'univers des mathématiques appliquées à la biologie. J'ai beaucoup apprécié la liberté qu'ils m'ont accordée tout en restant toujours présent pour répondre à mes questions. Leurs enthousiasmes, leurs points de vue et leurs conseils m'ont été d'un grand secours et m'ont permis de mener à bien mes travaux de recherche. Je les remercie aussi de m'avoir fait découvrir le monde de la recherche et de m'avoir proposé de participer à diverses conférences. J'y ai rencontré de nombreux chercheurs passionnants (mathématiciens et biologistes). Je n'oublie pas que ces voyages ont été financés par l'ERC Skipperad de Marie Doumic, je l'en remercie.

I am very grateful to José A.Cañizo for having taken time to review my thesis. Je remercie très chaleureusement Thierry Goudon d'avoir rapporté ma thèse et suis désolé de n'avoir pu trouver une date de soutenance lui permettant d'être présent. Je remercie Florence Hubert et Delphine Salort qui m'ont fait l'honneur d'être membres du jury. I would like to thank Klemens Fellner and Juan J.L. Velàzquez who honoured me by being members of the jury.

I am very grateful to Klemens Fellner for his warm welcome in Graz. I thank him for his precious advices and for giving me the opportunity to collaborate with him. Durant ma thèse, j'ai eu la chance de profiter des nombreuses idées et conseils de Marc Hoffmann pour aborder les problèmes d'estimation de paramètres et la construction de tests statistiques et je lui en suis très reconnaissant. Je tiens aussi à remercier les biologistes de l'Inra, Angélique, Davy, Vincent, Mohamed, Jan, de m'avoir toujours chaleureusement accueilli à Jouy-En-Josas et d'avoir répondu à mes nombreuses questions sur les maladies à prions. Je garderai un souvenir précieux de l'équipe Mamba et de ses membres pour l'accueil chaleureux et bienveillant. J'exprime plus généralement ma gratitude à tous les membres de l'Inria et du LJLL, croisés dans les couloirs ou en conférence, pour leur gentillesse et leur amabilité.

Si je peux garder un excellent souvenir de ma thèse, c'est essentiellement grâce aux personnes que j'ai côtoyées. Ce faisant, je remercie les personnes du troisième étage de l'Inria Alberto, Noémie, Elliot, Olivier, Hussam, Jan, Sebastien, Léa, Fabien W., Janelle, Florian, Jules pour les sorties sports, diners, etc, ainsi que la relève Matthias (le "Fanny"), Thibault, Liudi (la machine), Antoine, Van, Frédéric. Je souhaite également remercier Julia, Boris, Lara et Gaspard pour leur accueil à Vienne, les magnifiques balades à vélos (en montagne), etc. Je remercie aussi Malik, Igor, Lise, Mete, Frédérique, Hugo, Raphaël, Camille, Sofiane pour toutes les discussions plus ou moins poussées en maths, musique, démographie, compo du PSG en LDC, etc. Merci Chloé (et Fabien) pour les conseils et l'aide. Merci Gaétan, Nico (jambe de bois) et Fabien R. (le camarade) pour les nombreux échanges autours du plat du jour, les défis sportifs, les relectures de codes, etc.

Je souhaite aussi remercier les personnes rencontrées en dehors du cadre du travail. Merci Maxime,

Nicolas, Antoine, Geoffroy, David et autres coéquipiers du RCF. Merci aussi à Dumaz, Nicolas C., Géraldine, Agathe, Dom, Nina, Martin, Daman, Pierre, Elsa, Constance, Laura pour les soirées inoubliables. Merci aussi François, Martine, Valentine, Marie, Virginie... Merci Quentin, Julien et Raffaele pour les balades à Livry, les entrainements de tennis, etc. Un grand merci à Thibaut C..

Je remercie plus particulirèrement Quentin D. pour la lettre de recommendation sans laquelle je n'aurai pas pu faire cette thèse. Merci d'avoir cru en moi et de m'avoir poussé à faire des maths.

Enfin, je remercie ma famille pour leur amour inconditionnel et leur soutien.
Anne, pour m'avoir accompagné, supporté et aidé au quotidien et pour avoir rendu ces trois (plus trois) années si heureuses, merci.

Contents

Introduction

Generalities on Prion diseases

Prion diseases, also called transmissible spongiform encephalopathies (TSE) are fatal neurodegenerative and incurable disorders which affect both humans and animals. They are characterised by long incubation periods, neuronal loss with a failure to induce inflammatory response. Prion diseases occur when endogenous prion proteins, found on the surface of many cells, change their conformation and aggregate into fibrils in the brain or the central nervous system, causing brain damage.
This abnormal accumulation of protein in the central nervous system causes the following symptoms:

- behavioural symptoms such as rapidly developing dementia, hallucinations, confusions, fatigue,
- communication problems such as difficulty speaking and writing,
- memory and cognitive deficits,
- movement problems such as muscle stiffness, disturbance in balance, difficulty coordinating leading to clumsiness and shakiness.

These disorders are yet incurable and generally fatal.
The risk factors for prion diseases are ingesting blood or meat containing the pathological proteins and infection from contaminated medical equipment. For instance, the bovine spongiform encephalopathy (BSE), a TSE of bovines, is linked to the development of the human disease variant Creutzfeldt-Jakob disease (vCJD). The World Health Organization reported that 152 cases of vCJD have been diagnosed in the United Kingdom (UK), eight in France, two in Ireland and one in Canada, Italy and the United States

Human Prion Diseases	Animal Prion Diseases
Creutzfeldt-Jakob Disease (CJD)	Bovine Spongiform Encephalopathy (BSE)
Variant Creutzfeldt-Jakob Disease (vCJD)	Chronic Wasting Disease (CWD)
Gerstmann-Straussler-Scheinker Syndrome	Scrapie
Fatal Familial Insomnia	Transmissible Mink Encephalopathy
Kuru	Feline Spongiform Encephalopathy

Table 1 – Classification of the most common prion diseases (source: National Prion Disease Pathology Surveillance Center).

of America from October 1996 to November 2004. The wide variety of prion diseases are summarized in the Table 1, and more specific details on each disease can be found in [10, 11].
Protein aggregation process is a phenomenon of major importance. It is the cause of a class of neurodegenerative diseases also called amyloid diseases which affect significantly cattle but also human population through the prion diseases and also prion-like diseases (Alzheimer, Parkinson, Huntington, etc.). According to the Alzheimer's Association and Parkinson's Foundation, 5.8 million people are living with Alzheimer's dementia and 10 million people with Parkinson's disease. Although the protein aggregation phenomenon is extensively studied, it remains misunderstood, hence fascinating.

Prion diseases history

The first evidence of prion diseases takes place in the 18th century when farmers observed abnormal behaviour of sheep such as excessive licking and intense itching. The sheep would pathologically scrape against fences and hence the Scrapie was the first disease of a new class of neurological disorders known as transmissible spongiform encephalopathies (TSEs).
Several theories have been put forward to determine the responsible agent of TSEs. The researchers first thought that TSEs were caused by "slow viruses" because of the long time of incubation [146]. However, no virus could be isolated. In the 1960s, experiments designed to disrupt the large molecules using electron beams were used for the study of TSEs. Theses experiments showed that the size of the infectious agent is very small (much smaller than viruses). Moreover, scientists tried unsuccessfully to inactivate the scrapie agent with methods known to inactivate bacteria and viruses (UV irradiation, extreme heat, high pressures, etc.) [119, 3]. They reach the conclusion that the scrapie agent is replicating without nucleic acid and could be of protein origin [66].
In 1982, Prusiner gave credits to the hypothesis that the scrapie agent denoted PrP^{Sc} is a protein-only agent [130]. He purified the proteinaceous infectious particles (amyloid fibrils), named it prion (which stands for PRoteinaceous Infection ONly) and inactivated the infectious agent with methods that destroyed proteins.
The connection between the prion protein PrP^{c} and the PrP^{Sc} is established in [133]. Mice were genetically modified in order to be deficient in the *prnp* gene encoding the PrP^{c}. After inoculating scrapie-infected brain homogenate, mice developed resistance to experimental prion disease. The experiments demonstrated the requirement of PrP^{c} for prion infection.
A more detailed survey of prion diseases history can be found in [167]. All the previous research leads to establish the prion diseases as a growing scientific field of major importance which needs to be theorized in order to completely understand the mechanisms.

Key mechanisms of Prions replication

The aggregation of abnormally folded cellular prion protein is the reason for prion diseases. It involves the ubiquitous prion protein PrP^{c} which is mainly present in the central nervous system of healthy organisms. The PrP^{c} can also be found in the kidney, heart, skin, etc., and its physiological function

remains unknown. Mutations in the prion protein gene imply that the PrP^c can spontaneously change its conformation into the PrP^{Sc} and aggregate [132]. The pathological PrP^{Sc} is also able to convert PrP^c and propagate the disease.

The Prion Theory

TSEs are caused by an accumulation of abnormal isoform of proteins (amyloid fibrils) in the central nervous system. The structure, the physiological functions and the reasons behind the formation of the abnormal isoform are still unknown. Though *the prion hypothesis* is believed to be the most reasonable. The hypothesis stipulates that PrP^{Sc} is the infectious particle responsible for prion propagation and that it can replicate by inducing the autocatalytic conversion of PrP^c into its scrapie isoform [130]. Hence, two structurally distinct objects emerged from identical protein without any modification of the amino acid sequence.
Biochemical and biophysical measurements reveal that PrP^c is composed of two α-helix which represent 42% of its defined structure and a small portion of β-sheets (3%). However, the β-sheets amount to 43% of the scrapie agent PrP^{Sc} and the α-helix to 30% (cf [118] and Figure 1). The α-helix and the β-sheets are elements describing the tridimentional structure and the physicochemical properties of a protein. The α-helix is the arrangement of amino acids in a rotating structure (like an helix) and the β-sheets are made of β strands laterally connected by hydrogen bonds between atoms of the amino acids chain to form a folded plane (like an accordion). The physicochemical properties of the PrP^c and the infectious PrP^{Sc} are different. PrP^{Sc} forms an insoluble and protease-resistant aggregate. The PrP^c which leads to the formation of abnormal isoform is the result of mutations in the prion protein gene coming from an interaction between PrP^c and PrP^{Sc}. However the precise nature of the interaction remains unknown.

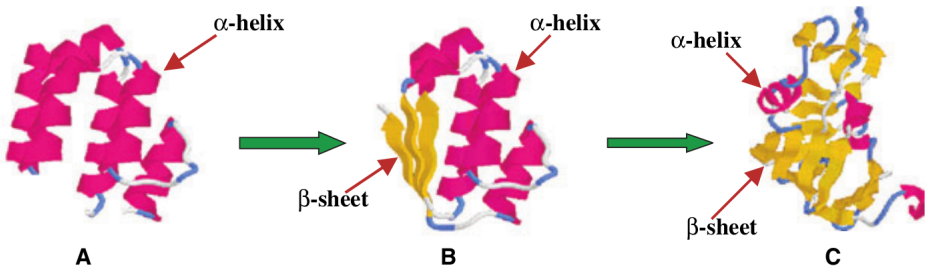

Figure 1 – **Secondary structure of prion proteins (source [35]).** A. Conformation of the PrP^c protein composed mainly of α-helices. B. Misfolding which causes the conversion of the structure. C. Final misfolded secondary structure of the PrP^{Sc} protein.

Moreover, pathologies due to protein aggregation and misassembly are separated in two subcategories: the prion-like diseases or prionoids and the prion diseases. This separation is contested because it is based on the hypothesis that there is no evidence of infectious agent in prionoids and that the disease is inherited. The understanding of the prion diseases challenges the scientific communities and requires a

multidisciplinary analysis (biochemistry, biophysics and mathematical modeling, numerical sciences, etc.) in order to propose convincing models and arguments.

Models of prion replication

In terms of pathogenic mechanisms, the prion paradigm unifies a number of neurodegenerative disorders that are caused by protein misfolding and aggregation [35]. These disorders include Alzheimer's, Parkinson's, Huntington's and prion diseases. In principle, host-encoded monomeric proteins are converted into misfolded and aggregated assemblies, which serve as templates for further conversion. Even if the molecular mechanisms of prion replication is still an open problem, the current models are mainly based either on an autocatalytic process (a chemical system where at least one of the products is a reactant) and on nucleation-elongation-fragmentation reactions. Mainly, two processes have been proposed respectively by Griffith [66], Prusiner [129] and Jarret, Lansbury [76], Caughey [33]. The main difference between these two processes lies in the role played by the PrP^{Sc} aggregates at the beginning of the replication mechanism.

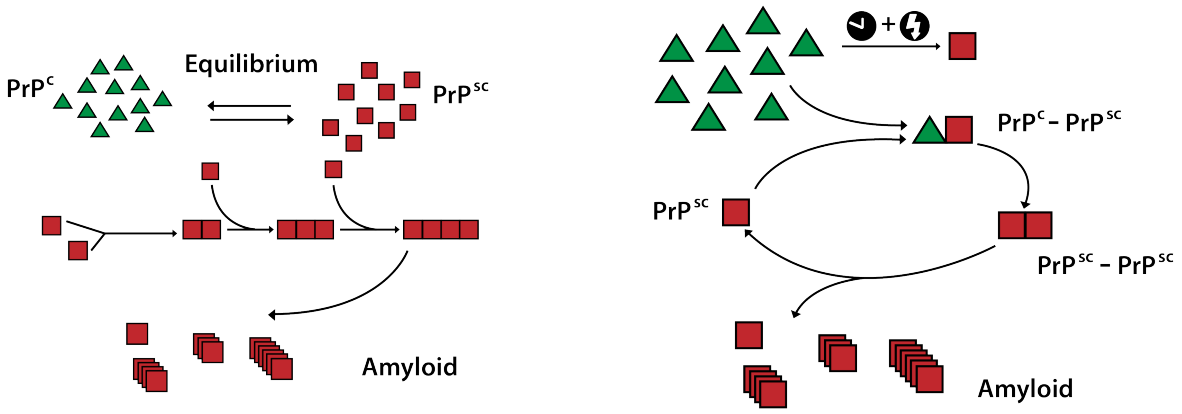

Figure 2 – Model of prion replication by Lansbury (left) and by Prusiner (Right)

In the model proposed by Lansbury [76], both PrP^c and PrP^{Sc} are assumed to exist naturally in the human organism. The two forms are in a reversible thermodynamic equilibrium that is perturbed in the presence of PrP^{Sc} aggregates, which provides favorable conditions for the conversion from PrP^c to PrP^{Sc} (cf. Figure 2). It should be pointed out that in this model the disease needs some PrP^{Sc} aggregates to start. The second model was presented by Prusiner in 1991 [129]. In this second model, an initial slow reaction with high activation energy converts PrP^c into PrP^{Sc} . The protein PrP^{Sc} is able to template and it forms a dimer with PrP^c (PrP^c-PrP^{Sc}). In the dimeric configuration PrP^c converts faster than the initial reaction. The newly created PrP^{Sc}-PrP^{Sc} dimer then dissociates and allows the formation of new PrP^{Sc}-PrP^c dimers propagating the disease (cf. Figure 2). In this case, PrP^{Sc} aggregates are not necessarily at the start.

The common ground of these two models of replication is that once the PrP^{Sc} proteins start to aggregate, they form structures called polymers characterised by the number of proteins composing the aggregates. Typically, PrP^{Sc} aggregates grow along a single axis creating organised filamentous structures called fibrillary filaments or fibrils. The fibrils can interact with each other and form higher order fibrillary aggregates called amyloids (cf [127] and Figure 3).

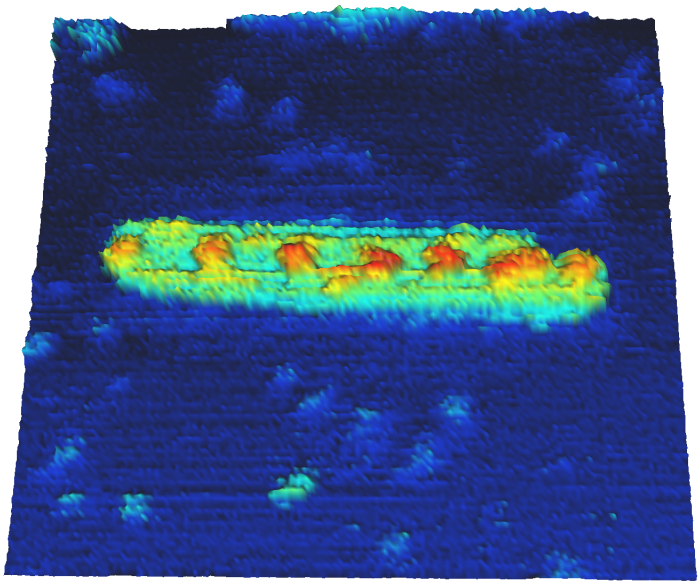

Figure 3 – Atomic Force Microscope image of a PrP^{Sc} aggregate (source VIM Inra 2017).

Open questions and problems on Prion mechanisms

The study of prions remains an active research topic. Since the discovery and the purification of the prions pathogenic form PrP^{Sc} in 1982 by Prusiner [130], no major scientific progress has been made to create a complete therapy of prion diseases. The main reasons lie in the lack of knowledge on prions. The exact reasons of occurrence of prion diseases are still unknown and discussed among specialists. The details of how prions induce toxicity are still unclear. Specifically, how does the aggregation take place ? Do aggregates grow by sequential additions of monomers ? Do they attach to dimers, trimers or i-mers ? How many type of aggregates are there and what are the interactions between each different kind of aggregates ? Which are the most toxic aggregates ? What is the size distribution evolution of the aggregates ? Which molecules or therapeutic processes induce prions clearance in living organisms ?

Some of these questions are partially solved, others remain unknown. Eventually, the response to all these questions would help to develop a rational therapy to prion and prion-like diseases.

Objective and contributions

The main objective of this thesis is seeking understanding on the kinetics of prion aggregation processes, especially on the occurrence of transient phenomena such as oscillations in the size distribution evolution of prion aggregates (see Figure 5).
The starting point of this work is the analysis of experimental results obtained by the VIM team at INRA. In these static light scattering experiments, damped oscillations are observed and distinguished from experimental noise thanks to a numerical procedure and a statistical test. Then, in order to understand the kinetics of these oscillations in depolymerisation experiments, we studied a polymerisation/depolymerisation kinetic model and added more details in order to obtain a (simplified) realistic model capable of displaying transient oscillations. In order to obtain these new dynamics in polymerisation/depolymerisation model, we developed a new hypothesis on the prion aggregation processes. It lead to the design of new experiments to justify the models. Lastly, new replication models on prions were able to corroborate experiments.

Statistical test of presence of oscillations.

In order to understand the aggregation processes for prion fibrils, we focus on experimental data obtained by Static Light Scattering (SLS) experiments. These experiments provide information on the evolution of size distribution of fibrils and display oscillations, however, the data are aggregated and difficult to exploit. The oscillations in SLS signals reveal the presence of transient phenomena and new mechanisms during the protein depolymerisation experiments. In **Chapter 1**, we define a rigorous procedure to detect and quantify oscillations in a signal. We design a statistical test of presence of oscillations or High Frequency features (HF features) and implement it on the experimental SLS data. The following results are detailed in **Chapter 1**.

Static light scattering experiment

When light is sent through a material, several interactions are possible : fluorescence, transmission, absorption, and scattering. In particular, scattering is the deflection of light from a straight trajectory, after encountering some physical object. The intensity of the scattered light is a function of the molecular weight and concentration of the scattering object. To measure such intensity we use a Static Light Scattering (SLS) device (cf Figure 4).

Static light scattering (SLS) is based on the electromagnetic mechanism of light scattering. From this theory it is known that light which interfers with a molecule, with a size inferior to its own wavelength, induces an oscillatory dipole. An oscillatory dipole is itself a source of electromagnetic radiation. Most of

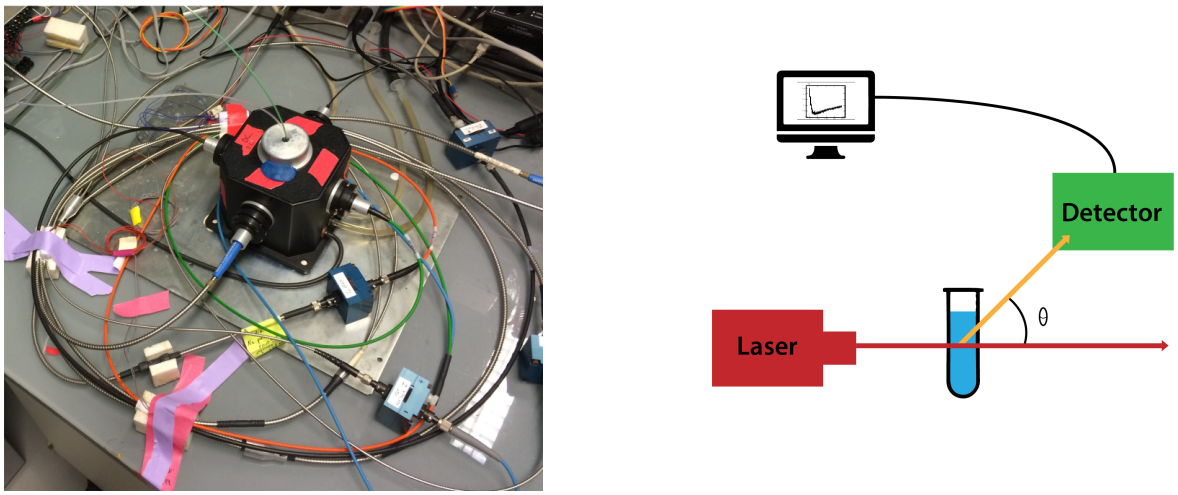

Figure 4 – Light scattering device from the unit VIM at Inra (left) and explanatory sheme (right).

the light is elastically scattered. The measured light intensity interpreted as scattered outcoming photons has been described and formalised by Rayleigh [45, 166]:

$$I_\theta = I_0 \alpha \frac{V_{scat}(\theta)}{r^2} CM$$

where I_0 is the intensity of the incident light, I_θ is the intensity of the scattered light, V_{scat} is the scattering volume seen from the detector and θ is the angle between the forward incident light and the scattered light (cf Figure 4). Moreover the scattered light intensity measure depends on the molecular weight M and the concentration C of molecules in the solution. The light received from a small light source decreases with distance r according to the inverse square law. α is a constant which depends on the particle's characteristics and the light's wavelength λ of the laser used. The constant α can be calculated as:

$$\alpha = \frac{4\pi^2 n_0 \left(\frac{dn}{dC}\right)^2}{N_A \lambda^4}$$

where n_0 is the refractive index of the solvent, $\frac{dn}{dC}$ is the refractive index increment of the solute/solvent system and $N_A = 6.022 \times 10^{23} \text{mol}^{-1}$ is Avrogado's number.
Hence, if the solution is composed of a mixture of polymers with different sizes, the scattered intensity is:

$$I_\theta = K \sum_i c_i M_i,$$

where $K = I_0 \bullet \alpha \bullet \frac{V_{scat}(\theta)}{r^2}$, c_i are the weight concentration of molecules and M_i the relative molecular weights. In the experiments on prions, amyloid fibrils are purified and observed through a thermostatic device using a 407-nm laser beam. Light-scattered signals were recorded at 112^o angle. The solution contains only monomers and polymers of different sizes. Denoting u_i the concentration of aggregates of

size i, the weight concentration c_i is defined as:

$$c_i = i u_i M_0$$

where M_0 is the weight of a monomer. Moreover the molecular weight of a polymer is proportional to its size, $M_i = iM_0$. In conclusion, the experimental data recorded by the SLS device are a linear transformation of the second moment of the concentration distribution. Given that monomers correspond to the size $i = 1$mer, we obtain the SLS signal at time t:

$$I_\theta(t) = k\left(v(t) + \sum_{i=i_0}^{i_1} i^2 u_i(t)\right) \tag{1}$$

where $v(t)$ is the concentration of monomers at time t, i_0 is the minimal size of the polymers and i_1 is the maximal size of the polymers. The parameter k is a constant depending on the experimental conditions.

Remark 1. *The SLS data are commonly read as the evolution of the average cluster size over time. In fact, the average molecular weight is defined as :*

$$\langle Mw \rangle = \frac{\sum_i c_i M_i}{\sum_i c_i} = \frac{\sum_i c_i M_i}{c_{tot}}$$

where c_{tot} denotes the total concentration of clusters. The average molecular weight is linked to the scattered light as follows:

$$\langle Mw \rangle = \frac{I_\theta}{k c_{tot}}.$$

Hence, the average cluster size denoted as $\langle i \rangle$ is defined as follows:

$$\langle i \rangle = \frac{\langle Mw \rangle}{M_0} = \frac{I_\theta}{M_0 k c_{tot}} = \frac{1}{\rho}\left(v + \sum_i i^2 u_i\right).$$

An interesting example of SLS signal is displayed in Figure 5. We observe fast oscillations in experimental measurements of the infectious agent in Prion diseases. A major difficulty to infer such transient oscillations and to evaluate their significance is that they are mixed up with noise. Hence, we propose a rigorous procedure which detects *high frequency features* (HF features) - amplitude, frequency - in real signals and to distinguish quantitatively these features of the signal from its noise.

Design of the statistical test of presence of oscillations.

The statistical test of presence of oscillations is based on three consecutive steps. We first introduce a parametric characterization of the high frequency features (HF features). Then, we design a parametric test of hypothesis and define a p-value which gives a quantitative indicator on the test results. Finally, we compute the test for the different SLS signals thanks to Python Library made for this study.

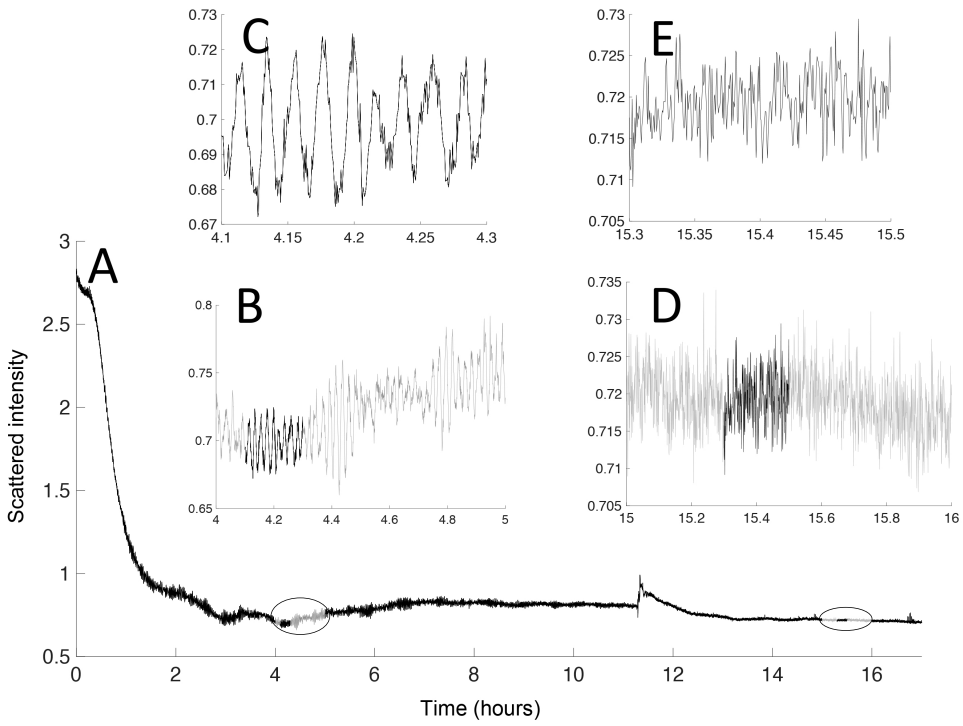

Figure 5 – **Human PrP amyloid fibrils (Hu fibrils) depolymerisation monitored by Static Light Scattering** . A: The overall view of the $\rho = 0.35\mu M$ Hu-fibrils depolymerisation at $55^0 C$. B-E corresponds to a zoom-in on different time-segments of the depolymerisation curve A. As shown in B and C, from time 4h to time 5h oscillations have been observed and for the time segment corresponding to time 15.3 to 15.5h only noise has been detected (D and E). (Figure taken from [55])

Model. We denote the SLS measurements as y_i^n, which corresponds to a noisy signal localized around i/n. Thus i is a location parameter and n a frequency parameter. We obtain

$$y_i^n = x_i^n + \sigma \xi_i^n, \qquad i = 0, \dots, n-1 \tag{2}$$

where $(x_i^n)_{0 \le i \le n-1}$ is the (unknown) signal of interest and the ξ_i are independent and identically distributed noise measurement, that we assume here to be standard Gaussian. The quantity $\sigma > 0$ is a (fixed) noise level. In order to analyze oscillations in a signal, we look at the projection of the signal in the Fourier basis. The discrete Fourier transform (DFT) $\mathsf{DFT}_n : \mathbb{R}^n \to \mathbb{R}^n$ transfers a real-valued discrete signal $(x_i^n)_{0 \le i \le n-1}$ of length n into a frequency domain via

$$\mathsf{DFT}_n\Big[(x_i^n)_{0 \le i \le n-1}\Big] = \Big(\sum_{i=0}^{n-1} x_i^n \mathrm{e}^{-j2\pi ki/n}\Big)_{0 \le k \le n-1} = \big(\vartheta_{n,k}\big)_{0 \le k \le n-1}. \tag{3}$$

The single-sided amplitude spectrum gives all the information needed to visualise the signal $(x_i^n)_{0\leq i\leq n-1}$ in the Fourier basis.

Parametric characterization of HF features in the Fourier Domain. For a discrete signal $(x_i^n)_{0\leq i\leq n-1}$ given in terms of its Fourier transform $\vartheta_n = (\vartheta_{n,k})_{0\leq i\leq n-1}$ via (3), we characterise a HF feature by two nonnegative parameters: a location parameter $\mathsf{g}(\vartheta_n)$ (in the frequency domain) and an intensity parameter $\mathsf{d}(\vartheta_n)$ (see Figure 6).

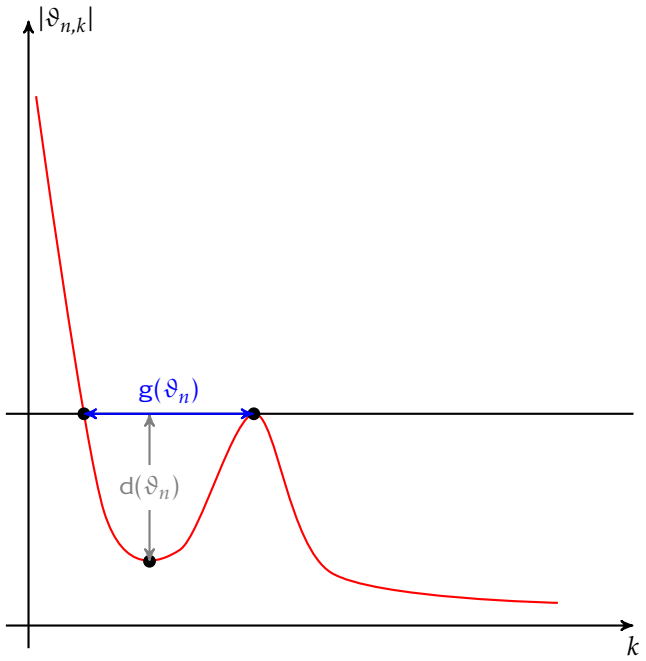

Figure 6 – **Idealized scheme of the parametrization of the HF features of a signal in the Fourier Domain.** The parameter $\mathsf{g}(\vartheta_n)$ is the location parameter in the frequency scale which corresponds to the distance of the HF features from the low-frequency components of the signal. The parameter $\mathsf{d}(\vartheta_n)$ is the intensity parameter which corresponds to the relative amplitude of the HF features.

A more precise definition of the characterisation of HF features is given in **Chapter 1**, Section 1.

Construction of the parametric test of hypothesis. Thanks to the characterisation of HF features, we test the null

$$\mathcal{H}^0_{n,m,\nu,c}:\ \mathsf{g}(\vartheta_n) < \nu, \quad \mathsf{d}(\vartheta_n) < c$$

against the local alternatives

$$\mathcal{H}^1_{n,m,\nu,c}:\ \mathsf{g}(\vartheta_n) \geq \nu \ \text{ and } \ \mathsf{d}(\vartheta_n) \geq c$$

where $\nu > 0$, $c > 0$ are thresholds to determine significant HF features. The null hypothesis $\mathcal{H}^0$, is that there is no significant HF feature in the signal tested. On the contrary, the hypothesis $\mathcal{H}^1$ implies that the

signal has significant HF feature.
In order to compute the p-value of the test, we design a Monte-Carlo procedure simulating a proxy of the data $(y_i)_{0\leq i\leq n-1}$ under the null $\mathcal{H}^0$ (cf **Chapter 1**, Section 1.3.2). Using the proxy, we define a reject region of our test for a risk level α and the p-value of the data $(y_i)_{0\leq i\leq n-1}$. The p-value obtained will be an indicator of the presence of oscillations in the signal tested.

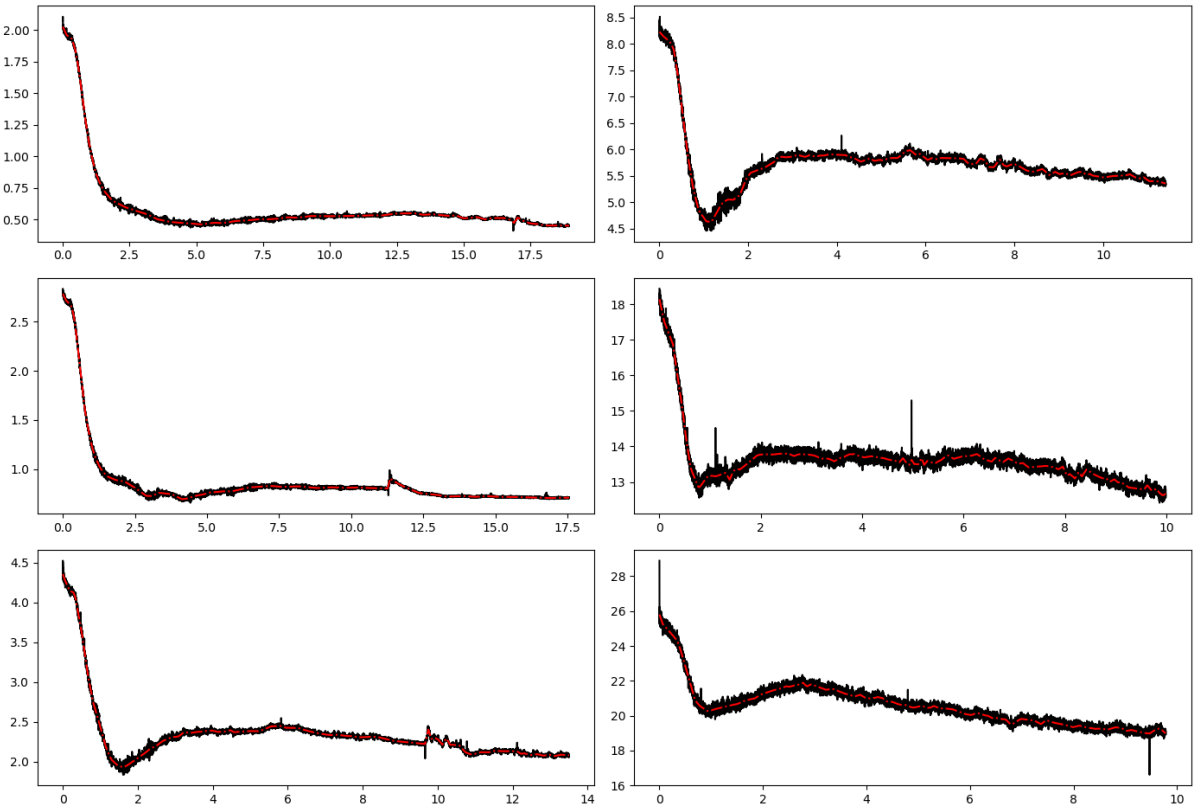

Figure 7 – **SLS experiments and trend estimates.** The x-axis is the time in hours. (Top left) Plot of $n = 32768$ samples of SLS outputs with initial concentration (ρ) of 0.25μmol of PrP^{Sc} fibrils.The dashed line is the trend estimate. (Middle left) $\rho = 0.35\mu$mol (Bottom left) $\rho = 0.5\mu$mol. (Top right) $\rho = 1\mu$mol. (Middle right) $\rho = 2\mu$mol. (Bottom right) $\rho = 3\mu$mol.

Results We first applied the procedure using test signals. This first test allowed us to check the robustness of our procedure. We note that for standard deviations of the noise between a tenth and twice the size of the amplitude of the oscillations, the p-value of the test is small. Hence we are inclined to reject the null hypothesis in favor of the alternative hypothesis. However, when the amplitude of the oscillations is ten times lower than the level noise, we cannot conclude that the signal displays significant oscillations. Moreover, for the test on the SLS signals displayed in Figure 7, we conclude that the signals have oscillations of significant amplitude compared to the noise and we obtain the HF features parameters for each signal. Finally, the numerical procedure to obtain the HF features

parameters of a signal and compute its p-value is implemented in *Python* language and is available online (`https://github.com/mmezache/HFFTest`).

A review on the kinetic models for polymerisation/depolymerisation process

The second objective of this thesis is to propose and study a new polymerisation-depolymerisation model capable of explaining oscillations, which have been observed experimentally in the prion protein polymerisation experiments. We first recall classical results on polymerisation/depolymerisation models for the discrete size setting and for the continuous size setting.

The Becker-Döring model, an overview.

The most natural departure point in the formulation of a suitable mathematical model is the Becker-Döring model of polymerisation and depolymerisation [9]. The Becker-Döring model is coherent with other biological measurements, and it is viewed in the protein polymerisation literature as the "primary pathway" model [18, 126].

Becker-Döring considers two reverse reactions: polymerisation through monomer addition, and depolymerisation due to monomer loss. Accordingly, the model is characterised by the following system of reactions, where $\mathcal{C}_i$ denotes polymers containing i monomers - so that $\mathcal{C}_1$ are the monomers - and a_i, b_i are the polymerisation resp. depolymerisation reaction rate coefficients:

$$\begin{cases} \mathcal{C}_1 + \mathcal{C}_i \xrightarrow{a_i} \mathcal{C}_{i+1}, & i \geq 1, \\ \mathcal{C}_i \xrightarrow{b_i} \mathcal{C}_{i-1} + \mathcal{C}_1, & i \geq 2. \end{cases}$$

The model was popularized in the mathematical communities by Penrose et al. in [122]. The model is formalised by an infinite-size ordinary differential equations (ODE) system. We let $c_i(t) \geq 0$ denote the concentration of polymers of size $i > 0$ at time t. The kinetics of the growth-fragmentation process is the following:

- The concentration of clusters of size i may grow when clusters of size $i-1$ become polymers of size i acquiring 1 monomer with the positive reaction rate a_{i-1} or when clusters of size $i+1$ depolymerise with rate b_{i+1}.

- The concentration of clusters of size i may decrease by polymerising with a monomer with the rate a_i or by depolymerising with the rate b_i.

Hence the rate of increase of the concentration of clusters of size i is

$$J_{i-1}(c) = a_{i-1}c_{i-1}c_1 - b_i c_i, \quad i \geq 2.$$

The variation of the concentrations of each c_i follows the differential equations:

$$\frac{d}{dt}c_i(t) = J_{i-1}(c)(t) - J_i(c)(t), \quad i \geq 2. \tag{4}$$

Monomers are involved in all the reactions, thus the evolution of monomers is denoted c_1 and is driven by the following differential equation:

$$\frac{d}{dt}c_1(t) = -2J_1(c)(t) - \sum_{i\geq 2} J_i(c)(t). \tag{5}$$

Furthermore, the Becker-Döring model describes the kinetics of aggregation-fragmentation process in a closed environment, there is no addition or depletion of element in the system. Consequently, the total mass is a conserved quantity:

$$\sum_{i\geq 1} i c_i(t) = \rho, \quad \forall t \geq 0,$$

where ρ is a constant which denotes the total mass of the system.

Well-posedness. The general result on existence and uniqueness on Becker-Döring first appeared in [7]. Ball et al. rigorously defined the solutions of the system (4)-(5), solutions which belong to the following Banach space:

$$X^+ := \left\{ c \in \mathbb{R}_+^{\mathbb{N}} \ : \ \|c\| = \sum_{i\geq 1} i|c_i| < \infty \right\}.$$

Definition 1. *Let $0 < T \leq \infty]$ and $c(0) := c^0 \in X^+$. A solution $c = (c_i)$ of (4)-(5) on $[0,\ T)$ is a function $c : [0,\ T) \mapsto X^+$ such that*

1. *each c_i is continuous and $\sup_{t\in[0,\ T)} \|c(t)\| < \infty$,*
2. *$\sum_{i\geq 1} a_i c_i \in L^1(0,t)$ and $\sum_{i\geq 1} b_i c_i \in L^1(0,t)$ and*

$$c_i(t) = c_i(0) + \int_0^t J_{i-1}(c)(s) - J_i(c)(s)ds, \quad i \geq 2,$$

$$c_1(t) = c_1(0) - \int_0^t J_1(c)(s) + \sum_{i\geq 2} J_i(c)(s)ds$$

for all $t \in [0,\ T)$.

Ball et al. proved the following theorem in [7] extending the results on a truncated system of finite size by using compactness arguments to pass to the limit.

Theorem 1 (Well-posedness, Theorems 2.2 and 3.6 in[7])**.** *Let $c^0 \in X^+$. Assume $a_i = O(i)$ and $\sum_{i\geq 1} i^2 c_i^0 < \infty$. The Becker-Döring equations* (4)-(5) *have a unique solution c on $[0,\ \infty)$ subject to the initial data c^0. Moreover*

for all $t \geq 0$,

$$\sum_{i\geq 1} i c_i(t) = \sum_{i\geq 1} i c_i^0 := \rho.$$

The well-posedness of the Becker-Döring system has been completed by Laurençot and Mischler in [88], the uniqueness is proved without extra condition on the initial data c^0. However, additional assumptions on the reaction rates are assumed:

$$a_i - a_{i-1} \leq K, \quad b_i - b_{i-1} \leq K, \quad i \geq 2$$

where $K > 0$ is a constant. The well-posedness of the Becker-Döring equations for general assumptions on the reaction rate is extensively studied.

Asymptotic behaviour. Equilibrium solutions $\bar{c} = (\bar{c}_i)_{i\geq 1}$ of (4)-(5) must satisfy the following condition:

$$J_i(\bar{c}) = 0, \quad \forall i \geq 1.$$

This condition leads to a recursion relation $\bar{c}_{i+1} = \frac{a_i}{b_{i+1}} \bar{c}_i$. Finally, we obtain the equilibrium states parametrized only by the monomers concentration $\bar{c}_1$:

$$\bar{c}_i = Q_i (\bar{c}_1)^i, \qquad Q_i := \prod_{j=2}^{i} \left(\frac{a_{j-1}}{b_j} \right) \quad \text{with} \quad Q_1 = 1.$$

Moreover, the equilibrium solutions must satisfy the mass conservation constraint:

$$\sum_{i\geq 1} i Q_i (\bar{c}_1)^i = \rho. \tag{6}$$

The equation (6) provides a delicate issue on the equilibrium solutions of the Becker-Döring system. To find the candidates of the equilibrium solutions leads to consider the power series whose coefficients are iQ_i. We denote the radius of these series z_s. z_s is explicitly obtained in terms of rate coefficients by the Cauchy-Hadamard theorem:

$$z_s^{-1} = \limsup_{i\to\infty} Q_i^{1/i}.$$

Hence, the equilibrium solutions are well defined for $0 \geq c_1 \geq z_s$. Moreover, this leads to meta-stability in the long time behaviour of the Becker-Döring system (cf [124]) since the initial mass of the system ρ may be considered larger as the *critical mass* ρ_s:

$$\rho_s = \sum_{i\geq 1} i Q_i z_s^i.$$

The solutions of (4)-(5) are divided into three categories: the sub-critical solution when $\rho < \rho_s$, the critical solution when $\rho = \rho_s$ and the super-critical solution when $\rho > \rho_s$.
A first result of convergence towards equilibrium was given by Ball et al. in [7]. The reaction rates are

chosen such that the radius of convergence $z_s = +\infty$ and the proof is based on the existence of a Lyapunov functional H which governs the trend to equilibrium:

$$H(c) = \sum_{i\geq 1} c_i \left(\ln\left(\frac{c_i}{Q_i}\right)\right), \quad \frac{d}{dt}H(c) = -p(c(t),$$

where the dissipation is

$$p(c(t)) = \sum_{i\geq 1} (a_i c_1 c_i - b_{i+1} c_{i+1})(\ln(a_i c_1 c_i) - \ln(b_{i+1} c_{i+1})).$$

The results on the convergence towards equilibrium in (4)-(5) was extended by Slemrod in [150], in particular the case where $0 < z_s < \infty$ is treated and the following theorem is established.

Theorem 2 (Convergence to equilibrium, Theorem 5.11 in [150])**.** *Let $c^0 \in X^+$ with mass $\sum_{i\geq 1} i c_i^0 = \rho$ such that $H(c^0) < \infty$. Assume $a_i = O(i)$, $b_i = O(i)$. Assume moreover there exists $z \in [0, z_s]$ such that $a_i z \leq b_i$ for sufficiently large i. Let c be the unique solution to the Becker-Döring equations* (4)-(5) *on $[0,\infty)$ with initial data c^0. Then we have:*

(i) If $0 \leq \rho \leq \rho_s$, then $\lim_{t\to\infty} \sum_{i\geq 1} i|c_i(t) - \bar{c}_i| = 0$.

(ii) If $\rho > \rho_s$, then, for every $i \geq 1$, $\lim_{t\to\infty} c_i(t) = \bar{c}_i$ with $\sum_{i\geq 1} i\bar{c}_i = \rho_s$.

Remark 2. *In Theorem 2 (ii), solutions have a mass ρ for all times, however, as the time goes to infinity, they converge in a weak sense to a steady-state having a strictly inferior mass. The excess $\rho - \rho_s$ is describing the formation of particles with infinite sizes and is related to phase transition [150, 123].*

The Becker-Döring model generated lots of interesting and new mathematical problems and significant results have been proved, e.g. the rate of convergence towards equilibrium [75, 30, 28]. For more results about the Becker-Döring theory, we recall the studies [69, 110, 121, 83, 29].

A continuous polymerisation/depolymerisation model: the Lifshitz-Slyozov model.

The Lifshitz-Slyozov model was first introduced in the seminal paper [95] and was originally designed to formalize the formation of a new phase in solid solution. It describes the formation of aggregates or polymers by the addition of monomers in a continuous size setting. In the following, we denote $v(t)$ the concentration of monomers at time t and $f(t,x)$ the concentration of polymers of size $x > 0$ at time t. In our study, the model describes the kinetics happening during SLS experiments, hence we assume a closed and space-homogeneous environment. This translates into the constraint that the total mass needs to be conserved:

$$v(t) + \int_0^\infty x f(t,x)dx = v(0) + \int_0^\infty x f(0,x)dx := \rho, \quad \forall t \geq 0. \tag{7}$$

We denote by ρ the total mass of monomers and $\int xf(t,x)dx$ can be interpreted as the concentration of monomers in the polymerised form. Hence, the concentration of polymers satisfies the following equation:

$$\frac{\partial f}{\partial t} + \frac{\partial}{\partial x}\Big[(a(x)v(t) - b(x))f(t,x)\Big] = 0, \quad f(0,x) = f_0(x) \geq 0. \tag{8}$$

Note that in (8), the depolymerisation rate is denoted by $b(x)$, the polymerisation rate is denoted by $a(x)$ and both rates can be size-dependent. In the original seminal paper [95], the authors assume the following reaction coefficients

$$a(x) = x^{\frac{1}{3}}, \quad b(x) = 1.$$

Using these definitions of the reaction rates, no boundary condition at $x = 0$ is required since the flux at zero is always going outward. Moreover, one key assumption for the phase transition model is that for larger sizes, the polymerisation rate is bigger than the depolymerisation rate, whereas the reverse is true for smaller sizes. This leads to the phenomenon called "Ostwald ripening" which describes the formation of larger and larger clusters at the expense of smaller ones (see e.g. [95, 109]).
The model containing Equation (8) can be completed by the mass conservation equation (7). Assuming more assumptions on $v(t)$, it can also be completed by the following equation for the concentration of monomers:

$$\frac{dv}{dt} = \int_0^\infty b(x)f(t,x)dx - v(t)\int_0^\infty a(x)f(t,x)dx, \quad v(0) = v_0. \tag{9}$$

From Becker-Döring to Lifshitz-Slyozov. In [39], the authors show that the Lifshitz-Slyozov system can be obtained as an asymptotic limit of the Becker-Döring system. The leading idea to demonstrate the asymptotic equivalence is to consider the functions $(c_i(t))_{i>1}$, the solution of the Becker-Döring system, as a discretisation in space of a function $f(t,x)$, that, with a function v for the monomer concentration, solves the Lifshitz-Slyozov system. The authors introduced a scaling parameter ε and showed that the solution of the Becker-Döring system converges to that of the Lifshitz-Slyozov system as ε goes to 0.

In the following, we describe the main steps to get this result. We start by rewriting the system (4)-(5) in a dimensionless form. The reference quantities used to rescale are:

- T: characteristic time,
- C_1: characteristic value for the monomer concentration,
- C: characteristic value for the polymers concentrations,
- A_1: characteristic value for the polymerisation coefficient a_1,
- A: characteristic value for the polymerisation coefficients a_i $i \geq 2$,
- B: characteristic value for the depolymerisation coefficients,
- M: characteristic value for the total mass,

- M_m: mass of one monomer.

We rescale every variable by its characteristic value:

$$\bar{t} = \frac{t}{T}, \quad \bar{c}_1 = \frac{c_1(\bar{t}T)}{C_1}, \quad \bar{c}_i = \frac{c_i(\bar{t}T)}{C}, \quad \bar{\rho} = \frac{\rho}{M},$$

$$\bar{a}_i = \frac{a_i}{A}, \quad \bar{a}_1 = \frac{a_1}{A_1}, \quad \bar{b}_i = \frac{b_i}{B}, \quad \text{for } i \geq 2.$$

We define the dimensionless parameters :

$$\gamma = \frac{C}{C_1}, \quad \mu = \frac{M}{M_m C_1}, \quad \alpha = ATC_1,$$

$$\alpha_1 = \frac{A_1 C_1}{AC}, \quad \beta = BT.$$

The dimensionless form of the system (4)-(5) is then (omitting the overlines):

$$\begin{cases} \frac{d}{dt}c_i = \alpha(a_{i-1}c_1c_{i-1} - a_ic_1c_i) + \beta(b_{i+1}c_{i+1} - b_ic_i) & i \geq 2, \\ \frac{d}{dt}c_2 = \alpha_1\alpha a_1 c_1^2 - \alpha a_2 c_1 c_2 + \beta(b_3c_3 - b_2c_2), \\ \frac{d}{dt}c_1 = -\gamma\left(2(\alpha_1\alpha c_1^2 - \beta b_2 c_2) + \sum_{i=2}^{\infty}(\alpha a_i c_1 c_i - \beta b_{i+1}c_{i+1})\right), \end{cases} \tag{10}$$

and the mass conservation is

$$c_1 + \gamma \sum_{i=2}^{\infty} i c_i = \mu\rho. \tag{11}$$

The dimensionless parameters γ, μ, α, α_1, β appear as coefficients in (10)-(11). Furthermore, we define the piecewise constant function $f^\varepsilon(t,x)$ as follows:

$$\begin{cases} f^\varepsilon(t,x) = c_i^\varepsilon(t) & \text{if} \quad x \in [i\varepsilon;(i+1)\varepsilon) \quad \text{for } i \geq 2,\ t > 0, \\ f^\varepsilon(t,x) = 0 & \text{if} \quad x \in [0,2\varepsilon), \end{cases}$$

where c_i^ε is the solution of the system (10) with the suitable choice of the dimensionless parameters [39]:

$$\gamma = \varepsilon^2, \quad \mu = 1, \quad \alpha = \beta = \frac{1}{\varepsilon}, \alpha_1 \leq 1.$$

With this choice of parameters, the rescaled version of the system (10)-(11) is:

$$\begin{cases} \frac{d}{dt}c_i = \frac{1}{\varepsilon}(a_{i-1}c_1c_{i-1} - a_ic_1c_i) + \frac{1}{\varepsilon}(b_{i+1}c_{i+1} - b_ic_i) \quad i \geq 2, \\ \\ \frac{d}{dt}c_2 = \frac{1}{\varepsilon}\alpha_1 a_1 c_1^2 - \frac{1}{\varepsilon}a_2c_1c_2 + \frac{1}{\varepsilon}(b_3c_3 - b_2c_2), \\ \\ \frac{d}{dt}c_1 = -\varepsilon\left(2(\alpha_1 c_1^2 - b_2c_2) + \sum_{i=2}^{\infty}(a_ic_1c_i - b_{i+1}c_{i+1})\right), \end{cases}$$

and the mass conservation equation

$$c_1^\varepsilon + \varepsilon^2 \sum_{i=2}^{\infty} i c_i^\varepsilon = \rho.$$

Collet et al. proved in [47] that for ε close to 0, the couple $(c_1^\varepsilon, f^\varepsilon)$ is an approximate solution of the Lifshitz-Slyozov system.

Theorem 3 (First-order approximation, Theorem 2.3 in [39])**.** *Assume that the kinetic coefficients a_i, b_i satisfy*

$$a_i, b_i \leq K, \quad |a_{i+1} - a_i| \leq \frac{K}{i}, \quad |b_{i+1} - b_i| \leq \frac{K}{i}$$

for some constant $k > 0$. Consider a sequence $\varepsilon_n \to 0$.
Then there exist a subsequence, still denoted by ε_n, and two functions $a, b \in W^{1,\infty}((0,\infty)) \cap L^\infty(\mathbb{R}^+)$ such that

$$\lim_{\varepsilon_n \to 0} \sup_{r/\varepsilon_n < i < R/\varepsilon_n} |a_i - a(i\varepsilon_n)| + |b_i - b(i\varepsilon_n)| = 0, \quad \forall\ 0 < r < R < \infty.$$

Assume, moreover, that there exist constants $0 < s \leq 1$, $M_0 < \infty$, $\rho < \infty$, $M_s < \infty$ for which for all $\varepsilon > 0$

$$\varepsilon \sum_{i=2}^{\infty} c_i^{0,\varepsilon} \leq M_0, \qquad c_1^{0,\varepsilon} + \varepsilon^2 \sum_{i=2}^{\infty} i c_i^{0,\varepsilon} = \rho, \qquad \varepsilon \sum_{i=2}^{\infty} (i\varepsilon)^{1+s} c_i^{0,\varepsilon} \leq M_s.$$

Then the subsequence ε_n may be chosen in such a way that

$$\begin{cases} f^{\varepsilon_n} \rightharpoonup f, \quad x f^{\varepsilon_n} \rightharpoonup xf \quad \textit{in} \quad C^0([0,T];\, \mathcal{M}^1(0,\infty) - \textit{weak} - \star), \\ \\ c_1^{\varepsilon_n}(t) \to c_1(t) \quad \textit{uniformly in} \quad C^0([0,T]), \end{cases}$$

where (c, f) is a solution to (7)-(8).

The space $\mathcal{M}^1(0,\infty)$ denotes the space of bounded measures on $(0,\infty)$, it is the dual of the space of continuous function on $(0,\infty)$ with compact support, namely $C_0^0(0,\infty)$. The function f is in this context a measure-valued solutions (see [37]). The proof of Theorem 3 relies on moment estimates and equicontinuity arguments. More details on the link between the Becker-Döring system and the Lifshitz-Slyozov system with different framework can be found in [88, 89, 110, 142].

Moreover, second-order approximations shed light on the link between the Becker-Döring and Fokker-Planck like equations. For example, in [39], the authors introduced the modified Lifshitz-Slyozov equations:

$$\begin{cases} \frac{\partial}{\partial_t} g + \frac{\partial}{\partial_x} G(g;t,x) &= 0, \\ G(g;t,x) &= (a(x)c(t) - b(x))g(t,x) - \varepsilon \frac{\partial}{\partial_x}\left(\frac{a(x)c(t)+b(x)}{2} g(t,x)\right), \\ (a(0)c(t) + b(0))g(t,0) &= 2a_1 c(t)^2, \end{cases} \tag{12}$$

with the mass-conservation law

$$c(t) + \int_0^\infty x g(t,x) dx = \rho.$$

The term with second derivative in space corresponds to a diffusion term. This diffusion term comes from the underlying mechanisms of the discrete Becker-Döring system.

Well-posedness. We recall now some results on the Lifshitz-Slyosov model (8)-(7) or (8)-(9). The well-posedness has been established by Collet and Goudon in [37]. The autors proved the following theorem, stating the existence and uniqueness of solutions of (8)-(7).

Theorem 4 (Well-posedness of the Lifshitz-Slyozov solutions, Theorem 1 in [37])**.** *Let a, b be C^1 functions on $[0,\infty)$ such that*

$$a(x) \geq 0, \quad b(x) \geq 0,$$

$$a(0)M - b(0) \leq 0,$$

$$|a'(x)| + |b'(x)| \leq K.$$

Let the initial data f_0 be nonnegative and satisfy

$$\int_0^\infty f_0(x) dx < \infty, \quad \int_0^\infty x f_0(x) dx < M.$$

Then the system (8)-(7) has a unique solution

$$(v,f) \quad \textit{where} \quad v \in C^0([0,T]), \quad xf \in L^\infty\Big([0,T]; L^1([0,\infty))\Big).$$

The condition $a(0)M - b(0) \leq 0$ ensures the fact that no boundary condition is needed. The proof of the theorem is based on the method of characteristic to obtain an expression of the density function in terms of the monomer concentration and then a fixed-point method.

Asymptotic behaviour. The asymptotic behaviour of the Lifshitz-Slyozov model for general assumptions on the reaction rates is still an open problem. However, Calvo, Doumic and Perthame recently established in [27] the exponential convergence towards a dirac mass in the following theorem.

Theorem 5 (Convergence to a critical mass, Theorem 1.1 in [27]). *Let $a(x) = 1$ and $b(x) \geq 0$ such that*

$$b \in C^1(\mathbb{R}_+), \exists\, \alpha, \beta > 0, \quad 0 < \alpha \leq b'(x) \leq \beta$$

$$v_0 > b(0) \ \geq 0.$$

Moreover, we assume that

$$f_0 \in L^1(\mathbb{R}_+, (1+x^2)dx) \quad with \quad \rho_0 = \int_0^\infty f_0(x)dx > 0.$$

Then there exists a unique solution $\bar{x} > 0$ to the equation

$$M = \rho_0 \bar{x} + b(\bar{x})$$

and the solution $(v, f) \in C^1(\mathbb{R}_+ \times C(\mathbb{R}_+, L^1((1+x^2)dx))$ to the Lifshitz-Slyozov system (8)-(9) is such that $f(t,x)$ converges to $\rho_0 \delta_{\bar{x}}$ exponentially fast in the sense of the Wasserstein distance: for some constant $C > 0$ we have

$$W_2(f(t,\cdot), \rho_0 \delta_{\bar{x}}) \leq Ce^{-\alpha t}, \quad |v(t) - b(\bar{x})| \leq Ce^{-\alpha t}.$$

The proof of Theorem 5 is based on Entropy inequalities. The study of the Lifshitz-Slyozov equations is still an active research field and open problems remain for more general assumptions on the reaction coefficients. Further results can be found in [111, 87, 112, 63, 31] The modified Lifshitz-Slyozov system with a diffusion term seems to be a more realistic continuous setting for the polymerisation/depolymerisation. However, some interesting questions on this continuous setting with diffusion are still under active research [161, 38, 44].

Kinetic models capable of displaying oscillations.

A key question of our study is thus the following: What kind of core elements should a model feature in order to explain the appearance of such oscillations? A recent study from Pego and Velazquez [120] shows that oscillations occur in a modified Becker-Döring-type model. The model considered is of finite size and the clusters of maximal size are subject to *atomization*, a chemical reaction which converts clusters into monomers. Pego and Velazquez proved the existence of Hopf bifurcations when the parameter corresponding to the atomization coefficient is varying. They introduced a Becker-Döring model with atomization in order to explain gas evolution oscillators in physical chemistry and its oscillatory behaviour is closely linked to atomization. However, in the experiments leading to Figure 5, no evidence of

atomization have been found. Moreover, the oscillations in the SLS signals are always damped, i.e. located on a specific time interval. Hence, growth-fragmentation models with atomization do not seem appropriate to explain transient oscillations in the prion fibrils experiments.
To date, very few mathematical models have taken into account the coexistence of multiple prion assemblies or multiple type of fibrils [41]. Indeed, most of the aggregation models have been built using the canonical nucleation-elongation-fragmentation process seminally reported by Bishop and Ferrone (see e.g. [18, 98, 126]), which is based on the existence of a structurally unique type of assemblies characterised only by their size distribution. The characterisation of multiple types of PrPSc subassemblies with different rates of polymerisation, depolymerisation requires new mathematical models. The analysis of the dynamics and relation between different subspecies leads to interesting new questions.

Discrete bi-monomeric Becker-Döring type model.

The most natural departure point in the formulation of a suitable mathematical model to describe the kinetics behind the SLS experiments in Figure 5 is the Becker-Döring model of polymerisation and depolymerisation. However damped oscillations, up to the best of our knowledge, have never been observed numerically or evidenced analytically. We thus needed a variant of the Becker-Döring model to explain the experimentally observed oscillations displayed in Figure 5. The model and its study is detailed in **Chapter 2**. We present here an overview of the results obtained.

Model. In [74], it was recently shown that PrPSc assemblies are in equilibrium with an oligomeric conformer (suPrP) encoding the entire strain information and constituting an elementary building block of PrPSc assemblies. The fact that such an oligomeric building block appears separately from the monomeric PrP points towards models with two different quasi-monomeric species (i.e. one monomer and one oligomeric conformer in contrast to the polymer species $\mathcal{C}_i$), each of which playing a role in a different reaction. A suitable mathematical model should also take into account the constraint that large polymers cannot interact directly, for reasons of size and order of magnitude of their concentrations. Hence, we assume that polymers can only interact indirectly, through the exchange of monomers or small oligomeric conformers.
We propose the following model system: Let $\mathcal{V}$ and $\mathcal{W}$ denote the two monomeric species. Let $\mathcal{C}_i$ be the polymers containing i monomers, where polymerisation signifies the amendment of a monomer $\mathcal{W}$ while depolymerisation only occurs when induced via the monomeric species $\mathcal{V}$. More precisely, we consider

$$\begin{cases} \mathcal{V}+\mathcal{W} & \xrightarrow{k} & 2\mathcal{W}, & \\ \mathcal{W}+\mathcal{C}_i & \xrightarrow{a_i} & \mathcal{C}_{i+1}, & 1 \le i \le n, \\ \mathcal{C}_i+\mathcal{V} & \xrightarrow{b_i} & \mathcal{C}_{i-1}+2\mathcal{V}, & 2 \le i \le n. \end{cases} \tag{13}$$

with a reaction rate constant k for the monomer/conformer dynamics and polymerisation/depolymerisation coefficients a_i and b_i.
We emphasize the two main differences of (13) as compared to the classical Becker-Döring system:

First, instead of one monomeric species c_1, we now consider two interacting species of monomers (or conformers), $\mathcal{V}$ and $\mathcal{W}$. Secondly, depolymerisation is modelled as a monomer induced, nonlinear process, which requires the catalytic action of $\mathcal{V}$. Note that this process is reminiscent of the cyclical behaviour of the three-species system:

$$\mathcal{V}+\mathcal{W} \quad \xrightarrow{k} \quad 2\mathcal{W}, \qquad \mathcal{W}+\mathcal{M} \quad \xrightarrow{a} \quad 2\mathcal{M}, \qquad \mathcal{M}+\mathcal{V} \quad \xrightarrow{b} \quad 2\mathcal{V}, \tag{14}$$

which is known to produce sustained periodic oscillations, see [162], where it is called the Ivanova system, or [158], where it is referred to as a simplification of the Belousov-Zhabotinsky system.
We denote by $c_i(t)$, $v(t)$ and $w(t)$ the concentrations at time t of the polymers containing i monomers, the depolymerising and the polymerising monomeric species. As in [124], we introduce the net rate of an i-polymer being converted to an $(i+1)$-polymer by

$$J_i = wa_ic_i - vb_{i+1}c_{i+1}, \qquad 1 \le i \le n-1.$$

With the convention $J_0 = J_n = 0$, by using the mass-action law, model (13) yields the following system of differential equations:

$$\begin{cases} \frac{dv}{dt} &= -kvw + v\sum\limits_{i=2}^{n} b_ic_i, & v(0) = v^0, \\ \frac{dw}{dt} &= -w\sum\limits_{i=1}^{n-1} a_ic_i + kvw, & w(0) = w^0, \\ \frac{dc_i}{dt} &= J_{i-1} - J_i, & c_i(0) = c_i^0, \quad 1 \le i \le n. \end{cases} \tag{15}$$

We first remark that solutions to System (15) have two conserved quantities, obtained by weighted sums of the equations:

1. The total concentration of polymerised species, since $\frac{d}{dt}\sum\limits_{i=1}^{n} c_i = 0$. This conservation law is linked to the fact that we neglect nucleation.

2. The total mass, since $\frac{d}{dt}\Big(v + w + \sum\limits_{i=1}^{n} ic_i\Big) = 0$, which indicates that there is no gain or loss of particles during the chemical reactions: the system is closed.

As a consequence of those two conservation laws, we introduce

$$P_0 := \sum_{i=1}^{n} c_i^0, \qquad M_{tot} := v^0 + w^0 + \sum_{i=1}^{n} ic_i^0.$$

Moreover, we denote as $M_k(t)$ the moment of order k of $c = (c_i)$ for $k \in \mathbb{N}^*$:

$$M_k(t) = \sum_{i\ge 1} i^k c_i(t). \tag{16}$$

The signal obtained by the SLS experiments is approximated by the second order moment of the size distribution of c in the model and the numerical simulations.

Well-posedness. We introduce the Banach sequence spaces

$$\ell_1^1 = \{y = (y_i) \,:\, \|y\| < \infty\}, \qquad \|y\| = \sum_{i=1}^{\infty} i|y_i|.$$

and

$$\mathcal{X} = \{x = (v, w, c) = (v, w, c_1, c_2, \ldots) \,:\, \|x\|_{\mathcal{X}} < \infty\}, \qquad \|x\|_{\mathcal{X}} = |v| + |w| + \|c\|.$$

Definition 2. *Let $0 < T \leq \infty$ and $c = (c_i)$. A nonnegative solution $x = (v, w, c)$ of (15) with $n = \infty$ on $[0, T)$ is a function $x \,:\, [0, T) \to \mathcal{X}$ such that*

1. *$x(t) \geq 0$ for all $t \in [0; T)$, i.e. $v(t) \geq 0$, $w(t) \geq 0$, $c_i(t) \geq 0$ for each i,*
2. *$v, w : [0, T) \to \mathbb{R}$ and $c_i : [0, T) \to \mathbb{R}$ for all $i \geq 1$ are continuous with $\sup_{t\in[0,T)} \|x(t)\|_{\mathcal{X}} < \infty$,*
3. *$\int_0^t \sum_{i=1}^{\infty} a_i c_i(s) ds < \infty$, $\int_0^t \sum_{i=2}^{\infty} b_i c_i(s) ds < \infty$ for all $t \in [0, T)$ and*
4. *v, w and c satisfy for all $t \in [0, T)$*

$$\begin{cases} v(t) = v_0 + \displaystyle\int_0^t \left(-kv(s)w(s) + v(s) \sum_{i=2}^{\infty} b_i c_i(s) \right) ds, \\ w(t) = w_0 + \displaystyle\int_0^t \left(-w(s) \sum_{i=1}^{\infty} a_i c_i(s) + kv(s)w(s) \right) ds, \\ c_i(t) = c_i^0 + \displaystyle\int_0^t \Big(J_{i-1}(s) - J_i(s) \Big) ds, \quad i \geq 1,\ J_0 = 0. \end{cases}$$

Theorem 6 (Well-posedness of the infinite dimensional system)**.**
Let $T > 0$ be arbitrary and consider $x_0 = (v_0, w_0, c_0)$ satisfy $\|x_0\|_{\mathcal{X}} < \infty$. Assume

$$a_i = O(i), \qquad b_{i+1} = O(i + 1), \qquad \forall\ i \geq 1.$$

Then, System (15) with $n = \infty$ has a nonnegative solution for $t \in [0, T)$ with $v(t) \geq 0$, $w(t) \geq 0$, $c_i(t) \geq 0$ for $t \geq 0$ and all $1 \leq i$ satisfying

$$v(t) + w(t) + \sum_{i=1}^{\infty} i c_i(t) = v_0 + w_0 + \sum_{i=1}^{\infty} i c_i^0, \qquad \sum_{i=1}^{\infty} c_i(t) = \sum_{i=1}^{\infty} c_i^0, \qquad \forall t \geq 0.$$

Moreover, if $\sum_{i=1}^{\infty} i^2 c_i^0 < \infty$, then the solution is unique and satisfies

$$\sup_{t\in[0,T)} \sum_{i=1}^{\infty} i^2 c_i(t) < \infty.$$

The proof of Theorem 6 adapts well-known results of the Becker-Döring system as presented in [7]. The main novelty lies in the nonlinearity of the depolymerisation terms, which requires the supplementary assumption for the b_i.

Asymptotic behaviour. The main issue encountered in the study of the asymptotic behaviour of the solutions of (15) is that no Lyapunov functional (Entropy) is known. Hence, in order to have some insights on its behaviour, we study the system when $n = 2$, $n \in \mathbb{N}$ with $n < \infty$ and $n = \infty$. First, we provide a complete and explicit study of the two-polymer case $n = 2$, which features a pivotal mechanism of damped periodic oscillations in the case of a large reaction rate k compared to the polymerisation coefficients.Let the reaction rates $a_1 = 1$, $b_2 = 1$ (for the sake of clarity). Using the conservation laws, the system (15) is reduced to two coupled differential equations:

$$\begin{cases} \frac{dv}{dt} = v\,[M - (k+1)w - v], & v(0) = v^0, \\ \frac{dw}{dt} = w\,[(M - P_0) + (k-1)v - w], & w(0) = w^0, \end{cases} \tag{17}$$

where $M = M_{tot} - P_0$. The above system is a generalization of the Lotka-Volterra system in its quadratic form. Under the assumption $P_0 \in \left(\frac{kM}{1+k}, kM\right)$, there is a unique positive steady-state for (17) which is the intersection of the null-clines. We denote this positive steady-state (v_∞, w_∞).

Theorem 7 (Exponential convergence to positive equilibrium)**.**
Let $P_0 \in \left(\frac{kM}{1+k}, kM\right)$ and consider v, w the solutions of (17) *with $(v_\infty, w_\infty) > 0$ the positive steady state. Let $H : \mathbb{R}_+^* \times \mathbb{R}_+^* \mapsto \mathbb{R}$ the differentiable function such that*

$$H(v, w) = v - v_\infty \log(v) + w - w_\infty \log(w).$$

Then, H is a convex Lyapunov functional.

$$\frac{d}{dt} H(v(t), w(t)) = -\frac{1}{k}\, p^2(v(t), w(t)),$$

with $p(v, w) := [(v - v_\infty) + (w - w_\infty)]$.

Moreover, for $\frac{1}{k} << 1$, every solution $(v(t), w(t))$ with initial data $(v_0, w_0) > 0$ converges exponentially to (v_∞, w_∞), i.e.

$$|v - v_\infty|^2 + |w - w_\infty|^2 \leq C\left(H(v^0, w^0) - H(v_\infty, w_\infty)\right) e^{-\frac{1}{k} rt},$$

where the positive rate r and constant C depend only on $H^0 := H(v^0, w^0)$ and (v_∞, w_∞).

Theorem 7 states the existence of a Lyapunov functional and proves exponential convergence to an equilibrium of solutions despite their highly oscillatory behaviour. The proof is based on convex local estimates around the degeneracy line $\frac{d}{dt} H = 0$ and the entropy dissipation method.

Secondly, we focus on the case where the maximal size of polymers n is finite. We study the existence of steady states and their stability. We introduce several parametric regions – graphically illustrated in Figure 8– which will defining the stability or instability regions of the boundary steady states (BSS).

$$n + \frac{b_n}{k} \leq \frac{M_{tot}}{P_0} \qquad \text{(region with horizontal green stripes in Fig. 8),} \tag{18}$$

$$n < \frac{M_{tot}}{P_0} < n + \frac{b_n}{k} \qquad \text{(light blue region in Fig. 8),} \tag{19}$$

$$\frac{M_{tot}}{P_0} \leq 1 + \frac{a_1}{k} \qquad \text{(grey diagonally hatched region in Fig. 8).} \tag{20}$$

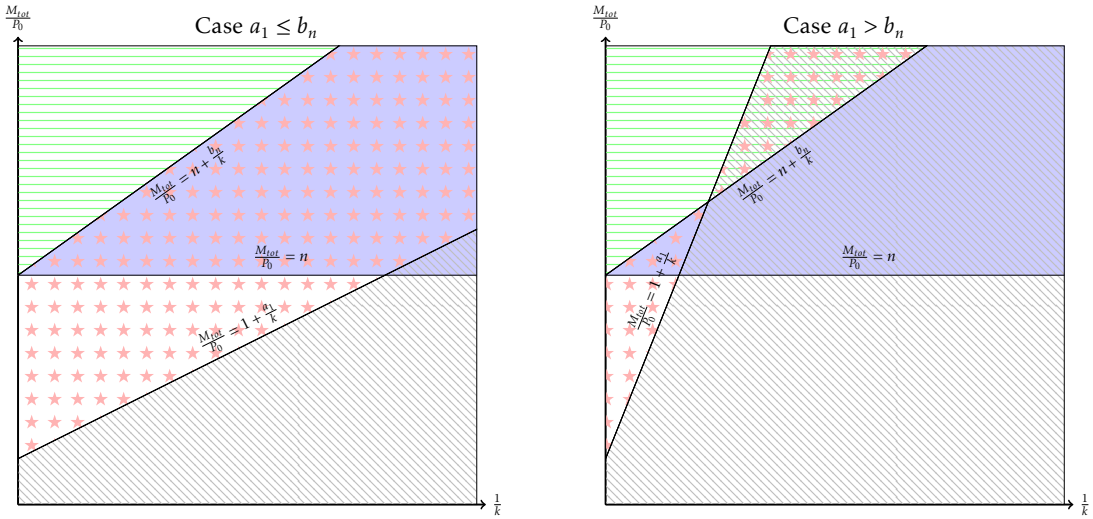

Figure 8 – Stability regions of the SSs of the finite system (15) in the $\frac{1}{k}$-$\frac{M_{tot}}{P_0}$ parametric space: (BSSa) are always unstable. Grey diagonally hatched zone $\iff$ (20) $\iff$ asymptotically stable (BSSb), which is unstable elsewhere. Green horizontal lines $\iff$ (18) $\iff$ asymptotically stable (BSSc). Light blue zone $\iff$ (19) $\iff$ unstable (BSSc). Zone with red stars $\iff$ existence of at least one PSS (in case $a_1 > b_n$ coexisting with a stable (BSSb) in the horizontally hatched region; otherwise coexisting only unstable BSSs.)

Proposition 1 (Nonnegative Steady States)**.**
Let $a_i > 0$, $b_{i+1} > 0$ for $1 \leq i \leq n-1$, let v_0, $w_0 > 0$ and $P_0 > 0$, $M_{tot} \geq v_0 + w_0 + P_0 > 0$. Then,

1. *there exists three kinds of boundary steady states (BBS):*

   (BSSa) There exist unstable BSSs: $\bar{v} = \bar{w} = 0$ and $(\bar{c}_i)_{1\leq i\leq n}$ satisfies $\sum_{i=1}^{n} \bar{c}_i = P_0$, $\sum_{i=1}^{n} i\bar{c}_i = M_{tot}$.

   (BSSb) There exists a BSS: $\bar{v} = M_{tot} - P_0 > 0$, $\bar{w} = 0$, $\bar{c}_1 = P_0$, $\bar{c}_i = 0$ for $2 \leq i \leq n$. This BSS is locally asymptotically stable under Assumption (20) *(grey diagonally hatched in Fig. 8) and unstable elsewhere.*

(BSSc) Under the additional assumption $\frac{M_{tot}}{P_0} > n$*, there exists another BSS:* $\bar{v} = 0$*,* $\bar{w} = M_{tot} - nP_0 > 0$*,* $(\bar{c}_i)_{1\le i\le n-1} = 0$ *and* $c_n = P_0$*. This BSS is locally asymptotically stable under Assumption* (18) *(green horizontal lines) and otherwise unstable, which corresponds to Assumption* (19) *(light blue zone).*

2. *There exists (at least one) positive steady state (PSS)* $(\bar{v}, \bar{w}, \bar{c}_i)_{1\le i\le n}$ *provided that the polynomial* $P(z)$ *defined as*

$$P(z) := \left[\frac{a_1}{k} + 1 - \frac{M_{tot}}{P_0}\right] + \sum_{i=2}^{n-1}\left[\left(\frac{a_i}{k} + i - \frac{M_{tot}}{P_0} + \frac{b_i}{k}\right)\prod_{j=0}^{i-1}\frac{a_j}{b_{j+1}}\right]z^{i-1} + \left[\left(n - \frac{M_{tot}}{P_0} + \frac{b_n}{k}\right)\prod_{j=0}^{n-1}\frac{a_j}{b_{j+1}}\right]z^{n-1} \tag{21}$$

has a root $\bar{z} > 0$*. Given* $\bar{z} > 0$*, we have*

$$\begin{aligned} \bar{v} &= \bar{c}_1 \sum_{i=1}^{n-1}\frac{a_i}{k}\bar{z}^{i-1}\prod_{j=0}^{i-1}\frac{a_j}{b_{j+1}}, & \bar{w} &= \bar{c}_1 \sum_{i=1}^{n-1}\frac{a_i}{k}\bar{z}^{i}\prod_{j=0}^{i-1}\frac{a_j}{b_{j+1}}, \\ \bar{c}_1 &= \frac{P_0}{\sum_{i=1}^{n}\bar{z}^{i-1}\prod_{j=0}^{i-1}\frac{a_j}{b_{j+1}}}, & \bar{c}_i &= \bar{z}^{i-1}\prod_{j=0}^{i-1}\frac{a_j}{b_{j+1}}\bar{c}_1, \quad 2 \le i \le n. \end{aligned} \tag{22}$$

If all BSSs are unstable, i.e. $1 + \frac{a_1}{k} < \frac{M_{tot}}{P_0} < n + \frac{b_n}{k}$*, then there exists at least one positive steady state. Moreover, if the sequences* (a_i)*,* (b_i) *are nondecreasing, the positive steady state is unique.*

Further details are obtained in the case of constant coefficients, where we discuss the various zones of stability or instability with respect to the parameters in **Chapter** 2, Section 2.4. Moreover, numerical simulations of the system illustrate the oscillatory behaviour of the size distribution of the concentration of polymers, see Figure 9.

Finally, we analyze steady states of the infinite system $n = \infty$. In the following, we assume that the coefficients satisfy

$$a_i > 0,\ b_{i+1} > 0, \quad \forall i \ge 1 \qquad \text{and} \qquad \exists\, K > 0 : \quad \max_{i\ge 1}\left\{\frac{a_i}{i}, \frac{b_i}{i}, \frac{a_i}{b_{i+1}}\right\} \le K. \tag{23}$$

Proposition 2 (Steady states of the infinite case system and their local stability)**.**
Let $v_0 > 0$*,* $w_0 > 0$*,* $P_0 > 0$ *and* $M_{tot} \ge v_0 + w_0 + P_0 > 0$*. Let* $(a_i, b_{i+1})_{i\ge 1}$ *satisfy* (23)*.*

Then, there exist the following steady states $(\bar{v}, \bar{w}, \bar{c}_{i\ge 1})$ *of System* (15) *with* $n = \infty$*:*

(BSSa) The trivial BSSs $\bar{v} = \bar{w} = 0$ *and* $\bar{c}_{i\ge 1} \in \ell^1_1$ *satisfying*

$$\sum_{i=1}^{\infty}\bar{c}_i = P_0, \qquad \text{and} \qquad \sum_{i=1}^{\infty} i\bar{c}_i = M_{tot},$$

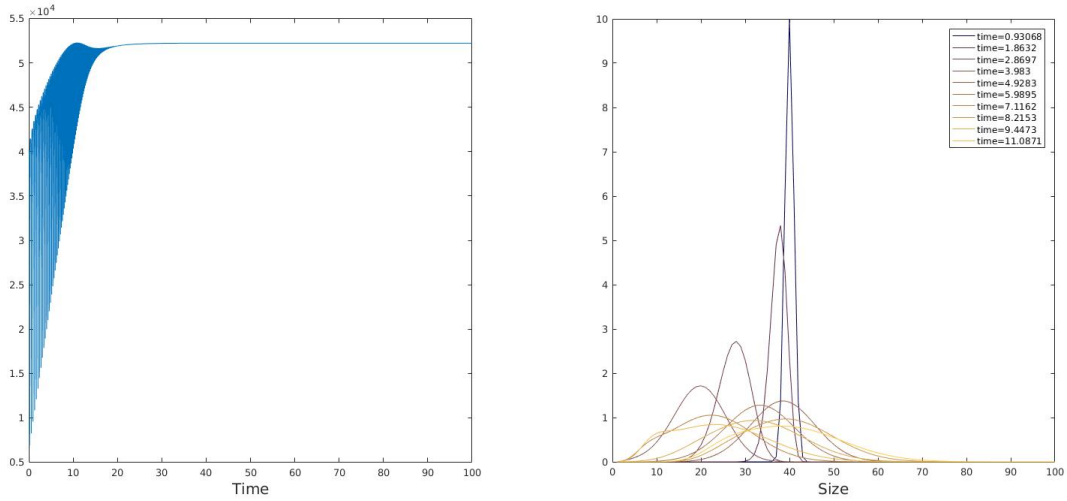

Figure 9 – Numerical simulation of convergence to (PSS):SLS simulation (left image) and evolution of the size distribution (right images). The reaction rates are constants. The parameters are $n = 100$, $k = 1.1$, $a = 1.5$, $b = 2$ and the assumption $1 + \frac{a}{k} < \frac{M_{tot}}{P_0} < n + \frac{b}{k}$ is fulfilled (all BSSs are unstable).

which are always linearly unstable.

(BSSb) *The BSS* $\bar{v} = M_{tot} - P_0$, $\bar{w} = 0$, $\bar{c}_1 = P_0$ *and* $\bar{c}_{i\geq 2} = 0$. *This steady state is locally asymptotically stable* iff

$$\frac{M_{tot}}{P_0} \leq \frac{a_1}{k} + 1. \tag{24}$$

(PSS) *Under assumption* (2.40), *there exists no positive steady state (PSS). Conversely, if*

$$\frac{M_{tot}}{P_0} > \frac{a_1}{k} + 1, \tag{25}$$

then there exists a unique PSS $(\bar{v}, \bar{w}, \bar{c}_{i\geq 1})$. *Note that as already noted for the n-polymer model, the stability of the PSS is an open problem.*

Proposition 2 proved that there exists a unique positive steady state under assumption (25). This assumption means that the ratio $\frac{M_{tot}}{P_0}$ needs to be "sufficiently large", else the polymers are unstable in the sense that all the mass goes back to the polymer of minimal size c_1. Moreover, two specific cases shed light on the damped oscillations: the constant coefficient case (i.e. $a_i = a$, $b_i = b$ for two positive constants a and b and for all i) and the linear coefficient case (where $a_i = ia$, $b_i = (i-1)b$, for two positive constants a and b and for all i).

Continuous bi-monomeric Lifshitz-Slyozov type model.

The study of a Becker-Döring type model for large clusters is a challenge, few results exist on non-linear infinite size differential systems and the computational cost for numerical simulations is a limiting obstacle. The maximum size in PrP^{Sc} fibrils is of order 10^4, hence considering a continuous size setting is beneficial in order to provide more insights on the kinetics of Prion process. The continuous setting is viewed as the "macroscopic" limit of the Becker-Döring type model and the mathematical structure of the resulting PDE-ODE system appears to be simpler. Hence, we introduce the corresponding bi-monomeric Lifshitz Slyozov type system and study its asymptotical behaviour. The following results are detailed in **Chapter 3** .

Model. In the previous Section, we detailed the study and results on the bi-monomeric Becker-Döring type system. We may now consider the size of clusters as a continuously varying variable $x > 0$ which now replace i. The quantity $f(t,x)$ denotes the density of aggregates of size x at time t, and $v(t)$, $w(t)$ denote the concentration of monomers. We then obtain the following equations:

$$\begin{cases} \partial_t f + \partial_x J = 0, \quad x > 0,\ t \geq 0, & f(0,x) = f^0(x), \\ J(t,x) = \Big(a(x)w(t) - b(x)v(t)\Big)f(t,x), & \\ \frac{d}{dt}v(t) = -kv(t)w(t) + v(t)\int_0^\infty b(x)f(t,x)dx, & v(0) = v_0 > 0, \\ \frac{d}{dt}w(t) = -w(t)\int_0^\infty a(x)f(t,x)dx + kv(t)w(t), & w(0) = w_0 > 0, \\ 0 = \Big(a(0)w(t) - b(0)v(t)\Big)f(t,0)\mathbb{1}_{\{a(0)w(t)-b(0)v(t)>0\}}, & \forall t > 0. \end{cases} \tag{26}$$

The system (26) is viewed as the "macroscopic" limit of the system (15) with $n = \infty$. Also, the solutions of the system (26) follow a conservation law of the total mass M of the population:

$$v(t) + w(t) + \int_0^\infty x f(t,x)dx = v_0 + w_0 + \int_0^\infty x f^0(x)dx = M. \tag{27}$$

We denote the moment of magnitude n by M_n:

$$M_n(t) = \frac{1}{n}\int_0^\infty x^n f(t,x)dx,$$

and the total number of polymers by ρ:

$$\rho(t) = \int_0^\infty f(t,x)dx.$$

The last equation of (26) is a boundary condition which can be interpreted as the absence of the nucleation phenomenon. It implies that total concentration of polymerised fibrils remains constant:

$$\rho(t) = \int_0^\infty f(t,x)dx = \int_0^\infty f_0(x)dx = \rho_0.$$

We are interested in the steady-state and we denote two kinds of steady-state:

- the trivial steady-states: $\overline{f}(x) = 0$ and $v_\infty + w_\infty = M$. It corresponds to a boundary steady-state and can be interpreted as the non pathological equilibrium. All fibrils are converted into the two species of monomers and the two species of monomers are at equilibrium.
- The nontrivial steady-state which enforce the following: there exists $x > 0$ such that $\overline{f}(x) \neq 0$. It can be interpreted as the pathological steady-state since polymers can be found at equilibrium.

We denote with $(v_\infty, w_\infty, \overline{f})$ the quantities at equilibrium.

Main results on the system (26)**.** We note that the system in (26) is a coupled PDE/ODE system. The ODE part of the system is the following:

$$\begin{cases} \frac{d}{dt}v(t) = -kv(t)w(t) + v(t)\int_0^\infty b(x)f(t,x)dx, \\ \\ \frac{d}{dt}w(t) = -w(t)\int_0^\infty a(x)f(t,x)dx + kv(t)w(t). \end{cases} \tag{28}$$

The solution of the PDE in (26) has an influence on the solutions of the ODE through an integral term. However, assuming some rightfully chosen hypothesis on the reaction coefficients $a(x)$ and $b(x)$, the system (26) has 2 conserved quantities:

- $\int_0^\infty xf(t,x)dx + v(t) + w(t) = M$,
- $\int_0^\infty f(t,x)dx = \rho_0$.

In order for the ODE system to be decoupled of the PDE solution in (26), the reaction coefficient functions have to be either constant, linear or affine function of the size variable $x > 0$. This comes from the fact that the integral terms in (28) is replaced by one of the conserved quantities.
An interesting result is obtained if we suppose that the reaction rates are both linear:

$$\exists a,\ b > 0, \quad a(x) = ax, \quad b(x) = bx.$$

In this case, the solutions (v, w) of (28) are periodic as well as the solution f of (26). We obtain the following result.

Proposition 3. *Let* $(v, w, f) \in \mathcal{C}_b^1(\mathbb{R}_+) \times \mathcal{C}_b^1(\mathbb{R}_+) \times \mathcal{C}\left(\mathbb{R}_+, L^1\right)$ *be any nonnegative solution of* (26) *and* (27) *such that the initial datum verifies* $v_0,\ w_0 > 0$ *and* $v_0 + w_0 < M$*. Assume that* $a, b \in \mathcal{C}^1(\mathbb{R}_+)^+$ *satisfy* $a(x) = ax, \quad b(x) = bx$ *with* $a,\ b > 0$ *and* $\forall x > 0$*. Then the following statements hold true:*

1. *The solutions $v(t), w(t)$ of* (28) *are periodic.*

2. *The solution f of* (26) *is periodic of the same period as v, w.*

The proof of this proposition is detailed in Chapter 3. This result shows that the solution of the bi-monomeric Lifshitz-Slyozov model (26) are periodic. Such a result is not observed in the experiments since the continuous model is a first order approximation of the "true" discrete model. The second order correction, a diffusion term, would dominate and change the behaviour of the solutions.
Moreover, even without the second order correction (the diffusion term), we show that the solutions of the system (26) display damped oscillations and f concentrate its mass at a critical size when $a(x) = 1$, $b(x) = bx$ with $b > 0$, $\forall x \geq 0$.

Theorem 8 (Concentration at a critical size)**.** *Assume that the initial datum verifies v_0, $w_0 > 0$ such that $v_0 + w_0 < M$ and $f_0 \in L^1(\mathbb{R}_+, (1+x^2)dx)$ with $\rho_0 = \int_0^\infty f_0(x)dx > 0$. Moreover let $k > 1$ with k sufficiently large and $0 < \rho_0 < kM$. And finally, assume that $a, b \in \mathcal{C}^1(\mathbb{R}_+)^+$ satisfy $a(x) = 1$, $b(x) = bx$ with $b > 0$, $\forall x \geq 0$.*
The solution $(v, w, f) \in \mathcal{C}_b^1(\mathbb{R}_+) \times \mathcal{C}_b^1(\mathbb{R}_+) \times \mathcal{C}\left(\mathbb{R}_+, L^1\right)$ to the system (26) *and* (27) *are such that $f(t,x)$ converges to $\rho_0 \delta_{\frac{w_\infty}{bv_\infty}}$ exponentially fast in the sense of the Wasserstein distance: for some constant $C > 0$ we have*

$$W_2\left(f(t,\cdot), \rho_0 \delta_{\frac{w_\infty}{bv_\infty}}\right) \leq Ce^{-\beta t}, \quad |X(t,z) - \tfrac{w_\infty}{bv_\infty}| \leq Ce^{-\beta t}.$$

The proof of Theorem 8 relies on one entropy inequalites, inspired by [27], and local convexity estimates for a Lyapunov functional, inspired by [55]. This result shows that the solution of the bi-monomeric Lifshitz-Slyozov system converges to a specific steady-state

$$(v(t), w(t), f(t,\cdot)) \quad \xrightarrow[t\to\infty]{} \quad \left(v_\infty, w_\infty, \rho_0 \delta_{\frac{w_\infty}{bv_\infty}}\right).$$

The behaviour of the continuous bi-monomeric model is closely linked to the form of the reaction coefficients. We proved the existence of periodic solution in case of linear reaction coefficients and the convergence towards a positive steady-state (assimilated as the pathological state) for linear depolymerisation and constant polymerisation coefficients. On the contrary, only damped and not sustained oscillatory solutions have been observed for the discrete bi-monomeric model. The solutions either converge to the positive steady-state or the boundary steady-state. This difference between the continuous and the discrete model can be explained by the absence of the diffusion term in the continuous model.

Biochemical evidence of heterogeneity of the structure of amyloid fibrils.

The experiments studied in **Chapter 4** provide new hypothesis on the molecular structure of Prion assemblies. In order to ascertain the new mechanisms in Prion assemblies, we model the kinetics and confront the experimental results with numerical simulations. Biochemical experiments and modeling

help to gain more insights and knowledge about prion diseases. In **Chapter 4**, we study the quaternary structure (size distribution and architecture) of prion assemblies. We first describe the experiments. Then we explain how experiments show the heterogeneity of prion assemblies and the existence of at least two sub-assemblies and how models comfort the hypothesis.

Biological experiments.

Protein Misfolded Cyclic Amplification (PMCA) experiments. PMCA (Protein Misfolded Cyclic Amplification) is an amplification protocol that accelerates the conversion of PrP^c protein to PrP^{Sc} in vitro. The technique consists of submitting a sample containing a small amount of PrP^{Sc} at an alternation of incubation and sonication phases. The incubation phases are intended to promote the polymerization of aggregates. For this purpose the sample is left to rest in the presence of a large amount of PrP^c. The sonication phases have the following objectives to significantly increase polymer fragmentation. The sample is then placed in a sonicator that breaks aggregates with ultrasound (cf Figure 10). The efficiency of the protocol depends in part on the duration of the various phases. PMCA is one of the method to reproduce in vitro the early replication stage of Prion diseases.

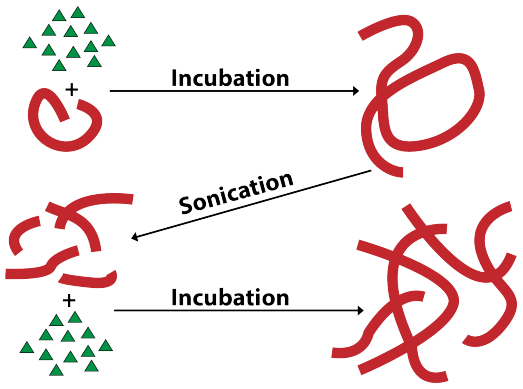

Figure 10 – Scheme of the Protein Misfolded Cyclic Amplification (PMCA) experimental process.

Size distribution by sedimentation velocity (S.V) experiments. Sedimentation velocity is an analytical ultracentrifugation (AUC) method that measures the rate at which molecules move in response to centrifugal force generated in a centrifuge [145, 36, 141]. This sedimentation rate provides information about both the molecular mass and the shape of molecules. This experimental method is used to detect aggregates in protein samples and to quantify the amount of aggregates. The sedimentation coefficient s is defined as the ratio of the linear velocity of sedimentation of a protein v over the the gravitational field $\omega^2 r$ (where ω is the angular velocity and r is the distance form the center of rotation):

$$s = \frac{v}{\omega^2 r}.$$

The forces acting on a particle during a sedimentation experiment are the gravitational field which depends on the mass of the particle M_p and the friction with the solvent. The friction is a counterforce exerted on the particle by the solvent and is characterized by the frictional coefficient f. The sedimentation coefficient satisfies also the following relationship [36]:

$$s = \frac{M_p(1 - \bar{v}\rho)}{f},$$

where $\bar{v}$ is the partial specific volume of the particle and ρ is the density of the solvent. $M_p(1 - \bar{v}\rho)$ characterizes the effective mass of the particle during the experiment. The negative term comes from the counterforce exerted by the mass of the solvent which is displaced when the particle sediments. More details on sedimentation velocity can be found in [36, 46, 101, 141] .

Several different methods using sedimentation velocity have been developed to perform a size distribution analysis of protein polymers [144, 72, 92]. During sedimentation velocity experiments, the particles with the most mass and the best hydrodynamic properties sediment the fastest.

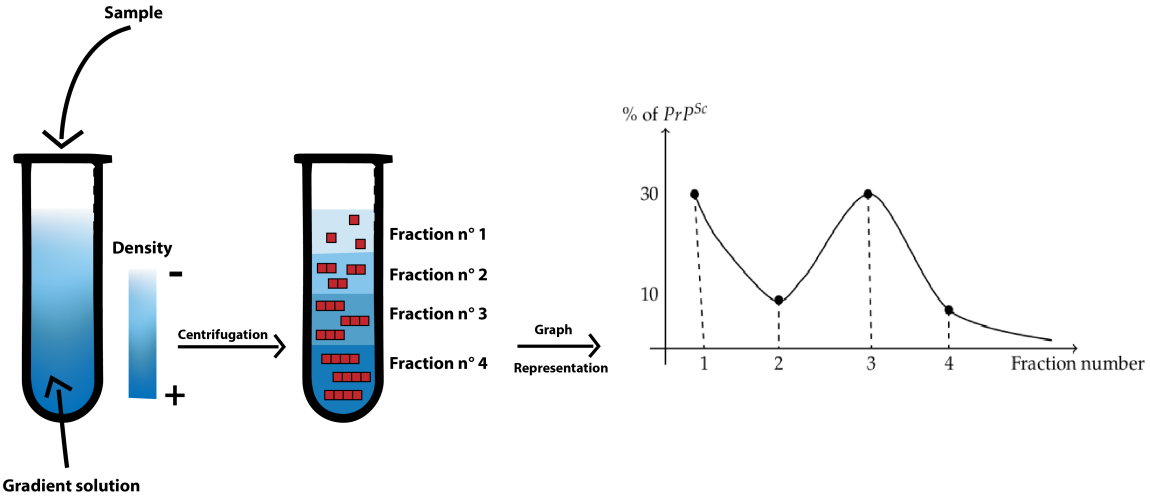

Figure 11 – Scheme of the Sedimentation Velocity (S.V) experiments in order to obtain the size distribution of the particles.

In **Chapter 4**, the method used to obtain information on the size distribution density is sediment velocity experiments combined to a density gradient media. The sample studied is loaded atop high-density solution of varying concentration (e.g. 10-25% iodixanol gradients [65, 64]) and a centrifugal force is applied to the test tube containing the sample and the gradient solution. The variation in the

density of the solution makes it possible to separate by size the particles in the sample studied. The small particles stagnate and remain at the top and the big particles or polymers sediment. The total solution in the test tube is segregated into equal fraction number and the average concentration of particles in each fraction is determined and renormalized over the total concentration particles in the sample (cf Figure 11). The data obtained by S.V are interpreted as a dilatation of a size distribution density, normalized at 100%, so that if u_i denotes the concentration of polymers formed of i monomers, the data represent $\frac{iu_i}{\sum_k ku_k}$. In order to obtain the evolution of the size distribution over time, the iteration of S.V experiments with more samples is one the existing methods.

Structural diversification of prion assemblies in early Prion replication stage.

In prion diseases, the prion protein PrP^C misfolds into PrP^{Sc} and auto-organizes into conformationally distinct assemblies or strains (polymers). The existence of PrP^{Sc} structural heterogeneity within prion strains suggests the emergence and coevolution of structurally distinct PrP^{Sc} assemblies during prion replication. Such PrP^{Sc} diversification processes remain poorly understood. Here, we characterize the evolution of the PrP^{Sc} quaternary structure during prion replication in vivo and in vitro by PMCA. The protein quaternary structure is the number and arrangement of multiple folded protein subunits (e.g. monomers, dimers or small oligomers). The molecular mechanisms of PrP^{Sc} replication and structural diversification is observed combining PMCA and S.V experiments.

Regardless of the strain studied, the early replication stage (commonly assimilated as an elongation process) results in the formation of small PrP^{Sc} oligomers, thus highlighting a quaternary structural convergence phenomenon. A bimodal behaviour is observed by the formation of two peaks (P_1, P_2) in the representation of the size distribution (Figure (12)). The amount of assemblies in P_1 decreases over time as the amount of assemblies in P_2 increases. We also note the absence of assemblies of intermediate size between these peaks. The experiments analyzed in **Chapter 4** rule out the hypothesis of a coagulation between polymers in favor of an autocatalytic process as an explanation for the increase of assemblies in P_2.

The kinetic model is the following. We consider two different kinds of oligomers: on the one hand, A_i, of size $2i$, are formed by the aggregation of i SuPrP formed of two monomers, and denoted A_1. Due to the fact that $i_A < 5$, as A_i assemblies are eluded in the first S.V fractions (cf Figure 12), we neglect here the oligomers A_i with $i > 1$ for the sake of clarity and simplicity. On the second hand, oligomers B_i, of size $3i$, able to aggregate by B_1- addition, where B_1 is another SuPrP formed of three monomers. However, A_1 may react with monomers to give rise to B_1. A convenient reaction scheme should also be such that without monomers, almost nothing happens (cf Figure 4.5 in **Chapter 4**).

1. A_1 and B_1 can form a complex C in a reversible way:

$$A_1 + B_1 \quad \underset{k_C^-}{\overset{k_C^+}{\rightleftharpoons}} \quad C.$$

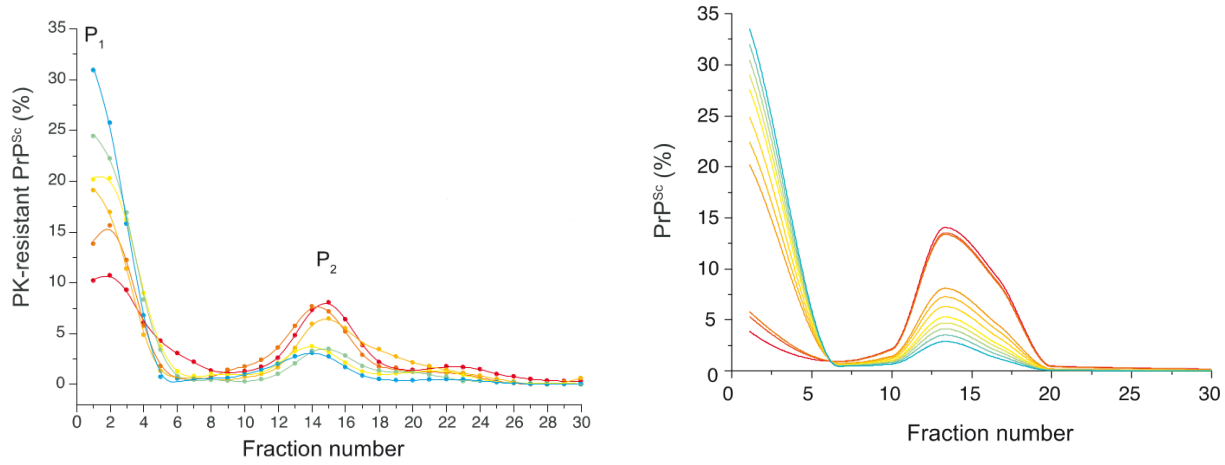

Figure 12 – **Size distribution evolution PrP assemblies at the early replication phase.** (Left) S.V profile describing, in vitro, the size distribution evolution of PrP assemblies obtained by PMCA from 127S-infected brain homogenates. (Right) Numerical simulation of the size distribution. The initial condition corresponds to the measures at the begining of the S.V experiments (blue curve of the graph on the left).

2. The complex C can then react with the monomer M to form two B_1:

$$M + C \xrightarrow{k_+} 2B_1.$$

3. The oligomers B_i follow a classical polymerisation/depolymerisation chain reaction, by B_1- addition:

$$B_1 + B_i \underset{k_{dep}^{i+1}}{\overset{k_{on}^{i}}{\rightleftharpoons}} B_{i+1}, \qquad 1 \leq i \leq n-1.$$

To validate the designed mechanism, we performed numerical simulations using the size distribution of the PrP^{Sc} assemblies immediately after cyclic amplification as the initial condition (blue curve in the left graph in Figure 12). Numerical simulations reproduce satisfactorily the results obtained by the experiments (cf Figure 12) and the mathematical model gives more insights about the kinetics and chemical relations between A_i and B_i. These oligomers undergo structural rearrangements, by a PrP^C-dependent, secondary templating pathway. This pathway provides mechanistic insights into prion structural diversification, a key determinant for prion toxicity and interspecies transmission. The uncovered processes are also key for a better understanding of misfolded assemblies propagating by a prion-like process in other neurodegenerative diseases.

General perspectives and future work

Characterisation of oscillations in a wavelet basis. The test to detect HF features detailed in **Chapter 1** is based on the projection of the signal in a discrete Fourier basis. The next step would be to define

the HF features in a wavelet basis. The definition of "high-frequency" features has to be specified in this framework. We can imagine a new parametric characterisation still taking into account the amplitude and the localization on the frequency-scale (or resolution-scale) but also adding a new parameter to locate these features on the time-scale. The multiresolution signal decomposition from the projection in a wavelet basis provides further information on signals without making a priori strong assumptions. The benefits are to get rid of the pre-processing step in the computation of the HF features and get a better characterisation of transient oscillatory phenomena (i.e. dumped oscillations only appearing in a fraction of the length of the signal). However, the number of parameters will then be equal to three (one for the resolution, one for the amplitude and one for the localization on the time-scale) and the test of hypothesis has to be extended to this framework.

Further results on the discrete bi-monomeric model. In **Chapter 2**, we study a bi-monomeric, nonlinear Becker-Döring-type model. A proof of the exponential convergence toward the nonnegative equilibrium is given considering the two-polymers system (cf Theorem 7). The explicit rate of convergence is still unknown.
The next step is to obtain the convergence toward the nonnegative equilibrium for the infinite size system. The main issue lies in the fact that we do not know if a Lyapunov functional exists. A method to obtain results on the asymptotic behaviour would consist of decoupling the ODE system for the monomeric species v, w and the system for the polymers concentrations using the conservation laws. Once decoupled, the system for the monomeric species can be analysed independently, and the results can be extended to the polymers system using the theory on asymptotically autonomous systems [97, 156]. An interesting question remains: what are the possible forms of reaction coefficients which allow the decoupling between the two ODE systems ?

Inverse problem on the SLS signals. Turning back to the experiments as shown in Figure 5, it also appears that much remains to be done before reaching a fully quantitative model. The first step is to integrate the reaction scheme proposed in **Chapter 2** in a more complete model, where "usual" reactions (like linear depolymerisation) would be the dominant reactions, governing the slow dynamics of the reactions, and nonlinear depolymerisation would be interpreted as local corrections. Using the same notations as in **Chapter 2**, an interesting reaction scheme to study is the following:

$$\begin{cases} \mathcal{V} + \mathcal{W} \xrightarrow{k} 2\mathcal{W} \\ \mathcal{W} + \mathcal{C}_i \xrightarrow{a_i} \mathcal{C}_{i+1} \quad i \geq 1 \\ \mathcal{C}_i + \mathcal{V} \xrightarrow{b_i} \mathcal{C}_{i-1} + 2\mathcal{V} \quad i \geq 2 \\ \mathcal{C}_{i+1} \xrightarrow{\beta_{i+1}} \mathcal{C}_i + \mathcal{W} \quad i \geq 1 \end{cases}$$

This reaction network is translated into the following infinite system of differential equations:

$$\begin{cases} \frac{dv}{dt} = -kvw + v\sum_{i=2}^{\infty} b_i c_i, & v(0) = v_0, \\ \frac{dw}{dt} = -w\sum_{i=1}^{\infty} a_i c_i + \sum_{i=2}^{\infty} \beta_i c_i + kvw, & w(0) = w_0, \\ \frac{dc_i}{dt} = J_{i-1} - J_i, & c_i(0) = c_i^0, \quad i \geq 1, \end{cases}$$

where J_i is the net rate at which a i-fibril is converted to a $(i+1)$-fibril by :

$$J_i = wa_i c_i - [vb_{i+1} + \beta_{i+1}]c_{i+1} \qquad 1 \leq i \leq n-1.$$

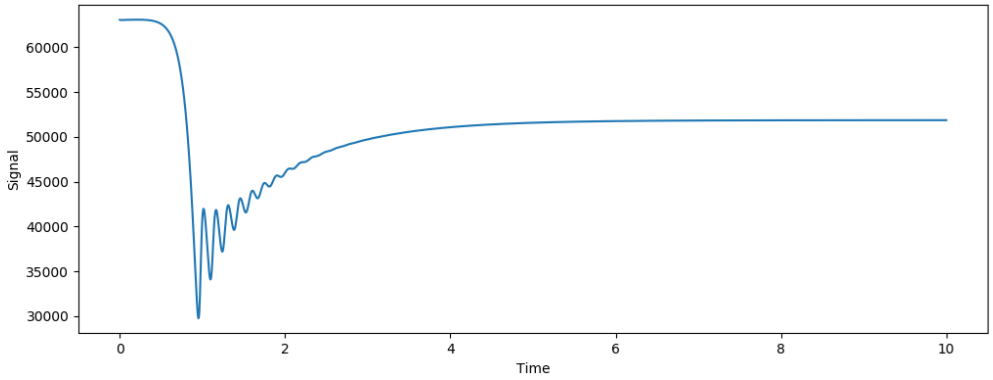

Figure 13 – **Simulation of the second moment of the size distributions.** The parameters are $k = 0.3$, $a_i = 2$, $b_i = 0.1$, $\beta_i = 1.9$ and the maximal size of polymers is 50. The initial size distribution is centered on the size 25, and $v_0 = 0.1$, $w_0 = 0.2$, $P_0 = 100.265$.

Note that if $k = b_i = 0$ we get the seminal Becker-Döring system. The numerical simulations of the second moment of this hybrid model are close to the SLS signals (cf Figure 13). The next step are experimental evidence and quantitative comparison, for instance through data assimilation strategies in the spirit of [5, 6].

Further results on the continuous bi-monomeric model. We propose a bi-monomeric, nonlinear Lifshitz-Slyozov-type system in **Chapter 3**. The results on the asymptotic behaviour of the continuous model differ from those of the discrete model, mainly because an underlying diffusion process takes place in the discrete model. We study the first-order approximation of the continuous model which neglects

the diffusion term. An interesting perspective is to derive and study the second order approximation which includes a diffusion term in the continuous size-setting.
The next step is to propose and study numerical scheme to approximate the solutions of this coupled ODE-PDE systems. The numerical analysis, in the spirit of [14, 31, 59], illustrates the results on the asymptotic behaviour and gives more insights and a better understanding of the model. The numerical analysis would also give further results on the convergence rate β (cf Theorem 8) of the ODE-PDE system. Moreover, the study of the behaviour of the PDE is performed in the case of linear reaction coefficients and in the case of one linear and one constant reaction coefficient:

$$a(x) = ax, \quad b(x) = bx \qquad \text{and} \qquad a(x) = 1, \quad b(x) = bx \quad \text{for} x \geq 0.$$

These choices were motivated by experimental data from biologists since the static light scattering (SLS) signals studied show a fall for the second moment of the size distribution of polymers in a closed in vitro environment. An interesting perspective would be to consider more general forms of the reaction coefficients, for instance $m_1 \leq a'(x) \leq m_2$, $m_1 \leq b'(x) \leq m_2$ with $m_1, m_2 > 0$. The main issue arising from this last choice of reaction coefficients is that the ODE-PDE system is coupled. We cannot use the conservation laws to study the behaviour of the ODE system independently. However, an appropriate entropy would probably solve this issue and give the corresponding asymptotic behaviour.

General perspectives. The study of the mechanisms governing the aggregation of proteins is of primary importance in order to understand and cure Prion and Prion-like diseases. Since few experimental tests are available to observe protein aggregation, studying these mechanisms experimentally is a real challenge. In the majority of cases, only very indirect measurements can be obtained. The direct consequence is to face ill-posed problems. The collaboration between biologists and mathematicians is required in order to gain more insights and understanding. For example, we introduce in **Chapter 1** a parametric characterisation of the oscillatory components in the SLS signals. One interesting next step is to design and study a sensitivity analysis of these parameters from different SLS signals. It can assert new hypothesis and shed lights on new problems which require specific experiments. Moreover, we introduce in **Chapters 2,3, 4** new models of polymerisation/depolymerisation process with different species. In order to enhance these models, biologists try to confirm the hypothesis made with experiments and provide precise data to include in the models. Furthermore, realistic models help to construct and test strategies counteracting Prion diseases. These strategies can be, first, tested with numerical simulations and in vitro experiments. Finally, designing in vivo experiments and finding their representation through mathematical models represent the remaining challenges to solve in order to finally find a cure for amyloid diseases.

Chapter 1

Testing for high frequency features in a noisy signal

1.1 Introduction

The aim of this study is to detect high frequency (HF) features in a noisy signal. We propose a parametric characterization in the Fourier domain of the HF features. Then we introduce a procedure to evaluate these parameters and compute a p-value which assesses in a quantitative manner the presence or absence of such features, that we also call "oscillations". The procedure is well adapted for real 1-dimensional signals. If the signal analyzed has singular events in the low frequencies, the first step is a data-driven regularization of its Fourier transform. In the second step, the HF features parameters are estimated. The third step is the computation of the p-value thanks to a Monte Carlo procedure. The test is conducted on sanity-check signals where the ratio amplitude of the oscillations/level of the noise is entirely controlled. The test detects HF features even when the level of the noise is five times larger than the amplitude of the oscillations. The test is also conducted on signals from Prion disease experiments and confirms the presence of HF features in these signals.
This study has been realised in collaborations with M. Doumic[1], M. Hoffmann[2] and H. Rezaei[3] and has been submitted to IMS Annals of Applied Statistics on August 2, 2019.

Motivation

In a one-dimensional signal, transient oscillations may reveal key features of the underlying processes. As an example, and original motivation for our study, fast oscillations have been visually observed in

[1]Sorbonne Universités, INRIA, Université Paris-Diderot, CNRS, Laboratoire Jacques-Louis Lions, F-75005 Paris, France, marie.doumic@inria.fr
[2]Université Paris-Dauphine PSL, CEREMADE, Place du Maréchal de Lattre de Tassigny, F-75016 Paris, hoffmann@ceremade.dauphine.fr
[3]INRA, UR892, Virologie Immunologie Moléculaires, 78350 Jouy-en-Josas, France, human.rezaei@inra.fr

experimental measurements of the infectious agent in Prion diseases, see Figure 1.1.

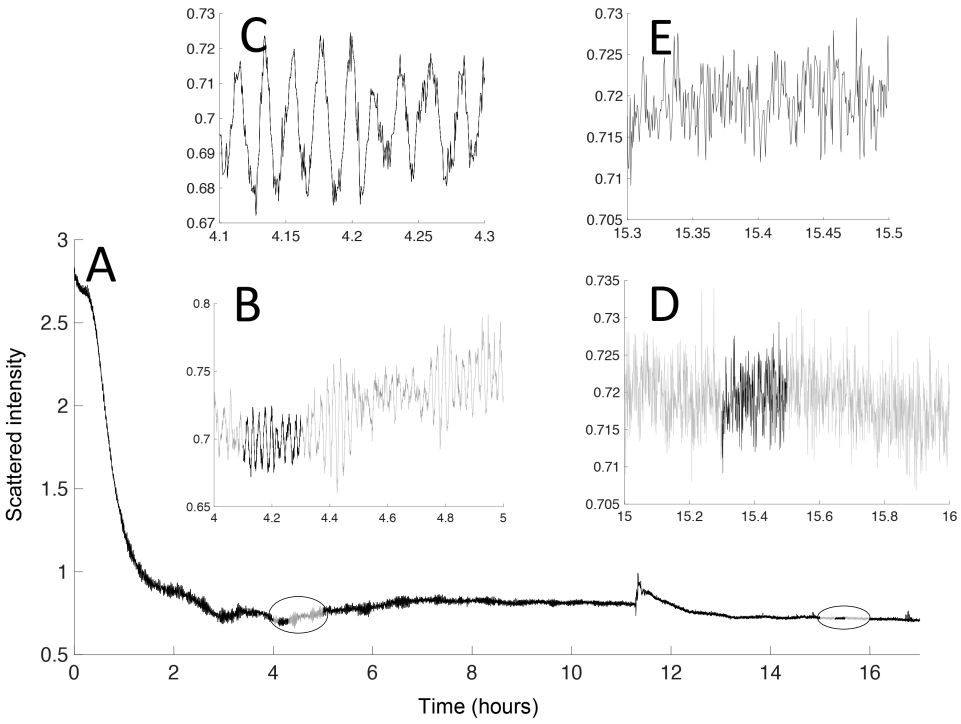

Figure 1.1 – **Human PrP amyloid fibrils (Hu fibrils) depolymerisation monitored by Static Light Scattering** (see Appendix for details). A: The overall view of the $0.35\mu M$ Hu-fibrils depolymerisation at $55^0 C$. B-E correspond to a zoom-in on different time-segments of the depolymerisation curve A. As shown in B, from time 4h to time 5h oscillations have been observed when for time segment corresponding to time 15.3 to 15.5h only noise has been detected (D). (Figure taken from [55])

A major difficulty to infer such transient oscillations and to evaluate their significance is that they are mixed up with noise. Hence it is of major interest to rely on a rigorous procedure which detects high frequency (HF) features - amplitude, frequency - in real signals and to distinguish quantitatively these features of the signal from its noise.

To our knowledge, there exist only few methods to detect and estimate the HF features in a signal. The Singular Spectrum Analysis (SSA) introduced by Broomhead and Jones in [22] is one of those and allows one to visualize qualitative dynamics from noisy experimental data. The SSA is based on the decomposition of a time series or signal into several additive components interpreted as trend components, oscillatory components, and noise components. It was then widely used to identify intermittent or modulated oscillations in time series, see e.g. [160, 117, 62].

A statistical test of hypothesis to discriminate between potential oscillations and noise has been introduced in [2] and [116]. This test is called the Monte Carlo SSA and has been applied almost exclusively to meteorological data. Since SSA transforms the original data in a complex way, no theoritical result has yet been proved on the Monte Carlo SSA. Prior knowledge on the signal (such as the trend or assumptions on the noise) are also needed in order to calibrate the procedure and improve the result of the statistical test. The Monte Carlo SSA is by construction a non-parametric procedure and the oscillations detected by this test are not characterized quantitatively but qualitatively.

In this study, we propose another method, based on the Fourier transform of the signal, to infer a parametric characterization of HF features, based on their amplitude and frequency detection. This method is detailed in Section 1.2. We then introduce a statistical test to discriminate HF features from noise in Section 1.4, apply our methodology to a simulated example in Section 1.3, and then to the experimental measurements of PrP protein displayed in Figure 1.12 in Section 1.5.

Model and assumptions

For some (large) $n \geq 1$, we have measurements y_i^n of a noisy signal localized around i/n. Thus i is a location parameter and n a frequency parameter. We may idealise our data via a representation of the form

$$y_i^n = x_i^n + \sigma \xi_i^n, \qquad i = 0, \dots, n-1 \tag{1.1}$$

where $(x_i^n)_{0 \leq i \leq n-1}$ is the true (unknown) signal of interest and the ξ_i are independent and identically distributed noise measurement, that we assume here to be standard Gaussian. The quantity $\sigma > 0$ is a (fixed) noise level. In this nonparametric regression setting, we aim at detecting from the data $(y_i^n)_{0 \leq i \leq n-1}$ whether $(x_i^n)_{0 \leq i \leq n-1}$ exhibits *high-frequency features* (HF features) such as oscillations, a term that still needs to be defined properly. Since we do not know in advance whether such high-frequency features are present and where they are located, we need to investigate the shape of $(x_i^n)_{0 \leq i \leq n-1}$, which requires some smoothing in order to get rid of the noise $(\xi_i^n)_{0 \leq i \leq n-1}$. However, any smoothing procedure tends to wipe out high-frequencies in the data, which is adversarial to our goal.

Results and organisation of the study

The statistical test to differentiate HF features from noise in a signal is data-driven and is based on the study of the projection of the signal in the Fourier domain. We propose in Section 1.2 a parametric characterization of the HF features of a signal. This characterization also provides an algorithmic procedure for the computation of the HF features, implemented in the Python language at *https://github.com/mmezache/HFFTest* (see Appendix 1.6.2). The procedure consists in three steps: in the first step, a regularization procedure is applied to the experimental data in order to smooth the fast variations that may exist in the low frequency range. The second step of the procedure is the detection and localization of significant peaks in the Fourier domain. The third step is the computation of the HF features parameters by selecting one of these peaks. The construction of the statistical test of hypothesis

and the computation of the p-value is described in Section 1.3.

The numerical examples are performed in Section 1.4 with sanity-check signals. They are constructed around parameters which control their trend, their transient oscillations and their noise. We vary the ratio of the amplitude of the HF features over the noise level (i.e. its standard deviation), which sheds light on the robustness of the procedure: the transient oscillations are detected by the procedure even if the noise level is significantly high. The procedure is then applied to static light scattering (SLS) experiments of PrP^{Sc} fibrils, in Section 1.5. They are characterised by their singular slow-varying components (non-monotonous trend) and their fast-varying components (isolated discontinuous jumps, transient oscillations, noise). We compute the HF features parameters of SLS signal experiments for different initial concentration of PrP^{Sc}. We conclude that these signals have significant HF features, i.e. the signals display transient oscillations coming from biochemical reactions and not from the experimental noise.

1.2 Characterisation of high frequency features

The discrete Fourier transform (DFT) $\mathsf{DFT}_n : \mathbb{R}^n \to \mathbb{R}^n$ transfers a real-valued discrete signal $(x_i^n)_{0\le i\le n-1}$ of length n into a frequency domain via

$$\mathsf{DFT}_n\Big[(x_i^n)_{0\le i\le n-1}\Big] = \Big(\sum_{i=0}^{n-1} x_i^n \mathrm{e}^{-j2\pi ki/n}\Big)_{0\le k\le n-1} = \Big(\vartheta_{n,k}\Big)_{0\le k\le n-1}. \tag{1.2}$$

The single-sided amplitude spectrum gives all the information needed to visualise the signal $(x_i^n)_{0\le i\le n-1}$ in the Fourier basis.

Our typical experimental signals have a specific low frequency trend combined with HF features or transient oscillations that shall persist beyond denoising. The presence of a trend implies that there are large Fourier coefficients $\vartheta_{n,k}$ on the scale corresponding to the low frequency information. Transient oscillations can be characterised by large coefficients in mid or high frequencies that are relatively well localised. As displayed by the test signal in Figure 1.2, a typical signal displaying oscillations would thus consist, in the frequency domain, of large coefficients in the low frequency, then a decay to a minimum value, and then one or more peaks in mid or high frequencies and a decay as the frequency grows further. Hence HF features in a signal corresponds to a level of energy (measured by the norm of the DFT coefficients) at a specific distance from the low frequency DFT coefficients in the frequency domain (cf Figure 1.3).

For a discrete signal $(x_i^n)_{0\le i\le n-1}$ given in terms of its Fourier transform $\vartheta_n = (\vartheta_{n,k})_{0\le i\le n-1}$ via (1.2), we characterise a HF feature by two nonnegative parameters: a location parameter $\mathsf{g}(\vartheta_n)$ (in the frequency domain) and an intensity parameter $\mathsf{d}(\vartheta_n)$ (see Figure 1.3).

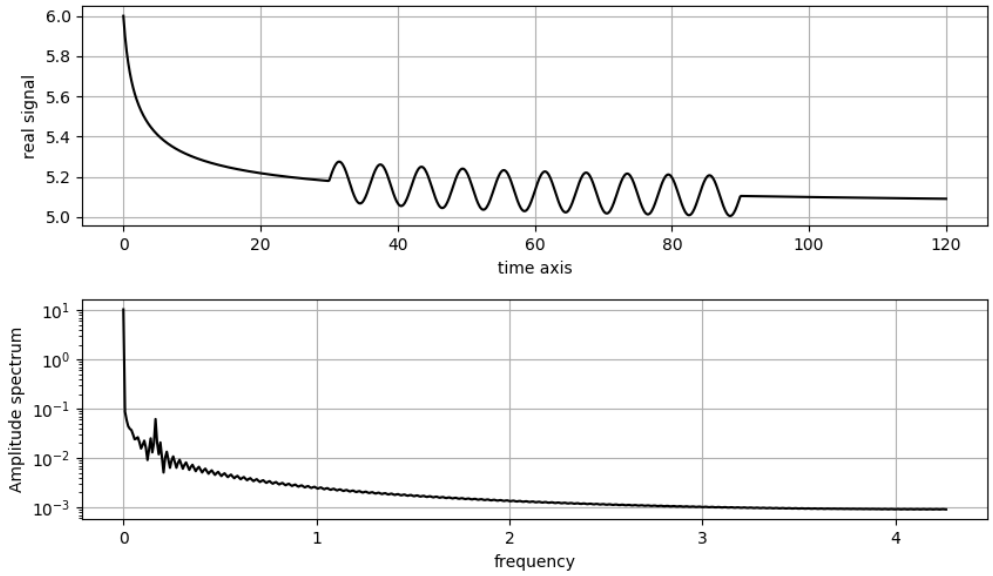

Figure 1.2 – **Graph of a test signal with HF features and its single-sided amplitude spectrum. Top:** Plot of $z_i = f(0.4i)$ for $i = 0,\dots,300$ where $f(x) = \frac{1}{\sqrt{x+1}} + 0.3\sin\left(\frac{2\pi x}{5}\right)\mathbb{1}_{[40,80]}(x)$. **Bottom:** Plot of the amplitude spectrum of $(z_i)_{0\le i\le 300}$ (logarithmic scale for the y-axis).

First step: Pre-processing the signal

Replacing x_i^n by $x_i^n + C$ for some arbitrary constant C, with no loss of generality, we may (and will) assume that

$$|\vartheta_{n,0}| > \max_{0\le k\le n-1} |\vartheta_{n,k}|. \tag{1.3}$$

Condition (1.3) is in force from now on. We transform $\vartheta_n = (\vartheta_{n,k})_{0\le i\le n-1}$ into a non-decreasing sequence $\mu_n^{(m)} = (\mu_{n,j}^{(m)})_{m\le j\le n-m}$ that depends on a certain smoothing parameter m (with $0 \le m \le n-1$) defined as follows:

$$\mu_{n,m}^{(m)} = \min_k \vartheta_{n,k}^{(m)} \le \mu_{n,m+1}^{(m)} \le \dots \le \mu_{n,j}^{(m)} \le \mu_{n,n-m}^{(m)} = \max_k \vartheta_{n,k}^{(m)}$$

where

$$\vartheta_{n,k}^{(m)} = \left(\frac{1}{2m+1}\sum_{l=k-m}^{k+m} |\vartheta_{n,l}|^2\right)^{1/2}, \quad m \le k \le n-m-1. \tag{1.4}$$

In other words, the sequence $\mu_n^{(m)}$ is the order statistics of a $2m$-regularised version of ϑ_n.

Remark 3. *The smoothing parameter m is needed as soon as the signal observed displays singularities e.g. a jump discontinuity or a fast transition of monotonicity of the trend. These phenomena are approximated by the harmonic sequence $\{e^{j2\pi k\cdot}, k \in \mathbb{Z}\}$, and when projected in the Fourier domain, the amplitude spectrum displays a serie of spikes (cf Figure 1.4). These phenomena are related to Gibbs phenomenon ([169], chapter 2) and give*

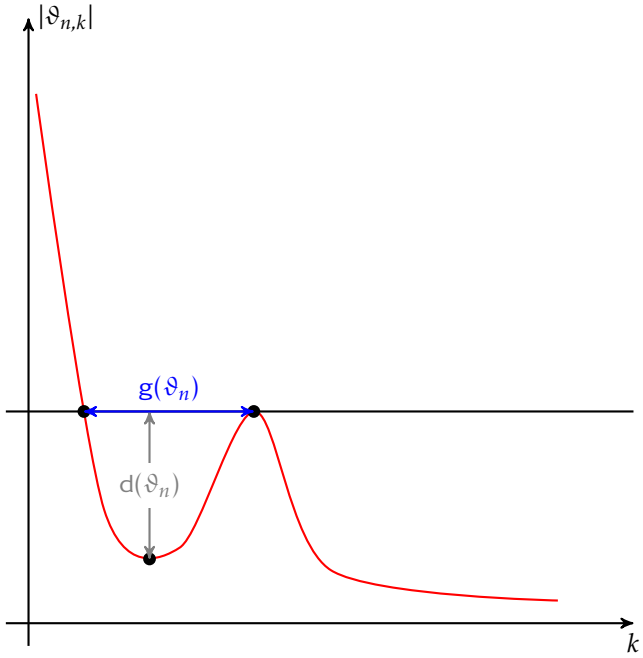

Figure 1.3 – **Idealized scheme of the parametrization of the HF features of a signal in the Fourier Domain.** The parameter $g(f)$ is the location parameter in the frequency scale which corresponds to the distance of the HF features from the low-frequency components of the signal. The parameter $d(f)$ is the intensity parameter which corresponds to the relative amplitude of the HF features.

rise to spikes in the Fourier domain which can be falsely interpreted as HF features. The regularization with an adequate choice of the parameter m solves this issue (cf Figure 1.4 and Section 1.4).

Remark 4. *The regularisation of order $2m$ transforms the sequence ϑ_n of n terms into a sequence of $n-2m$ terms in order to avoid boundary effects. We label the indices of the series from m to $n-m-1$ in so that the parameter k in $\vartheta_{n,k}^{(m)}$ is reminiscent of a frequency parameter and we formally have $\vartheta_{n,k}^{(0)} = |\vartheta_{n,k}|$.*

Second Step: Detection and Localization of significant features in the Fourier domain.

Define, for $x \geq 0$

$$\mathsf{a}(x) = \mathsf{a}_n^{(m)}(x) = \min\left\{k \mid m \leq k \leq n-m-1,\ \vartheta_{n,k}^{(m)} \leq x\right\} \tag{1.5}$$

and

$$\mathsf{b}(x) = \mathsf{b}_n^{(m)}(x) = \max\left\{\arg\max\left\{\vartheta_{n,k}^{(m)} \mid \mathsf{a}(x) \leq k \leq n-m-1\right\}\right\}. \tag{1.6}$$

Remark 5. *The index $\mathsf{a}(x)$ is the minimal frequency at which searching for HF features starts, getting rid of the potentially high energy levels arising from the low frequency part of the signal. The index $\mathsf{b}(x)$ is a maximal frequency for which the energy level x is reached in the search zone $\{\mathsf{a}(x), \mathsf{a}(x)+1, \ldots, n-m\}$.*

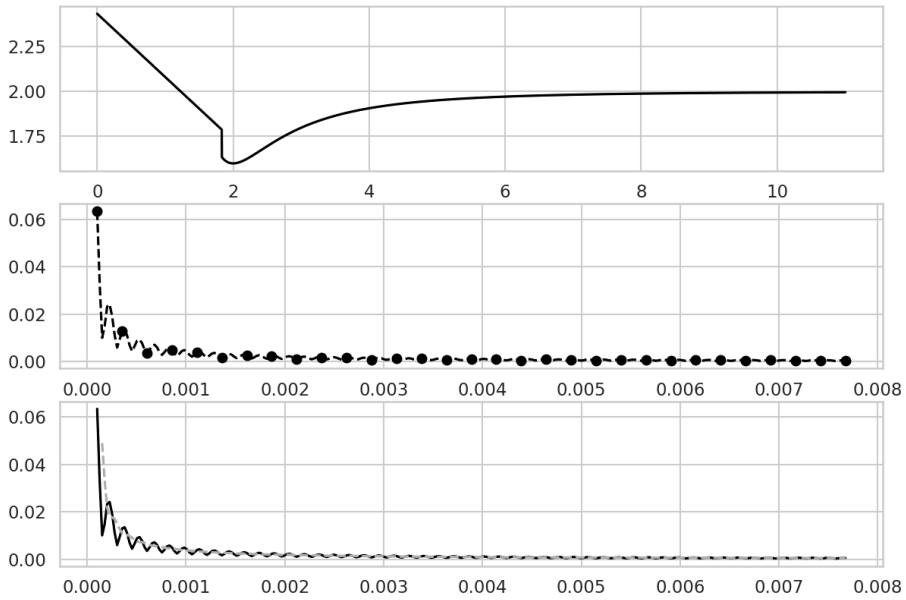

Figure 1.4 – **Graph of a test signal with a jump and a change of monotonicity and its single-sided amplitude spectrum. Top:** Graph of the signal with a decreasing, increasing and stationary part. **Middle:** Zoom on the low frequency of the amplitude spectrum for $n = 10000$ samples of the signal. The blue dot markers emphasize one over ten samples of the signal. **Bottom:** Plot of the amplitude spectrum of the test signal (plain line). The dash line corresponds to the plot of $(\vartheta^{(3)}_{n,k})_{3\leq k\leq n-4}$ defined by (1.4) with $m = 3$.

Define the sets

$$\mathcal{A}_n^{(m)} = \left\{\mu_{n,j}^{(m)} \mid \mu_{n,j}^{(m)} = \vartheta^{(m)}_{n,\mathsf{b}(\mu_{n,j}^{(m)})},\ m \leq j \leq n-m-1\right\}$$

and

$$\mathcal{S}_n^{(m)} = \left\{\mu_{n,j}^{(m)} \in \mathcal{A}_n^{(m)} \mid \mathsf{b}(\mu_{n,j}^{(m)}) > \mathsf{a}(\mu_{n,j}^{(m)}),\ m \leq j \leq n-m-1\right\}.$$

Remark 6. *The set $\mathcal{A}_n^{(m)}$ represents potential candidates for maximum energy levels of a HF feature, while $\mathcal{S}_n^{(m)}$ represents the set of intensities of the spikes of ϑ_n.*

Third Step: Definition of the HF features parameters.

To define the HF features, we now select in the set $\mathcal{S}_n^{(m)}$ the feature with maximum relative amplitude. Let us define

$$\mathsf{d}(x) = \mathsf{d}_n^{(m)}(x) = x - \min\left\{\vartheta_{n,k}^{(m)} \mid m \leq k \leq \mathsf{b}_n^{(m)}(x)\right\} \tag{1.7}$$

and we obtain a maximum intensity of HF feature as

$$\iota_n^{(m)}(\vartheta_{n,\cdot}) \in \max\left\{\arg\max_{x\in\mathcal{S}}\left(x - \min_{m\le k\le \mathsf{b}_n^{(m)}(x)} \vartheta_{n,k}^{(m)}\right)\right\} = \max\left\{\arg\max_{x\in\mathcal{S}} \mathsf{d}_n^{(m)}(x)\right\}$$

if $\mathcal{S}_n^{(m)}$ is non empty and $\iota_n^{(m)}(\vartheta_{n,\cdot}) = 0$ otherwise. Moreover if the set $\arg\max_{x\in\mathcal{S}} \mathsf{d}_n^{(m)}(x)$ is not reduced to a singleton taking its maximum ensures us to obtain a unique element for $\iota_n^{(m)}(\vartheta_{n,\cdot})$ i.e. the feature of maximum relative amplitude and maximum intensity. We are ready to give a quantitative definition of a HF feature:

Definition 3. *To any discrete signal $\vartheta_n = (\vartheta_{n,k})_{0\le i\le n-1}$ given in the Fourier domain, we associate a high-frequency feature (HF feature) $\left(\mathsf{G}_{n,m}(\vartheta_n), \mathsf{D}_{n,m}(\vartheta_n)\right)$ at discretisation level $n \ge 1$ and smoothing level $m \le \frac{n-1}{2}$ as follows:*

$$\mathsf{G}_{n,m}(\vartheta_n) = \mathsf{b}_n^{(m)}\left(\iota_n^{(m)}(\vartheta_n)\right) - \mathsf{a}_n^{(m)}\left(\iota_n^{(m)}(\vartheta_n)\right)$$

and

$$\mathsf{D}_{n,m}(\vartheta_n) = \mathsf{d}_n^{(m)}\left(\iota_n^{(m)}(\vartheta_n)\right),$$

where $\mathsf{b}_n^{(m)}$, $\mathsf{a}_n^{(m)}$ and $\mathsf{d}_n^{(m)}$ are defined in (1.6), (1.5) *and* (1.7) *respectively.*

Remark 7. *The parameters $\mathsf{G}_{n,m}(\vartheta_n)$ and $\mathsf{D}_{n,m}(\vartheta_n)$ are two distances ($\mathsf{G}_{n,m}(\vartheta_n)$ is a distance on the frequency axis and $\mathsf{D}_{n,m}(\vartheta)$ on the intensity axis). This couple of parameters provides a characterization in the discrete Fourier domain of events defined as HF features. For each signal, the parametric characterization is unique. It describes the peak with the highest distance between its amplitude and the minimum amplitude of the Fourier coefficients of lower frequencies (with $\mathsf{D}_{n,m}(\vartheta_n)$). The parameter $\mathsf{G}_{n,m}(\vartheta_n)$ gives the distance in frequency indices between the peak and the components in the low frequencies with the same intensity (see Figure 1.3).*

1.3 Testing for HF features

We keep-up with the statistical setting introduced in Equation (1.1): we observe

$$y_i^n = x_i^n + \sigma\xi_i^n, \quad i = 0,\dots,n-1, \tag{1.8}$$

where $(x_i^n)_{0\le i\le n-1}$ is the signal of interest and the $\sigma\xi_i^n$ are independent centred Gaussian random variables with noise variance σ^2, for some (large) $n \ge 1$, interpreted as a maximal discretisation resolution level or equivalently a maximal frequency of observation. Applying the discrete Fourier transform DFT_n on both sides of (1.8), we equivalently observe

$$\widehat{\vartheta}_{n,k} = \vartheta_{n,k} + \sigma\widetilde{\xi}_{k,n}, \quad k = 0,\dots,n-1,$$

where the $\sigma\widetilde{\xi}_{k,n}$ are independent centred Gaussian random variables with variance σ^2 as well, thanks to the fact that DFT_n is an orthogonal linear mapping. From data $(y_i^n)_{0\le i\le n-1}$ or rather $(\widehat{\vartheta}_{n,k})_{0\le k\le n-1}$, we

wish to construct a statistically significant test of the absence of HF feature as the null, against a set of local alternatives where some HF features are present.

1.3.1 Construction of a statistical test

Thanks to the characterisation of HF features via $\left(\mathsf{D}_{n,m}(\vartheta_n), \mathsf{G}_{n,m}(\vartheta_n)\right)$ given in Definition 3, we test the null

$$\mathcal{H}^0_{n,m,\nu,c}: \ \mathsf{G}_{n,m}(\vartheta_n) < \nu, \quad \mathsf{D}_{n,m}(\vartheta_n) < c$$

against the local alternatives

$$\mathcal{H}^1_{n,m,\nu,c}: \ \mathsf{G}_{n,m}(\vartheta_n) \geq \nu \ \text{ and } \ \mathsf{D}_{n,m}(\vartheta_n) \geq c$$

where $\nu > 0$, $c > 0$ are thresholds to determine significant HF features. The null hypothesis $\mathcal{H}^0$, is that there is no significant HF feature in the signal tested. On the contrary, the hypothesis $\mathcal{H}^1$ implies that the signal has significant HF feature. For the test to be powerful, the main problem is to define the couple (ν, c): for too small values any signal shall reject $\mathcal{H}^0$ whereas for large values, any signal shall accept $\mathcal{H}^0$. We obtain simple test statistics for $\left(\mathsf{G}_{n,m}(\vartheta_n), \mathsf{D}_{n,m}(\vartheta_n)\right)$ by setting

$$\widehat{\mathsf{G}}_{n,m} = \mathsf{G}_{n,m}(\widehat{\vartheta}_n) = \mathsf{b}^{(m)}_n\left(\iota^{(m)}_n(\widehat{\vartheta}_n)\right) - \mathsf{a}^{(m)}_n\left(\iota^{(m)}_n(\widehat{\vartheta}_n)\right)$$

and

$$\widehat{\mathsf{D}}_{n,m} = \mathsf{D}_{n,m}(\widehat{\vartheta}_n) = \mathsf{d}^{(m)}_n\left(\iota^{(m)}_n(\widehat{\vartheta}_n)\right).$$

In order to compute the p-value of the test, we design a Monte-Carlo procedure simulating a proxy of the data $(y_i)_{0\leq i\leq n-1}$ under the null $\mathcal{H}^0$. Using the proxy, we define a reject region of our test for a risk level α and the p-value of the data $(y_i)_{0\leq i\leq n-1}$.

Rejection zone at risk level α.

We first simulate N times $y^{(0)}_{\lambda,n}$ defined in (1.14) below, which is a simulated proxy of the data $(y^n_i)_{0\leq i\leq n-1}$ with HF features removed from the signal $(x^n_i)_{0\leq i\leq n-1}$. Repeating independently N times the procedure, we obtain a Monte-Carlo sequence

$$y^{(0),k}_{\lambda,n} \ k = 1, \ldots, N.$$

In a second step, we denote by E^0_N the cloud of points representing the HF features parameters of these simulated signals (with HF features removed but with Gaussian noise):

$$E^0_N = \left\{\left(\mathsf{G}_{n,m}\left(\mathsf{DFT}[y^{(0),k}_{\lambda,n}]\right), \mathsf{D}_{n,m}\left(\mathsf{DFT}[y^{(0),k}_{\lambda,n}]\right)\right) \mid k = 1, \ldots, N\right\}. \tag{1.9}$$

We define the function $P : \mathbb{R}_+^2 \to F \subset [0;1]$:

$$P(g,d) = N^{-1} \sum_{k=1}^{N} \mathbf{1}_{\left\{ \mathsf{G}_{n,m}\left(\mathsf{DFT}[y_{\lambda,n}^{(0),k}]\right) \geq g,\ \mathsf{D}_{n,m}\left(\mathsf{DFT}[y_{\lambda,n}^{(0),k}]\right) \geq d \right\}}. \tag{1.10}$$

Hence $P(g,d)$ is the proportion of points in E_N^0 located in the North-East quarter of the plane centered on (g,d) (cf Figure 1.5). In order to reduce the computation cost, we only consider the restriction of P to the set E_N^0. Thus if E_N^0 is reduced to a singleton, then the image set $P(E_N^0)$ is equal to $\{1\}$, on the contrary if E_N^0 contains N disjoint points then the minimal bound on $P(E_N^0)$ is $\frac{1}{N}$. For a risk level $\alpha \in P(E_N^0)$, the

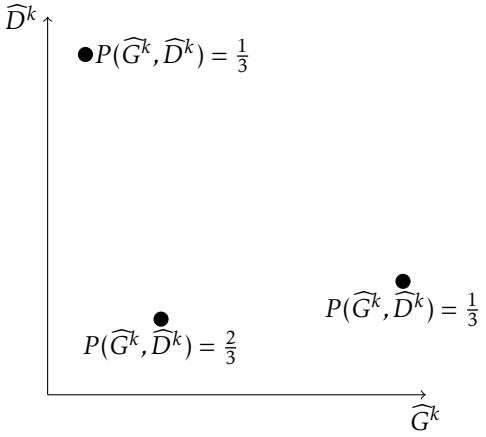

Figure 1.5 – Cloud of points $\left(\widehat{\mathsf{G}}^k, \widehat{\mathsf{D}}^k\right) = \left(\mathsf{G}_{n,m}\left(\mathsf{DFT}[y_{\lambda,n}^{(0),k}]\right), \mathsf{D}_{n,m}\left(\mathsf{DFT}[y_{\lambda,n}^{(0),k}]\right)\right)$ for $k = 1, 2, 3$.

rejection zone of our test is defined as

$$\mathcal{R}_{m,n}\left(\kappa_1^\alpha, \kappa_2^\alpha\right) = \left\{ (y_i)_{1 \leq i \leq n} \text{ defined by (1.1) s.t. } \widehat{\mathsf{G}}_{n,m} \geq \kappa_1^\alpha,\ \widehat{\mathsf{D}}_{n,m} \geq \kappa_2^\alpha \right\} \tag{1.11}$$

where $(\widehat{\mathsf{G}}_{n,m}, \widehat{\mathsf{D}}_{n,m})$ is the test statistics and $\left(\kappa_1^\alpha, \kappa_2^\alpha\right) \in E_N^0$ are such that

$$P(\kappa_1^\alpha, \kappa_2^\alpha) = \alpha. \tag{1.12}$$

Remark 8. *The risk level α is imposed by the Monte-Carlo sequence, $\alpha \in P(E_N^0) \subset [\frac{1}{N}; 1]$. For example, Figure 1.5 represents an arbitrary set E_N^0 for $N = 3$. Consequently, we note that $\frac{1}{3} \leq \alpha \leq 1$ in order to obtain candidates $\kappa_1^\alpha, \kappa_2^\alpha$. For $\alpha < \frac{1}{3}$ no candidate can be obtained by this procedure and its associated reject region is not defined. Moreover there can be multiple reject regions defined for the same risk level α (in the example whe have two reject regions for $\alpha = \frac{1}{3}$).*

The main idea behind the computation of the couples $\left(\mathsf{G}_{n,m}\left(\mathsf{DFT}[y_{\lambda,n}^{(0),k}]\right), \mathsf{D}_{n,m}\left(\mathsf{DFT}[y_{\lambda,n}^{(0),k}]\right)\right)$ is to generate random outcomes under the null $\mathcal{H}^{(0)}$ that enable us to compute risk level by Monte-Carlo. The couples correspond to the relative amplitude and the frequency gap for a non-oscillating signal

with noise. We also get reject region(s) of level α thanks to the threshold(s) $\left(\kappa_1^\alpha, \kappa_2^\alpha\right)$. We do not need uniqueness of the reject region in order to define and compute the p-value, see below.

Definition of the p – value.

The p – value of the observations $(y_i^n)_{0\le i\le n-1}$ is defined as

$$\mathrm{p-value}\Big((y_i^n)_{0\le i\le n-1}\Big) = \min\Big\{\alpha \in P(E_N^0) \,|\, \widehat{\mathsf{G}}_{n,m} \ge \kappa_1^\alpha, \quad \widehat{\mathsf{D}}_{n,m} \ge \kappa_2^\alpha\Big\}. \tag{1.13}$$

An equivalent definition of the p-value of the observations $(y_i^n)_{0\le i\le n-1}$ is obtained via

$$\mathrm{p-value}\Big((y_i^n)_{0\le i\le n-1}\Big) = \inf\Big\{\alpha \in P(E_N^0) | \, (y_i^n)_{0\le i\le n-1} \in \mathcal{R}_{m,n}\Big(\kappa_1^\alpha, \kappa_2^\alpha\Big)\Big\}.$$

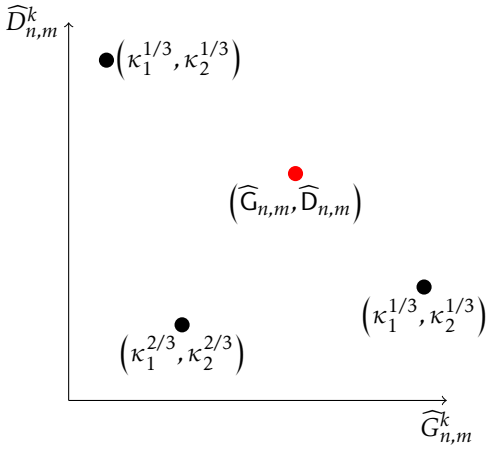

Figure 1.6 – **Point cloud $\left(\widehat{\mathsf{G}}_{n,m}^k, \widehat{\mathsf{D}}_{n,m}^k\right)$ for $k = 1, 2, 3$ (black dots) and HF feature parameters $\left(\widehat{\mathsf{G}}_{n,m}, \widehat{\mathsf{D}}_{n,m}\right)$ (red dot).**

Remark 9. *The computation of the* p – *value is illustrated schematically in Figure 1.6. We observe the point cloud formed by $\left(\widehat{\mathsf{G}}_{n,m}^k, \widehat{\mathsf{D}}_{n,m}^k\right)$ (the black dots) for $k = 1, 2, 3$. On the vertical axis we have the relative amplitude and on the horizontal axis we have the gap in frequency between the oscillations and the trend in the Fourier domain. The red dot illustrates the HF features parameters subject to the test. We use the $\left(\widehat{\mathsf{G}}_{n,m}^k, \widehat{\mathsf{D}}_{n,m}^k\right)$ as our grid to compute the p-value. Using* (1.12)*, we compute the level α and obtain consequently the $\left(\kappa_1^\alpha, \kappa_2^\alpha\right)$ for each element of the grid. The p-value is $\frac{2}{3}$ in this example.*

The p – value gives a confidence index for non-rejecting the null. This index is meaningful provided the test has a good power, *i.e.* if the probability of making a type II error is small. Hence the p – value of $\left((y_i^n)_{0\le i\le n-1}\right)$ is our measure of confidence in non-rejection of the null $\mathcal{H}^0$. The main difficulty however lies in solving (1.11) since ϑ_n remains unknown under the null and that there are no reason that $\widehat{\mathsf{G}}_{n,m}$ or

$\widehat{\mathsf{D}}_{n,m}$ are pivotal statistics under the null. We describe below a numerical procedure based on Monte-Carlo simulation that estimates $y^{(0)}_{\lambda,n}$ a proxy of the data with HF features removed but with noise.

1.3.2 A Monte-Carlo procedure for the simulation of the null

In order to evaluate (1.11) and (1.13), we first build a low-frequency estimator $\widehat{x}^{(0)}_{\lambda,n}$ from the data $(y^n_i)_{0\le i\le n-1}$ that removes the potential HF features. The estimator depends on a regularisation parameter λ. We next define

$$y^{(0)}_{\lambda,i,n} = \widehat{x}^{(0)}_{\lambda,i,n} + \widehat{\sigma}_n \epsilon^n_i, \;\; i = 0,\dots,n-1, \tag{1.14}$$

where the ϵ^n_i are independent centred Gaussian random variables that we simulate and $\widehat{\sigma}_n$ is an estimator of the standard deviation of the noise. The simulated signal $(y^{(0)}_{\lambda,i,n})_{0\le i\le n-1}$ obtained by estimating a proxy of f with HF features removed with additional simulated noise serves as a proxy of the data $(y^n_i)_{0\le i\le n-1}$ under the null $\mathcal{H}^0$.

Numerical computation of $\widehat{f}^{(0)}_{\lambda,n}$

Trend estimation or filtering for mimicking a signal with HF features removed has many applications and hence it has been extensively studied. It has given rise to the smoothing and filtering methods such as the moving average [164], smoothing splines [136], Hodrick-Prescott filtering [134], ℓ_1-trend filtering [82] and so on. The trend is considered as the general shape of a signal or a time series. Although the trend is often understood and perceived intuitively, its estimator relies on the definitions given to the trend. The differences between the various definitions of the trend are a matter of interpretation. Considering the different definitions of the trend, the choice of the method to estimate this component is more likely qualitative. In the following, the trend is considered as the underlying slowly varying component of the signal and we choose the ℓ_1-trend filtering method described in [82] to estimate it. The estimator of $\widehat{x}^{(0)}_{\lambda,n}$ as a n-dimensional vector is then the solution of the following optimisation problem:

$$\widehat{x}^{(0)}_{\lambda,n} \in \underset{x\in\mathbb{R}^n}{\arg\min}\, \frac{1}{2}\sum_{i=1}^{n-1}(y^n_i - x^n_i)^2 + \lambda \sum_{i=1}^{n-2} |x^n_{i-1} - 2x^n_i + x^n_{i+1}|, \tag{1.15}$$

where $\lambda \ge 0$ is a regularisation parameter which controls the trade-off between the smoothness of $\widehat{x}^{(0)}_{\lambda,n}$ and the residual $\sum_{i=0}^{n-1}\left(\widehat{x}^{(0)}_{\lambda,n,i} - y^n_i\right)^2$. We note that the second term $\sum\limits_{i=1}^{n-2} |x^n_{i-1} - 2x^n_i + x^n_{i+1}|$ is the ℓ^1-norm of the second order variations of the sequence (x^n) (i.e. the discretization of the corresponding L^1-norm of the second derivative of a function). Moreover, for any sequence (x^n),

$$|x^n_{i-1} - 2x^n_i + x^n_{i+1}| = 0,\ \forall i = 0,\dots,n-1 \iff x^n_i = \alpha i + \beta, \text{ with } \alpha,\beta\in\mathbb{R},\ \forall i = 0,\dots,n-1.$$

Thus only an affine function has its ℓ^1-norm equal to 0. Hence this method gives an estimator of the trend such that:

(i) $\widehat{x}^{(0)}_{\lambda,n}$ is computed numerically in $\mathcal{O}(n)$ operations,

(ii) as $\lambda \to 0$, $\max_{0\le i\le n-1} |\widehat{x}^{(0)}_{\lambda,n} - y^n_i| \to 0$, the estimator converges to the original data,

(iii) as $\lambda \to \infty$, the estimator converges to the best affine fit of the observations. This convergence happens for a finite value of λ [82].

(iv) $\widehat{x}^{(0)}_{\lambda,n}$ is piecewise linear, i.e. there are indices $0 = j_1 < j_2 < \ldots < j_K = n-1$ for which:

$$\widehat{x}^{(0)}_{\lambda,n,i} = \alpha_k i + \beta_k, \quad j_k < i < j_{k+1}, \quad k = 1,\ldots,K-1.$$

The ℓ_1-trend filtering method is well suited to extract the trend components of the signals studied in Section 1.4. Since the signals display singularities such as discontinuous jumps, the trend extracted is well approximated by a piecewise linear function. Moreover the HF features in the signals are components looking like sine waves and varying at an intermediate pace. However interpolating a sine wave by a piecewise linear function requires a fine scale and thus the parameter λ has to be close to 0. Rising slightly the value of λ allows us to capture the trend without the HF features. Moreover there exists a threshold $\lambda_{\max} \in \mathbb{R}_+$ [82] such that $\widehat{x}^{(0)}_{\lambda_{\max},n}$ is the trend estimator corresponding to the best affine fit. It implies that the choice of λ is restricted to the bounded open interval $(0,\ \lambda_{\max})$. Since there is no optimal criterium to choose λ, the choice of the parameter is qualitative and motivated empirically (see Section 1.4).

Numerical estimation of the noise level $\widehat{\sigma}_n$

The estimator of the standard deviation of the noise is the second ingredient needed in order to compute $\widehat{f}^{(0)}_{\lambda,n}$ in (1.14). The methods to estimate the level of noise are closely linked to the methods of signal denoising and thus have been extensively studied. The method chosen to estimate the noise level is the median absolute deviation and the denoised signal is obtained thanks to the wavelet shrinkage methods [49, 50, 52, 51].

We assume that our data $y = (y_i)_{0\le i\le n-1}$ are such that $n = 2^{J+1}$ for $J > 0$. We then consider an orthogonal wavelet transform matrix $\mathcal{W}$ for a given filter. Choosing wavelets (e.g. Coiflet, Daubechies, Haar) and varying the combinations of parameters M (number of vanishing moments), S (support width) and j_0 (low-resolution cut-off) one may construct various orthogonal matrices $\mathcal{W}$ (see for details [96], chapter 7). In this study we use the Symmlet with parameter 8 which has $M = 7$ vanishing moments and support length $S = 15$. The wavelet coefficients of y are denoted by w and

$$w = \mathcal{W}x + \sigma\widetilde{\xi},$$

where $\widetilde{\xi} = \mathcal{W}\xi$ is a standard Gaussian random vector by orthogonality of $\mathcal{W}$. For convenience, we index dyadically the vector of the wavelet coefficients

$$w_{j,k} \quad j = 0,\ldots,J, \quad k = 0,\ldots,2^j - 1.$$

We make the legitimate assumption that empirical wavelet coefficients at the finest resolution level J are essentially pure noise. Hence the standard deviation estimator $\widehat{\sigma_n}$ is the median absolute deviation

$$\widehat{\sigma_n} = \frac{\text{median}(w_{J,\cdot})}{\Phi^{-1}(3/4)}, \tag{1.16}$$

where $\Phi^{-1}(\cdot)$ is the inverse of the cumulative distribution function for the standard normal distribution. Thus $\widehat{\sigma_n}$ is a consistent estimator of σ. It is interesting to note that further computations give the VisuShrink estimator $\widehat{x_n}$ of the signal $(x_i^n)_{0\leq i\leq n-1}$

$$\widehat{x_n} = \mathcal{W}^T \bullet \widehat{w}^{n,j_0} \bullet \mathcal{W}, \tag{1.17}$$

where j_0 denotes a low resolution cut-off and $\widehat{w}^{n,j_0}$ is the estimator in the wavelet domain

$$\widehat{w}^{n,j_0} = \begin{cases} w_{j,\cdot} & j < j_0 \\ \text{sign}(w_{j,\cdot})\left(|w_{j,\cdot}| - \widehat{\sigma_n}(2\log n)^{1/2}\right)_+ & j_0 \leq j \leq J \end{cases}.$$

The first reason that motivated this choice is that the shrinkage methods attempt to remove whatever noise is present and retain whatever signal is present regardless of the frequency [51]. The goal of this study is to estimate HF features in noisy signals. However the traditional methods of noise removal such as low-pass filters are based on frequency-dependent estimators, which can also impact and distort the results of the HF feature procedure. The second reason is that these methods are data-driven and no specific assumptions on the signal are required. The wavelet shrinkage is spatially adapted and the method is efficient for a wide variety of signals even when the signals exhibit spatial inhomogeneities [51]. Finally these methods are proven to be nearly optimal for the mean squared error criterion when the smoothness of the original signal is unknown [52].

1.4 Simulation example: sanity check of the procedure.

Pre-processing: a data-driven choice of m

We first address the delicate issue of choosing the smoothing parameter m. Define a sequence $(m_i)_{1\leq i\leq K}$ such that

$$1 = m_1 < m_2 < \ldots < m_K \leq \tfrac{n-1}{2}.$$

We can take for instance $m_i = i$ for $i = 1,\ldots,K$. Note that $K \in \{1,\ldots,\frac{n-1}{2}\}$ is the parameter defining the length of the finite sequence $(m_i)_{1\leq i\leq K}$. This parameter can be fixed by the user in order to reduce the number of iterations of the procedure to compute the HF features. However, a standard choice of K to obtain a data-driven procedure is $K = \frac{n-1}{2}$, since averaging the signal over more than half of the sample size is obviously meaningless. A good rule of thumbs is that $K = n^{\frac{1}{2}}$, since it reduces the number of

calculations and remains pertinent compared to the range of the signal. Let

$$i^\star \in \underset{1\leq i\leq K}{\arg\max} \left|\widehat{\mathsf{G}}_{n,m_i} - \widehat{\mathsf{G}}_{n,m_{i-1}}\right|,$$

then

$$\widehat{m} = \begin{cases} m_{i^\star} & \text{if} \quad \widehat{\mathsf{G}}_{n,m_{i^\star}} > \widehat{\mathsf{G}}_{n,m_{i^\star-1}} \\ m_{i^\star-1} & \text{otherwise.} \end{cases} \tag{1.18}$$

As previously stated in Remark 3, the empirical signals observed are non-monotonous, contain singularities and transient oscillations. Their amplitude spectra display a series of spikes in the low-frequencies and in the mid or high frequencies. Hence without a pre-processing step, the HF feature parameters (Definition (3)) characterize the low frequencies features (i.e. the trend represented in the amplitude spectrum by spikes in the low frequencies, see Figure 1.4).
In order to solve this problem, we regularize the Fourier coefficients as defined in (1.4). The sequence $(m_k)_{1\leq k\leq K}$ gradually smoothes the Fourier amplitude spectrum: the spikes in the low frequencies merge together whereas the isolated spikes in the mid or high frequencies (corresponding to transient oscillations) slightly decrease in amplitude but remain significant. The data-driven choice of m is well adapted to regularize the empirical signals since it chooses the parameter $\widehat{m}$ from the sequence $(m_k)_{1\leq k\leq K}$ which maximizes the difference between the localisation parameters $\widehat{\mathsf{G}}$ for two consecutive smoothing parameters. Thus the spikes located in a close frequency range have been smoothed and the remaining spikes of significant amplitude for the regularization parameter $\widehat{m}$ are isolated in the Fourier amplitude spectrum.

Defining a test signal

To study numerically the validity of the procedure and the statistical test, we first compute a simulated signal where all the parameters are known. To do so, we superimpose three signals: one for the general trend of the curve, one for the HF features, and one for the noise. The signal obtained is the vector $(S_i)_{0\leq i\leq n-1}$:

$$S_i = T_i + O_i + \sigma\xi_i, \tag{1.19}$$

where $\sigma > 0$ is the parameter corresponding to the level of noise and ξ_i are realizations of independent and identically normally distributed random variables. Moreover $(T_i)_{0\leq i\leq n-1}$ corresponds to the trend and $(O_i)_{0\leq i\leq n-1}$ to the HF features (cf Figure 1.7).

For the general trend, we choose the Lennard Jones potential [77], since we notice that its DFT is not monotonously decreasing in the low frequency range (see Figure 1.2) and that it displays a similar shape as the experimental signals presented in Section 1.5. The Lennard Jones potential is defined by P_i:

$$P_i = \left(c_1\left[\left(\frac{c_2}{i}\right)^p - c_3\left(\frac{c_2}{i}\right)^q\right] + c_4\right).$$

Since this potential is not defined at 0, we link the potential to an affine function. Hence we introduce the index j ($0 < j < n-1$) which connects the potential to the affine function. We denote the trend by the vector $(T_i)_{0\leq i\leq n-1}$:

$$T_i = \left(\frac{P_{j+1} - P_j}{j+1} i + P_j\right) \mathbb{1}_{\{0\leq i\leq j\}} + P_i \mathbb{1}_{\{j+1\leq i\leq n-1\}}.$$

The HF features in the test signal correspond to sine waves and are located at a specific time interval.

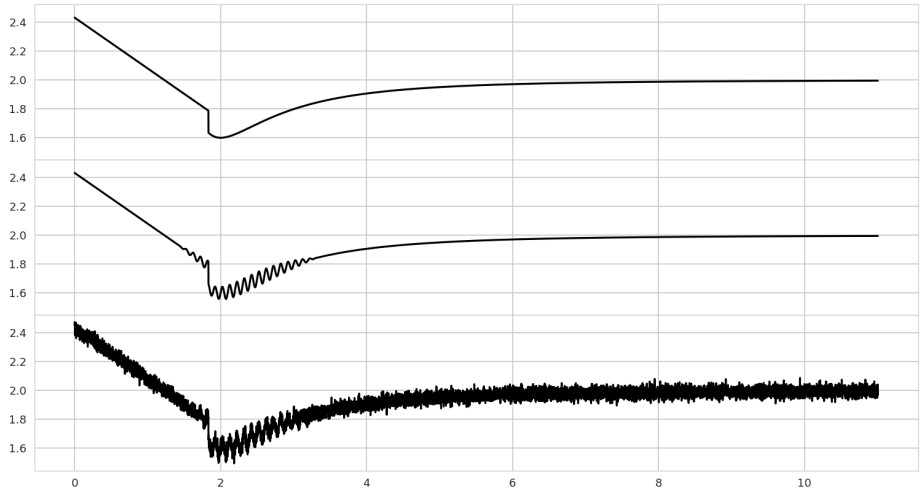

Figure 1.7 – **Simulation of the test signal defined by** (1.19)**.**The x-axis is the time in hours. (Up) Plot of $(T_i)_{0\leq i\leq 10^5}$ with parameters $c_1 = 0.4$, $c_2 = c_3 = c_4 = 2$, $\frac{p}{2} = q = 3$, $j_0 = 1700$, $j_1 = 3400$. (Middle) Plot of $(T_i + O_i)_{0\leq i\leq 10^5}$ with the same parameters and $c_a = 0.05$, $c_f = 10$. (Down) Plot of $(S_i)_{0\leq i\leq 10^5}$ with the same parameters and $\sigma = 0.025$.

Hence we introduce the indices $0 < j_0 < j_1 < n-1$ which localize the oscillations in the signal, and we define the oscillations by the vector $(O_i)_{0\leq i\leq n-1}$:

$$O_i = c_a(i - j_0)(j_1 - i)\sin(2\pi c_f i)\left(\frac{4}{(j_1 - j_0)^2}\right)\mathbb{1}_{\{j_0\leq i\leq j_1\}} \tag{1.20}$$

where c_a (resp. c_f) is the parameter for the amplitude (resp. the frequency) of the oscillations.

Numerical computations and robustness of the procedure. We want to understand the robustness of the numerical procedure when the frequencies and the amplitudes of the oscillations are fixed but the level of noise varies. Other said, for which parameters of the oscillations and for which level of noise does the test return that the signal oscillates (or not)? In order to answer this question, we propose the following sensitivity analysis.

σ	$\frac{1}{10}c_a$	$\frac{1}{2}c_a$	c_a	$2c_a$	$10c_a$
$\widehat{m}$	6	6	6	6	24
$\widehat{\mathsf{G}}_{n,\widehat{m}}$ (Hz)	2.069e−3	2.044e−3	2.145e−3	1.943e−3	8.437e−2
$\widehat{\mathsf{D}}_{n,\widehat{m}}$	1.73e−4	1.807e−4	1.807e−4	1.844e−4	2.768e−3
p-value	5e−5	5e−5	5e−5	5e−5	4.023e−1

Figure 1.8 – **Table of estimators and p-values of the sanity-check signals.** The simulation of the null is performed with the real trend of the signals.

First we remind the parameters in our system. From the signal construction, we have three parameters :

- σ the standard deviation of the normal distributed noise,
- c_a the parameter corresponding to the amplitude of the oscillations,
- c_f the parameter corresponding to the frequency of the oscillations (since the time scale is in hours, $c_f/3600$ is expressed in Hz).

The smoothing parameter $\widehat{m}$ is chosen thanks to the data-driven procedure described previously (1.18).

The relevant output of our model is the p-value of the signals computed thanks to the numerical procedure. A natural way to study the sensitivity of the p-value to the parameters is to fix all parameters but one and observe the effect on the p-values obtained. In this example the varying parameter is the level of noise $\sigma \in \left\{\frac{1}{10}c_a,\ \frac{1}{2}c_a,\ c_a,\ 2c_a,\ 10c_a\right\}$.

First sanity check test

Since we are working with a constructed sanity check signal, we obtained $(\widehat{\mathsf{G}}^k_{n,\widehat{m}}, \widehat{\mathsf{D}}^k_{n,\widehat{m}})$ in Figure 1.9 by applying the procedure of detection of the HF feature parameters setting $c_a = c_f = 0$ (it corresponds to $S_i = T_i + \sigma\xi_i$ in (1.19)). Thus the simulation of the null in Section 1.3.2 is performed using the real trend of the signal in (1.14). Then the signal tested (Figure 1.9) are constructed signal with parameters $c_a = 0.05$, $c_f = 10$ and $\sigma \in \{\frac{1}{10}c_a,\ \frac{1}{2}c_a,\ c_a,\ 2c_a,\ 10c_a\}$ in (1.19). The results of the detection of HF features and the statistical test are in Table 1.8. We note that for standard deviations of the noise between a tenth and the double of the amplitude of the oscillations, the p-value of the test is equal to 5e − 5. Hence, we are inclined to reject the hypothesis $\mathcal{H}^0$ which corresponds to the event that the signal displays no oscillations. Moreover we note that the signals with standard deviations of the noise between $\frac{1}{10}c_a$ and $2c_a$ have almost the same HF feature parameters where $(\widehat{\mathsf{G}}_{n,\widehat{m}}, \widehat{\mathsf{D}}_{n,\widehat{m}}) \approx (2\text{e}-3, 1.8\text{e}-4)$. In contrast, for the

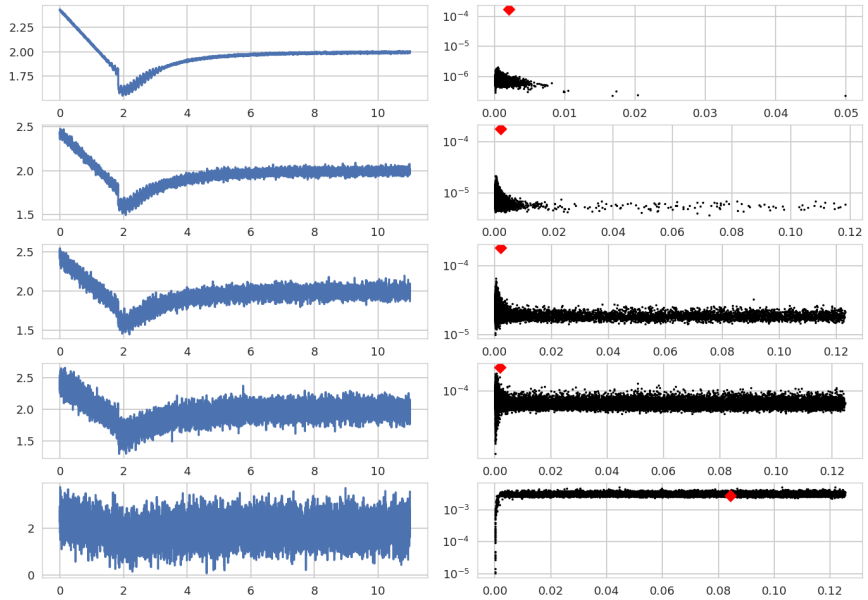

Figure 1.9 – **Numerical results of the procedure on the sanity-check signal when the simulation of the null is performed with the real trend.** (Left column) Plot of $(S_i)_{1\leq i\leq 10^5}$ (1.19) with the parameters $c_1 = 0.4$, $c_2 = c_3 = c_4 = 2$, $\frac{p}{2} = q = 3, j_0 = 1700$, $j_1 = 3400$, $c_a = 0.05$, $c_f = 10$ and $\sigma \in \left\{\frac{1}{10}c_a,\ \frac{1}{2}c_a,\ c_a,\ 2c_a,\ 10c_a\right\}$ from top to bottom. The x-axis is the time in hours. (Right column) The black dots are the cloud of points of the simulation of the null, for $N = 20000$. The red diamond corresponds to the HF features parameters of the corresponding signal on the left column. The x-axis is the localization parameters $\widehat{G}_{n,\widehat{m}}$ and the y-axis is the relative amplitude $\widehat{D}_{n,\widehat{m}}$.

signal with the standard deviation of the noise of $10c_a$, the p-value is equal to 0.4, hence we are inclined to accept that the signal has not significant enough HF feature.

Second sanity check test

The second step is to test the procedure on the same signals but using the trend estimate given by (1.15) and the noise estimation procedure described in the first step of Section 1.3.2. The method chosen to estimate the trend of the signal is the ℓ_1-trend filtering [82]. As displayed in Figure 1.10, the trend estimation is less robust as the standard deviation of the noise rises. However this method is qualitatively the right one to estimate the trend of a signal displaying jumps or spikes.

Hence we compute the procedure to obtain the HF features parameters for the sanity check signals using (1.19) with standard deviation level $\sigma \in \left\{\frac{1}{10}c_a,\ \frac{1}{2}c_a,\ c_a,\ 2c_a,\ 10c_a\right\}$. The p-values are computed using the ℓ_1-trend estimators in order to obtain the couples $(\widehat{\mathrm{G}}^k_{n,\widehat{m}}, \widehat{\mathrm{D}}^k_{n,\widehat{m}})$ where $k = 1,\dots,20000$. The results are in Table 1.11. Similarly to the first sanity check, the p-values for the signals with a level of noise from $\frac{1}{10}c_a$ to $2c_a$ is equal to $5\mathrm{e}-5$. Hence the procedure detect significant HF features where $\widehat{\mathrm{G}}_{n,\widehat{m}} \approx (2\mathrm{e}-3, 2\mathrm{e}-4)$. Also for a standard deviation of the noise of $10c_a$, the p-value is 5.32e−2, so that HF feature parameters are not significant enough.

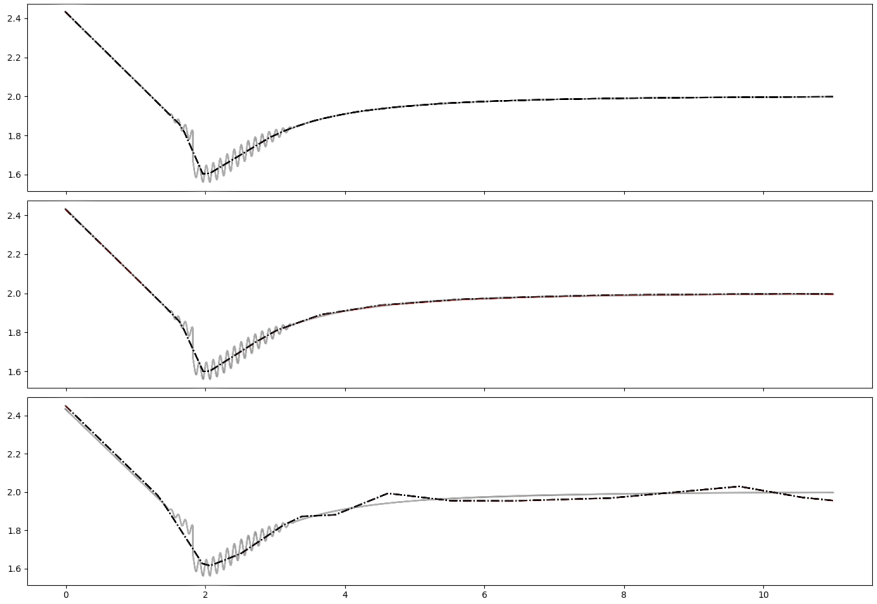

Figure 1.10 – **Numerical estimation of the trend on the sanity check signals.** The x-axis is the time in hours.The parameter in the ℓ_1-trend filtering is $\lambda = 301$. (Up) Plot of $(P_i + O_i)_{0\leq i\leq 10^5}$ in (1.19) with parameters $c_1 = 0.4$, $c_2 = c_3 = c_4 = 2$, $\frac{p}{2} = q = 3, j_0 = 1700$, $j_1 = 3400$ $c_a = 0.05$, $c_f = 10$. The dashed line is the ℓ_1-trend estimator when $\sigma = \frac{1}{10}c_a$. (Middle) The dashed line is the ℓ_1-trend estimator when $\sigma = c_a$. (Down)The dashed line is the ℓ_1-trend estimator when $\sigma = 10c_a$.

σ	$\frac{1}{10}c_a$	$\frac{1}{2}c_a$	c_a	$2c_a$	$10c_a$
$\widehat{m}$	3	3	3	3	18
$\widehat{\mathsf{G}}_{n,\widehat{m}}$ (Hz)	2.095e−3	2.095e−3	2.044e−3	2.12e−3	1.181e−1
$\widehat{\mathsf{D}}_{n,\widehat{m}}$	1.768e−4	1.784e−4	1.918e−4	2.394e−4	3.593e−3
p-value	5e − 5	5e−5	5e−5	5e−5	5.32e−2

Figure 1.11 – **Table of estimators and p-values of the sanity-check signals.** The simulation of the null is performed with the ℓ_1-estimate of the trend (1.15) of the signals.

1.5 Empirical analysis on biological data

The Prion diseases, also known as transmissible spongiform encephalopathies (TSEs), are a group of animal and human brain diseases. The neurodegenerative processes are poorly understood and hence fatal. However the largely accepted hypothesis suggests that the infectious agent (PrPsc) is the misfolded form of the normal Prion protein (PrPc). The PrPsc forms multimeric assemblies (fibrils) which are the prerequisite for the replication and propagation of the diseases [131]. To follow the aggregation kinetics of these fibrils, compare it to mathematical models and get a better understanding of these diseases,

several experimental and measurement devices are used, among which the Static Light Scattering (SLS). The Static Light Scattering (SLS) signal is an experimental measurement which describes the temporal dynamics of PrP amyloid assemblies formed in vitro [93] see Fig. 1.1 taken from [54] (see Appendix 1.6.1).These signals correspond to an affine transformation of the second moment of the size distribution of protein polymers or fibrils through time [128]:

$$\sum_{i\in\mathcal{I}} i^2 c_i(t) + \sigma,$$

where $\mathcal{I}$ denotes the set of the sizes of the fibrils, c_i the concentration of fibrils of size i which is varying with the time t and $\sigma > 0$ is the experimental noise (σ can be time-dependent). At the beginning of the experiment the fibrils are large, containing in average several hundreds of monomers, which undergo an overall depolymerization process and leads to a decay in the signal. The experiment is carried out with six initial concentrations of fibrils (Figure 1.12) ranging from 0.25μmol to 3μmol; at higher initial concentrations (0.5μmol and higher), a re-polymerisation process can be observed, which may be viewed by the fact that the trend of the signal increases again before reaching a plateau. Moreover the SLS signals differ in terms of variance of noise and amplitude of oscillations (noticed by sight). We thus study each signal independently.

In order to test whether the signals display HF features, we submit the observations to the statistical test described above. The denoised signal and hence the standard deviation of the noise are estimated thanks to the VisuShrink method and the median absolute deviation (cf [51], [50]) using the symmlet wavelet with 8 vanishing moments and the library Wavelab [25] (the same results have been obtained with the homemade python library, see Appendix 1.6.2). The trend of the signal is estimated with the ℓ_1-trend filtering method with the parameter $\lambda = 31$ (λ is fixed qualitatively in order for the trend to include the discontinuous jumps of the SLS experiments). The results of the statistical test are summarized in Table 1.13.

We note that all signals display oscillations more or less pronounced (cf. Figure 1.14). The relative amplitude of the oscillations $\widehat{\mathsf{D}}_{n,\widehat{m}}$ differs from one signal to another for three reasons. First of all, each signal corresponds to an experiment with a specific initial concentration. The calibration of the experiments is not identical for experiments with different initial concentrations. Secondly, the signals are not on the same scale. The signal with initial concentration of 0.25μmol goes from 0.5 to 2.2 in amplitude, and the signal of initial concentration of 3μmol goes from 16 to 28 in amplitude. Finally, they do not have the same regularization coefficient $\widehat{m}$.

However the frequency localization parameters are comparable. In Table 1.13, we note that the parameters $\widehat{\mathsf{G}}_{n,\widehat{m}}$ are in the same range of value with a factor of less than 4 between the minimum and maximum $\widehat{\mathsf{G}}_{n,\widehat{m}}$. Finally all the p-value of the tests are equal to $5e-5$, the tests confirm that the signals display significant HF features.

Through this study, we demonstrated the existence of oscillatory behavior in the SLS experiments. The immediate biochemical consequences are the coexistence of structurally distinct PrP assemblies within

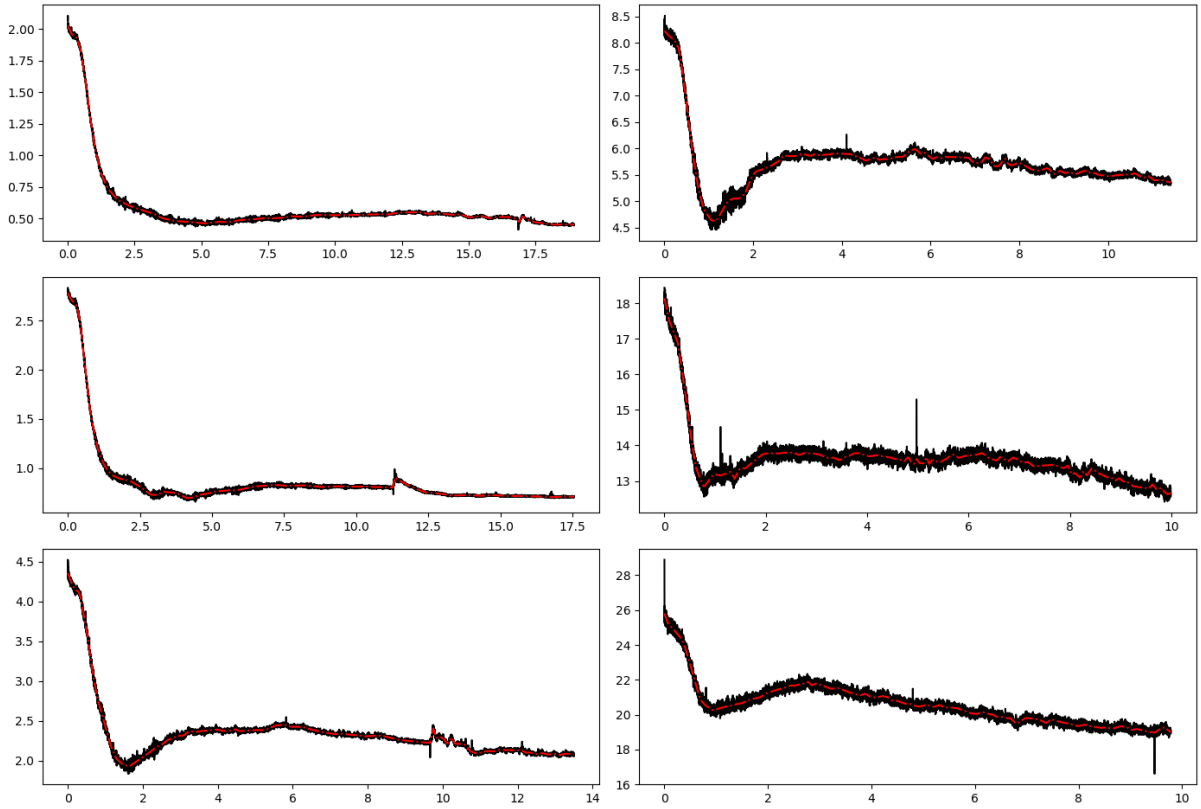

Figure 1.12 – **SLS experiments and trend estimates.** The x-axis is the time in hours. The parameter in the ℓ_1-trend filtering is $\lambda = 31$. (Top left) Plot of $n = 32768$ samples of SLS outputs with initial concentration (I_0) of 0.25μmol of PrP^{Sc} fibrils.The dashed line is the ℓ_1-trend estimator. (Middle left) $I_0 = 0.35\mu$mol (Bottom left) $I_0 = 0.5\mu$mol. (Top right) $I_0 = 1\mu$mol. (Middle right) $I_0 = 2\mu$mol. (Bottom right) $I_0 = 3\mu$mol.

Concentration (μmol)	0.25	0.35	0.5	1	2	3
$\widehat{\sigma}$	3.553e – 3	4.72e – 2	1.11e – 2	3.09e – 2	8.44e – 2	1.287e – 1
$\widehat{m}$	4	3	5	7	9	7
$\widehat{\mathsf{G}}_{n,\widehat{m}}$ (Hz)	4.954e–3	7.53e–3	5.656e–3	8.375.e–3	2.698e–3	4.971e–3
$\widehat{\mathsf{D}}_{n,\widehat{m}}$	9.649e–6	1.863e–5	1.012e–4	6.526e–4	3.345e–4	1.01e–3
p-value	5e – 5	5e–5	5e–5	5e–5	5e–5	5e–5

Figure 1.13 – **Table of estimators and p-values for the test of presence of HF features in the SLS experiments**

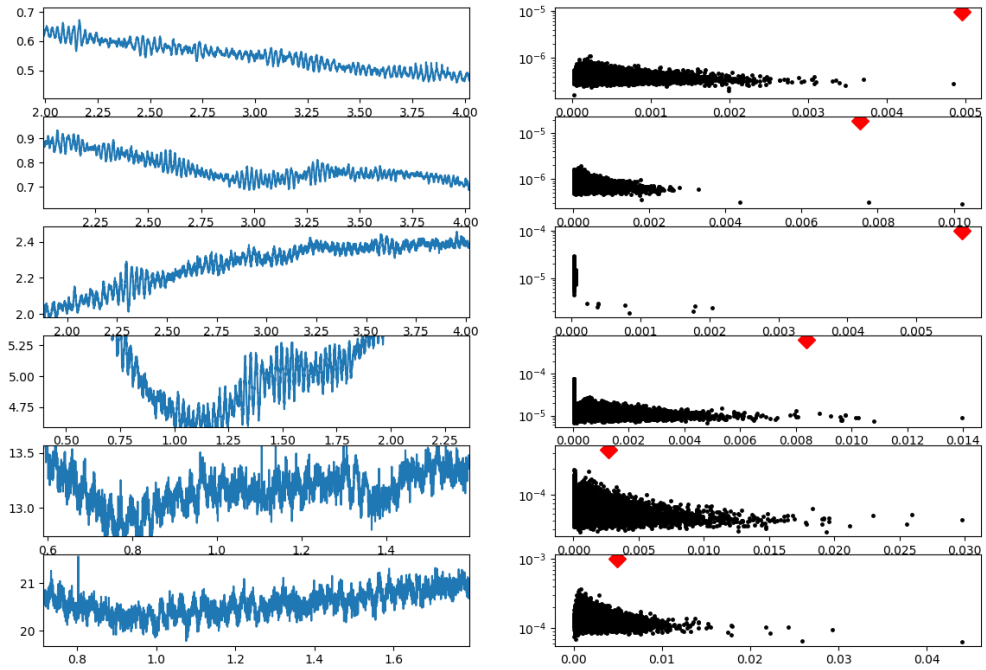

Figure 1.14 – **HF features of the SLS experiments and numerical results of the estimation of the HF features parameters.**(Left column) Zoom on the SLS experimentation signals with initial concentration in μmol from the top to the bottom of $I_0 \in \{0.25,\ 0.35,\ 0.5,\ 1,\ 2,\ ,3\}$ The x-axis is the time in Hours. (Right column) The black dots are the cloud of points $(\widehat{\mathsf{G}}^k_{n,\widehat{m}}, \widehat{\mathsf{D}}^k_{n,\widehat{m}})$ corresponding to the simulation of the null for $k = 1,\dots,20000$. The red diamond corresponds to the HF features parameters $(\widehat{\mathsf{G}}_{n,\widehat{m}}, \widehat{\mathsf{D}}_{n,\widehat{m}})$, defined by Definition 3, of the corresponding signal on the left column. The x-axis is the localization parameter of the HF features and the y-axis is the relative amplitude of the HF .

the same media and the unstable behavior, i.e. out of the thermo-dynamical equilibrium, of the chemical system formed by theses assemblies. Indeed the observation of oscillations in these light-scattering experiments has shed light on the existence of a complex chemical reaction network beyond the existing aggregation-fragmentation models. This has paved the way for new mechanistic models, e.g. a system of reactions which possibly involve several conformations of PrP assemblies [54], capable of explaining such phenomena. Also it has been reported that the existence of multiple conformations of PrP assemblies within an isolate contributes to the adaptation and evolution of Prion as a pathogen to a new environment and a new host [94].

Further biochemical characterizations are required to explore the dynamics of these oscillations and to establish more precise kinetic models. The methodology developed in the present work will lead to analyze and characterize with specific parameters transient oscillations. These parameters will lead to evaluate physico-chemical conditions as well as the dynamic of the present complex system.

Summary

In this study, we have introduced a method, based on the discrete Fourier transform, to quantify the high frequency features of a given non stationary discrete signal, and then test whether the parameters characterizing these features may be considered as significant or not. We then tested our method on simulated and experimental data, which shed light on its efficiency, since HF features may be detected even with a noise of the same amplitude. Moreover, the two parameters estimated from the data to characterize the HF are informative *per se*: they could be used by the experimentalists to compare different experimental conditions and their influence on such transient phenomena in the signals. They may also reveal useful in the search for quantitative comparison between mechanistic models, such as the one proposed in [54], and experimental data.

The test to detect HF feature is based on the projection of the signal in a discrete Fourier basis. A further step, in order to localize them, would be to define them in a wavelet basis. The number of parameters will then be equal to three (one for the resolution, one for the amplitude and one for the localisation on the time-scale), and the test of hypothesis has to be extended to this framework. This is a direction for future work.

1.6 Supplementary and appendix

1.6.1 Materials and methods of the depolymerisation experiment shown in Figures 1.1 and 1.12

Formation of amyloid fibrils: PrP amyloid fibrils were formed using the manual setup protocol described previously in [21]. Fibril formation was monitored using a ThT binding assay [21]. Samples were dialysed in 10 mM sodium acetate, pH 5.0. Then fibrils were collected by ultracentrifugation and resuspended in 10 mM sodium acetate, pH 5.0. A washing step was performed by repeating the ultracentrifugation and resuspension steps in 10 mM sodium acetate, pH 5.0. Static light scattering: Static light scattering kinetic experiments were performed with a thermostatic homemade device using a 407-nm laser beam. Light-scattered signals were recorded at a 112^0 angle. Signals were processed with a homemade MatLab program. All experiments have been performed at 55^0C in a 2mmX10mm cuve.

1.6.2 Library in python to implement the numerical simulation

The numerical simulations have been made with the library python accessible at *https://github.com/mmezache/HFFTest*. The functions of the library are explicitely commented in the file "README.md". The functions are organized in four categories in the library:

1. the procedure to compute the HF features parameters,

2. the procedure to simulate the null hypothesis,
3. the Monte-Carlo procedure to compute the p-value,
4. the procedure to compute test signals such as the ones displayed in Figures 1.2, 1.4, 1.7.

The file "ExampleHFF.py" is a python program which compute the complete procedure for a test signal. The users may change at will the following parameters:

- the length of the signal,
- the standard deviation of the noise,
- the amplitude of the oscillations,
- the parameter of the ℓ^1-trend filtering,
- the number of iteration of the Monte-Carlo procedure,
- the choice of the test signal.

The program displays the test signal obtained, the trend estimate, the cloud of points corresponding to the HF features of the null (blue dots) and the point corresponding to the HF features of the tested signal (red dot), and the single-sided amplitude spectrum of the signal which emphasizes the points where the computations of the HF features are computed (cf Figure 1.3).

The time of computations may be significantly long if the number of iteration of the Monte-Carlo procedure is big (over 100). However the Monte-Carlo procedure can be computed in a parallelized framework which reduces drastically the time of computations.

Moreover the automatic choice of the smoothing parameter $\widehat{m}$ is efficient for signals which display oscillations of "high" frequency, i.e. if the spike corresponding to the oscillations in the single sided amplitude spectrum is located away from the low-frequency components (cf Section 1.4 and example 2 in "ExampleHFF.py"). The procedured was designed to identify oscillations "hidden" in the noise, a situation which corresponds to the experimental signals. If the signal tested has oscillations located in the low-frequencies, the users are advised to fix the smoothing parameters (cf example 1 in "ExampleHFF.py").

Chapter 2

A bi-monomeric system to capture oscillatory aggregation kinetics

2.1 Introduction

The aim of this chapter is to propose and study a new polymerisation-depolymerisation model capable of explaining oscillations, which have been observed experimentally in the time-course of prion protein polymerisation experiments. Up to our knowledge, such oscillations have never been observed, either theoretically or numerically, in the family of growth-fragmentation-nucleation equations, which are most often used to model protein polymerisation. In order to understand the appearance of oscillations observed in protein aggregation experiments, we propose, motivate and analyse mathematically the differential system describing the kinetics of the following reactions:

$$\begin{cases} \mathcal{V}+\mathcal{W} & \xrightarrow{k} & 2\mathcal{W}, & \\ \mathcal{W}+\mathcal{C}_i & \xrightarrow{a_i} & \mathcal{C}_{i+1}, & 1 \le i \le n, \\ \mathcal{C}_i+\mathcal{V} & \xrightarrow{b_i} & \mathcal{C}_{i-1}+2\mathcal{V}, & 2 \le i \le n, \end{cases}$$

with n finite or infinite. This system may be viewed as a variant of the seminal Becker-Döring system, and is capable of displaying sustained though damped oscillations.
This work is the result of a collaboration with M. Doumic[1], K. Fellner[2] and H. Rezaei[3] and has been published in the Journal of Theoritical Biology [55].

[1]Sorbonne Universités, Inria, Université Paris-Diderot, CNRS, Laboratoire Jacques-Louis Lions, F-75005 Paris, France, marie.doumic@inria.fr
[2]University of Graz, Austria, Institute of Mathematics and Scientific Computing, 8010 Graz, klemens.fellner@uni-graz.at
[3]INRA, UR892, Virologie Immunologie Moléculaires, 78350 Jouy-en-Josas, France, human.rezaei@inra.fr

Biological background and motivation

The prion phenomenon (prion being derived from 'proteinaceous infectious only particle') involves the self-propagation of a biological information through structural information transfer from a protein in a prion-state (i.e. misfolded resp. infectious) to the same protein in a non-prion state. Such a concept is key to the regulation of diverse physiological systems and to the pathogenesis of prion diseases [40, 135, 154]. Recently, prion-like mechanisms have been involved in the propagation and gain of toxic functions of proteins or peptides associated with other neurodegenerative disorders such as Alzheimer, Parkinson and Huntington diseases [80]. Elucidating the mechanisms driving prion-like aggregation is thus of key importance, and, as explained below, still requires new mathematical modelling and analysis.

During the evolution of prion pathology, the host encoded monomeric prion protein (PrPC) is converted into misfolded aggregating conformers (PrPSc) [19]. PrPSc assemblies have the ability to self-replicate and self-organise in the brain through a still unresolved molecular mechanism commonly called *templating*. Differences in disease phenotypes (distinctive symptomologies, incubation times, and infectious characters of PrPSc) are reported within the same host species. These phenotypic differences are assigned to structural differences in PrPSc assemblies, introducing the concept of *prion strains* based on structural diversity/heterogeneity of PrPSc assemblies [73]. In the prion literature a plethora of evidences strongly suggest that within a given prion strain a PrPSc structural heterogeneity exists, which suggests that in a given environment structurally different PrPSc subassemblies with different biological and physico-chemical properties coexist [94] even if the mechanism of this diversification remains elusive. To date, very few mathematical models have taken into account the coexistence of multiple prion assemblies or multiple type of fibrils [41]. Indeed, most of the aggregation models have been built using the canonical nucleation-elongation-fragmentation process seminally reported by Bishop and Ferrone (see e.g. [18, 98, 126]), which is based on the existence of a structurally unique type of assemblies characterised only by their size distribution. The characterisation of multiple types of PrPSc subassemblies with different rates of aggregation, depolymerisation and exchange requires new mathematical models and analyses to describe the dynamics and relation between different subspecies.

In order to explore the consequence of the coexistence of structurally different PrPSc assemblies within the same environment, the depolymerisation kinetics of recombinant PrP amyloid fibrils have been explored by Static Light Scattering (SLS) [100]. A detailed study of those experiments revealed a surprising, transient oscillatory phenomenon, as the time evolution of the SLS measurement (see Appendix 2.6.2 for details) shows in Figure 2.1. First note that when denoting by $c_i(t)$ the concentrations at time t of the polymers containing i monomers, we can interpret the signal of an experimental SLS measurement, as in [126], as the time evolution of the second moment of the polymers, *i.e.*

$$M_2(t) := \sum_{i=1}^{n} i^2 c_i(t). \tag{2.1}$$

Hence, at the beginning of the experiments, after a short lag phase, quick depolymerisation is observed. This is followed by a transient phase ranging from approximately 1h to 11 hours, when slow variations

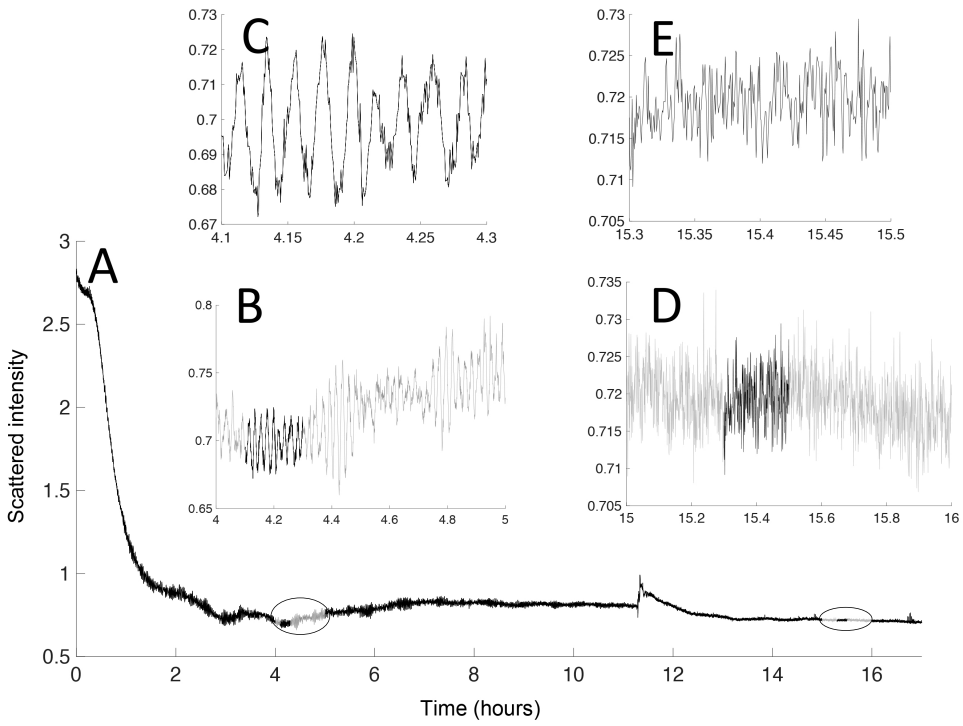

Figure 2.1 – Human PrP amyloid fibrils (Hu fibrils) depolymerisation monitored by Static Light Scattering (see Appendix 2.6.2 for details). A: The overall view of the $0.35\mu M$ Hu-fibrils depolymerisation at 55^0C. B-E correspond to a zoom-in on different time-segments of the depolymerisation curve A. As shown in B, from time 4 to time 5h oscillations have been observed when for time segment corresponding to time 15.3 to 15.5h only noise has been detected (D).

were superimposed by fast periodic oscillations with a frequency around 0.01 to 0.02 Hz, see Figures 2.1B and 2.1C. Both the variations and the oscillations progressively disappear, and a constant signal with noise is observed at the end of the experiments (Figure 2.1, D and E). This specific phenomenon may be used to gain new insight into the underlying biological mechanism.

A first key question of our study is thus the following: What kind of core elements should a model feature in order to explain the appearance of such oscillations?

The most natural departure point in the formulation of a suitable mathematical model is the Becker-Döring model of polymerisation and depolymerisation [9]. The Becker-Döring model is coherent with other biological measurements [100], and it is viewed in the protein polymerisation literature as the "primary pathway" model [18, 126].

Becker-Döring considers two reverse reactions: polymerisation through monomer addition, and depolymerisation due to monomer loss. Accordingly, the model is characterised by the following system

of reactions, where $\mathcal{C}_i$ denotes polymers containing i monomers - so that $\mathcal{C}_1$ are the monomers - and a_i, b_i are the polymerisation resp. depolymerisation reaction rate coefficients:

$$\begin{cases} \mathcal{C}_1 + \mathcal{C}_i \xrightarrow{a_i} \mathcal{C}_{i+1}, & i \geq 1, \\ \mathcal{C}_i \xrightarrow{b_i} \mathcal{C}_{i-1} + \mathcal{C}_1, & i \geq 2. \end{cases}$$

The Becker-Döring system, however, satisfies the detailed balance condition [7], which implies the existence of a Lyapunov functional and no sustained oscillations are possible. Also damped oscillations, up to the best of our knowledge, have never been observed numerically or evidenced analytically. We thus needed a variant of the Becker-Döring model to explain the experimentally observed oscillations displayed in Figure 2.1.

In [74], it was recently shown that PrPSc assemblies are in equilibrium with an oligomeric conformer (suPrP) encoding the entire strain information and constituting an elementary building block of PrPSc assemblies. The fact that such an oligomeric building block appears separately from the monomeric PrP points towards models with two different quasi-monomeric species (i.e. one monomer and one oligomeric conformer in contrast to the polymer species $\mathcal{C}_i$), each of which playing a role in a different reaction. A suitable mathematical model should also to take into account the constraint that large polymers cannot interact directly, for reasons of size and order of magnitude of their concentrations. Hence, we assume that polymers can only interact indirectly, through the exchange of monomers or small oligomeric conformers.

A third crucial modelling aspect concerns the details of the depolymerisation reaction rates, which are linear in the original Becker-Döring system. However, numerical studies (see below for a more detailed discussion and numerical illustrations) as well as the content of this study strongly suggests that sustained or damped oscillations require a nonlinear (more precisely, a monomer induced) depolymerisation process, which we detail in the following section.

2.2 Introduction of the proposed model system

We propose the following model system: Let $\mathcal{V}$ and $\mathcal{W}$ denote the two monomeric species, where the second, conformer species is taken monomeric for the sake of simplicity (but a slight modification of the model would allow to consider it as oligomeric). Let $\mathcal{C}_i$ be the polymers containing i monomers, where polymerisation signifies the amendment of a monomer $\mathcal{W}$ while depolymerisation only occurs when induced via the monomeric species $\mathcal{V}$. More precisely, we consider

$$\begin{cases} \mathcal{V} + \mathcal{W} \xrightarrow{k} 2\mathcal{W}, & \\ \mathcal{W} + \mathcal{C}_i \xrightarrow{a_i} \mathcal{C}_{i+1}, & 1 \leq i \leq n, \\ \mathcal{C}_i + \mathcal{V} \xrightarrow{b_i} \mathcal{C}_{i-1} + 2\mathcal{V}, & 2 \leq i \leq n. \end{cases} \tag{2.2}$$

with a reaction rate constant k for the monomer/conformer dynamics and polymerisation/depolymerisation coefficients a_i and b_i. Note that large values for k compared to a_i, b_i introduce a slow-fast behaviour into (2.2) and yields a mechanism of oscillations which is detailed in a fully rigorous way for a two-polymer system (i.e. $n = 2$) in Section 2.3.

We emphasise the two main differences of (2.2) as compared to the classical Becker-Döring system: First, instead of one monomeric species $\mathcal{C}_1$, we now consider two interacting species of monomers (or conformers), $\mathcal{V}$ and $\mathcal{W}$. Secondly, depolymerisation is modelled as a monomer induced, nonlinear process, which requires the catalytic action of $\mathcal{V}$. Note that this process is reminiscent of the cyclical behaviour of the three-species system

$$\mathcal{V}+\mathcal{W} \quad \xrightarrow{k} \quad 2\mathcal{W}, \qquad \mathcal{W}+\mathcal{M} \quad \xrightarrow{a} \quad 2\mathcal{M}, \qquad \mathcal{M}+\mathcal{V} \quad \xrightarrow{b} \quad 2\mathcal{V}, \tag{2.3}$$

which is known to produce sustained periodic oscillations, see [162], where it is called the Ivanova system, or [158], where it is referred to as a simplification of the Belousov-Zhabotinsky system.

To reiterate and further illustrate the reasons which guided us towards model (2.2), let us isolate those two main ingredients. Firstly, let us modify the Becker-Döring system by taking two monomeric species [74], but with a standard linear depolymerisation reaction, i.e. we consider the following system:

$$\begin{cases} \mathcal{V}+\mathcal{W} & \xrightarrow{k} & 2\mathcal{W}, & \\ \mathcal{W}+\mathcal{C}_i & \xrightarrow{a_i} & \mathcal{C}_{i+1}, & 1 \le i \le n, \\ \mathcal{C}_i & \xrightarrow{b_i} & \mathcal{C}_{i-1}+\mathcal{V}, & 2 \le i \le n. \end{cases} \tag{2.4}$$

Figure 2.2 compares the behaviours of the bi-monomeric Becker-Döring system (2.4) to model (2.2) under conditions when both feature oscillations (which is systematic in the nonlinear depolymerisation model (2.2), yet only occurs for some parameters in the bi-monomeric Becker-Döring system (2.4)). Nevertheless, even if the bi-monomeric Becker-Döring system (2.4) shows oscillatory behaviour, those oscillations are far less sustained and cannot serve as an explanation of the experimental observations.

Interestingly, nonlinear depolymerisation leads not only to much more sustained oscillations, but also yields faster convergence to its size-distribution equilibrium (data not shown), while the linear bi-monomeric Becker-Döring system (2.4) exhibits similar metastability as observed for the Becker-Döring system [123].

Secondly, when considering a monomeric Becker-Döring system with second-order depolymerisation reaction:

$$\mathcal{V}+\mathcal{C}_i \quad \xrightarrow{a_i} \quad \mathcal{C}_{i+1}, \quad 1 \le i \le n, \qquad \mathcal{C}_i+\mathcal{V} \quad \xrightarrow{b_i} \quad \mathcal{C}_{i-1}+2\mathcal{V}, \quad 2 \le i \le n, \tag{2.5}$$

numerical simulations do not display any kind of oscillations, see second row in Figure 2.3.

Let us also remark that in model (2.2), the first polymer species $\mathcal{C}_1$ could also denote a smallest polymer of size $n_0 > 1$, i.e. it represents the smallest "active" polymer size. This means that no nucleation, as modelled by $\mathcal{C}_1+\mathcal{C}_1 \to \mathcal{C}_2$ in the Becker-Döring system, is considered. This is in line with the time-scale of the considered experiment where nucleation is negligible compared with other reactions.

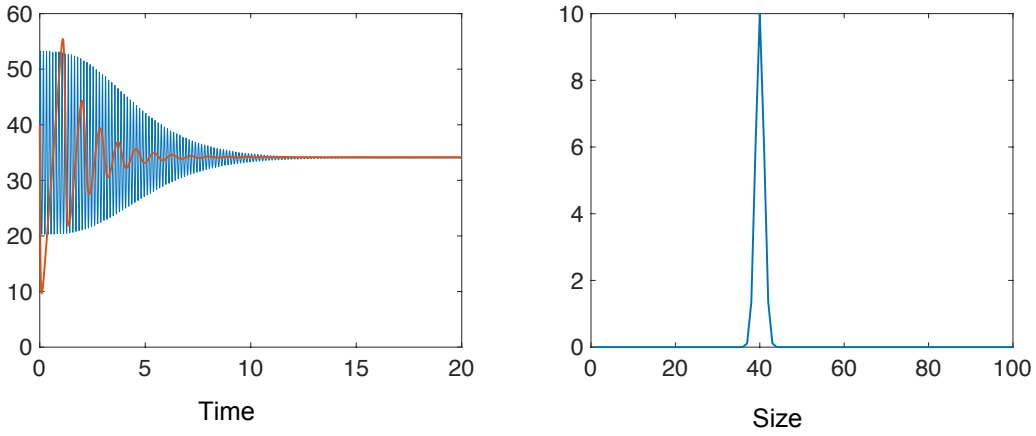

Figure 2.2 – Left images: Comparison of the oscillatory behaviour of the monomer concentration v of the proposed model (2.2) (blue) with the bi-monomeric Becker-Döring system (2.4) with linear depolymerisation (red) subject to the same initial distribution (Right image).

Finally, the original Becker-Döring system (for $n = \infty$) allows to model phase transitions where polymers of infinite size are created in finite time depending on the polymerisation coefficients; a phenomenon called *gelation* or also *Ostwald ripening* [7]. In this paper, we shall consider both finite or infinite systems and discuss similarities and differences. However, in view of our application background of understanding amyloid fibrils, we are never interested in the appearance of gelation or Ostwald ripening and only consider polymerisation coefficients, where the average size of polymers, though possibly large, remains finite.

The purpose of this study is to provide a first insight into this new, in our opinion highly promising model. In particular, the model system (2.6) in the following section reveals extremely rich behaviour and is capable of displaying various types of dynamics such as sustained and damped periodic oscillations.

2.2.1 A bi-monomeric nonlinear Becker-Döring model: Formal properties

We denote by $c_i(t)$, $v(t)$ and $w(t)$ the concentrations at time t of the polymers containing i monomers, the depolymerising and the polymerising monomeric species. We assume the reactant's concentrations to be sufficiently large to neglect stochastic effects and consider a deterministic setting. By using the mass-action law, model (2.2) yields the following system of differential equations:

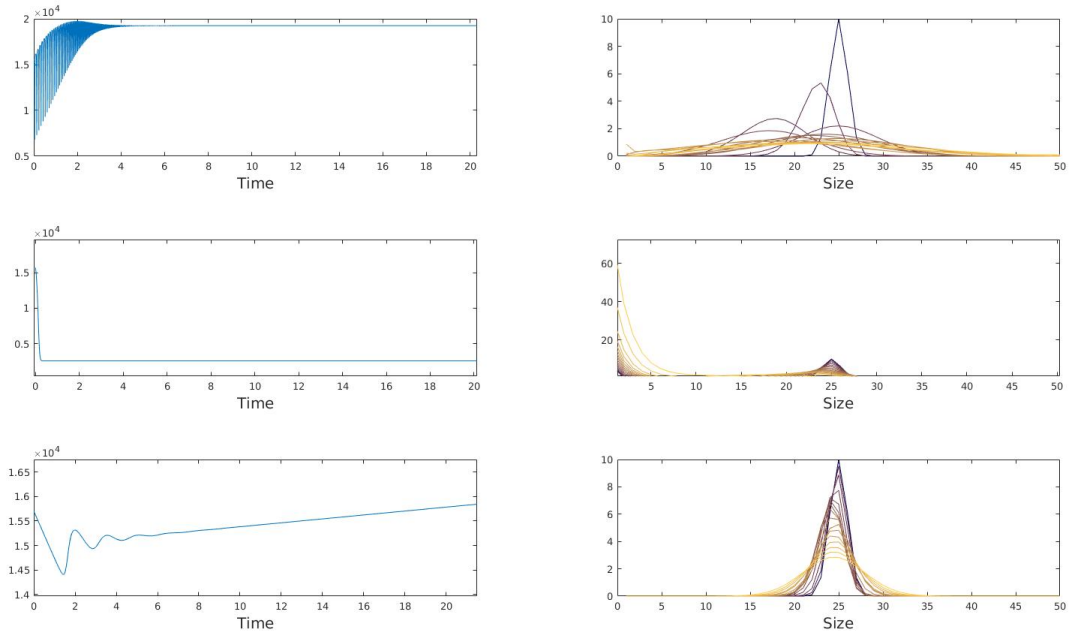

Figure 2.3 – Numerical results corresponding to SLS measurement, *i.e.* the quantity M_2 defined by (2.1) (Left Column) and the evolution of the size distribution of polymers (Right Column). First Row: The here proposed model (2.2) with parameters $n = 50$, $k = 9.5$, $a_i = 4.8$, $b_i = 8$. Second Row: The model (2.5) with c_1 multiplied by 10 in order to ignite the reactions in the system. Third row: The model (2.4) with parameters $n = 50$, $k = 0.95$, $a_i = 0.48$, $b_i = 0.8$.

$$\begin{cases} \frac{dv}{dt} = -kvw + v\sum_{i=2}^{n} b_i c_i, & v(0) = v^0, \\ \frac{dw}{dt} = -w\sum_{i=1}^{n-1} a_i c_i + kvw, & w(0) = w^0, \\ \frac{dc_1}{dt} = -wa_1 c_1 + vb_2 c_2, & c_1(0) = c_1^0, \\ \frac{dc_i}{dt} = w(-a_i c_i + a_{i-1} c_{i-1}) + v(b_{i+1} c_{i+1} - b_i c_i), \quad 2 \le i \le n-1, & c_i(0) = c_i^0, \\ \frac{dc_n}{dt} = wa_{n-1} c_{n-1} - vb_n c_n, & c_n(0) = c_n^0, \end{cases}$$

where the last equation is only to be considered when n is finite.

As in [124], we introduce the net rate of an i-polymer being converted to an $(i+1)$-polymer by

$$J_i = wa_i c_i - vb_{i+1} c_{i+1}, \qquad 1 \le i \le n-1.$$

With the convention $J_0 = J_n = 0$, we can thus rewrite the above system as

$$\begin{cases} \frac{dv}{dt} = -kvw + v\sum_{i=2}^{n} b_i c_i, & v(0) = v^0, \\ \frac{dw}{dt} = -w\sum_{i=1}^{n-1} a_i c_i + kvw, & w(0) = w^0, \\ \frac{dc_i}{dt} = J_{i-1} - J_i, & c_i(0) = c_i^0, \quad 1 \le i \le n. \end{cases} \tag{2.6}$$

In this chapter, we shall always assume the initial conditions and reaction rates to be such that there exists a unique solution $(v, w, c_i) \in \mathcal{C}^1(0,T)^2 \times \mathcal{C}^1(0,T,\ell^1_1)$, where we denote

$$\ell^1_s := \left\{ (x_i)_{i\ge 1} \in \mathbb{R}^{\mathbb{N}} \;\middle|\; \sum_{i\ge 1} i^s x_i < \infty \right\}, \qquad \text{for} \quad s \in \mathbb{R}.$$

We first remark that solutions to System (2.6) in ℓ^1_1 have two conserved quantities, obtained by weighted sums of the equations:

1. The total number of polymers, since $\frac{d}{dt}\sum_{i=1}^{n} c_i = 0$. This conservation law is linked to the fact that we neglect nucleation.
2. The total mass, since $\frac{d}{dt}\left(v + w + \sum_{i=1}^{n} i c_i\right) = 0$, which indicates that there is no gain or loss of particles during the chemical reactions: the system is closed.

As a consequence of those two conservation laws, we introduce

$$P_0 := \sum_{i=1}^{n} c_i^0, \qquad M_{tot} := v^0 + w^0 + \sum_{i=1}^{n} i c_i^0.$$

Overview: The chapter is organised from the simplest to the most complete cases: In Section 2.3, we provide a complete and explicit study of the two-polymer case $n = 2$, which features a pivotal mechanism of damped periodic oscillations in the case of a large reaction rate k compared to the polymerisation coefficients, see Corollary 1. To understand this mechanism, Theorem 9 states the existence of a Lyapunov functional, which is also the Hamiltonian of an underlying Lotka-Volterra models and proves exponential convergence to an equilibrium of solutions despite their highly oscillatory behaviour, see e.g. the left blue solution in Figure 2.2. The main difficulty lies in the fact that the time derivative of the Lyapunov functional vanishes across some lines in phase-space, which necessitates precise estimates.

In Section 2.4, we focus on the case where the maximal size of polymers n is finite. We study the existence of steady states and their stability (Proposition 5). Further details are obtained in the case of constant coefficients, where we discuss the various zones of stability or instability with respect to the parameters.

In the final Section 2.5, we analyse well-posedness and steady states of the infinite system $n = \infty$. Two specific cases shed light on the damped oscillations: the constant coefficient case (i.e. $a_i = a$, $b_i = b$ for

two positive constants a and b and for all i) and the linear coefficient case (where $a_i = ia$, $b_i = (i-1)b$, for two positive constants a and b and for all i).

2.3 The two-polymer model

In this section, we study the bi-monomeric system (2.2) coupled to only two sizes of polymers in the case of normalised coefficients $a_1 = b_2 = 1$ for the sake of the clearest possible presentation. We thus investigate the following two-polymer model

$$\begin{cases} \frac{dv}{dt} = v\,[-kw + c_2], \\ \frac{dw}{dt} = w\,[kv - c_1], \end{cases} \qquad \begin{cases} \frac{dc_1}{dt} = -wc_1 + vc_2, \\ \frac{dc_2}{dt} = wc_1 - vc_2, \end{cases} \tag{2.7}$$

subject to the nonnegative initial data $v(0) = v^0$, $w(0) = w^0$, $c_1(0) = c_1^0$ and $c_2(0) = c_2^0$.

The purpose of this section is to explicitly exemplify a mechanism of transient oscillatory behaviour of (2.2) under the assumption that the reaction rate constant k is large (compared to the other parameters). More precisely, for a sufficiently small parameter $\varepsilon = \frac{1}{k}$, we will prove that under general conditions solutions to (2.7) converge exponentially to a positive equilibrium state while undergoing $O(1/\varepsilon)$ many transient oscillations.

This result is a consequence of proving that the two-polymer model (2.7): i) features a convex Lyapunov functional which entails exponential convergence to equilibrium via a generalised entropy method and ii) can be reformulated as a regular perturbation of a classical Hamiltonian-conserving Lotka-Volterra system, for which the perturbative terms are of order ε and cause exponential convergence to equilibrium on a time scale of order $1/\varepsilon$.

First, we recall that System (2.7) conserves the total number of polymers and the total mass. This implies the following two mass conservation laws for all $t \geq 0$:

$$c_1(t) + c_2(t) = P_0 = c_1^0 + c_2^0, \qquad \text{and} \qquad v(t) + w(t) + c_2 = M_{tot} - P_0 =: M.$$

Expressing c_1 and c_2 in terms of these two conservation laws allows to reduce System (2.7) into

$$\begin{cases} \frac{dv}{dt} = v\,[M - (k+1)w - v], \\ \frac{dw}{dt} = w\,[(M - P_0) + (k-1)v - w], \end{cases} \tag{2.8}$$

which constitutes a generalised Lotka-Volterra system of predator-prey type, see e.g. see [20] or [70], for which possible behaviours have been extensively listed and studied, and for which convergence may either be proved using an appropriate Lyapunov functional or using the Poincaré-Bendixson theorem and the Poincaré-Dulac theorem. However, up to our knowledge, these methods do not provide a rate of convergence, or explicit estimates.

Besides the boundary equilibria $(\bar{v}, \bar{w}) = (M, 0)$ and $(\bar{v}, \bar{w}) = (0, M - P_0)$ (in the case $M \geq P_0$), System

(2.8) has the equilibrium

$$v_\infty := \frac{P_0}{k}\left(1+\frac{1}{k}\right) - \frac{M}{k}, \qquad w_\infty := \frac{M}{k} - \frac{P_0}{k^2},$$

and $(v_\infty, w_\infty) > 0$ provided that $P_0 \in \left(\frac{kM}{1+k}, kM\right)$, which we shall assume henceforth.

We observe that the equilibrium (v_∞, w_∞) takes values of order $\varepsilon := 1/k$. This suggests the rescaling

$$v \to \frac{v}{k} = \varepsilon v, \qquad \text{and} \qquad w \to \frac{w}{k} = \varepsilon w,$$

and yields the rescaled equilibrium values

$$v_\infty = P_0(1+\varepsilon) - M, \qquad \text{and} \qquad w_\infty = M - \varepsilon P_0, \tag{2.9}$$

By using (2.9) and $v_\infty + w_\infty = P_0$, System (2.8) rescales to the following two-polymer system, which we shall study subsequently:

$$\begin{cases} \frac{dv}{dt} = v\,[w_\infty - w] - \varepsilon\, v\,[v - v_\infty + w - w_\infty], \\ \frac{dw}{dt} = w\,[v - v_\infty] - \varepsilon\, w\,[v - v_\infty + w - w_\infty]. \end{cases} \tag{P2}$$

First, we point out that the rescaled two-polymer model (P2) in the limiting case $\varepsilon = 0$ constitutes the classical Lotka-Volterra system, i.e.

$$\begin{cases} \frac{dv_0}{dt} = v_0\,[w_\infty - w_0] = v_0\, w_0\left(-\frac{\partial H}{\partial w_0}\right), \\ \frac{dw_0}{dt} = w_0\,[v_0 - v_\infty] = w_0\, v_0 \frac{\partial H}{\partial v_0}, \end{cases} \tag{2.10}$$

which is defined by, and conserves, the Hamiltonian:

$$\begin{aligned} &H(v,w) = v - v_\infty \ln v + w - w_\infty \ln w, \\ &\frac{d}{dt}H(v_0(t), w_0(t)) = \frac{\partial H}{\partial v}\frac{dv_0}{dt} + \frac{\partial H}{\partial w}\frac{dw_0}{dt} = 0. \end{aligned} \tag{2.11}$$

Moreover, for positive equilibria $(v_\infty, w_\infty) > 0$, the Hamiltonian H is the sum of the convex functions $v - v_\infty \ln v$ and $w - w_\infty \ln w$ with minima at v_∞ and w_∞. Hence, any positive equilibrium $(v_\infty, w_\infty) > 0$ is the unique minimiser of the associated Hamiltonian (2.11) and $H(v,w) > H(v_\infty, w_\infty)$ for all $(v,w) \neq (v_\infty, w_\infty)$.

2.3.1 Large-time behaviour and entropy functional

The following theorem proves large-time convergence to the positive equilibrium (v_∞, w_∞) by using the Hamiltonian (2.11) as a Lyapunov functional of the full system (P2).

Theorem 9 (Exponential convergence to positive equilibrium)**.**
Consider $P_0 \in \left(\frac{kM}{1+k}, kM\right)$ and hence a positive equilibrium $(v_\infty, w_\infty) > 0$.

Then, the Hamiltonian (2.11) *is a convex Lyapunov functional for System* (P2) *with a decay rate of order ε.*

More precisely,

$$\frac{d}{dt}H(v(t),w(t)) = -\varepsilon\, p^2(v(t),w(t)), \quad \textit{with} \quad p(v,w) := [(v-v_\infty)+(w-w_\infty)]. \tag{2.12}$$

Moreover, for ε sufficiently small, every solution $(v(t),w(t))$ to (P2) *subject to positive initial data $(v_0,w_0)>0$ converges exponentially to the positive equilibrium (v_∞,w_∞), i.e.*

$$|v-v_\infty|^2+|w-w_\infty|^2 \le C\left(H^0-H_\infty\right)e^{-\varepsilon r t}, \tag{2.13}$$

where the positive rate r and constant C depend only on the initial value of the Hamiltonian $H^0 := H(v^0,w^0)$ and the values of the positive equilibrium (v_∞,w_∞).

Proof. The decay rate of the Hamiltonian (2.12) follows from direct calculations when evaluating H along the flow of (P2).

In the following, we prove the exponential convergence (2.13) via a modified entropy method. The standard entropy method consists in proving a functional inequality, which bounds the entropy production functional (i.e. the entropy decay rate) from below by the relative entropy with respect to the equilibrium, see e.g. [47, 48, 58, 57] in the context of nonlinear reaction-diffusion system. For the present Hamiltonian decay (2.12), however, this approach would aim for an estimate like $p^2(v,w) \ge r(H(v,w)-H_\infty)$ for a rate $r>0$, which cannot hold since p^2 vanishes at a straight line through the equilibrium point:

$$p=0 \quad \Longleftrightarrow \quad w-w_\infty = -(v-v_\infty).$$

In order to prove exponential convergence to the equilibrium in such a case, we shall provide explicit estimates that all solution trajectories only spend a finite amount of time near this line of degeneracy. We first observe from (P2) that the null-cline $\dot v = 0$ is also a straight line, which passes through the equilibrium:

$$\dot v = 0 \quad \Longleftrightarrow \quad w-w_\infty = -\lambda_\varepsilon (v-v_\infty), \qquad \lambda_\varepsilon := \frac{\varepsilon}{1+\varepsilon} < 1,$$

Note that since $\lambda_\varepsilon < 1$, the nullcline $\dot v = 0$ is below $p=0$ for $v \le v_\infty$ and above $p=0$ for $v \ge v_\infty$. Next, we introduce a line W_λ between $\dot v = 0$ and p with a slope $\lambda \in (\lambda_\varepsilon, 1)$ to be chosen later:

$$W_\lambda: \quad w-w_\infty = -\lambda(v-v_\infty), \qquad \lambda \in (\lambda_\varepsilon, 1).$$

Similarly, on the opposite side of $p=0$ we define the line W_Λ:

$$W_\Lambda: \quad w-w_\infty = -\Lambda(v-v_\infty), \qquad \Lambda := 2-\lambda > 1.$$

In the following, we denote by $\triangle_\lambda^-$ the open triangle in the phase space $(v,w) \in \mathbb{R}^2_+$, which is defined by the interior between the lines W_λ, W_Λ and $v=0$. Note that on $\triangle_\lambda^-$ we have $0 < v < v_\infty$ and $w_\infty < w < w_\infty + \Lambda v_\infty$. Analog, the open triangle $\triangle_\lambda^+$ is defined as the interior of the lines W_λ, W_Λ and $w=0$, i.e. we consider $v_\infty < v < v_\infty + w_\infty/\lambda$ and $0 < w < w_\infty$.

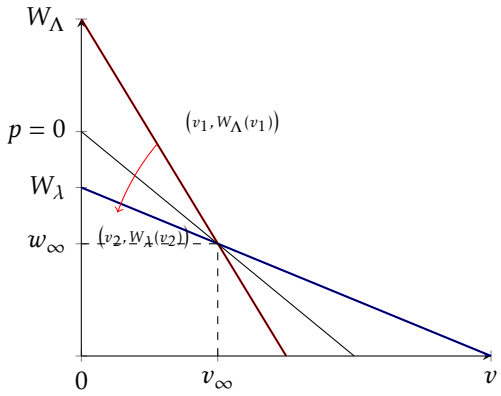

Figure 2.4 – Phase space for System (P2)

In the following, we shall detail the estimates in the triangle $\triangle_\lambda^-$ for $0 < v < v_\infty$, while the estimates for $\triangle_\lambda^+$ follow analogously (e.g. by exchanging the variables v and w and the roles of λ and Λ). We first observe that $w - w_\infty \in (-\lambda(v - v_\infty), -\Lambda(v - v_\infty))$, which implies

$$(1 - \lambda)(v - v_\infty) \leq p \leq (1 - \Lambda)(v - v_\infty).$$

Moreover, we point out that $\dot{v} < 0$ and $\dot{w} < 0$ are strictly negative on $\triangle_\lambda^-$. Hence, whenever a solution trajectory enters $\triangle_\lambda^-$ at some time t_1 at a point $(v(t_1), w(t_1)) = (v_1, W_\Lambda(v_1))$ with $v_1 < v_\infty$, then it must leave $\triangle_\lambda^-$ again at a time t_2 at a point $(v(t_2), w(t_2)) = (v_2, W_\lambda(v_2))$, for which holds that $0 < v_2 < v_1$. For later use, we shall refer to the duration of crossing $\triangle_\lambda^-$ as the sojourn time $t_2 - t_1$. In Lemma 3 of Appendix 2.6.1, we show that the sojourn time is bounded from below and above independently of the trajectories.

In order to ensure that all solution trajectories which pass through the line of degeneracy $p = 0$ where $\dot{H} = 0$ are crossing the line of degeneracy, we shall prove that $p^2(t)$ is a strictly convex function near $p = 0$ with a positive lower bound for $\ddot{p}$ within the triangle $\triangle_\lambda^-$ (and $\triangle_\lambda^+$) for λ chosen sufficiently close to one, i.e. that $p(t) = 0$ can only occur at discrete points in time.

We begin by calculating

$$\dot{p} = \dot{v} + \dot{w} = d - \varepsilon(v + w)p, \qquad \text{with} \quad d := vw_\infty - wv_\infty.$$

Note that $d = (v - v_\infty)w_\infty - (w - w_\infty)v_\infty$ and in the triangle $\triangle_\lambda^-$, we have

$$\text{in } \triangle_\lambda^- \ : \ d < 0 \quad \text{with} \quad -(v - v_\infty)[w_\infty + \lambda v_\infty] \leq |d| \leq -(v - v_\infty)[w_\infty + \Lambda v_\infty]. \tag{2.14}$$

Next,

$$\dot{d} = -[(v - v_\infty)v_\infty w + (w - w_\infty)vw_\infty] - \varepsilon d p,$$

and

$$\begin{aligned}\ddot{p} = &-[(v-v_\infty)v_\infty w + (w-w_\infty)vw_\infty] \\ &- 2\varepsilon d p - \varepsilon(v+w)d + \varepsilon^2(v+w)p^2 + \varepsilon^2(v+w)^2 p.\end{aligned}$$

If $p(t_0) = 0$, then

$$p^2(t) = \underbrace{p^2(t_0)}_{=0} + 2\underbrace{p^2(t_0)}_{=0}\dot{p}(t_0)(t-t_0) + 2\Big[(\dot{p})^2 + p\ddot{p}\Big](\theta)\,\frac{(t-t_0)^2}{2} = \Big[(\dot{p})^2 + p\ddot{p}\Big](\theta)\,(t-t_0)^2,$$

for some $\theta \in (t, t_0) \subset (t_1, t_2)$. Hence, by using Lemma 2 (see Appendix 2.6.1) and for ε sufficiently small

$$\begin{aligned}(\dot{p})^2 + p\ddot{p} &= d^2 - [(v-v_\infty)v_\infty w + (w-w_\infty)vw_\infty]\,p + O(\varepsilon) \\ &\geq \kappa(v(\theta)-v_\infty)^2 \geq \kappa(v_1-v_\infty)^2\end{aligned}$$

for a constant $\kappa > 0$. Now, for any solution trajectory, we estimate

$$\begin{aligned}\int_{t_1}^{t_2} \dot{H}\,dt &= -\varepsilon\int_{t_1}^{t_2} p^2(t)\,dt = -\varepsilon\int_{t_1}^{t_2}\Big[(\dot{p})^2 + p\ddot{p}\Big](\theta)(t-t_0)^2\,dt \\ &\leq -\varepsilon\kappa(v_1-v_\infty)^2\int_{t_1}^{t_2}(t-t_0)^2\,dt \leq -\varepsilon\kappa\int_{t_1}^{t_2} C_1(v(t)-v_\infty)^2\,dt\,\frac{\int_{t_1}^{t_2}(t-t_0)^2\,dt}{t_2-t_1} \\ &\leq -\varepsilon\kappa\,C_1 K\int_{t_1}^{t_2}(v(t)-v_\infty)^2\,dt,\end{aligned}$$

where $C_1 = \frac{(v_1-v_\infty)^2}{(v_2-v_\infty)^2} < 1$ since $v_2 < v(t) < v_1$ for all $t \in (t_2, t_1)$ and K is a constant only depending on the lower bound of the sojourn time $t_2 - t_1$ provided in Lemma 3.

Next, we observe that the convexity of the Hamiltonian H together with the decay of the Hamiltonian $H(v(t), w(t)) \leq H^0$ for all $t \geq 0$ imply uniform-in-time positive lower and upper bounds on v and w subject to initial data with finite $H^0 = H(v^0, w^0) < +\infty$. By using this lower and upper bounds, we estimate

$$\begin{aligned}H(v,w) - H(v_\infty, w_\infty) &= v_\infty h\Big(\frac{v}{v_\infty}\Big) + w_\infty h\Big(\frac{w}{w_\infty}\Big) \\ &\leq C_2(v_\infty, w_\infty, H^0)\Big[(v-v_\infty)^2 + (w-w_\infty)^2\Big],\end{aligned} \tag{2.15}$$

where $h(z) = (z-1) - \ln z \geq 0$ is non-negative and convex and $h(z) \leq C_2(z_*, z^*)(z-1)^2$ for $z \in (z_*, z^*)$. Hence, on $\triangle_\lambda^-$, we have $H(v,w) - H(v_\infty, w_\infty) \leq C_3(v-v_\infty)^2$ with a constant $C_3 = C_3(C_2, \lambda)$ and conclude that

$$\int_{t_1}^{t_2}\dot{H}\,dt \leq -\varepsilon\kappa C_1 K C_3^{-1}\int_{t_1}^{t_2} H(v,w) - H(v_\infty, w_\infty)\,dt \tag{2.16}$$

Note that an analogous estimate to (2.16) holds also in $\triangle_\lambda^+$.

Outside $\triangle_\lambda = \triangle_\lambda^- \cup \triangle_\lambda^+$, there exists a constant $C_\lambda > 0$ such that the estimate $|p|^2 \geq C_\lambda\Big[(v-v_\infty)^2 + (w-w_\infty)^2\Big]$ holds. Moreover, the uniform lower and upper bounds on $v(t), w(t)$ imply that there exists a positive constant $C_4 = C_4(v_\infty, w_\infty, H^0)$

$$0 < C_4 := \min_{\{(v,w):H(v,w)\leq H^0\}\setminus\triangle_\lambda} \left\{ \frac{[(v-v_\infty)+(w-w_\infty)]^2}{v_\infty h\Big(\frac{v}{v_\infty}\Big) + w_\infty h\Big(\frac{w}{w_\infty}\Big)} \right\},$$

which implies $p^2 \geq C_4(H(v,w) - H(v_\infty, w_\infty)$ and

$$\dot{H} \leq -\varepsilon\, C_4(H(v,w) - H(v_\infty, w_\infty)) \qquad \text{outside of} \quad \triangle_\lambda. \tag{2.17}$$

Estimate (2.17) proves exponential convergence (of order ε) towards equilibrium first in the relative Hamiltonian distance $(H(v,w) - H(v_\infty, w_\infty))$ as long as a solution trajectory is outside the critical area $\triangle_\lambda$. Consequently, the reversed estimate (2.15) (which holds equally true on all points with $H(v,w) \leq H^0$) implies exponential convergence to the equilibrium in the Euclidian distance.

Within the critical area $\triangle_\lambda$, this exponential convergence is hampered by the line of degeneracy where $p = 0$. However, (2.16) and the lower crossing time estimates in Lemma 3 of Appendix 2.6.1 show that solutions trajectories do not get stuck (or significantly slowed down) within $\triangle_\lambda$. More precisely, since the speed of trajectories outside $\triangle_\lambda$ is bounded above, for any fixed $\lambda < 1$ (sufficiently close to one), all solution trajectories will remain within $\triangle_\lambda$ for only a small fraction (let say 10%) of the time spent on one rotation around (v_∞, w_∞). Moreover, recall that trajectories can only reach (v_∞, w_∞) outside of $\triangle_\lambda$ due to the sign conditions on $\dot{v}$ and $\dot{w}$.

Finally, this small fraction of time spent within $\triangle_\lambda$ per rotation can not degenerate near (v_∞, w_∞), since classical linearisation techniques shows eigenvalues of the form

$$\mu = -\varepsilon\frac{P_0}{2} \pm i\sqrt{(P_0 - M)M + \varepsilon P_0(2M - P_0) - \frac{5}{4}\varepsilon^2 P_0^2} \quad \xrightarrow{\varepsilon\to 0} \quad \pm i\sqrt{v_\infty w_\infty}, \tag{2.18}$$

where the right hand side values corresponds to the eigenvalues (and thus finite oscillation period) of the zero order Lotka-Volterra system (2.10).

Altogether, we obtain the exponential convergence to equilibrium with a rate εr as in (2.13), where r can be estimated explicitly in terms of the constants in (2.17) and (2.16) as well as the crossing times in Lemma 3. ∎

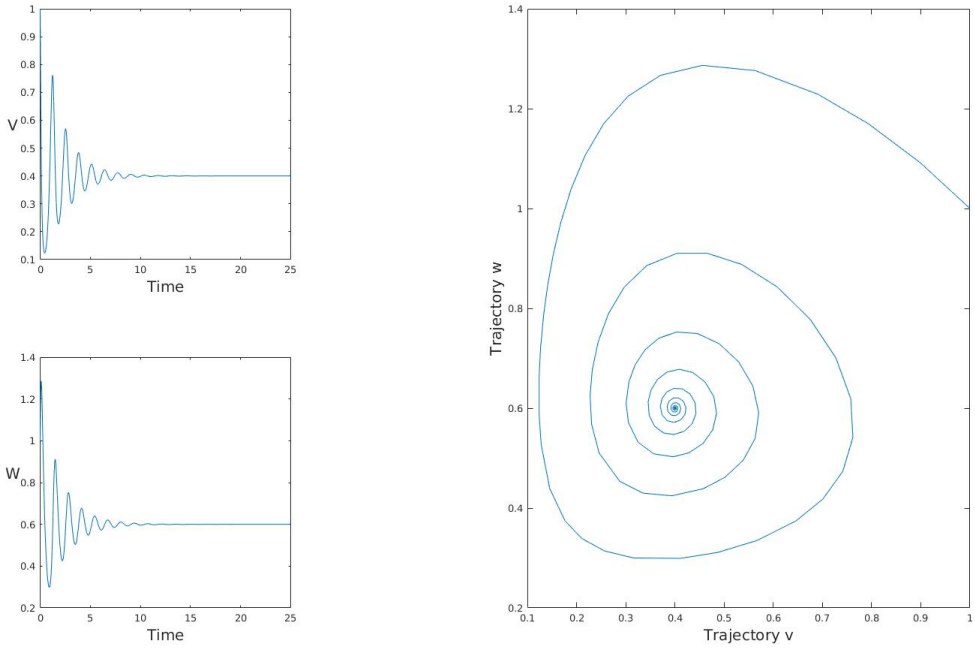

Figure 2.5 – Trajectories of the monomeric concentrations v and w for the two-polymer model for $k = 10$, $a = b = 1$ and $\frac{kM}{1+k} < P_0 < kM$.

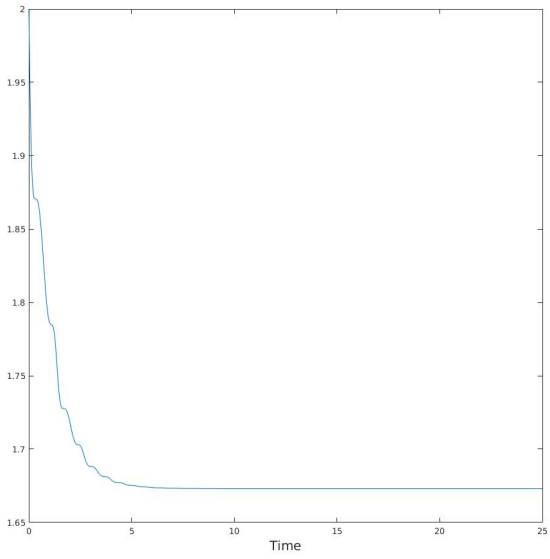

Figure 2.6 – Monotone decay of the Lyapunov functional (2.12) for the two-polymer model for $k = 10$, $a = b = 1$ and $\frac{kM}{1+k} < P_0 < kM$.

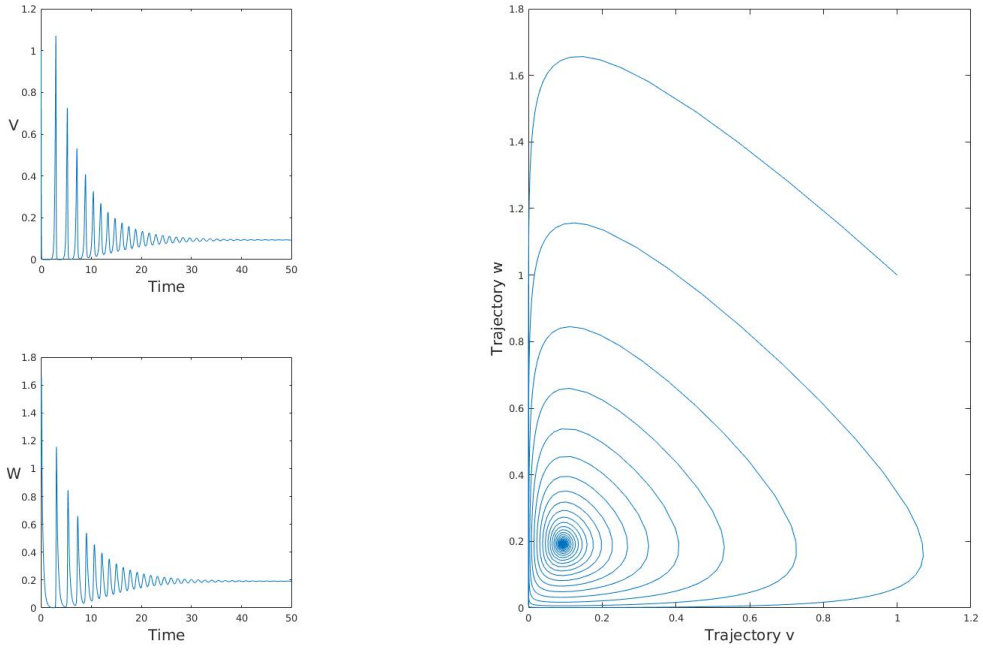

Figure 2.7 – Trajectories of the monomeric concentrations v and w for the two-polymer model for $k = 35$, $a = b = 1$ and $\frac{kM}{1+k} < P_0 < kM$.

2.3.2 Asymptotic expansion for fast monomer-conformer exchange

In the following, we show that System (P2), i.e.

$$\begin{cases} \frac{dv}{dt} = v\,[w_\infty - w] - \varepsilon\, v\,[v - v_\infty + w - w_\infty], \\ \frac{dw}{dt} = w\,[v - v_\infty] - \varepsilon\, w\,[v - v_\infty + w - w_\infty]. \end{cases}$$

constitutes a regular perturbation in terms of ε of the zero order Lotka-Volterra system (2.10). This is summarised in the following corollary.

Corollary 1 (Fast transient oscillations)**.**
Assume ε sufficiently small as in the second part of Proposition 9.

Then, by applying the ansatz

$$v = v_0 + \varepsilon v_1 + O(\varepsilon^2), \qquad \text{and} \qquad w = w_0 + \varepsilon w_1 + O(\varepsilon^2), \tag{2.19}$$

solutions to System (P2) *can be approximated in a regular asymptotic expansion in ε which features the Lotka-Volterra system* (2.10) *as zero order approximation. Hence, the zero order terms $(v_0(t), w_0(t))$ are periodic solutions with period $T > 0$ to the Lotka-Volterra system* (2.10) *while the first order terms $(v_1(t), w_1(t))$ are*

solutions to the following non-autonomous linear inhomogeneous system

$$\begin{pmatrix} \dot{v_1} \\ \dot{w_1} \end{pmatrix} = \underbrace{\begin{pmatrix} w_\infty - w_0 & -v_0 \\ w_0 & v_0 - v_\infty \end{pmatrix}}_{=:A(t)} \cdot \begin{pmatrix} v_1 \\ w_1 \end{pmatrix} - \underbrace{\begin{pmatrix} v_0(v_\infty - v_0 + w_\infty - w_0) \\ w_0(v_\infty - v_0 + w_\infty - w_0) \end{pmatrix}}_{=:g_1(t)}. \tag{2.20}$$

Hence, the solutions $(v(t), w(t))$ of System (P2) *are perturbed from the zero order solutions $(v_0(t), w_0(t))$ not more than $O(\varepsilon)$ far on a time interval of size $O(T)$ and hence undergo $O(1/\varepsilon)$ many oscillations before converging to (v_∞, w_∞) as proven in Theorem 9.*

Proof. Global existence of the first order terms $(v_1(t), w_1(t))$ follows from classical ODE theory. In fact, since $(v_0(t), w_0(t))$ is periodic with period T, also $A(t)$ and $g_1(t)$ are T-periodic and Floquet theory implies that solutions to (2.20) are T-periodic if and only if one is not a Floquet multiplier, i.e. an eigenvalue of the associated monodromy matrix, see e.g. [153, Chapter 3.6]. However, the Lyapunov structure and the exponential decay of Proposition 9 imply that System (2.20) has to be entirely unstable and that both Floquet multipliers have to be larger than one.

Moreover, all higher order expansion terms $(v_n(t), w_n(t))$ for $n \geq 2$ satisfy systems analogous to (2.20) with the same non-autonomous system matrix $A(t)$ and similar inhomogeneities $g_n(t)$ only depending on the previously determined asymptotic expansion terms $(v_0, w_0), \ldots, (v_{n-1}, w_{n-1})$.

Hence, (2.19) constitutes a regular asymptotic expansion of the solution (v, w) up to arbitrarily high order. In particular, this implies that the change of the full solution (v, w) compared to the zero order approximation (v_0, w_0) over one period is of order ε and that (v, w) will undergo order $1/\varepsilon$ many oscillations before finally converging to the equilibrium (v_∞, w_∞). ■

Figures 2.5, 2.6 and 2.7 illustrate Corollary 1 for values $k = 10$ and $k = 35$. Clearly, the number of oscillations increases with k, while all other parameters being left unchanged. Moreover, Figure 2.6 shows the monotone decay of the Lyapunov functional in the case $k = 10$: we observe a general exponential decay despite the successive plateaux, which occur when solutions cross the lines of degeneracy $p = 0$.

2.4 The $n-$polymer model

Let us now turn to System (2.6) in the case where $3 \leq n < \infty$. Let us begin by recalling a well-posedness result.

Proposition 4 (Well-posedness of the finite dimensional system)**.**
Let $n \in \mathbb{N}$, and $v^0, w^0, c_i^0 \geq 0$ for $1 \leq i \leq n$. Then System (2.6) *has a unique time-continuous nonnegative solution $v(t) \geq 0$, $w(t) \geq 0$, $c_i(t) \geq 0$ for $t \geq 0$ and all $1 \leq i \leq n$ satisfying*

$$v(t) + w(t) + \sum_{i=1}^{n} i c_i(t) = v_0 + w_0 + \sum_{i=1}^{n} i c_i^0, \qquad \sum_{i=1}^{n} c_i(t) = \sum_{i=1}^{n} c_i^0, \quad \forall t \geq 0.$$

2.4.1 Steady states analysis

System (2.6) with finite n features both boundary steady states (BSS), where at least one concentration is zero, and positive steady state (PSS), where all concentrations are strictly positive.

Let us first introduce several parametric regions – graphically illustrated in Figure 2.8– which will defining the stability or instability regions of the boundary steady states (BSS).

$$n + \frac{b_n}{k} \leq \frac{M_{tot}}{P_0} \quad \text{(region with horizontal green stripes in Fig. 2.8),} \tag{2.21}$$

$$n < \frac{M_{tot}}{P_0} < n + \frac{b_n}{k} \quad \text{(light blue region in Fig. 2.8),} \tag{2.22}$$

$$\frac{M_{tot}}{P_0} \leq 1 + \frac{a_1}{k} \quad \text{(grey diagonally hatched region in Fig. 2.8).} \tag{2.23}$$

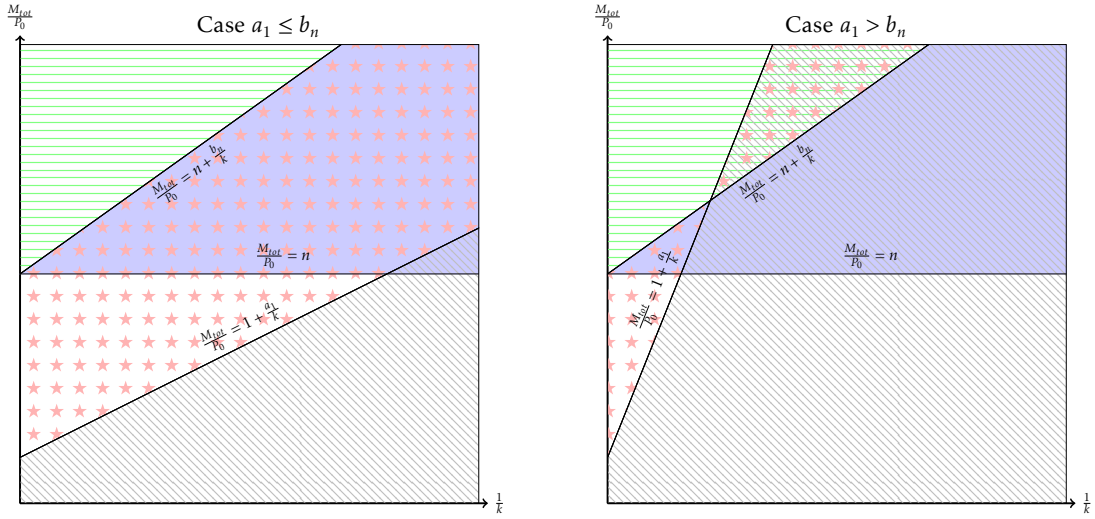

Figure 2.8 – Stability regions of the SSs of the finite system (2.6) in the $\frac{1}{k}$-$\frac{M_{tot}}{P_0}$ parametric space: (BSSa) are always unstable. Grey diagonally hatched zone $\iff$ (2.23) $\iff$ asymptotically stable (BSSb), which is unstable elsewhere. Green horizontal lines $\iff$ (2.21) $\iff$ asymptotically stable (BSSc). Light blue zone $\iff$ (2.22) $\iff$ unstable (BSSc). Zone with red stars $\iff$ existence of at least one PSS (in case $a_1 > b_n$ coexisting with a stable (BSSb) in the horizontally hatched region; otherwise coexisting only unstable BSSs.)

Proposition 5 (Nonnegative Steady States)**.**
Let $a_i > 0$, $b_{i+1} > 0$ for $1 \leq i \leq n-1$, let v_0, $w_0 > 0$ and $P_0 > 0$, $M_{tot} \geq v_0 + w_0 + P_0 > 0$. Then,

1. *there exists three kinds of boundary steady states (BBS):*

   (BSSa) There exist unstable BSSs: $\bar{v} = \bar{w} = 0$ and $(\bar{c}_i)_{1\leq i\leq n}$ satisfies $\sum_{i=1}^{n} \bar{c}_i = P_0$, $\sum_{i=1}^{n} i\bar{c}_i = M_{tot}$.

(BSSb) There exists a BSS: $\bar{v} = M_{tot} - P_0 > 0$, $\bar{w} = 0$, $\bar{c}_1 = P_0$, $\bar{c}_i = 0$ for $2 \le i \le n$. This BSS is locally asymptotically stable under Assumption (2.23) *(grey diagonally hatched in Fig. 2.8) and unstable elsewhere.*

(BSSc) Under the additional assumption $\frac{M_{tot}}{P_0} > n$, there exists another BSS: $\bar{v} = 0$, $\bar{w} = M_{tot} - nP_0 > 0$, $(\bar{c}_i)_{1\le i\le n-1} = 0$ and $c_n = P_0$. This BSS is locally asymptotically stable under Assumption (2.21) *(green horizontal lines) and otherwise unstable, which corresponds to Assumption* (2.22) *(light blue zone).*

2. *There exists (at least one) positive steady state (PSS) $(\bar{v}, \bar{w}, \bar{c}_i)_{1\le i\le n}$ provided that the polynomial $P(z)$ defined as*

$$P(z) := \left[\frac{a_1}{k} + 1 - \frac{M_{tot}}{P_0}\right] + \sum_{i=2}^{n-1}\left[\left(\frac{a_i}{k} + i - \frac{M_{tot}}{P_0} + \frac{b_i}{k}\right)\prod_{j=0}^{i-1}\frac{a_j}{b_{j+1}}\right]z^{i-1} + \left[\left(n - \frac{M_{tot}}{P_0} + \frac{b_n}{k}\right)\prod_{j=0}^{n-1}\frac{a_j}{b_{j+1}}\right]z^{n-1} \quad (2.24)$$

has a root $\bar{z} > 0$. Given $\bar{z} > 0$, we have

$$\begin{aligned} \bar{v} &= \bar{c}_1 \sum_{i=1}^{n-1}\frac{a_i}{k}\bar{z}^{i-1}\prod_{j=0}^{i-1}\frac{a_j}{b_{j+1}}, & \bar{w} &= \bar{c}_1 \sum_{i=1}^{n-1}\frac{a_i}{k}\bar{z}^{i}\prod_{j=0}^{i-1}\frac{a_j}{b_{j+1}}, \\ \bar{c}_1 &= \frac{P_0}{\sum_{i=1}^{n}\bar{z}^{i-1}\prod_{j=0}^{i-1}\frac{a_j}{b_{j+1}}}, & \bar{c}_i &= \bar{z}^{i-1}\prod_{j=0}^{i-1}\frac{a_j}{b_{j+1}}\bar{c}_1, \quad 2 \le i \le n. \end{aligned} \quad (2.25)$$

If all BSSs are unstable, i.e. $1 + \frac{a_1}{k} < \frac{M_{tot}}{P_0} < n + \frac{b_n}{k}$, then there exists at least one positive steady state. Moreover, if the sequences (a_i), (b_i) are nondecreasing, the positive steady state is unique.

Remark 10. *The existence of positive roots of the polynomial P can be analysed in more detail in the case of constant polymerisation coefficients, see Proposition 6 below. Also, the computation of those roots can be done numerically. While the linear stability of the BSSs can be calculated explicitly, the stability of the PSS constitutes a difficult problem, which can be explicitly confirmed in the two-polymer model, see* (2.18)*, but seems otherwise only possible by numerical calculations.*

Proof. For simplicity of notations, we drop the $\bar{\cdot}$ in what follows, and postpone the proofs of stability to Appendix 2.6.2. The steady states of System (2.6) satisfy the following relations:

$$\begin{cases} -kvw + v\sum_{i=2}^{n} b_i c_i = 0, & -w\sum_{i=1}^{n-1} a_i c_i + kvw = 0, \qquad J_1 = \ldots = J_{n-1} = 0, \\ \sum_{i=1}^{n} c_i = P_0, & v + w + \sum_{i=1}^{n} i c_i = M_{tot}. \end{cases} \quad (2.26)$$

1. First, we discuss the existence of BSSs, where at least one of the two monomeric species vanishes:

(a) If $w = v = 0$, then any distribution (c_i) such that $\sum_{i=1}^{n} c_i = P_0$ and $\sum_{i=1}^{n} ic_i = M_{tot}$ is a steady state solution.

(b) If $w = 0$ and $v \neq 0$, then by the first equation we have $v\sum_{i=2}^{n} bc_i = 0$, hence $c_i = 0$ for $i \geq 2$, so that $c_1 = P_0$ and v is such that $v + c_1 = M_{tot}$.

(c) If $v = 0$ and $w \neq 0$, then by the second equation we have $w\sum_{i=1}^{n-1} ac_i = 0$, hence $c_i = 0$ for $i \leq n-1$, so that $c_n = P_0$ and w is such that $w + nc_n = M_{tot}$.

2. Let us now consider $v > 0$ and $w > 0$. Since $J_i = 0$, we have by immediate recursion

$$c_i = \frac{a_{i-1}w}{b_i v}c_{i-1} = \cdots = \left(\prod_{j=0}^{i-1}\alpha_j\right)z^{i-1}c_1, \qquad \forall\ 2 \leq i \leq n,$$

where $\alpha_i = \frac{a_i}{b_{i+1}}$, $\alpha_0 = 1$ and $z = \frac{w}{v}$. Inserting this identity into (2.26), yields

$$kv = c_1\sum_{i=1}^{n-1} a_i z^{i-1}\prod_{j=0}^{i-1}\alpha_j, \qquad P_0 = c_1\sum_{i=1}^{n} z^{i-1}\prod_{j=0}^{i-1}\alpha_j,$$

and

$$\begin{aligned} M_{tot} &= v(1+z) + c_1\sum_{i=1}^{n} iz^{i-1}\prod_{j=0}^{i-1}\alpha_j = c_1\left(\sum_{i=1}^{n-1}\frac{a_i}{k}z^{i-1}(1+z)\prod_{j=0}^{i-1}\alpha_j + \sum_{i=1}^{n} iz^{i-1}\prod_{j=0}^{i-1}\alpha_j\right) \\ &= c_1\left(\sum_{i=1}^{n-1}\frac{a_i}{k}z^{i-1}\prod_{j=0}^{i-1}\alpha_j + \sum_{i=2}^{n}\frac{a_{i-1}}{k}z^{i-1}\prod_{j=0}^{i-2}\alpha_j + \sum_{i=1}^{n} iz^{i-1}\prod_{j=0}^{i-1}\alpha_j\right) \\ &= c_1\left(\frac{a_1}{k} + 1 + \sum_{i=2}^{n-1}\left(\left(\frac{a_i}{k} + i\right)\alpha_{i-1} + \frac{a_{i-1}}{k}\right)\prod_{j=0}^{i-2}\alpha_j z^{i-1} + \left(\frac{a_{n-1}}{k} + n\alpha_{n-1}\right)\prod_{j=0}^{n-2}\alpha_j z^{n-1}\right). \end{aligned}$$

We deduce

$$\begin{aligned} \frac{M_{tot}}{c_1} &= \frac{M_{tot}}{P_0}\sum_{i=1}^{n} z^{i-1}\prod_{j=0}^{i-1}\alpha_j \\ &= \frac{a_1}{k} + 1 + \sum_{i=2}^{n-1}\left(\left(\frac{a_i}{k} + i\right)\alpha_{i-1} + \frac{a_{i-1}}{k}\right)\prod_{j=0}^{i-2}\alpha_j z^{i-1} + \left(\frac{a_{n-1}}{k} + n\alpha_{n-1}\right)\prod_{j=0}^{n-2}\alpha_j z^{n-1}, \end{aligned}$$

and finally

$$P(z) = \left[\frac{a_1}{k} + 1 - \frac{M_{tot}}{P_0}\right] + \sum_{i=2}^{n-1}\left[\left(\left(\frac{a_i}{k} + i - \frac{M_{tot}}{P_0}\right)\alpha_{i-1} + \frac{a_{i-1}}{k}\right)\prod_{j=0}^{i-2}\alpha_j\right]z^{i-1} + \left[\left(\left(n - \frac{M_{tot}}{P_0}\right)\alpha_{n-1} + \frac{a_{n-1}}{k}\right)\prod_{j=0}^{n-2}\alpha_j\right]z^{n-1} = 0.$$

If $1 + \frac{a_1}{k} < \frac{M_{tot}}{P_0} < n + \frac{b_n}{k}$, we have $P(0) < 0$ and $P(+\infty) = +\infty$, so that P admits at least one positive root. Moreover if the sequences (a_i) and (b_i) are nondecreasing, it implies that there is exactly one change of sign of the coefficients of the polynomial P and hence there is exactly one positive real root for P thanks to Descartes' rule of signs.

■

Discussion and biological interpretation: The steady state analysis of Proposition 5 revealed different parametric regions. A key quantity appears to be the ratio $\frac{M_{tot}}{P_0}$, which is easily interpreted as the sum of the average size of polymers plus the ratio representing the relative numbers of monomers to polymers, i.e.

$$\frac{M_{tot}}{P_0} = \frac{\sum ic_i}{P_0} + \frac{v+w}{P_0}.$$

Figure 2.8 illustrates Proposition 5. The extrem case $\frac{\sum ic_i}{P_0} = n$ is equivalent to $c_n = P_0$. Therefore, the zones $\frac{M_{tot}}{P_0} > n$ (green horizontal lines and light blue zone) can be interpreted either as situations with a high amount of very large polymers close to the maximal size n or as situations with a large amount of the monomeric species v and w (compared to P_0). From a biological view, both those situations seem very unlikely. Hence (BSSc) and its stability is conjectured to have little biological relevance. Moreover, (BSSc) will disappear in the limit $n \to \infty$, see Section 2.5.

The biologically more realistic zone $\frac{M_{tot}}{P_0} < n$ is divided into only two parts: either Assumption (2.23) is fulfilled, and (BSSb) is locally asymptotically stable (grey diagonally hatched region), or all BSSs are unstable whereas there exists a PSS (red stars zone). Assumption (2.23) has a direct interpretation that there is not enough initial mass to ignite the polymerisation hierarchy in the sense that all polymers depolymerise into the species $\mathcal{C}_1$. Indeed (BSSb), which is stable under Assumption (2.23), features $\bar{c}_1 = P_0$ while $\bar{c}_i = 0$ for $2 \le i \le n$. Conversely, in the red star region, the system features a PSS (which is conjectured to be stable). In the dichotomy of stable (BSSb) versus existence of a PSS, the convergence to (BSSb) could be considered as non-proliferation of a disease in a more specific prionic model while otherwise a prionic assembly gets established in terms of the PSS.

From a more conceptional modelling viewpoint, the n-polymer model couples the bi-monomeric equations for v and w to a finite range of polymers of sizes 1 to n, which are considered as biologically "active", *i.e.* they interact with the monomeric species. More than the two-polymer model, the n-polymer model with increasing n describes the interaction of the bi-monomeric dynamics for v and w with a larger

and larger hierarchy of polymerising and depolymerising polymers. The nonlinear feedback from the polymer-hierarchy is sufficient to introduce sustained oscillatory behaviour already in the two-polymer model, but it can be hypothesised that with larger n the dynamical interplay between monomer species and polymer hierarchy becomes more intricate, cf. Figure 2.12 below.

In any case, the model system (2.6) should be understood as a prototypical building block of more realistic and prion specific models. In the experiment illustrated in Figure 2.1, for instance, oscillations appear only during a specific time range; other reactions may have occured before, giving progressively rise to polymers belonging to the "active" range of the n-polymer model. Moreover, from a mathematical perspective, the n-polymer model is an interesting intermediate before turning to the infinite system.

Case of constant polymerisation coefficients

If the reaction coefficients are constant, *i.e.* the polymerisation/depolymerisation speed is the same for all polymers regardless of their size, the polynomial P defined in (2.24) (characterising PSSs) takes a simpler expression, which is stated in the following corollary.

Corollary 2 (Positive steady states in the constant coefficients case)**.**
Let k, b, a, P_0 and M_{tot} be positive real constants. Let $a_i = a$ and $b_{i+1} = b$ for $1 \leq i \leq n$ in System (2.6)*. Let $n \geq 3$. Then,*

1. *if the initial conditions and parameters satisfy the condition*

$$\frac{M_{tot}}{P_0} = \left(\frac{a}{k} + \frac{b}{k}\right)\frac{n-1}{n} + \frac{n+1}{2}, \tag{2.27}$$

there exists a unique positive steady state (PSS) to System (2.6)*, which is defined by*

$$\bar{c}_i := \frac{P_0}{n} \qquad \forall\ 1 \leq i \leq n, \qquad \bar{v} = \frac{a}{k}P_0, \qquad \bar{w} = \frac{b}{k}P_0.$$

2. *If* (2.27) *is not satisfied, then the PSSs of System* (2.6) *are given by $(\gamma, \bar{v}, \bar{w}, \bar{c}_1)$ where $\gamma \neq 1$ is a root of the following polynomial*

$$Q(\gamma) := P(\frac{b}{a}\gamma) = \left(\frac{a}{k} - \frac{M_{tot}}{P_0} + 1\right) + \sum_{i=1}^{n-2}\left(\frac{a}{k} + \frac{b}{k} - \frac{M_{tot}}{P_0} + i + 1\right)\gamma^i + \left(\frac{b}{k} - \frac{M_{tot}}{P_0} + n\right)\gamma^{n-1}, \tag{2.28}$$

and $(\bar{c}_1, \bar{v}, \bar{w})$ are defined from γ by

$$\bar{c}_1 := P_0\frac{1-\gamma}{1-\gamma^n}, \qquad \bar{v} := \frac{a}{k}P_0\frac{1-\gamma^{n-1}}{1-\gamma^n}, \qquad \bar{w} := \frac{b}{k}P_0\frac{\gamma-\gamma^n}{1-\gamma^n}. \tag{2.29}$$

Remark 11. *The relation* (2.27) *shall never be satisfied in practice, but it may be* roughly *satisfied in the sense that if n is large, it corresponds to the case where the average size of the polymers is initially taken around $\frac{n}{2}$. We shall see later (Proposition 3) how this average size is related to the cases $\gamma < 1$ or $\gamma > 1$.*

Proof. We apply Proposition 5 and notice that $P(z) = Q(\gamma)$ with $\gamma = \frac{a}{b}z$ and Q defined by (2.28). We then distinguish according to $\gamma = 1$ or $\gamma \neq 1$.

1. For $\gamma = 1$, we have

$$\begin{aligned} Q(1) &= \frac{a}{k} - \frac{M_{tot}}{P_0} + 1 + (n-2)\left(\frac{a}{k} + \frac{b}{k} - \frac{M_{tot}}{P_0} + 1\right) + \frac{(n-1)(n-2)}{2} - \frac{M_{tot}}{P_0} + \frac{b}{k} + n \\ &= (n-1)\left(\frac{a}{k} + \frac{b}{k} + \frac{n-2}{2} + 1\right) - n\frac{M_{tot}}{P_0} + n, \end{aligned} \tag{2.30}$$

   so that $Q(\gamma) = 0$ *iff* the relation (2.27) is satisfied, and the value for c_i, v and w immediately follow from (2.25).

2. If $\gamma \neq 1$, we obtain (2.29) directly from (2.25).

■

For the existence of PSS, we study roots of the polynomial Q by applying Descartes' rule.

Lemma 1 (Descartes' rule of signs [68])**.**
Given a univariate real polynomial P, the number of positive real roots of P is bounded by the number of sign variations of the ordered (by exponent) sequence of the coefficients of P.

The following proposition characterises different cases, leading to zero, one or two positive steady states.

Proposition 6 (Existence and number of PSSs of System (2.6) with constant coefficients)**.**
Consider System (2.6) *with constant polymerisation/depolymerisation coefficients a and b under the assumptions of Corollary 2. Assume that* (2.27) *is not satisfied. Then, we have the following cases.*

1. *If one of the following assumptions is satisfied:*

$$\frac{M_{tot}}{P_0} < \min\left\{1 + \frac{a}{k}, n + \frac{b}{k}\right\}, \tag{2.31}$$

$$\frac{M_{tot}}{P_0} > \max\left\{n + \frac{b}{k}, n + \frac{b}{k} + \frac{a}{k} - 1\right\}, \tag{2.32}$$

   then, System (2.6) *with constant coefficients has no PSS.*

2. *If either*

$$1 + \frac{a}{k} < \frac{M_{tot}}{P_0} < n + \frac{b}{k}, \tag{2.33}$$

   or

$$n + \frac{b}{k} < \frac{M_{tot}}{P_0} < 1 + \frac{a}{k}, \tag{2.34}$$

   holds, then System (2.6) *with constant coefficients has a unique PSS.*

3. *If*

$$\max\left\{\frac{b}{k}+n, \frac{a}{k}+1\right\} < \frac{M_{tot}}{P_0} < n+\frac{b}{k}+\frac{a}{k}-1, \tag{2.35}$$

holds, then System (2.6) *with constant coefficients has at most two PSSs.*

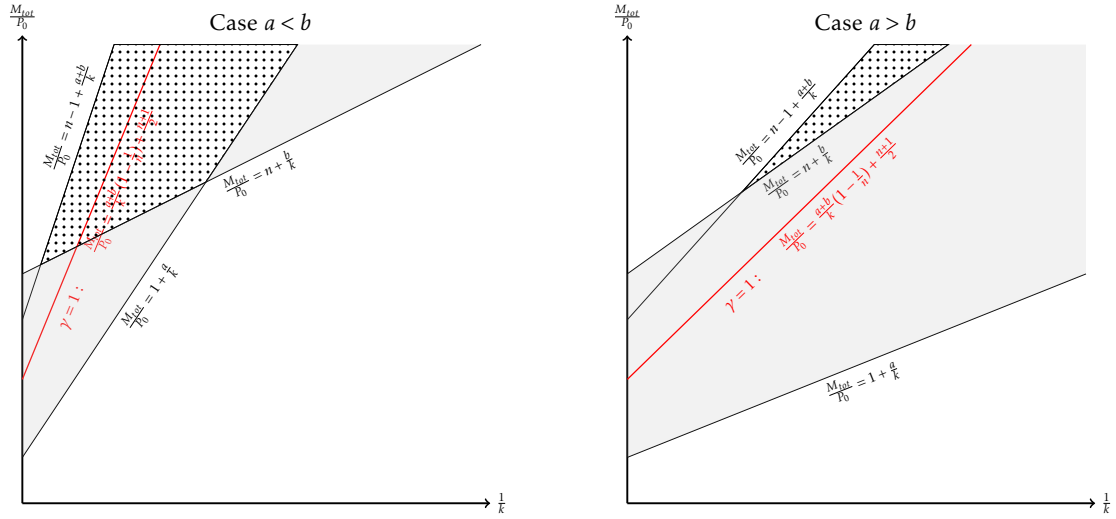

Figure 2.9 – Zones with zero (white), one (light grey) or two (dotted domain) PSSs. In red is the line of assumption (2.27): above we have $\gamma > 1$, below $\gamma < 1$.

Proof. Using the results of Corollary 2, we look for roots of the polynomial $Q(\gamma) = \sum_{i=0}^{n-1} u_i \gamma^i$, where

$$u_0 = \frac{a}{k} - \frac{M_{tot}}{P_0} + 1, \qquad u_i = \frac{a}{k} + \frac{b}{k} - \frac{M_{tot}}{P_0} + i + 1 = u_0 + \frac{b}{k} + i, \qquad u_{n-1} = \frac{b}{k} - \frac{M_{tot}}{P_0} + n.$$

and we apply the Descartes' rule. We notice that (u_i) is strictly increasing in i for $0 \le i \le n-2$, and $u_{n-1} = u_{n-2} - \frac{a}{k} + 1$.

1. If $u_0 > 0$ and $u_{n-1} > 0$, *i.e.* if assumption (2.31) is satisfied, then, all coefficients are positive. If $u_{n-2} < 0$ and $u_{n-1} < 0$, *i.e.* if assumption (2.32) is satisfied, then, all coefficients are negative. In both cases, there exists no PSS.

2. If $u_0 < 0$ and $u_{n-1} > 0$, *i.e.* under assumption (2.33), or if $u_0 > 0$ and $u_{n-1} < 0$, *i.e.* assumption (2.34), there is exactly one change of sign in the coefficients. In these cases, there exists at most one PSS. In fact, there exists exactly one PSS, because $P(0) = u_0$ and $P(z) \sim u_{n-1} z^{n-1}$ as $z \to \infty$ are of opposite sign.

3. If $u_0 < 0$, $u_{n-2} > 0$ and $u_{n-1} < 0$, *i.e.* under assumption (2.35), there are two changes of signs in the coefficients, so that there exist at most two PSSs.

■

Discussion and biological interpretation: The conditions (2.31)-(2.35) are summarised in Figure 2.9: The grey region is the region, where assumptions (2.33) and (2.34) are satisfied, i.e. there is a unique PSS. The region with dots corresponds to assumption (2.35), where there exist at most two PSSs. The white region in the figure corresponds to assumptions (2.31) and (2.32) with no PSS. As in the general coefficient case, we see that the zone where there is at least one steady state corresponds to the intermediate zone, where $\frac{M_{tot}}{P_0}$ is neither "small" nor "large" as compared to the reaction parameters. Moreover, more than one PSS can only occur in the biologically unrealistic region where $\frac{M_{tot}}{P_0} > n$.

In the case of a unique PSS, let us now study the respective values of $\gamma \gtreqless 1$. This is of key importance, since if $\gamma \geq 1$, then the corresponding PSS has no finite limit as $n \to \infty$.

Corollary 3 (Values of the root γ)**.**
Let the assumptions of Proposition 6 be satisfied and assume moreover inequality (2.33)*. Let γ be the unique positive root of the polynomial Q. Then,*

- *if* $\frac{M_{tot}}{P_0} = \left(\frac{a}{k} + \frac{b}{k}\right)\frac{n-1}{n} + \frac{n+1}{2}$, *we have* $\gamma = 1$,
- *if* $\frac{M_{tot}}{P_0} > \left(\frac{a}{k} + \frac{b}{k}\right)\frac{n-1}{n} + \frac{n+1}{2}$, *we have* $\gamma > 1$,
- *if* $\frac{M_{tot}}{P_0} < \left(\frac{a}{k} + \frac{b}{k}\right)\frac{n-1}{n} + \frac{n+1}{2}$, *we have* $\gamma < 1$.

Proof. Under Assumption (2.33), $Q(0) < 0$ and $Q(\infty) > 0$, so that $\gamma > 1$ iff $Q(1) < 0$. We have already calculated $Q(1)$ in (2.30), from which the result follows immediately. ∎

Remark 12. *Letting n tend to infinity while keeping M_{tot} and P_0 finite ensures $\gamma < 1$: Hence, the steady state $(c_i)_{1\leq i\leq n-1} = (c_1\gamma^{i-1})_{1\leq i\leq n-1}$ defines a converging series and thus a possible steady state for the infinite system. Note that that the assumption of constant polymerisation coefficients prevents gelation (as for the classical Becker-Döring system).*

2.4.2 Simulation results and discussion

Experiments can either measure the total polymerised mass $M_1(t)$ (by Thioflavine T, see e.g. [165]) or the second moment $M_2(t)$ (by Static Light Scattering, see e.g. [126]) defined by

$$M_1 := \sum_{i=1}^{n} i c_i = M_{tot} - v - w, \qquad M_2 := \sum_{i=1}^{n} i^2 c_i(t). \tag{2.36}$$

The following numerical simulations exemplify the dynamical behaviour of System (2.6) in two biologically plausible cases: Figures 2.10, 2.11 and 2.12 illustrate damped oscillations converging to a positive steady state (PSS) under Assumption (2.33) while Figure 2.13 shows convergence to (BSSb) (recall $\bar{w} = 0$ and $\bar{c}_1 = P_0$) under Assumption (2.23).

Figure 2.10: The size distribution of the polymers (right image), initially taken as a sharp Gaussian, oscillates in the sense that the Gaussian moves from left to right and right to left periodically in its

entirety while progressively diffusing. Figure 2.11: For initial states very close to the steady state, the oscillations remain numerous, though of smaller amplitude. Figure 2.12: An example concerning the influence of the initial average size of the polymers and of the total number of polymers n shows that smaller initial average size implies stronger damping of the oscillations. This supports an intuition that the role played by k in the two-polymer model might be here played by the average size of the polymers, which is about $\frac{n}{2}$ in this example.

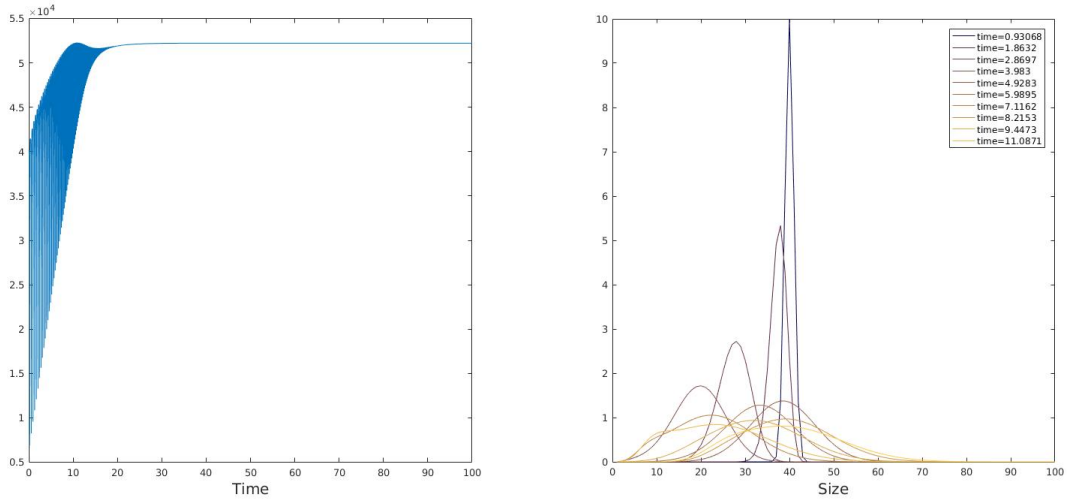

Figure 2.10 – Numerical simulation of convergence to (PSS) as in Proposition 5: $M_2(t)$ defined by (2.1) (left image) and evolution of the size distribution (right images). The parameters are $n = 100$, $k = 1.1$, $a = 1.5$, $b = 2$ and Assumption (2.33): $1 + \frac{a}{k} < \frac{M_{tot}}{P_0} < n + \frac{b}{k}$.

2.5 The infinite system

Let us now turn to the infinite system (2.6) with $n = \infty$, where no restriction is imposed on the maximal size of a fibril. Infinite size systems like the classical Becker-Döring model or a prion model [98, 126] are considered the most natural way to model such aggregation processes [18]. In this section, we first present a well-posedness result and, second, a study of all steady states. Finally, we point out the link between the infinite model and Lotka-Volterra systems in two specific cases: constant coefficients and linear coefficients.

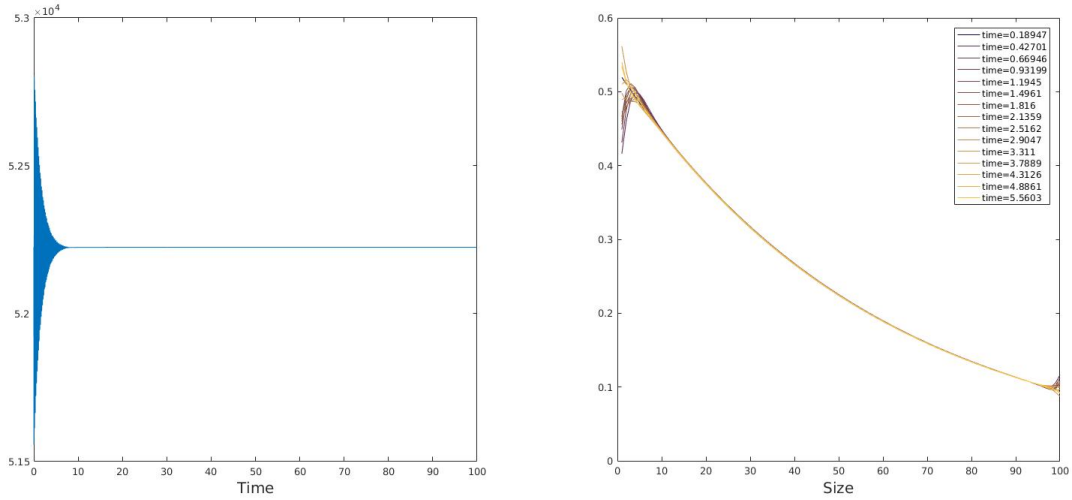

Figure 2.11 – Numerical simulation of convergence to (PSS) as in Proposition 5: M_2 defined by (2.1) (left images) and time evolution of the size distribution (right image). The initial condition is the (numerical) PSS, but $\bar{v}$ and $\bar{w}$ are perturbed by a constant of order 10^{-1} away of their equilibrium values. The parameters are $n = 100$, $k = 1.1$, $a = 1.5$, $b = 2$ and Assumption (2.33): $1 + \frac{a}{k} < \frac{M_{tot}}{P_0} < n + \frac{b}{k}$.

2.5.1 Well-posedness

We introduce the Banach sequence spaces

$$\ell^1_1 = \{y = (y_i) \,:\, \|y\| < \infty\}, \qquad \|y\| = \sum_{i=1}^{\infty} i|y_i|.$$

and

$$\mathcal{X} = \{x = (v, w, c) = (v, w, c_1, c_2, \ldots) \,:\, \|x\|_{\mathcal{X}} < \infty\}, \qquad \|x\|_{\mathcal{X}} = |v| + |w| + \|c\|.$$

Definition 4. *Let $0 < T \leq \infty$ and $c = (c_i)$. A nonnegative solution $x = (v, w, c)$ of (2.6) with $n = \infty$ on $[0, T)$ is a function $x : [0, T) \to \mathcal{X}$ such that*

1. *$x(t) \geq 0$ for all $t \in [0; T)$, i.e. $v(t) \geq 0$, $w(t) \geq 0$, $c_i(t) \geq 0$ for each i,*

2. *$v, w : [0, T) \to \mathbb{R}$ and $c_i : [0, T) \to \mathbb{R}$ for all $i \geq 1$ are continuous with $\sup_{t\in[0,T)} \|x(t)\|_{\mathcal{X}} < \infty$,*

3. *$\int_0^t \sum_{i=1}^{\infty} a_i c_i(s) ds < \infty$, $\int_0^t \sum_{i=2}^{\infty} b_i c_i(s) ds < \infty$ for all $t \in [0, T)$ and*

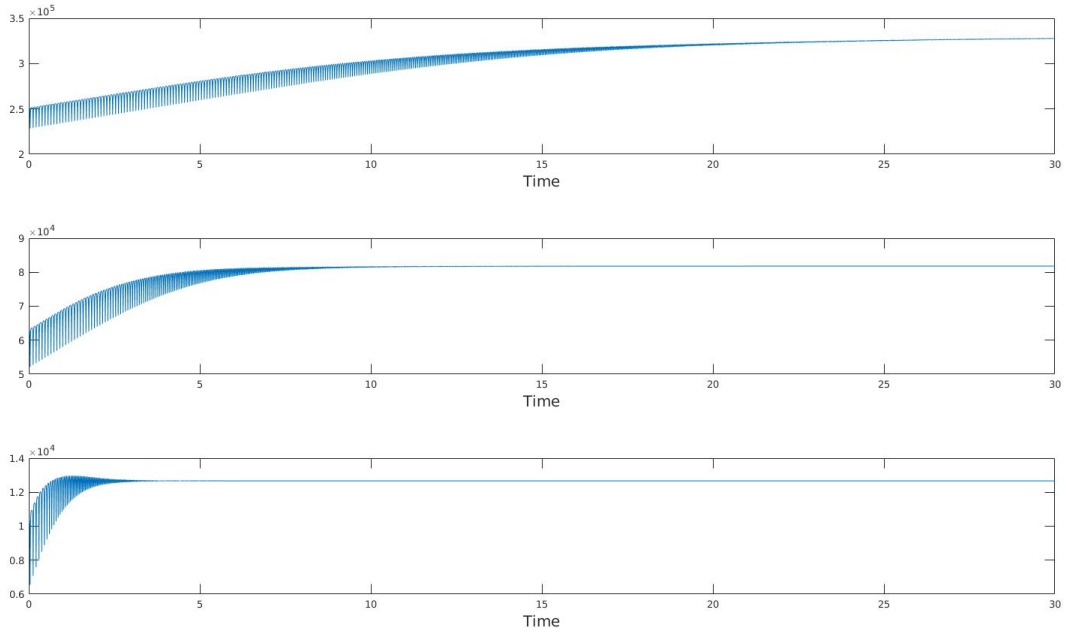

Figure 2.12 – Numerical simulation of convergence to (PSS) as in Proposition 5: M_2 defined by (2.1) and its sensitivity to the number of polymers. The number of polymers are 100 (up), 50 (middle) and 20 (bottom). The initial size distributions are centered on $\frac{n}{2}$. The parameters are $k = 10$, $a = 1.5$, $b = 2$ and Assumption (2.33): $1 + \frac{a}{k} < \frac{M_{tot}}{P_0} < n + \frac{b}{k}$.

4. *v, w and c satisfy for all $t \in [0, T)$*

$$\begin{cases} v(t) = v_0 + \int_0^t \left(-kv(s)w(s) + v(s) \sum_{i=2}^{\infty} b_i c_i(s) \right) ds, \\ w(t) = w_0 + \int_0^t \left(-w(s) \sum_{i=1}^{\infty} a_i c_i(s) + kv(s)w(s) \right) ds, \\ c_i(t) = c_i^0 + \int_0^t \left(J_{i-1}(s) - J_i(s) \right) ds, \quad i \geq 1,\ J_0 = 0. \end{cases} \tag{2.37}$$

Theorem 10 (Well-posedness of the infinite dimensional system)**.**
Let $T > 0$ be arbitrary and consider $x_0 = (v_0, w_0, c_0)$ satisfy $\|x_0\|_{\mathcal{X}} < \infty$. Assume

$$a_i = O(i), \qquad b_{i+1} = O(i+1), \qquad \forall\ i \geq 1.$$

Then, System (2.6) *with $n = \infty$ has a nonnegative solution for $t \in [0, T)$ with $v(t) \geq 0$, $w(t) \geq 0$, $c_i(t) \geq 0$ for*

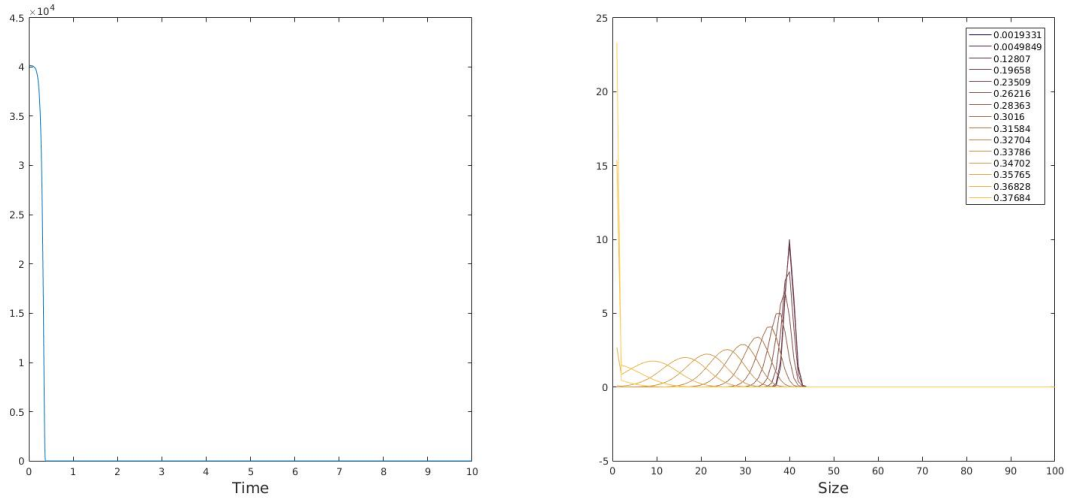

Figure 2.13 – Numerical simulation of convergence to (BSSb) as in Proposition 5: M_2 defined by (2.1) (left images) and time evolution of the size distribution (right image). The initial size distribution is centred around the size 40. The parameters are $n = 100$, $k = 2$, $a = 80$, $b = 1$ and $\frac{M_{tot}}{P_0} < 1 + \frac{a}{k}$ (Assumption (2.23), lower white zone in Figure 2.9, diagonally hatched zone in Figure 2.8).

$t \geq 0$ and all $1 \leq i$ satisfying

$$v(t) + w(t) + \sum_{i=1}^{\infty} i c_i(t) = v_0 + w_0 + \sum_{i=1}^{\infty} i c_i^0, \qquad \sum_{i=1}^{\infty} c_i(t) = \sum_{i=1}^{\infty} c_i^0, \qquad \forall t \geq 0.$$

Moreover, if $\sum_{i=1}^{\infty} i^2 c_i^0 < \infty$, then the solution is unique and satisfies

$$\sup_{t \in [0,T)} \sum_{i=1}^{\infty} i^2 c_i(t) < \infty. \tag{2.38}$$

The proof of Theorem 10 adapts well-known results of the Becker-Döring system as presented in [7] and is postponed to Appendix 2.6.2. The main novelty lies in the nonlinearity of the depolymerisation terms, which requires the supplementary assumption for the b_i.

2.5.2 Steady states and their local stability

In the following, we assume that the coefficients satisfy

$$a_i > 0,\ b_{i+1} > 0, \quad \forall i \geq 1 \qquad \text{and} \qquad \exists\, K > 0 : \quad \max_{i\geq 1}\left\{\frac{a_i}{i}, \frac{b_i}{i}, \frac{a_i}{b_{i+1}}\right\} \leq K. \tag{2.39}$$

The following result can be seen as the limit as $n \to \infty$ of Proposition 5.

Proposition 7 (Steady states of the infinite case system and their local stability)**.**
Let $v_0 > 0$, $w_0 > 0$, $P_0 > 0$ and $M_{tot} \geq v_0 + w_0 + P_0 > 0$. Let $(a_i, b_{i+1})_{i\geq 1}$ satisfy (2.39)*.*

Then, there exist the following steady states $(\bar{v}, \bar{w}, \bar{c}_{i\geq 1})$ of System (2.6) *with $n = \infty$:*

(BSSa) The trivial BSSs $\bar{v} = \bar{w} = 0$ and $\bar{c}_{i\geq 1} \in \ell^1_1$ satisfying

$$\sum_{i=1}^{\infty} \bar{c}_i = P_0, \qquad \text{and} \qquad \sum_{i=1}^{\infty} i\bar{c}_i = M_{tot},$$

which are always linearly unstable.

(BSSb) The BSS $\bar{v} = M_{tot} - P_0$, $\bar{w} = 0$, $\bar{c}_1 = P_0$ and $\bar{c}_{i\geq 2} = 0$. This steady state is locally asymptotically stable iff

$$\frac{M_{tot}}{P_0} \leq \frac{a_1}{k} + 1. \tag{2.40}$$

(PSS) Under assumption (2.40)*, there exists no positive steady state (PSS). Conversely, if*

$$\frac{M_{tot}}{P_0} > \frac{a_1}{k} + 1, \tag{2.41}$$

then there exists a unique PSS $(\bar{v}, \bar{w}, \bar{c}_{i\geq 1})$. Note that as already noted for the n-polymer model, the stability of the PSS is an open problem.

Proof.
First step: Existence of the steady states. After dropping the notation $\bar{\cdot}$ for simplicity, any steady state satisfy

$$kvw = v\sum_{i=2}^{\infty} b_i c_i, \qquad w\sum_{i=1}^{\infty} a_i c_i = kvw, \qquad J_i = J_{i-1} \implies v b_{i+1} c_{i+1} = w a_i c_i, \qquad \forall\, i \geq 1.$$

Let us first suppose $v = 0$. Then, the equation for w implies either $w = 0$ or $c_i = 0$ for all i. The first case yields (BSSa) by taking into account the conservation of mass and of the number of polymers. The second case is not possible under the assumption $P_0 > 0$. Hence, (BSSa) gathers all BSSs with $v = 0$.

Next, suppose $v \neq 0$ and $w = 0$. By the equalities $v b_{i+1} c_{i+1} = 0$, we deduce $c_{i\geq 2} = 0$. Consequentially, $c_1 = \sum_{i=1}^{\infty} c_i = P_0$ and $v = M_{tot} - w - \sum_{i=1}^{\infty} i c_i = M_{tot} - P_0$, which is (BSSb).

Let us finally assume both $v \neq 0$, $w \neq 0$. We can divide the equations for c_i by v. By denoting $z = \frac{w}{v}$, $\alpha_i = \frac{a_i}{b_{i+1}}$ for $i \geq 1$, $\alpha_0 = 1$, we calculate

$$c_{i+1} = \frac{w}{v}\frac{a_i}{b_{i+1}}c_{i-1} = z\alpha_i c_i = \cdots = z^i c_1 \prod_{j=0}^{i} \alpha_j.$$

Under assumption (2.39), this series with coefficients $\prod_{j=1}^{i} \alpha_j$ has a strictly positive convergence radius R and since we are looking for steady states in ℓ^1_1, we consider here only $z < R$. Moreover, the equations for v and w as well as the mass and polymer conservation laws yield the relations:

$$kv = c_1 \sum_{i=1}^{\infty} a_i z^{i-1} \prod_{j=0}^{i-1} \alpha_j, \qquad P_0 = c_1 \sum_{i=1}^{\infty} z^{i-1} \prod_{j=0}^{i-1} \alpha_j,$$

$$M_{tot} = v(1+z) + c_1 \sum_{i=1}^{\infty} i z^{i-1} \prod_{j=0}^{i-1} \alpha_j = c_1 \left(\sum_{i=1}^{\infty} \frac{a_i}{k} z^{i-1}(1+z) \prod_{j=0}^{i-1} \alpha_j + \sum_{i=1}^{\infty} i z^{i-1} \prod_{j=0}^{i-1} \alpha_j \right).$$

We deduce

$$\frac{M_{tot}}{c_1} = \frac{M_{tot}}{P_0} \sum_{i=1}^{\infty} z^{i-1} \prod_{j=0}^{i-1} \alpha_j = \sum_{i=1}^{\infty} z^{i-1} \left(\left(\frac{a_i}{k} + i \right) \prod_{j=0}^{i-1} \alpha_j + \mathbb{1}_{i\geq 2} \frac{a_{i-1}}{k} \prod_{j=0}^{i-2} \alpha_j \right).$$

We recognise a relation of the form $\frac{M}{P_0} F_1(z) = F_2(z)$ and notice that F_1 and F_2 are two increasing functions in z, which are both defined by series with convergence radii $R > 0$. Moreover F_2 increases faster than F_1 since all its coefficients are strictly larger. Hence, there exists no solution iff $\frac{M_{tot}}{P_0} F_1(0) < F_2(0)$, which is exactly assumption (2.40). Conversely, if $\frac{M_{tot}}{P_0} F_1(0) \geq F_2(0)$, there exists a unique solution $z < R$, which ensures *a posteriori* the validity of our assumption to only consider $z < R$. Given the solution z, the explicit expressions for c_1, v and w follow. Note that $z = 0$ in the limit case where $\frac{M_{tot}}{P_0} F_1(0) = F_2(0)$ and we are back to (BSSb).

Second step: Linear stability or instability of the steady states. Linearisation of System (2.6) around the steady states yields the following cases:

1. Linearisation around a state $(0, 0, \bar{c}_i)$: The equation for v gives $\frac{d\widetilde{v}}{dt} = \widetilde{v} \sum_{i=2}^{\infty} b_i \bar{c}_i$, which has the positive eigenvector $(1, 0, c_i = 0)$ for the positive eigenvalue $\lambda = \sum_{i=2}^{\infty} b_i \bar{c}_i$. Hence, these steady states are linearly unstable.

2. Linearisation around the state $(M_{tot} - P_0, 0, P_0, c_{i\geq 2} = 0)$. As for the asymptotic stability result, we may pass to the limit $n \to \infty$ in the corresponding part of the proof of Proposition (1).

■

2.5.3 Link with oscillatory models

We proved in the previous section the well-posedness of the infinite model and that there exists a unique positive steady state under assumption (2.41). This assumption means that the ratio $\frac{M_{tot}}{P_0}$ needs to be "sufficiently large", else the polymers are unstable in the sense that all the mass goes back to the polymer of minimal size c_1. There are two ways for this ratio to be "sufficiently large": either the monomeric species are in large excess, so that $\frac{v^0+w^0}{P_0}$ is large, and/or the average polymer size, namely $\frac{M_{tot}-v^0-w^0}{P_0}$ is large, *i.e.* far enough from the BSS $\bar{c}_1 = P_0$ for which $\frac{M_{tot}}{P_0} = 1$ has its minimum. Proposition 7 leaves the question open if the unique positive steady state is asymptotically stable under this assumption, but we expect this to be true.

In this subsection, in order to give some insights into the question of damped oscillations towards the positive equilibrium, we focus on two specific cases for the parameters of the model: the constant coefficient case and the linear coefficient case. Results for general reaction rate coefficients are difficult and open questions, beyond the scope of this study.

The constant coefficient case and its link to a predator-prey Lotka-Volterra system

As for the finite system, assuming constant coefficients permits to derive an explicit formula for the positive steady state.

Corollary 4 (Non-trivial steady state for constant reaction coefficients)**.**
Under the assumptions of Proposition 7 with $a_i = a$, $b_i = b$ and under assumption (2.41)*, the strictly positive steady state $(\bar{v}, \bar{w}, \bar{c}_{i\geq 1})$ of* (2.6) *is explicitly given by*

$$\bar{v} = \frac{a}{k}P_0, \qquad \bar{w} = \gamma\frac{b}{k}P_0, \qquad \bar{c}_1 = (1-\gamma)P_0, \qquad \bar{c}_i = \gamma^{i-1}(1-\gamma)P_0, \quad \forall i \geq 2,$$

where

$$\gamma = \frac{1}{2}\left(-\frac{a}{b} + \frac{kM_{tot}}{bP_0} + 1 - \sqrt{\left(\frac{a}{b} - \frac{kM_{tot}}{bP_0} + 1\right)^2 + \frac{4k}{b}}\right).$$

Proof. The straightforward computations proving Corollary 4 are postponed to Appendix 2.6.2. ∎

Discussion and biological interpretation: Corollary 4 supposes assumption (2.41), which constitutes the biologically most relevant case since from a modelling point of view we are interested in $\frac{M_{tot}}{P_0} \gg 1$, which means that the average size of polymers is initially large, and/or that there are enough monomeric species v and w. Accordingly, Corollary 4 states the existence of a PSS, which is conjectured to be stable. The opposite condition (2.40) concerns cases where the disease cannot spread due to a too small amount of large polymers and monomeric species compared to small polymers (see the discussion for n finite after Proposition 5).

In the case of constant polymerisation coefficients, we obtain the following system

$$\frac{dv}{dt} = -kvw + bv(P_0 - c_1), \qquad \frac{dw}{dt} = -awP_0 + kvw, \qquad \frac{dc_i}{dt} = J_{i-1} - J_i, \qquad 1 \leq i. \tag{2.42}$$

and observe that if c_1 is negligible compared to P_0, *i.e.* $P_0 - c_1 \simeq P_0$, with P_0 being a constant, then the equations for (v, w) in (2.42) constitute a Lotka-Volterra system with v taking the role of the prey and w being the predator. Hence, System (2.42) can be interpreted as a *perturbation of the Lotka-Volterra system* by the concentration of the polymer of minimal size c_1. Note that this observation is in accordance with the numerically observed oscillations, which are progressively damped towards the steady state and are more pronounced for smaller c_1 - the oscillatory behaviour of System (2.42) is also reflected in oscillations of M_1 and M_2 defined by (2.36).

The linear coefficient case and its link to a cyclic reaction system

As in the constant coefficients case, an explicit formula for the positive steady state is easily computed in the case of linear polymerisation coefficients.

Corollary 5 (Non-trivial steady state for linear reaction coefficients)**.**
Under the assumptions of Proposition 7 with $a_i = ia$, and $b_{i+1} = ib$ for $i \geq 1$, and under assumption (2.41)*, the strictly positive steady state $(\bar{v}, \bar{w}, \bar{c}_{i\geq 1})$ of* (2.6) *is given by*

$$\bar{v} = \frac{a}{k(1-\gamma)}P_0, \qquad \bar{w} = \frac{b\gamma}{k(1-\gamma)}P_0, \qquad \bar{c}_1 = (1-\gamma)P_0, \qquad \bar{c}_i = \gamma^{i-1}(1-\gamma)P_0, \quad \forall i \geq 2$$

and

$$\gamma = \frac{M_{tot}k - P_0(a+k)}{M_{tot}k + P_0 b} \in (0,1).$$

Proof. Again, we postpone the straightforward calculations of the proof of the corollary to Appendix 2.6.2. ■

Discussion and biological interpretation: Keeping the same notation of the total polymer mass $M_1(t) = M_{tot} - v - w$ as in the previous section, assuming linear polymerisation coefficients yields the simplified system:

$$\frac{dv}{dt} = -kvw + vb(M_1 - P_0), \qquad \frac{dw}{dt} = -waM_1 + kvw, \qquad \frac{dM_1}{dt} = waM_1 - vb(M_1 - P_0). \tag{2.43}$$

System (2.43) differs from (2.42) by featuring an interplay between the two monomer species and the total polymer mass $M_1(t)$, which varies in time as a kind of quasi-variable (and in contrast to total number of polymers P_0 being constant).

In situations when $P_0 \ll M_1$ (*i.e.* when the average polymer size remains sufficiently large), we recover the already cited Ivanova differential system (2.3). The Ivanova system displays sustained oscillations [162]. In our specific case, the total number of polymers P_0 is a perturbation which has an impact on the behaviour of the solutions of (2.43). The mass conservation of System (2.43) implies

$M_1(t) = M_{tot} - v(t) - w(t)$. Hence, we can further reduce (2.43):

$$\begin{cases} \frac{dv}{dt} = -kvw + vb\left((M_{tot} - P_0) - v - w\right), \\ \frac{dw}{dt} = -wa(M_{tot} - v - w) + kvw. \end{cases} \tag{2.44}$$

System (2.44) is a well known quadratic Lotka-Volterra system, see [20] or [70]. By using Poincaré-Bendixson theorem and the Poincaré-Dulac theorem, it follows that solutions of (2.44) converge to a steady state. Also, the oscillatory behaviour near the steady states follows from the (well-known) eigenvalues of the linearised system. We expect that global oscillatory behaviour of the solutions can be shown by similar arguments as in the two-polymer case, see Corollary 1. Moreover, exponential convergence to the steady state can probably be proven by developing an analog proof as for Theorem 9. These results, however, are beyond the scope of this study.

Summary and Perspectives

In this chapter, we propose a bi-monomeric, nonlinear Becker-Döring-type system, where one monomer species is involved in the polymerisation process while the other monomeric species is able to induce depolymerisation (with an accordingly nonlinear depolymerisation rate). Moreover, the polymerising/depolymerising hierarchy of polymers provides a nonlinear feedback to the evolution of the monomeric species.

A key observation of this paper highlights that the nonlinear coupling between monomeric species and polymer hierarchy leads to generic oscillatory behaviours of solutions, which is in special parametric cases linked to Lotka-Volterra models. A key concept of this paper is that the proposed mathematical model may play a pivotal role in explaining oscillatory behaviour in prion assemblies depolymerisation experiments, and thus become a building block for more specific models for the development of prion diseases.

Furthermore, we performed a full study of the model in the case of only two polymers. We have proven exponential convergence to equilibrium as well as provided an explanation for the damped oscillations, which occur when the monomer dynamics is fast compared to polymerisation/depolymerisation. For the finite and infinite models, we have analysed the existence, uniqueness and stability of the boundary steady states (BSSs) and characterised the existence of positive steady states (PSSs).

Several questions remain open, especially interesting ones for the infinite system: What is the stability of the positive steady state? What is the (nonlinear) rate of convergence to equilibrium? Does a Lyapunov functional exist (at least in a suitable neighbourhood of the PSSs)? How to rigorously prove the existence of damped oscillations?

Turning back to the experiments as shown in Figure 2.1, it also appears that much remains to be done before reaching a fully quantitative model: integrating the proposed reaction scheme in a more complete model, where "usual" reactions (like linear depolymerisation) would be the dominant reactions, governing the slow dynamics of the reactions, and these ones local corrections; experimental evidence

and quantitative comparison, for instance through data assimilation strategies in the spirit of [5, 6].

Finally, in a similar fashion as the Lifshitz-Slyozov system for Becker-Döring, a continuous approximation of our system could provide interesting insights into the interplay between the different scales, in particular the role of the average size of the polymers, and lead us to new mathematical problems.

Acknowledgments. M.D., M.M. and H.R. have been supported by the ERC Starting Grant SKIPPER^{AD} (number 306321). The authors thank Josef Hofbauer and Jean-Pierre Françoise for illuminating discussions. K.F. was partially supported by NAWI Graz.

2.6 Supplementary and appendix

2.6.1 The two-polymer model continued

Lemma 2 (Local convexity estimate of the Hamiltonian decay)**.**
Consider as above $\triangle_\lambda^-$ to be the interior of the triangle between $v = 0$ and the lines $W_\lambda \,:\, w - w_\infty = -\lambda(v - v_\infty)$ and $W_\Lambda \,:\, w - w_\infty = -\Lambda(v - v_\infty)$.

Then, for all $\lambda_\varepsilon < \lambda < 1$ sufficiently close to one, we have

$$d^2 - [(v - v_\infty)v_\infty w + (w - w_\infty)v w_\infty]\, p \geq \kappa (v - v_\infty)^2, \tag{2.45}$$

for a positive constant $\kappa = \kappa(\lambda, v_\infty, w_\infty) > 0$.

Proof. We set

$$q := [(v - v_\infty)v_\infty w + (w - w_\infty)v w_\infty]$$

and observe that $q > 0$ is equivalent to

$$w - w_\infty > -(v - v_\infty)\frac{v_\infty}{v}\frac{w}{w_\infty},$$

where on $\triangle_\lambda^-$ both $\frac{v_\infty}{v} > 1$ and $\frac{w}{w_\infty} > 1$. It is easily checked that the line $q = 0$ as a function of v is a curve through the equilibrium (v_∞, w_∞), where it has the line $p = 0$ as tangent. Moreover, on $\triangle_\lambda^-$ the line $q = 0$ is strictly convex and intersects the line W_Λ (and thus enters $\triangle_\lambda^-$) at the point

$$v = \frac{v_\infty(w_\infty + \Lambda v_\infty)}{\Lambda(v_\infty + w_\infty)} < v_\infty.$$

In order to prove (2.45), we need to estimate $d^2 - qp$ below. Note that $qp > 0$ holds on two subdomains of $\triangle_\lambda^-$: I) the intersection of the domains $q > 0$ and $p > 0$ up to the line W_Λ, which we shall denote as $\triangle_{\lambda,I}^-$ and II) the domain $\triangle_{\lambda,II}^-$ between the lines W_λ, $p = 0$ and the domain $q < 0$, where thus both $q < 0$ and $p < 0$.

On $\triangle_{\lambda,I}^-$, we estimate $0 \leq q \leq v_\infty w_\infty p$ with $0 \leq p \leq (1 - \Lambda)(v - v_\infty)$. Together with (2.14), this implies

$$\text{on } \triangle_{\lambda,I}^- \,:\quad d^2 - qp \geq (v - v_\infty)^2 \Big[(w_\infty + \lambda v_\infty)^2 - (1 - \Lambda)^2 v_\infty w_\infty\Big]$$

By observing that $(1-\Lambda)^2 = (\lambda-1)^2$, we obtain

$$\kappa = (w_\infty + \lambda v_\infty)^2 - (\lambda-1)^2 v_\infty w_\infty > 0$$

for λ close enough to one.

On $\triangle^-_{\lambda,II}$, where $q<0$, we estimate

$$\begin{aligned}|q| &= -(v-v_\infty)v_\infty(w-w_\infty) - (w-w_\infty)(v-v_\infty)w_\infty - v_\infty w_\infty p \\ &\le (v-v_\infty)^2(v_\infty+w_\infty)\Lambda - v_\infty w_\infty p.\end{aligned}$$

Since $(1-\lambda)(v-v_\infty) \le p \le 0$ and $(1-\Lambda)^2 = (\lambda-1)^2$, we obtain

$$\begin{aligned}d^2 - qp &\ge (v-v_\infty)^2\Big[(w_\infty+\lambda v_\infty)^2 + (v_\infty+w_\infty)\Lambda(1-\lambda)(v-v_\infty) - v_\infty w_\infty(\lambda-1)^2\Big] \\ &\ge \kappa(v-v_\infty)^2\end{aligned}$$

for λ close enough to one. ∎

Lemma 3 (Sojourn time estimates)**.**
Consider $\triangle^-_\lambda$ as above. Let t_1 be the time when a solution trajectory enters $\triangle^-_\lambda$ at a point $(v_1, W_\Lambda(v_1)$ and t_2 the time when the same trajectory leaves $\triangle^-_\lambda$ at a point $(v_2, W_\lambda(v_2))$ with $v_2 < v_1$ and $W_\lambda(v_2) < W_\Lambda(v_1)$.

Then, for ε sufficiently small and all $v_1 \in (0, v_\infty)$, we have that the sojourn time $t_2 - t_1$ is bounded below and above, i.e.

$$\frac{c_1}{c_2}\frac{1}{2\Lambda[v_\infty+w_\infty]} \le t_2 - t_1 \le \frac{2(\Lambda-\lambda)}{w_\infty}, \tag{2.46}$$

where $c_1, c_2 > 0$ are trigonometric constants. Note that $c_1 = O(\lambda-1)$ while $c_2 = O(1)$.

Proof. We estimate the second equation of (P2) by using that $p \ge (1-\lambda)(v-v_\infty)$, $w_\infty \le w \le w_\infty + \Lambda v_\infty$ and $v - v_\infty = -|v-v_\infty|$ holds on $\triangle^-_\lambda$:

$$\begin{aligned}-\dot w &= -w(v-v_\infty) + \varepsilon w p \ge w_\infty|v-v_\infty| - \varepsilon(1-\lambda)w|v-v_\infty| \\ &\ge |v-v_\infty|[w_\infty - \varepsilon(1-\lambda)(w_\infty+\Lambda v_\infty)] \\ &\ge \frac{w_\infty}{2}|v-v_\infty| \ge \frac{w_\infty}{2}|v_1-v_\infty|,\end{aligned}$$

where the second last inequality holds for sufficiently small ε, e.g. $\varepsilon \le \frac{w_\infty}{2(1-\lambda)(\Lambda v_\infty + w_\infty)}$. Hence,

$$w(t_1) - w(t_2) = \int_{t_1}^{t_2} -\dot w\, dt \ge \frac{w_\infty}{2}|v_1 - v_\infty|(t_2 - t_1).$$

On the other hand, since $w(t_1) - w(t_2) \le W_\Lambda(v_1) - W_\lambda(v_1)$ as $v_2 = v(t_2) < v_1 = v(t_1)$, we have

$$w(t_1) - w(t_2) \le w_\infty - \Lambda(v_1 - v_\infty) - w_\infty + \lambda(v_1 - v_\infty) = (\Lambda - \lambda)|v_1 - v_\infty|$$

which yields the upper bound (2.46). For the lower bound, we estimate with $w \le w_\infty + \Lambda v_\infty$

$$\begin{aligned} -\dot{w} &= -w(v - v_\infty) + \varepsilon w p \le |v - v_\infty|[w_\infty + \Lambda v_\infty](1 + \varepsilon(\Lambda - 1)) \\ &\le 2\Lambda[v_\infty + w_\infty]|v - v_\infty| \le 2\Lambda[v_\infty + w_\infty]|v_2 - v_\infty|, \end{aligned}$$

for ε sufficiently small, e.g. $\varepsilon(\Lambda - 1) \le 1$. Hence

$$w(t_1) - w(t_2) = \int_{t_1}^{t_2} -\dot{w}\, dt \le 2\Lambda[v_\infty + w_\infty]|v_2 - v_\infty|(t_2 - t_1) \tag{2.47}$$

and we require a lower bound for $w(t_1) - w(t_2)$, which we derive as follows. From

$$\begin{aligned} -\dot{v} &= v[w - w_\infty] + \varepsilon v p \le v_\infty \Lambda |v - v_\infty| + \varepsilon v_\infty (\Lambda - 1)|v - v_\infty| \\ &\le |v - v_\infty| \Lambda v_\infty \end{aligned}$$

for ε sufficiently small, e.g. $\varepsilon(\Lambda - 1) \le \Lambda$ and by recalling $-\dot{w} \ge \frac{w_\infty}{2}|v - v_\infty|$ from above, we estimate

$$\frac{dw}{dv} = \frac{-\dot{w}}{-\dot{v}} \ge \frac{w_\infty}{2\Lambda v_\infty}.$$

The lower bound on $\frac{dw}{dv}$ implies that the solution trajectory starting at $(v_1, w_1 = W_\Lambda(v_1))$ and leaving $\triangle_\lambda^-$ at $(v_2, w_2 = W_\lambda(v_2))$ lies below the straight line $\mathcal{W}$ through (v_1, w_1) with slope $\frac{w_\infty}{2\Lambda v_\infty}$. By denoting $\hat{v}_1, \hat{w}_1$ the crossing between $\mathcal{W}$ and W_λ, we have that $\hat{v}_1 < v_2 < v_1$ and $\hat{w}_1 > w_2$. Moreover, the length l of $\mathcal{W}$ within $\triangle_\lambda^-$ is proportional both to $v_1 - v_\infty$ and $\hat{v}_1 - v_\infty$ by trigonometric constants. Since $\hat{v}_1 < v_2 < v_1$, l is therefore also proportional to $v_2 - v_\infty$, i.e. there exist a trigonometric constant c_1 such that $l = c_1|v_2 - v_\infty|$. Finally, l is also proportional to $w_1 - \hat{w}_1$, i.e. $l = c_2(w_1 - \hat{w}_1)$. Altogether, that implies that

$$w(t_1) - w(t_2) = w_1 - w_2 \ge w_1 - \hat{w}_1 = \frac{l}{c_2} = |v_2 - v_\infty|\frac{c_1}{c_2},$$

which yields together with (2.47) the lower bound (2.46). This finishes the proof. ■

2.6.2 Stability of the steady states for the finite system

Proof of stability of the boundary steady states (Proposition 5)

(BSSa) $v = w = 0$.

To analyse linear stability, we linearise system (2.6) around those equilibria and obtain the

following matrix

$$A_{(0,0)} = \begin{pmatrix} \sum_{i=2}^{n} b_i c_i & 0 & 0 & \cdots & 0 \\ 0 & -\sum_{i=1}^{n-1} a_i c_i & 0 & \cdots & 0 \\ b_2 c_2 & -a_1 c_1 & 0 & \cdots & 0 \\ \cdots & \cdots & 0 & \cdots & 0 \\ b_{i+1} c_{i+1} - b_i c_i & -a_i c_i + a_{i-1} c_{i-1} & 0 & \cdots & 0 \\ -b_n c_n & w a_{n-1} & 0 & \cdots & 0 \end{pmatrix},$$

which has an n-fold zero eigenvalue as well as $\lambda_+ = \sum_{i=2}^{n} b_i c_i > 0$ and $\lambda_- = -\sum_{i=1}^{n-1} a_i c_i \leq 0$. Hence, these steady states are always unstable.

(BSSb) $w = 0$ and $c_2 = c_3 = \ldots = c_n = 0$.

The linearised system is then described by $A_{(v,0)}$ defined by

$$A_{(v,0)} := \begin{pmatrix} 0 & -kv & 0 & b_2 v & \cdots & b_i v & b_{i+1} v & \cdots & b_n v \\ 0 & kv - a_1 P_0 & 0 & 0 & \cdots & 0 & 0 & \cdots & 0 \\ 0 & -a_1 P_0 & 0 & b_2 v & \cdots & 0 & 0 & \cdots & 0 \\ 0 & a_1 P_0 & 0 & -b_2 v & b_3 v & 0 & 0 & \cdots & 0 \\ 0 & 0 & 0 & 0 & \cdots & -b_i v & b_{i+1} v & 0 & 0 \\ 0 & 0 & \cdots & 0 & 0 & 0 & 0 & \cdots & 0 \\ 0 & 0 & \cdots & 0 & 0 & 0 & 0 & 0 & -b_n v \end{pmatrix}.$$

This is exactly symmetric to the case of $A_{(0,w)}$: Zero is an eigenvalue of order two, and the other eigenvalues are $\lambda_i = -b_i v$ for $2 \leq i \leq n$ and $\lambda_1 = kv - a_1 P_0 = kM_{tot} - P_0(k + a_1)$, so that it is unstable iff $M_{tot} > P_0(1 + \frac{a_1}{k})$.

(BSSc) $v = 0$ and $c_1 = c_2 = \ldots = c_{n-1} = 0$.

The linearised system is given by $\frac{dX}{dt} = AX$ with $w = M_{tot} - nP_0$:

$$A_{(0,w)} = \begin{pmatrix} -kw + b_n P_0 & 0 & 0 & \cdots & \cdots & \cdots & 0 & 0 \\ kw & 0 & -a_1 w & \cdots & -a_i w & \cdots & -a_{n-1} w & 0 \\ 0 & 0 & -a_1 w & 0 & 0 & \cdots & 0 & 0 \\ \cdots & \cdots & \cdots & \cdots & \cdots & \cdots & \cdots & \cdots \\ 0 & 0 & \cdots & a_{i-1} w & -a_i w & 0 & \cdots & 0 \\ \cdots & \cdots & \cdots & \cdots & \cdots & \cdots & 0 & 0 \\ b_n P_0 & 0 & 0 & \cdots & 0 & a_{n-2} w & -a_{n-1} w & 0 \\ -b_n P_0 & 0 & 0 & \cdots & 0 & 0 & a_{n-1} w & 0 \end{pmatrix},$$

The eigenvalues are thus 0 (twofold), $\lambda_0 = -kw + b_n P_0$ and $\lambda_i = -a_i w < 0$ for $1 \le i \le n-1$. This steady state is thus unstable iff $\lambda_0 > 0$, *i.e.* $b_n P_0 > k(M_{tot} - nP_0)$. Note that such a steady state is physically relevant only if it is nonnegative, *i.e.* $M_{tot} \ge nP_0$.

The infinite system.

Well-posedness

Proof.[Theorem 10] **First step: Existence.** Let $x_0^n = (v_0, w_0, c_1^0, \dots, c_n^0)$. By Proposition 4, System (2.6) has a unique solution x^n on $[0,\infty)$ with $v^n(t) \ge 0$, $w^n(t) \ge 0$,$c_i^n(t) \ge 0$, for $1 \le i \le n$ and

$$v^n(t) + w^n(t) + \sum_{i=1}^{n} i c_i^n(t) = v_0 + w_0 + \sum_{i=1}^{n} i c_i^0, \qquad \sum_{i=1}^{n} c_i(t) = \sum_{i=1}^{n} c_i^0.$$

We construct a sequence $(x^n)_{n\ge1}$ in $\mathcal{X}$ such that $x^1 = v$, $x^2 = w$, $x^i = c_{i-2}^n, 1 \le i-2 \le n$ and $x^i = 0, \forall i \ge n+2$. Thus, $\|x^n\|_{\mathcal{X}} \le \|x_0\|_{\mathcal{X}}$ and $0 \le v^n(t) \le \|x_0\|_{\mathcal{X}}$, $0 \le w^n(t) \le \|x_0\|_{\mathcal{X}}$, $0 \le c_i^n(t) \le i^{-1}\|x_0\|_{\mathcal{X}}, \forall\ t \ge 0$ and all i and n. Therefore, using the assumptions on a_i, b_i, we obtain the bounds

$$|\dot{c}_1^n| \le \left(a_1 + \frac{b_2}{2}\right)\|x_0\|_{\mathcal{X}}^2,$$

$$|\dot{c}_i^n| \le \left(\frac{a_{i-1}}{i-1} + \frac{a_i}{i} + \frac{b_{i+1}}{i+1} + \frac{b_i}{i}\right)\|x_0\|_{\mathcal{X}}^2 \le K_2 < \infty, \qquad i \ge 2.$$

Therefore, for all i the function $c_i^n(.)$ are equicontinuous on $[0,\infty)$. Thanks to the Arzelá-Ascoli theorem, we can extract a subsequence $n_k \to \infty$ such that there exists a continuous function $c_i : [0,\infty) \mapsto \mathbb{R}$ such that $c_i^{n_k} \to c_i$ uniformly on compact subsets of $[0,\infty)$ as $k \to \infty$. Note that $c_i \ge 0$ and $\sum_{i=1}^{N} i c_i(t) = \lim_{k\to\infty} \sum_{i=1}^{N} i c_i^{n_k}(t) \le \|x_0\|_{\mathcal{X}}$. Hence, we obtain

$$\sum_{i=1}^{\infty} i c_i(t) \le \|x_0\|_{\mathcal{X}}, \qquad \forall t \ge 0. \tag{2.48}$$

Using the assumptions on a_i, b_i and (2.48), we get

$$\sum_{i=1}^{\infty} a_i c_i(t) \le K_1\|x_0\|_{\mathcal{X}} < \infty, \qquad \sum_{i=2}^{\infty} b_i c_i(t) \le K_2\|x_0\|_{\mathcal{X}} < \infty, \qquad \forall t \ge 0. \tag{2.49}$$

Therefore, we also obtain

$$|\dot{v}^n(t)| \le (k + K_3)\|x_0\|_{\mathcal{X}} \qquad \text{and} \qquad |\dot{w}^n(t)| \le (k + K_4)\|x_0\|_{\mathcal{X}}.$$

Using the same reasoning and thanks to the the Arzelá-Ascoli theorem, there exist continuous functions $v : [0,\infty) \mapsto \mathbb{R}$ and $w : [0,\infty) \mapsto \mathbb{R}$), respectively, such that $v^{n_k} \to v$, (resp. $w^{n_k} \to w$) uniformly on compact subsets of $[0,\infty)$ as $k \to \infty$ and $v \ge 0$, $w \ge 0$.

Finally we pass to the limit as $k \to \infty$ in

$$v^{n_k}(t) = v_0 + \int_0^t \left(-kv^{n_k}(s)w^{n_k}(s) + v^{n_k}(s) \sum_{i=2}^{\infty} b_i c_i^{n_k}(s) \right) ds,$$

$$w^{n_k}(t) = w_0 + \int_0^t \left(-w^{n_k}(s) \sum_{i=1}^{\infty} a_i c_i^{n_k}(s) + kv^{n_k}(s)w^{n_k}(s) \right) ds,$$

$$c_1^{n_k}(t) = c_i^0 + \int_0^t \left(-a_1 c_1^{n_k}(s)w^{n_k}(s) + b_2 c_2^{n_k}(s)v^{n_k}(s) \right) ds,$$

$$c_i^{n_k}(t) = c_i^0 + \int_0^t \left((a_{i-1}c_{i-1}^{n_k}(s) - a_i c_i^{n_k}(s))w^{n_k}(s) + (b_{i+1}c_{i+1}^{n_k}(s) - b_i c_i^{n_k}(s))v^{n_k}(s) \right) ds, \quad i \geq 2.$$

We get (2.37) at the limit thanks to the uniform convergence and the bounds obtained in (2.49).

Moreover, in order to obtain a priori estimates (2.38), we compute:

$$\frac{d}{dt} \sum_{i=1}^{n_k} i^2 c_i^{n_k} = \sum_{i=1}^{n_k - 1} (2i+1)(a_i w^{n_k} c_i^{n_k} - b_{i+1} v^{n_k} c_{i+1}^{n_k}).$$

Using the bounds on w^{n_k}, v^{n_k} and the assumptions on a_i, b_{i+1}, we get

$$\sum_{i=1}^{n_k} i^2 c_i^{n_k} \leq \sum_{i=1}^{\infty} i^2 c_i^0 + K \left(\int_0^t \sum_{i=1}^{n_k} i^2 c_i^{n_k} \right),$$

where the constant K is independent of k. Since $\sum_{i=1}^{\infty} i^2 c_i^0 < \infty$ and using Gronwall's inequality we get:

$$\sum_{i=1}^{l} i^2 c_i^{n_k} + \sum_{i=l+1}^{n_k} i^2 c_i^{n_k} \leq M e^{Kt},$$

for all $t \geq 0$ where M is a constant independent of k. Letting $k \to \infty$ then $l \to \infty$, we deduce

$$\sum_{i=1}^{\infty} i^2 c_i \leq M e^{Kt}$$

and (2.38).

We can also obtain the following conserved quantities for the solution of System (2.6) with $n = \infty$. Since (2.37) holds, we get for $n > 1$, $t \geq 0$

$$\sum_{i=1}^{n} c_i(t) - \sum_{i=1}^{n} c_i^0 = -\int_0^t J_n(s) ds.$$

Since v, w are bounded and (2.49), we have $\lim_{n\to\infty} -\int_0^t J_n(s)ds = 0$ and

$$\sum_{i=1}^{\infty} c_i(t) = \sum_{i=1}^{\infty} c_i^0.$$

We also have

$$\sum_{i=1}^{n} ic_i(t) - \sum_{i=1}^{n} ic_i^0 = \int_0^t \sum_{i=1}^{n} i\left(J_{i-1}(s) - J_i(s)\right) ds = -\int_0^t nJ_n(s)ds + \int_0^t \sum_{i=1}^{n-1} J_i(s)ds, \tag{2.50}$$

and

$$\sum_{i=n+1}^{\infty} c_i(t) - \sum_{i=n+1}^{\infty} c_i^0 = \int_0^t J_n(s)ds.$$

We obtain the following result from (2.48)

$$\lim_{n\to\infty} (n+1) \sum_{i=n+1}^{\infty} c_i(t) \le \lim_{n\to\infty} \sum_{i=n+1}^{\infty} ic_i(t) = 0,$$

whence $\lim_{n\to\infty} \int_0^t nJ_n(s)ds = 0$. Then, by passing to the limits and adding v and w to (2.50) we obtain

$$v(t) + w(t) + \sum_{i=1}^{\infty} ic_i(t) = v_0 + w_0 + \sum_{i=1}^{\infty} ic_i^0. \tag{2.51}$$

Second step: Uniqueness. Let $x_1 = (v_1, w_1, c)$ and $x_2 = (v_2, w_2, d)$ be absolutely continuous in time solutions of System (2.6) with $n = \infty$ and the same initial condition $x_0 = (v_0, w_0, c_0)$. Then, we note

$$J_i^{(1)} = a_i w_1 c_i - b_{i+1} v_1 c_{i+1}, \qquad J_i^{(2)} = a_i w_2 d_i - b_{i+1} v_2 d_{i+1}, \quad \forall i \ge 1,$$

and $J_0^{(1)} = J_0^{(2)} = 0$. Let $V(t) = v_1(t) - v_2(t)$, $W(t) = w_1(t) - w_2(t)$ and $y_i(t) = c_i(t) - d_i(t)$. Then, for a.e. $t \in [0, T)$ we have

$$\begin{aligned}
\frac{d}{dt}|V| + |W| &= \operatorname{sign}(V)\left(-kVw_1 - kv_2W + V\sum_{i=2}^{\infty} b_i c_i + v_2 \sum_{i=2}^{\infty} b_i y_i\right) \\
&\quad + \operatorname{sign}(W)\left(kv_1 W + kVw_2 - W\sum_{i=1}^{\infty} a_i c_i - w_2 \sum_{i=1}^{\infty} a_i y_i\right), \\
&= |V|\left(-kw_1 + \operatorname{sign}(VW)kw_2 + \sum_{i=2}^{\infty} b_i c_i\right) + |W|\left(kv_1 - \operatorname{sign}(VW)kv_2 - \sum_{i=1}^{\infty} a_i c_i\right) \\
&\quad + \left(\operatorname{sign}(V)v_2 \sum_{i=2}^{\infty} b_i y_i - \operatorname{sign}(W)w_2 \sum_{i=1}^{\infty} a_i y_i\right).
\end{aligned}$$

We have by (2.49) and (2.51) that

$$\frac{d}{dt}|V|+|W| \le K_1\left(|V|+|W|+\sum_{i=1}^{\infty} i|y_i|\right). \tag{2.52}$$

Integrating (2.52) we obtain for $t \in [0,T)$

$$|V(t)|+|W(t)| \le K_1 \int_0^t \left(|V|+|W|+\sum_{i=1}^{\infty} i|y_i|\right) ds. \tag{2.53}$$

We also have for a.e. $t \in [0,T)$

$$\frac{d}{dt}\sum_{i=1}^{n} i|y_i| = \sum_{i=1}^{n} (J_i^{(1)} - J_i^{(2)})[(i+1)\operatorname{sign}(y_{i+1}) - i\operatorname{sign}(y_i)] - (n+1)\operatorname{sign}(y_{n+1})(J_{n+1}^{(1)} - J_{n+1}^{(2)}). \tag{2.54}$$

Now

$$\begin{aligned}(J_i^{(1)} - J_i^{(2)})[(i+1)\operatorname{sign}(y_{i+1}) - i\operatorname{sign}(y_i)] &= (a_i y_i w_1 + a_i d_i W - b_{i+1} y_{i+1} v_1 - b_{i+1} d_{i+1} V)\\ &\quad \times[(i+1)\operatorname{sign}(y_{i+1}) - i\operatorname{sign}(y_i)],\\ &= a_i w_1 |y_i|[(i+1)\operatorname{sign}(y_{i+1} y_i) - i] - b_{i+1}|y_{i+1}| v_1 [(i+1) - i\operatorname{sign}(y_{i+1} y_i)]\\ &\quad + (a_i d_i W - b_{i+1} d_{i+1} V)[(i+1)\operatorname{sign}(y_{i+1}) - i\operatorname{sign}(y_i)],\end{aligned}$$

hence

$$(J_i^{(1)} - J_i^{(2)})[(i+1)\operatorname{sign}(y_{i+1}) - i\operatorname{sign}(y_i)] \le a_i w_1 |y_i| + (2i+1)(a_i d_i |W| + b_{i+1} d_{i+1}|V|). \tag{2.55}$$

Integrating (2.54) and using (2.55), we therefore obtain for $t \in [0,T)$

$$\begin{aligned}\sum_{i=1}^{n} i|y_i| \le \int_0^t \sum_{i=1}^{n} a_i w_1 |y_i| ds + \int_0^t \sum_{i=1}^{n} (2i+1)(a_i d_i |W| + b_{i+1} d_{i+1}|V|) ds\\ - (n+1)\int_0^t \operatorname{sign}(y_{n+1})(J_{n+1}^{(1)} - J_{n+1}^{(2)}) ds.\end{aligned} \tag{2.56}$$

Using the assumption on a_i, b_{i+1} we have by (2.38) that

$$\sup_{t\in[0,T)} \sum_{i=1}^{\infty} (2i+1) a_i d_i(t) < \infty, \qquad \sup_{t\in[0,T)} \sum_{i=1}^{\infty} (2i+1) b_{i+1} d_{i+1}(t) < \infty. \tag{2.57}$$

By the same arguments as in the first step, we deduce

$$\lim_{n\to\infty} (n+1)\int_0^t \operatorname{sign}(y_{n+1})(J_{n+1}^{(1)} - J_{n+1}^{(2)}) ds = 0, \quad t \in [0,T). \tag{2.58}$$

Using (2.56)–(2.58), $a_i = O(i)$ and letting $n \to \infty$, we therefore obtain for $t \in [0, T)$

$$\sum_{i=1}^{\infty} i|y_i|(t) \leq K_2 \int_0^t \left(|V| + |W| + \sum_{i=1}^{\infty} i|y_i| \right) ds. \tag{2.59}$$

Summing the two inequalities (2.53) and (2.59) and using Gronwall's inequality, we obtain that

$$|V(t)| + |W(t)| + \sum_{i=1}^{\infty} i|y_i(t)| = 0, \qquad t \in [0, T)$$

and thus $(v_1, w_1, c) = (v_2, w_2, d)$ and uniqueness. ∎

Explicit formula for the positive steady state.

Proof.[Corollary 4] We define $\gamma = \frac{a}{b} z = \alpha z$ and use the expressions obtained in the Proposition 7,

$$\bar{c}_i = \gamma^{i-1} \bar{c}_1, \qquad \frac{\bar{c}_1}{1-\gamma} = P_0, \qquad k\bar{v} = a\frac{\bar{c}_1}{1-\gamma} = aP_0,$$

$$\bar{v} + \bar{w} + \frac{\bar{c}_1}{(1-\gamma)^2} = \frac{a}{k} P_0 + \frac{b\bar{v}\gamma}{a} + \frac{P_0}{1-\gamma} = P_0 \left(\frac{a}{k} + \frac{b\gamma}{k} + \frac{1}{1-\gamma} \right) = M_{tot},$$

which gives us immediately a second-order equation for γ. We define

$$\beta_1 = \frac{b}{k}, \quad \beta_2 = \frac{a}{k}, \qquad \mu = \frac{M_{tot}}{P_0},$$

hence

$$\frac{a}{k}(1-\gamma) + \frac{b}{k}\gamma(1-\gamma) + 1 = \frac{M_{tot}}{P_0}(1-\gamma),$$

$$\beta_2(1-\gamma) + \beta_1\gamma(1-\gamma) + 1 = \mu(1-\gamma),$$

$$\beta_1\gamma^2 + \gamma(\beta_2 - \mu - \beta_1) + \mu - 1 - \beta_2 = 0.$$

We calculate the discriminant

$$\Delta = (\beta_2 - \mu - \beta_1)^2 - 4\beta_1(\mu - 1 - \beta_2) = (\beta_2 - \mu + \beta_1)^2 + 4\beta_1,$$

$$\gamma_{\pm} = \frac{1}{2} \left(-\frac{\beta_2}{\beta_1} + \frac{\mu}{\beta_1} + 1 \pm \sqrt{(\frac{\beta_2}{\beta_1} - \frac{\mu}{\beta_1} + 1)^2 + \frac{4}{\beta_1}} \right).$$

We see easily that for any value of the parameters we have $\gamma_+ > 1$: Indeed, we have

$$\gamma_+ > \frac{1}{2} \left(-\frac{\beta_2}{\beta_1} + \frac{\mu}{\beta_1} + 1 + |\frac{\beta_2}{\beta_1} - \frac{\mu}{\beta_1} + 1| \right) \geq 1.$$

Thus, the only admissible solution is γ_-. We see similarly that it is always smaller than 1

$$\gamma_- < \frac{1}{2}\left(-\frac{\beta_2}{\beta_1} + \frac{\mu}{\beta_1} + 1 - |\frac{\beta_2}{\beta_1} - \frac{\mu}{\beta_1} + 1|\right) \leq 1.$$

And we have $\gamma_- > 0$ under the assumption (2.41). ■

Proof.[Corollary 5] Using the same notations as previously, we have

$$\gamma = \frac{a\bar{w}}{b\bar{v}}, \qquad \bar{c}_i = \gamma^{i-1}\bar{c}_1, \qquad \frac{\bar{c}_1}{1-\gamma} = P_0,$$

and denoting $f(\gamma) = \frac{1}{1-\gamma} = \sum_{i=0}^{\infty} \gamma^i$

$$k\bar{v} = a\bar{c}_1 \sum_{i=1}^{\infty} i\gamma^{i-1} = aP_0(1-\gamma)f'(\gamma) = \frac{aP_0}{(1-\gamma)}, \qquad k\bar{w} = bc_1 \sum_{i=1}^{\infty} i\gamma^i = \frac{bP_0\gamma}{(1-\gamma)}$$

$$\bar{v} + \bar{w} + \frac{c_1}{(1-\gamma)^2} = \frac{aP_0}{k(1-\gamma)} + \frac{bP_0\gamma}{k(1-\gamma)} + \frac{P_0}{(1-\gamma)} = M_{tot},$$

and thus

$$M_{tot}k(1-\gamma) = P_0(a + b\gamma + k), \qquad \gamma = \frac{M_{tot}k - P_0(a+k)}{M_{tot}k + P_0 b} < 1.$$

We have $\gamma > 0$ iff the assumption (2.41) is fulfilled. ■

Materials and methods of the depolymerisation experiment shown in Figure 2.1

Formation of amyloid fibrils: PrP amyloid fibrils were formed using the manual setup protocol described previously in [21]. Fibril formation was monitored using a ThT binding assay [21]. Samples were dialysed in 10 mM sodium acetate, pH 5.0. Then fibrils were collected by ultracentrifugation and resuspended in 10 mM sodium acetate, pH 5.0. A washing step was performed by repeating the ultracentrifugation and resuspension steps in 10 mM sodium acetate, pH 5.0. Static light scattering: Static light scattering kinetic experiments were performed with a thermostatic homemade device using a 407-nm laser beam. Light-scattered signals were recorded at a 112^0 angle. Signals were processed with a homemade MatLab program. All experiments have been performed at 55^0C in a 2mmX10mm cuve.

Chapter 3

A continuous bi-monomeric Lifshitz-Slyozov type model.

3.1 Introduction

We study the following system of reactions in a continuous size-setting where the depolymerisation is catalysed by a monomeric species. Let us recall the discrete-size chemical model where we denote $\mathcal{V}$ and $\mathcal{W}$ respectively the monomeric depolymerising and polymerising species, and $\mathcal{C}_i$ the polymers containing i monomers.

$$\begin{cases} \mathcal{V} + \mathcal{W} \xrightarrow{k} 2\mathcal{W} \\ \mathcal{W} + \mathcal{C}_i \xrightarrow{a_i} \mathcal{C}_{i+1} \quad i \geq 1 \\ \mathcal{C}_i + \mathcal{V} \xrightarrow{b_i} \mathcal{C}_{i-1} + 2\mathcal{V} \quad i \geq 2 \end{cases} \tag{3.1}$$

$\mathcal{C}_1$ represents the minimal size of the polymers however it could as well represent already large fibrils, of any given size $n_0 \in \mathbb{N}^*$. The infinite size-structured ordinary differential equations (ODE) systems corresponding to (3.1) has previously been studied (cf Chapter 2, [55]). The new framework model the phenomenon of protein aggregation process by three coupled equations: a transport equation representing the evolution in time of the concentration of clusters of specific sizes and two differential equations representing the evolution in time of the concentration of the two monomeric species. The infinite ODE systems leads to high computational costs whereas the partial derivative equations (PDE) coupled with two ODE seems easier to handle both theoretically and numerically.
In this study, we are interested in the long-term behaviour of a polymerisation/depolymerisation equations modeling the kinetics of large polymers in a spatially and closed environment. We prove that depending on the assumptions on the reaction coefficients the existence of either sustained oscillations or damped oscillations and the convergence towards a steady-state. We first recall some results on the seminal Lifshitz-Slyozov equations.

3.1.1 A continuous polymerisation/depolymerisation model: the Lifshitz-Slyozov model.

The Lifshitz-Slyozov model was first introuced in the seminal paper [95], was originally designed to model the formation of a new phase in solid solution. It describes the formation of aggregates or polymers by the continuous addition of monomers. In the following, we denote $v(t)$ the concentration of monomers at time t and $f(t,x)$ the concentration of polymers of size $x > 0$ at time t. The model is an attempt to describe the kinetics happening during SLS experiments, hence we assume a closed and space-homogeneous environment. This translates into the constraint that the total mass needs to be conserved:

$$v(t) + \int_0^\infty x f(t,x)dx = v(0) + \int_0^\infty x f(0,x)dx := \rho, \quad \forall t \geq 0. \tag{3.2}$$

We denote by ρ the total mass of monomers and $\int x f(t,x)dx$ can be interpreted as the concentration of monomers in the polymerised form. Hence, the concentration of polymers satisfies the following equation:

$$\frac{\partial f}{\partial t} + \frac{\partial}{\partial x}\Big[(a(x)v(t) - b(x))f(t,x)\Big] = 0, \quad f(0,x) = f_0(x) \geq 0. \tag{3.3}$$

Note that in (3.3), the depolymerisation rate is denoted by $b(x)$, the polymerisation rate is denoted by $a(x)$ and both rates can be size-dependent. In the original seminal paper [95], the authors assume the following reaction coefficients

$$a(x) = x^{\frac{1}{3}}, \quad b(x) = 1.$$

Using these definitions of the reaction rates, no boundary condition at $x = 0$ is required since the flux at zero is always going outward. Moreover, one key assumption for the phase transition model is that for larger sizes, the polymerisation rate is bigger than the depolymerisation rate, whereas the reverse is true for smaller size. This lead to the phenomenon called "Ostwald ripening" which describes the formation of larger and larger clusters at the expense of smaller ones (see e.g. [95, 109]).
The model containing equation (3.3) can either be completed by the mass conservation equation (3.2) or equivalently by the following equation for the concentration of monomers:

$$\frac{dv}{dt} = \int_0^\infty b(x)f(t,x)dx - v(t)\int_0^\infty a(x)f(t,x)dx, \quad v(0) = v_0. \tag{3.4}$$

We recall now some results on the Lifshitz-Slyosov model (3.3)-(3.2) or (3.3)-(3.4). The well-posedness has been established by Collet and Goudon in [37]. The autors proved the following theorem, stating the existence and uniqueness of solutions of (3.3)-(3.2).

Theorem 11 (Well-posedness [37].). *Let a, b be C^1 functions on $[0,\infty)$ such that*

$$a(x) \geq 0, \quad b(x) \geq 0,$$

$$a(0)M - b(0) \leq 0,$$

$$|a'(x)| + |b'(x)| \leq K.$$

Let the initial data f_0 be nonnegative and satisfy

$$\int_0^\infty f_0(x)dx < \infty, \quad \int_0^\infty x f_0(x)dx < M.$$

Then the system (3.3)-(3.2) *has a unique solution*

$$(v,f) \quad \textit{where} \quad v \in C^0([0,T]), \quad xf \in L^\infty\Big([0,T]; L^1([0,\infty))\Big).$$

The condition $a(0)M - b(0) \leq 0$ ensures the fact that no boundary condition is needed. The proof of the theorem is based on the method of characteristic to obtain an expression of the density function in terms of the monomer concentration and then a fixed-point method.
The asymptotic behaviour of the Lifshitz-Slyozov model for general assumptions on the reaction rates is still an open problem. However, Calvo, Doumic and Perthame recently established in [27] the exponential convergence towards a dirac mass in the following theorem.

Theorem 12 (Exponential convergence to a critical mass [27]). *Let $a(x) = 1$ and $b(x) \geq 0$ such that*

$$b \in C^1(\mathbb{R}_+), \exists\ \alpha, \beta > 0, \quad 0 < \alpha \leq b'(x) \leq \beta$$

$$v_0 > b(0) \geq 0.$$

Moreover, let

$$f_0 \in L^1(\mathbb{R}_+, (1+x^2)dx) \quad \textit{with} \quad \rho_0 = \int_0^\infty f_0(x)dx > 0.$$

Then there exists a unique solution $\bar{x} > 0$ to the equation

$$M = \rho_0 \bar{x} + b(\bar{x})$$

and the solution $(v,f) \in C^1(\mathbb{R}_+ \times C(\mathbb{R}_+, L^1((1+x^2)dx))$ to the Lifshitz-Slyozov system (3.3)-(3.4) *is such that $f(t,x)$ converges to $\rho_0 \delta_{\bar{x}}$ exponentially fast in the sense of the Wasserstein distance: for some constant $C > 0$ we have*

$$W_2(f(t,\cdot), \rho_0 \delta_{\bar{x}}) \leq Ce^{-\alpha t}, \quad |v(t) - b(\bar{x})| \leq Ce^{-\alpha t}.$$

The proof of Theorem 12 is based on Entropy inequalities. The study on the Lifshitz-Slyozov equations is still an active research field and open problems remain for more general assumptions on the reaction coefficients. Further results can be found in [111, 87, 112, 63, 31]

3.1.2 From Becker-Döring to Lifshitz-Slyozov system.

In [39], the authors show that the Lifshitz-Slyozov system can be obtained as an asymptotic limit of the Becker-Döring system. The leading idea to demonstrate the asymptotic equivalence is to consider the functions $(c_i(t))_{i>1}$, the solution of the Becker-Döring system, as a discretisation in space of a function $f(t,x)$, that, with a function v for the monomer concentration, solves the Lifshitz-Slyozov system. Collet et al in [39] introduced a scaling parameter ε and showed that the solution of the Becker-Döring system converges to that of the Lifshitz-Slyozov system as ε goes to 0.

In the following, we describe the main steps to get this result. We start by rewriting the Becker-Döring system in a dimensionless form. The reference quantities used to rescale are:

- T: characteristic time,
- C_1: characteristic value for the monomer concentration,
- C: characteristic value for the polymers concentrations,
- A_1: characteristic value for the polymerisation coefficient a_1,
- A: characteristic value for the polymerisation coefficients a_i $i \geq 2$,
- B: characteristic value for the depolymerisation coefficients,
- M: characteristic value for the total mass,
- M_m: mass of one monomer.

We rescale every variable by its characteristic value:

$$\bar{t} = \frac{t}{T}, \quad \bar{c}_1 = \frac{c_1(\bar{t}T)}{C_1}, \quad \bar{c}_i = \frac{c_i(\bar{t}T)}{C}, \quad \bar{\rho} = \frac{\rho}{M},$$

$$\bar{a}_i = \frac{a_i}{A}, \quad \bar{a}_1 = \frac{a_1}{A_1}, \quad \bar{b}_i = \frac{b_i}{B}, \quad \text{for } i \geq 2.$$

We define the dimensionless parameters :

$$\gamma = \frac{C}{C_1}, \quad \mu = \frac{M}{M_m C_1}, \quad \alpha = ATC_1,$$

$$\alpha_1 = \frac{A_1 C_1}{AC}, \quad \beta = BT.$$

The dimensionless form of the Becker-Döring system is then (omitting the overlines):

$$\begin{cases} \frac{d}{dt}c_i = \alpha(a_{i-1}c_1c_{i-1} - a_ic_1c_i) + \beta(b_{i+1}c_{i+1} - b_ic_i) & i \geq 2, \\ \frac{d}{dt}c_2 = \alpha_1\alpha a_1c_1^2 - \alpha a_2c_1c_2 + \beta(b_3c_3 - b_2c_2), \\ \frac{d}{dt}c_1 = -\gamma\left(2(\alpha_1\alpha c_1^2 - \beta b_2c_2) + \sum_{i=2}^{\infty}(\alpha a_ic_1c_i - \beta b_{i+1}c_{i+1})\right), \end{cases} \tag{3.5}$$

and the mass conservation is

$$c_1 + \gamma\sum_{i=2}^{\infty} ic_i = \mu\rho. \tag{3.6}$$

The dimensionless parameters γ, μ, α, α_1, β appear as coefficients in (3.5)-(3.6). Furthermore, we define the piecewise constant function $f^\varepsilon(t,x)$ as follows:

$$\begin{cases} f^\varepsilon(t,x) = c_i^\varepsilon(t) & \text{if} \quad x \in [i\varepsilon;(i+1)\varepsilon) \quad \text{for } i \geq 2,\ t > 0, \\ f^\varepsilon(t,x) = 0 & \text{if} \quad x \in [0,2\varepsilon), \end{cases}$$

where c_i^ε is the solution of the system (3.5) with the suitable choice of the dimensionless parameters [39]:

$$\gamma = \varepsilon^2, \quad \mu = 1, \quad \alpha = \beta = \frac{1}{\varepsilon}, \alpha_1 \leq 1.$$

With this choice of parameters, the rescaled version of the system (3.5)-(3.6) is:

$$\begin{cases} \frac{d}{dt}c_i = \frac{1}{\varepsilon}(a_{i-1}c_1c_{i-1} - a_ic_1c_i) + \frac{1}{\varepsilon}(b_{i+1}c_{i+1} - b_ic_i) & i \geq 2, \\ \frac{d}{dt}c_2 = \frac{1}{\varepsilon}\alpha_1a_1c_1^2 - \frac{1}{\varepsilon}a_2c_1c_2 + \frac{1}{\varepsilon}(b_3c_3 - b_2c_2), \\ \frac{d}{dt}c_1 = -\varepsilon\left(2(\alpha_1c_1^2 - b_2c_2) + \sum_{i=2}^{\infty}(a_ic_1c_i - b_{i+1}c_{i+1})\right), \end{cases}$$

and the mass conservation equation

$$c_1^\varepsilon + \varepsilon^2\sum_{i=2}^{\infty} ic_i^\varepsilon = \rho.$$

Collet et al proved in [47] that for ε close to 0, the couple $(c_1^\varepsilon, f^\varepsilon)$ is an approximate solution of the Lifshitz-Slyozov system.

Theorem 13 (First-order approximation [39]). *Assume the kinetic coefficients a_i, b_i satisfy*

$$a_i, b_i \leq K, \quad |a_{i+1} - a_i| \leq \frac{K}{i}, \quad |b_{i+1} - b_i| \leq \frac{K}{i}$$

for some constant $k > 0$. Consider a sequence $\varepsilon_n \to 0$.
Then there exist a subsequence, still denoted by ε_n, and two functions $a, b \in W^{1,\infty}((0,\infty)) \cap L^\infty(\mathbb{R}^+)$ such that

$$\lim_{\varepsilon_n \to 0} \sup_{r/\varepsilon_n < i < R/\varepsilon_n} |a_i - a(i\varepsilon_n)| + |b_i - b(i\varepsilon_n)| = 0, \quad \forall\ 0 < r < R < \infty.$$

Assume, moreover, that there exist constants $0 < s \leq 1$, $M_0 < \infty$, $\rho < \infty$, $M_s < \infty$ for which for all $\varepsilon > 0$

$$\varepsilon \sum_{i=2}^{\infty} c_i^{0,\varepsilon} \leq M_0, \qquad c_1^{0,\varepsilon} + \varepsilon^2 \sum_{i=2}^{\infty} i c_i^{0,\varepsilon} = \rho, \qquad \varepsilon \sum_{i=2}^{\infty} (i\varepsilon)^{1+s} c_i^{0,\varepsilon} \leq M_s.$$

Then the subsequence ε_n may be chosen in such a way that

$$\begin{cases} f^{\varepsilon_n} \rightharpoonup f, \quad x f^{\varepsilon_n} \rightharpoonup x f \quad in \quad C^0([0,T];\, \mathcal{M}^1(0,\infty) - weak - \star), \\ \\ c_1^{\varepsilon_n}(t) \to c_1(t) \quad uniformly\ in \quad C^0([0,T]), \end{cases}$$

where (c, f) is a solution to (3.2)-(3.3).

The space $\mathcal{M}^1(0,\infty)$ denotes the space of bounded measures on $(0,\infty)$, it is the dual of the space of continuous function on $(0,\infty)$ with compact support, namely $C_0^0(0,\infty)$. The function f is in this context a measure -valued solutions (see [37]). The proof of Theorem 13 relies on moment estimates and equicontinuity arguments. More details on the link between the Becker-Döring system and the Lifshitz-Slyozov system with different framework can be found in [88, 89, 110, 142].

Moreover, second-order approximations shed light on the link between the Becker-Döring and Fokker-Planck like equations. For example, in [39], the authors introduced the modified Lifshitz-Slyozov equations:

$$\begin{cases} \frac{\partial}{\partial_t} g + \frac{\partial}{\partial_x} G(g;t,x) &= 0, \\ \\ G(g;t,x) &= (a(x)c(t) - b(x))g(t,x) - \varepsilon \frac{\partial}{\partial_x}\left(\frac{a(x)c(t)+b(x)}{2} g(t,x)\right), \\ \\ (a(0)c(t) + b(0))g(t,0) &= 2a_1 c(t)^2, \end{cases} \tag{3.7}$$

with the mass-conservation law

$$c(t) + \int_0^\infty x g(t,x) dx = \rho.$$

The term with second derivative in space can be assimilated as a diffusion term. This diffusion term is coming from the underlying mechanisms of the discrete Becker-Döring system. The modified Lifshitz-Slyozov system with a diffusion term seems to be a more realistic continuous setting for the polymerisation/depolymerisation. Further details on the growth/fragmentation model with diffusion can be found in [161, 38, 44].

3.2 Long-time behaviour of the bi-monomeric Lifshitz-Slyozov type model.

3.2.1 Notations and framework assumptions

The model subsequently studied corresponds to the reaction network in (3.1). The chemical system is neither detailed nor complex balanced. The chemical reactions in (3.1) are not at equilibrium (not detailed balanced) and neither the complex of the chemical reactions (cf [71]).

Discrete setting. It is translated in a discrete size setting into the following infinite system of differential equations, where we denote respectively $c_i(t)$, $v(t)$ and $w(t)$ the concentrations at time t of the polymers containing i monomers, the depolymerising and the polymerising monomeric species. Without loss of generality, we assume that the smallest size of polymers n_0 is equal to 1.

$$\begin{cases} \frac{dv}{dt} = -kvw + v\sum_{i=2}^{\infty} b_i c_i, & v(0) = v_0, \\ \frac{dw}{dt} = -w\sum_{i=1}^{\infty} a_i c_i + kvw, & w(0) = w_0, \\ \frac{dc_1}{dt} = -wa_1c_1 + vb_2c_2, & c_1(0) = c_1^0 \\ \frac{dc_i}{dt} = w(-a_ic_i + a_{i-1}c_{i-1}) + v(b_{i+1}c_{i+1} - b_ic_i), & c_i(0) = c_i^0,\ i \geq 2. \end{cases} \tag{3.8}$$

As classically done for the Becker-Döring systems (e.g. [39, 7, 53]), we define the net rate at which a i-fibril is converted to a $(i+1)$-fibril by :

$$J_i = wa_ic_i - vb_{i+1}c_{i+1} \qquad 1 \leq i \leq n-1.$$

With the convention $J_0 = 0$ we can rewrite the system (3.8) as :

$$\begin{cases} \frac{dv}{dt} = -kvw + v\sum_{i=2}^{\infty} b_i c_i, & v(0) = v_0, \\ \frac{dw}{dt} = -w\sum_{i=1}^{\infty} a_i c_i + kvw, & w(0) = w_0, \\ \frac{dc_i}{dt} = J_{i-1} - J_i, & c_i(0) = c_i^0, \quad i \geq 1. \end{cases} \tag{3.9}$$

Remarks and notations : This system has two conserved quantities :

- the total concentration of polymerised fibrils $\frac{d}{dt}\left(\sum_{i=1}^{\infty} c_i\right) = 0$, due to the fact that the smallest and largest fibrils do not polymerise,

- the conservation of mass $\frac{d}{dt}\left(v + w + \sum_{i=1}^{\infty} i c_i\right) = 0$ which indicates that there is no gain or loss of particles during the chemical reaction.

We denote the total concentration of polymerised fibrils and the total mass of the system by P_0 and M_{tot}:

$$P_0 = \sum_{i=1}^{\infty} c_i^0, \qquad M_{tot} = v_0 + w_0 + \sum_{i=1}^{\infty} i c_i^0.$$

The bi-monomeric Becker-Döring type system has been extensively studied in [55]. The well-posedness has been established and the solutions of (3.9) admit a locally attractive nonnegative steady-state under some conditions on the reaction rate and the initial conditions (see [55]).

Continuous setting. We may now consider the size of clusters as a continuously varying variable $x > 0$ which now replace i. The quantity $f(t,x)$ denotes the density of aggregates of size x at time t, and $v(t)$, $w(t)$ denote the concentration of monomers. We then obtain the following equations:

$$\begin{cases} \partial_t f + \partial_x J = 0, \quad x > 0,\ t \geq 0, & f(0,x) = f^0(x), \\ J(t,x) = \Big(a(x)w(t) - b(x)v(t)\Big) f(t,x), & \\ \frac{d}{dt} v(t) = -k v(t) w(t) + v(t) \int_0^{\infty} b(x) f(t,x) dx, & v(0) = v_0 > 0, \\ \frac{d}{dt} w(t) = -w(t) \int_0^{\infty} a(x) f(t,x) dx + k v(t) w(t), & w(0) = w_0 > 0, \\ 0 = \Big(a(0)w(t) - b(0)v(t)\Big) f(t,0) \mathbb{1}_{\{a(0)w(t) - b(0)v(t) > 0\}}, & \forall t > 0. \end{cases} \tag{3.10}$$

The system (3.10) is viewed as the "macroscopic" limit of the system (3.9). The connection between these two models is similar to the link between the Becker-Döring system and its Lifshitz-Slyozov limit which has been investigated in [39, 53, 89].
Moreover the solutions of the system (3.10) follows a conservation law of the total mass M of the population:

$$v(t) + w(t) + \int_0^{\infty} x f(t,x) dx = v_0 + w_0 + \int_0^{\infty} x f^0(x) dx = M. \tag{3.11}$$

We denote the moment of magnitude n by M_n:

$$M_n(t) = \frac{1}{n}\int_0^\infty x^n f(t,x)dx, \tag{3.12}$$

and the total number of polymers by ρ:

$$\rho(t) = \int_0^\infty f(t,x)dx.$$

The last equation of (3.10) is a boundary condition depending on the assumptions on the reaction coefficients $a(x)$, $b(x)$. This condition can be interpreted as the absence of the nucleation phenomenon and implies that total concentration of polymerised fibrils remain constant.

Lemma 4. *Let $(v,w,f) \in \mathcal{C}^1_b(\mathbb{R}_+)\times\mathcal{C}^1_b(\mathbb{R}_+)\times\mathcal{C}\left(\mathbb{R}_+, L^1\right)$ be any nonnegative solution of* (3.10) *and $a,b \in \mathcal{C}^1(\mathbb{R}_+)$ such that $a(0)w(t) > b(0)v(t) \quad \forall t > 0$. Then the total number of polymers is constant:*

$$\rho(t) = \int_0^\infty f(t,x)dx = \int_0^\infty f_0(x)dx := \rho_0.$$

The Lemma 4 is proved by a simple integration. We note that the boundary condition is needed for (3.10) to be well-posed only when $a(0)w(t) > b(0)v(t)$.

We are interested in the steady-state. We denote with $(v_\infty, w_\infty, f^\infty)$ the quantities at equilibrium. In the discrete size-setting, the solutions admits damped oscillations and converge locally towards a nonnegative steady-state under the correct assumptions. In the continuous size-setting, we denote two kinds of steady-state:

- the trivial steady-states: $f^\infty(x) = 0$ and $v_\infty + w_\infty = M$. It corresponds to a boundary steady-state and can be interpreted as the non pathological equilibrium. All fibrils are converted into the two species of monomers and the two species of monomers are at equilibrium.
- The nontrivial steady-state which enforces the following: there exists $x > 0$ such that $f^\infty(x) \neq 0$. It can be interpreted as the pathological steady-state since polymers can be found at equilibrium.

3.2.2 Main results

We note that the system in (3.10) is a coupled PDE/ODE system. The ODE part of the system is the following:

$$\begin{cases} \frac{d}{dt}v(t) &= -kv(t)w(t) + v(t)\int_0^\infty b(x)f(t,x)dx, \\ \\ \frac{d}{dt}w(t) &= -w(t)\int_0^\infty a(x)f(t,x)dx + kv(t)w(t). \end{cases} \tag{3.13}$$

The solution of the PDE in (3.10) has an influence on the solutions of the ODE through an integral term. However, assuming some rightfully chosen hypothesis on the reaction coefficients $a(x)$ and $b(x)$, the

system (3.10) has 2 conserved quantities:

- $v(t) + w(t) + \int_0^\infty x f(t,x)dx = M$,
- $\int_0^\infty f(t,x)dx = \rho_0$.

In order for the ODE system to be decoupled of the PDE solution in (3.10), the reaction coefficient functions have to be either constant, linear or affine function of the size variable $x > 0$. This comes from the fact that the integral terms in (3.13) are replaced by one of the conserved quantities.

In the following we restrict ourselves to the following assumptions on the reaction coefficients:

- the reaction coefficients are linear, $a(x) = ax$ and $b(x) = bx$ with $a, b > 0$,
- the reaction coefficients are constant, $a(x) = a$ and $b(x) = b$ with $a, b > 0$,
- one of the coefficient is linear and the other is constant.

An interesting result can be obtained if we suppose that the reaction rates are both linear:

$$\exists a,\ b > 0, \quad a(x) = ax, \quad b(x) = bx.$$

In this case, the solutions (v, w) of (3.13) are periodic as well as the solution f of (3.10). We obtain the following result.

Proposition 1. *Let $(v, w, f) \in \mathcal{C}_b^1(\mathbb{R}_+) \times \mathcal{C}_b^1(\mathbb{R}_+) \times \mathcal{C}\left(\mathbb{R}_+, L^1\right)$ be any nonnegative solution of* (3.10) *and* (3.11) *such that the initial datum verifies $v_0, w_0 > 0$ and $w_0 + w_0 < M$. Assume that $a, b \in \mathcal{C}^1(\mathbb{R}_+)^+$ satisfy* (3.16)*. Then the following statements hold true:*

1. *The solutions $v(t), w(t)$ of* (3.17) *are periodic of the same period.*
2. *The solution f of* (3.10) *is periodic of the same period as $v(t)$, $w(t)$.*

The proof of this proposition is detailed in Section 3.3. This result shows that the solution of the bi-monomeric Lifshitz-Slyozov model (3.10) are periodic when the size-dependency ratio is constant. The size-dependency ratio is formalised as

$$\frac{\text{polymerisation rate}}{\text{depolymerisation rate}}(x).$$

We obtain periodic solutions $v(t)$ and $w(t)$ of the same period. Hence the transport term of the PDE of (3.10) is a periodic function and its integral in time over one period is null. Such a result is not observed in the experiment since the continuous model is a first order approximation of the "true" discrete model. The second order correction, a diffusion term, would dominate and change the behaviour of the solutions.

Moreover, even without the second order correction (the diffusion term), we show that the solutions of System (3.10) display damped oscillations and f concentrates its mass at a critical size when the size-dependency ratio is decreasing. The equation for f in (3.10) is a non-linear transport equation. The characteristic curves defined below are closely related to the asymptotic behaviour of f.

Definition 5. *(Characteristic curves). Given $z \in [0,\infty)$, let $X : [0,\infty)^2 \to [0,\infty)$ be the $\mathcal{C}^1$ solution of*

$$\frac{d}{dt}X(t,z) = a(X(t,z))w(t) - b(X(t,z))v(t), \quad X(0,z) = z. \tag{3.14}$$

We also recall some classical formulae on the characteristic curves:

- The expression of the solution in terms of the characteristic curves:

$$f(t,X(t,z)) = f_0(z)\exp\left\{\int_0^t b'(X(s,z))v(s) - a'(X(s,z))w(s)ds\right\}.$$

- The derivation in size of the characteristic curve:

$$\frac{\partial X(t,z)}{\partial_z} = \exp\left\{\int_0^t a'(X(s,z))w(s) - b'(X(s,z))v(s)ds\right\}.$$

Let

$$b > 0 \quad a(x) = 1,\ b(x) = bx,\ \forall x > 0. \tag{3.15}$$

Using the characteristic curves, we obtain the following asymptotic result.

Theorem 14 (Concentration at a critical size)**.** *Let the initial data satisfies $v_0, w_0 > 0$ and $v_0 + w_0 < M$ and $f_0 \in L^1(\mathbb{R}_+, (1+x^2)dx)$ with $\rho_0 = \int_0^\infty f_0(x)dx > 0$. Moreover let $k > 1$ with k large and $0 < \rho_0 < kM$. And finally, assume that $a, b \in \mathcal{C}^1(\mathbb{R}_+)^+$ satisfy* (3.15)*.*
The solution $(v,w,f) \in \mathcal{C}_b^1(\mathbb{R}_+) \times \mathcal{C}_b^1(\mathbb{R}_+) \times \mathcal{C}\left(\mathbb{R}_+, L^1\right)$ to the system (3.10) *and* (3.11) *satisfies*

1. *for all $z \geq 0$,*
$$\int_0^\infty |X(t,z) - x|^2 f(t,x)dx \leq e^{-2bC_0 t}\int_0^\infty |z-x|^2 f_0(x)dx,$$

2. $\lim_{t\to\infty} v(t) = v_\infty = \frac{\rho_0}{k}$, $\lim_{t\to\infty} w(t) = w_\infty = \frac{b}{k+b}\left(M - \frac{\rho_0}{k}\right)$ *and* $\lim_{t\to\infty} X(t,z) = \frac{w_\infty}{bv_\infty}$, *with*
$$|X(t,z) - \tfrac{w_\infty}{bv_\infty}|^2 \leq Ce^{-\gamma t},$$
where $\gamma > 0$ is a nonnegative rate of convergence depending on the initial conditions (v_0, w_0, ρ_0), the reaction coefficients k, b and $C > 0$ is a constant,

3. *$f(t,x)$ converges to $\rho_0\delta_{\frac{w_\infty}{bv_\infty}}$ exponentially fast in the sense of the Wasserstein distance: for $z \geq 0$ and some constant $C > 0$ we have*
$$W_2\left(f(t,\cdot), \rho_0\delta_{\frac{w_\infty}{bv_\infty}}\right) \leq Ce^{-\beta t},$$

where $\beta > 0$ is a nonnegative rate depending on the rate γ, the initial conditions (v_0, w_0, ρ_0), the reaction coefficients k, b and $C > 0$ is a constant.

The proof of Theorem 14 is detailed in Section 3.4. It relies on an entropy inequalites, inspired by [27], and local convexity estimates for a Lyapunov functional, inspired by [55]. This result shows that the solution of the bi-monomeric Lifshitz-Slyozov system converges to a specific steady-state

$$(v(t), w(t), f(t,\cdot)) \quad \xrightarrow[t\to\infty]{} \quad \left(v_\infty, w_\infty, \rho_0 \delta_{\frac{w_\infty}{b v_\infty}}\right).$$

3.3 Sustained oscillations for the bi-monomeric Lifshitz-Slyozov system.

In this section we show that solutions of (3.10) are oscillating for linear reaction coefficients, hence the solutions are not converging toward a steady state.

Linear coefficients. We first assume the reaction coefficients to be linear:

$$a, b > 0 \quad a(x) = ax,\ b(x) = bx,\ \forall x > 0. \tag{3.16}$$

Using the mass conservation (3.11) and the hypothesis on the reaction coefficients (3.16), the variables (v, w) are solutions of the following closed system:

$$\begin{cases} \frac{dv}{dt} = v\Big(bM - bv - (k+b)w\Big), \quad v(0) = v_0 > 0, \\ \\ \frac{dw}{dt} = w\Big(-aM + (k+a)v + aw\Big), \quad w(0) = w_0 > 0 \end{cases} \tag{3.17}$$

Remark 13. *We note that the system obtained in* (3.17) *is a quadratic Lotka-Volterra system for two species v, w (cf [70]). The system* (3.17)*, in its rewritten form, is actually known under other names such as the Ivanova system [162] or the reduced Belousov-Zhabothinsky system [125]:*

$$\mathcal{V} + \mathcal{W} \to 2\mathcal{W}, \quad \mathcal{W} + \mathcal{M}_1 \to 2\mathcal{M}_1, \quad \mathcal{M}_1 + \mathcal{V} \to 2\mathcal{V}.$$

These chemical reactions lead to a differential system of size three where the species have a circular cooperative/competitive connections as in the classical Lotka-Volterra system. We recover System 3.17 using the mass conservation laws $v(t) + w(t) + M_1(t) = M$ and rewriting $M_1(t) = M - v(t) - w(t)$. We also note that the trivial steady-state of the system are $(0,0)$, $(0,M)$, $(M,0)$ and the non-trivial steady state is the unique solution

(v_∞, w_∞) *of the isoclines :*

$$\begin{cases} M = v + \frac{k+b}{b} w, \\ M = \frac{k+a}{a} v + w, \end{cases}$$

and therefore $(v_\infty, w_\infty) = \left(\frac{a}{k+b+a} M, \frac{b}{k+b+a} M\right)$.

We can now prove the existence of oscillatory solutions for the system (3.10).

Proof.[Proposition 1.] The proof of the periodic solution of System (3.17) is classical and can be found in Chapter 12 [162]. It uses the fact that the trajectories are included in closed curves. We recall the proof. We denote by $\mathcal{S}$ the convex open set

$$\mathcal{S} = \{(x, y) \in \mathbb{R}^2 \mid x > 0,\ y > 0,\ M > x + y\}.$$

The set $\mathcal{S}$ is the set of admissible solutions of (3.17). Some computations give us the relation:

$$\Phi(v(t), w(t)) = (M - v(t) - w(t))^k v(t)^a w(t)^b = (M - v_0 - w_0)^k v_0^a w_0^b = c_0 > 0. \tag{3.18}$$

The function Φ vanishes on the boundary of $\mathcal{S}$ and take its maximal value at an interior point Φ_0 of $\mathcal{S}$. Therefore the trajectories of the form (3.18) are closed curves in the (v, w)-plane for $0 < c_0 < \Phi_0$ and one readily check that the velocity cannot vanish. Then the solution of (3.17) are periodic and we denote their period by $T \geq 0$.
To prove the second item, we use the method of characteristics to express f as a function of v and w:

$$f(t, X(t, x)) = f_0(x) \exp\left(\int_0^t bv(s) - aw(s) ds\right).$$

Moreover using the fact that v and w are periodic of period T, we get:

$$\begin{aligned} \int_0^T \frac{1}{v(s)} \frac{d}{dt} v(s) ds = & \quad bMT - b\int_0^T v(s) ds - (k+b)\int_0^T w(s) ds, \\ \ln(v(T)) - \ln(v(0)) = & \quad bMT - b\int_0^T v(s) ds - (k+b)\int_0^T w(s) ds, \\ 0 = & \quad bM - b\frac{1}{T}\int_0^T v(s) ds - (k+b)\frac{1}{T}\int_0^T w(s) ds. \end{aligned}$$

We denote $\tilde{v} = \frac{1}{T}\int_0^T v(s) ds$ and $\tilde{w} = \frac{1}{T}\int_0^T w(s) ds$, using the same argument for $\tilde{w}$, we obtain the following system:

$$\begin{cases} bM = b\tilde{v} + (k+b)\tilde{w}, \\ aM = (k+a)\tilde{v} + a\tilde{w}. \end{cases}$$

Then $(\tilde{v},\tilde{w}) = \left(\frac{a}{k+b+a}M, \frac{b}{k+b+a}M\right)$, and

$$\int_0^T aw(s) - bv(s)ds = 0. \tag{3.19}$$

Since (3.19) is verified, f is a periodic function of the same period T as v an w. ■

3.4 Damped oscillations and concentration at a critical size.

In this section, we consider that the depolymerization dominates i.e. the depolymerization coefficient is linear with respect to the size whereas the polymerization coefficient is constant:

$$a(x) = 1 \quad b(x) = bx, \quad b > 0,\ x \geq 0.$$

The size-dependency-ratio is then decreasing.

3.4.1 Asymptotic behaviour of the decoupled dynamical system

Using the lemma 4 and the hypothesis on the reaction coefficients (3.15), the variables (v,w) are solutions of the following quadratic Lotka-Volterra system:

$$\begin{cases} \frac{dv}{dt} = v(bM - bv - (k+b)w), & v(0) = v_0 > 0, \\ \\ \frac{dw}{dt} = w(kv - \rho_0), & w(0) = w_0 > 0. \end{cases} \tag{3.20}$$

Theorem 15. *Let $(v,w,f) \in \mathcal{C}^1_b(\mathbb{R}_+) \times \mathcal{C}^1_b(\mathbb{R}_+) \times \mathcal{C}\left(\mathbb{R}_+, L^1\right)$ be any nonnegative solution of (3.10) and (3.11) such that the initial datum verifies $v_0, w_0 > 0$ and $v_0 + w_0 < M$. Assume that $a, b \in \mathcal{C}^1(\mathbb{R}_+)^+$ satisfy (3.15). Let $k > 1$ with k large enough and $0 < \rho_0 < kM$.*
Then the following statements hold true:

1. *$0 < v(t) < M$ and $0 < w(t) < M$ for any t.*
2. *The function $F : (0,\infty)^2 \mapsto \mathbb{R}$ such that*

$$F(v,w) = k(v - v_\infty \ln(v)) + (k+b)(w - w_\infty \ln(w))$$

   is a Lyaponuv function and for all $k \geq 1$ $(v(t),w(t))$ is converging towards the steady-state $(v_\infty, w_\infty) = \left(\frac{\rho_0}{k}, \frac{b}{k+b}(M - \frac{\rho_0}{k})\right)$.
3. *For $k \gg 1$, every solutions $(v(t),w(t))$ to (3.20) converge exponentially fast toward the positive equilibrium (v_∞, w_∞), i.e.*

$$|v - v_\infty|^2 + |w - w_\infty|^2 \leq Ce^{-\alpha t}, \tag{3.21}$$

where $\alpha > 0$ is a nonnegative rate only depending on the initial conditions (v_0, w_0), the reaction coefficients k, b and $C > 0$ is a constant.

Remark 14. *Note that the condition $0 < \rho_0 < kM$ is necessary to establish the existence of a positive steady-state. We recall that the positive steady-state is assimilated to the pathological cases with the existence of prion fibrils at equilibrium. Moreover, if $\rho_0 \geq kM$ then the solutions of System 3.20 admit a locally linearly attractive boundary steady-state $(v_\infty, w_\infty) = (M, 0)$. Hence, the last inequality translates the fact that if only small assemblies and monomers are present initially, the solutions are locally attracted towards a healthy case where the fibrils depolymerise and only monomers remain at equilibrium.*

Proof. [Theorem 15.] We first focus on the proof of the first item. The positivity of the solutions $v(t)$, $w(t)$ follows from the computations:

$$\frac{dv}{dt} = v\,(bM_1(t) - kw),$$
$$v(t) \geq v_0 \exp\left(\int_0^t bM_1(s) - kw(s)ds\right) > 0,$$

and similarly

$$w(t) \geq w_0 \exp\left(\int_0^t kv(s) - \rho_0 ds\right) > 0.$$

The positivity of the solutions $v(t)$, $w(t)$ and the mass conservation equation (3.11) imply that the upper bound is verified for $v(t)$ and $w(t)$.

Proof of 2. We note that the following function $F : (0,\infty)^2 \to \mathbb{R}$ is a Lyapunov functional for the solution of (3.20):

$$F(v,w) = k(v - v_\infty \ln(v)) + (k+b)(w - w_\infty \ln(w)),$$

since we have

$$\frac{d}{dt}F(v,w) = -kb(v - v_\infty)^2.$$

Hence the solution (v,w) converges to the invariant subset of K:

$$K = \{\frac{d}{dt}F = 0\} = \{(x,y) \in \mathbb{R}^2 |\, x = v_\infty,\ y > 0\}.$$

Though the ω-limit set reduces to the only positive steady-state (v_∞, w_∞). This conclude the proof of the second item.

Proof of 3. The proof of exponential convergence towards the positive steady-state is based on the dissipation of the Lyapunov functional $F(v(t), w(t))$ and local convexity estimates when the time derivative of the Lyapunov functional is null as it was used in [55]. The proof is postponed in the Appendix 3.5.1. Let us briefly summarize the main step of the proof. For the sake of clarity, we suppose that the parameter b of the depolymerisation rate is equal to 1 in the proof. We first rescale our system with the parameter

$\varepsilon = \frac{1}{k}$. The main issue, for both the system and its rescaled form, is coming from the fact that the time derivative of the Lyapunov is equal to 0 on a straight line of the phase portrait:

$$v(t) = v_\infty \implies \frac{d}{dt}F(v(t), w(t)) = 0.$$

In order to prove that the solutions do not get stuck on this degeneracy line, we establish local estimates which prove that the trajectory of the solutions does not get stuck on the line but crosses it. The condition to prove the existence of such estimates is based on the assumptions $0 < \rho_0 < kM$ and $k > 1$ with k large enough. $\rho_0 < kM$ can be interpreted as the following: either there is enough polymerised assemblies to ignite the chemical reactions or few polymers assemblies are initially present and the reaction rate which governs the exchange between the two monomeric species is large. The last interpretation implies a strong competition between the monomeric species.
Finally, we obtain an exponential convergence towards the positive steady-state with rate r for the rescaled system (r is of order $\frac{1}{k}$). Since the solution of the rescaled system converges exponentially fast, we deduce that the solution of the original system (3.20) also converges towards its equilibrium exponentially fast. We denote α its exponential rate of convergence, hence α depends on the scale parameter $\frac{1}{k}$, the initial conditions. ■

We obtain the convergence of the trajectory (w, v) towards a positive steady-state (w_∞, v_∞).

3.4.2 Asymptotic behaviour for the PDE

The study of the asymptotic behaviour and the techniques used are inspired by [27]. We recall the characteristics for the specific reaction coefficients (3.15):

$$\frac{d}{dt}X(t,z) = w(t) - bv(t)X(t,z), \quad X(0,z) = z \quad \text{for} \quad z \geq 0,$$

and we have the implicit formula

$$X(t,z) = \left(z + \int_0^t w(s)\exp\left\{\int_0^s bv(\sigma)d\sigma\right\}ds\right)\exp\left\{\int_0^t -bv(s)ds\right\}.$$

Lemma 5. *Under the assumptions of Theorem 15, let $(v, w, f) \in \mathcal{C}_b^1(\mathbb{R}_+)\times\mathcal{C}_b^1(\mathbb{R}_+)\times\mathcal{C}\left(\mathbb{R}_+, L^1\right)$ be any nonnegative solution of* (3.10) *and* (3.11) *such that $0 < \int f(0,x)dx < kM$. Then the following statements hold true:*

1. *there is a constant $C_0 > 0$ depending only on the initial conditions (v_0, w_0) such that $C_0 < v(t)$, $C_0 < w(t)$ for $t > 0$,*

2. *the characteristics always remain bounded:*

$$X(t,z) \leq z + \tfrac{M}{bC_0},$$

3. *let* $\int_0^\infty x^s f_0(x)dx < \infty$ *for* $s > 0$ *then* $\int_0^\infty x^s f(t,x)dx < \infty$.

Proof.[Lemma 5] **Proof of item 1**: Since v and w are continuous functions such that $v(t) > 0,\ w(t) > 0$ with $t \in [0,T]$ for any finite time T and since

$$(v(t), w(t)) \xrightarrow[t\to\infty]{} (v_\infty, w_\infty) \in (\mathbb{R}_+^*)^2$$

then it exists a constant $C_0 > 0$ such that $C_0 < v(t),\ C_0 < w(t)$ for $t > 0$.

Proof of item 2: thanks to (3.15) and the first item, we have

$$\tfrac{dX(t,z)}{dt} \le w(t) - bC_0 X(t,z).$$

Hence

$$X(t,z) \le e^{-bC_0 t}\left(z + \int_0^t w(s)e^{bC_0 s}ds\right) \le z + \tfrac{M}{bC_0}.$$

Proof of item 3. We use the characteristics to represent the solutions as

$$f(t, X(t,z)) = f_0(z)\exp\left\{\int_0^t bv(\tau)d\tau\right\}. \tag{3.22}$$

We also note that

$$\frac{\partial X(t,z)}{\partial z} = \exp\left\{-\int_0^t bv(\tau)d\tau\right\}. \tag{3.23}$$

We define the characteristics in $\mathbb{R}_-$ then we define $\bar{z}(t)$, the value such that $X(t,\bar{z}) = 0$. Then we proceed to a change of variables using (3.22) and (3.23),

$$\begin{aligned}\int_0^\infty x^s f(t,x)dx &= \int_{\bar{z}(t)}^\infty X(t,z)^s f(t,X(t,z))\frac{\partial X(t,z)}{\partial z}dz\\ &= \int_{\bar{z}(t)}^\infty X(t,z)^s f(t,X(t,z))\exp\left\{-\int_0^t bv(\tau)d\tau\right\}dz\\ &= \int_{\bar{z}(t)}^\infty X(t,z)^s f_0(z)dz \le \int_0^\infty \left(z + \tfrac{M}{bC_0}\right)^s f_0(z)dz\end{aligned}$$

where we used the second item for the last step. ∎

Lemma 6 (Concentration of the mass along the characteristic curves)**.** *Under the assumptions of Lemma 5, let us define, for any* $z \ge 0$

$$g(t,z) = \int_0^\infty f(t,x)|X(t,z) - x|^2 dx.$$

We have

$$g(t,z) \leq g(0,z)e^{-2bC_0 t}.$$

Proof.[Proof of Lemma 6] An immediate calculation gives

$$\begin{aligned}\frac{d}{dt}g(t,z) &= \int_0^\infty \tfrac{\partial}{\partial_t}(f(t,x))|X(t,z)-x|^2 + 2f(t,x)\tfrac{d}{dt}(X(t,z))(X(t,z)-x)dx \\ &= \int_0^\infty \Big(\tfrac{\partial}{\partial_x}[(bv(t)x-w(t))f(t,x)]|X(t,z)-x|^2 \\ &+ 2f(t,x)(w(t)-bv(t)X(t,z))(X(t,z)-x)\Big)dx.\end{aligned}$$

Then after integrating by part, we obtain:

$$\begin{aligned}\frac{d}{dt}g(t,z) &= \int_0^\infty 2f(t,x)\Big[(bv(t)x-w(t))(X(t,z)-x) \\ &\quad + 2f(t,x)(w(t)-bv(t)X(t,z))(X(t,z)-x)\Big]dx \\ &= -2bv(t)g(t,z) \leq -2bC_0 g(t,z).\end{aligned}$$

Then $g(\cdot,z) \in L^1_t(0,\infty)$with the announced decay. ∎

Proof.[Theorem 14.] **Proof of 1.** The first point of the theorem is proved by Lemma 6 and shows that the mass concentrates along any characteristic curve.

Proof of 2. Theorem 15 gives the convergence of the monomeric species $(v(t),w(t))$ towards the steady-state (v_∞,w_∞). We now prove the convergence of the characteristic curves using theorems on asymptotically autonomous system [97, 156]. We denote by $X(t,z)$ a characteristic curve of (3.10) with initial data z at time 0:

$$\tfrac{d}{dt}X(t,z) = w(t)-bv(t)X(t,z) = h(t,X(t,z)), \quad X(0,z) = z \geq 0. \tag{3.24}$$

We note that the characteristic curves are defined by an asymptotically autonomous differential equation (see Appendix 3.5.2). Then we get the limit differential equation:

$$\tfrac{d}{dt}y(t) = w_\infty - bv_\infty y(t). \tag{3.25}$$

Hence for any positive initial data $y_0 > 0$, the solution $y(t)$ of (3.25) converges exponentially fast toward

$\frac{w_\infty}{bv_\infty}$:

$$\lim_{t\to\infty} y(t) = \frac{w_\infty}{bv_\infty}, \quad |y(t) - \frac{w_\infty}{bv_\infty}|^2 \le Ce^{-2bv_\infty t} \quad \text{for} \quad t \ge 0,$$

where $C = C(b, v_\infty, w_\infty, y_0) > 0$. Moreover, thanks to Theorem 1.2 in [156], we get

$$\lim_{t\to\infty} X(t,z) = \frac{w_\infty}{bv_\infty}.$$

Using the exponential convergence in the euclidian distance of $(v(t), w(t))$ toward the positive steady-state (cf Theorem 15) and the exponential convergence for the limit differential equation of the characteristics, we deduce that the characteristics converge exponentially fast toward $\frac{w_\infty}{bv_\infty}$, i.e.

$$|X(t,z) - \frac{w_\infty}{bv_\infty}|^2 \le Ce^{-\gamma t}.$$

We denote $\gamma > 0$ the positive rate of convergence which depends on the rate α, the reaction coefficients k, b and the initial conditions. $C > 0$ is a constant. *(Further details and results on the convergence rate β is currently under study.)*

Proof of 3. We recall the Wasserstein distance, let $g_1, g_2 \in L^1(0,\infty)$. The Wasserstein distance W_2 between g_1 and g_2 is defined as follows:

$$W_2(g_1,g_2) := \left(\int_0^\infty \int_0^\infty |x-y|^2 g_1(x) g_2(y) dx dy\right)^{\frac{1}{2}}.$$

We write,

$$\begin{aligned} W_2\left(f(t,\cdot), \rho_0 \delta_{\frac{w_\infty}{bv_\infty}}\right) &\le \left(\int\int |x-y|^2 \rho_0 \delta_{\frac{w_\infty}{bv_\infty}}(y) f(t,x) dy dx\right)^{1/2}, \\ &\le \left(\int |x - \tfrac{w_\infty}{bv_\infty}|^2 \rho_0 f(t,x) dx\right)^{1/2}, \\ &\le \left(2|X(t,z) - \tfrac{w_\infty}{bv_\infty}|^2 \rho_0^2 + 2\int |X(t,z) - x|^2 \rho_0 f(t,x) dx\right)^{1/2}. \end{aligned}$$

Using Lemma 6 and the exponential convergence of the characteristics in item 2 of this proof, we get

$$W_2\left(f(t,\cdot), \rho_0 \delta_{\frac{w_\infty}{bv_\infty}}\right) \le Ce^{-\beta t},$$

where $\beta > 0$ is the rate of convergence such that $\beta = \min(\gamma/2, bC_0)$ and $C > 0$ is a constant. This conclude the proof of Theorem 14. ∎

Discussions and perspectives

In this Chapter, we propose a bi-monomeric, nonlinear Lifshitz-Slyozov-type system. It extends the previous work in [55] in a continuous size setting. The results on the asymptotic behaviour of the continuous model differ from those of the discrete model, mainly because an underlying diffusion process takes place in the discrete model. We study the first-order approximation of the continuous model which neglects the diffusion term. An interesting perspective is to work on the second order approximation which includes a diffusion term in the continuous size-setting.
Furthermore, the study of the behaviour of the PDE is performed in the case of linear reaction coefficients and in the case of one linear and one constant reaction coefficient. These choices were motivated by experimental data from biologists. The static light scattering (SLS) signals studied show a fall for the second moment of the size distribution of polymers in a closed in vitro environment. This observation strongly suggests the size-dependency ratio is decreasing, i.e. the depolymerisation dominates the polymerisation. However, considering more general forms of reaction coefficients leads to interesting new mathematical problems .
Several questions remain open: What is the convergence rate to equilibrium ? How to rigorously prove the existence of damped oscillations when the concentration converges to a critical mass ? What is the correct framework (assumptions on the reaction coefficients, on the initial data, etc) to establish well-posedness of the system ?
The next step is to propose and study numerical scheme to approximate the solutions of this coupled ODE-PDE systems. The numerical analysis, in the spirit of [14, 31, 59], illustrates the results on the asymptotic behaviour and gives more insights and a better understanding of the model.
Finally, much remains to be done before reaching a fully quantitative model of the polymerisation/depolymerisation process of prion fibrils: integrating the proposed reaction scheme in a more complete model (e.g. where linear depolymerisation is added), considering other structure of fibrils (where the elementary block unit is a dimer or a trimer) and other forms of reaction coefficients (power functions of size, etc), experimental evidence and quantitative comparison through data assimilation strategies.

Acknowledgments. M.M. has been supported by the ERC Starting Grant SKIPPER^{AD} (number 306321). The author is thankful for the precious comments and discussions with Klemens Fellner and Carsten Wiuf. The author thanks a lot Marie Doumic for her precious help and her corrections.

3.5 Supplementary and appendix

3.5.1 Exponential convergence in the theorem 15

In this section, we study the system of differential equations (3.20) assuming the reaction coefficients follow (3.15). We prove that the solutions of (3.20) converge exponentially to the positive equilibrium for a sufficiently small parameter $\varepsilon = \frac{1}{k}$. The parameter b is set to $b = 1$ for the sake of the clearest possible

presentation. We obtain the following system:

$$\begin{cases} \frac{dv}{dt} = v(M - v - (k+1)w), \\ \\ \frac{dw}{dt} = w(kv - \rho_0). \end{cases} \tag{3.26}$$

This system has the equilibrium:

$$v_\infty = \frac{\rho_0}{k}, \quad w_\infty = \frac{1}{k+1}\left(M - \frac{\rho_0}{k}\right),$$

and $(v_\infty, w_\infty) > 0$ provided that $0 < \rho_0 < kM$. If $\rho_0 \geq kM$, one checks that the boundary steady-state (M, O) is linearly locally stable. We observe that the equilibrium (v_∞, w_∞) takes values of order $\varepsilon := \frac{1}{k}$. This suggests the rescaling

$$v \to \frac{v}{k} = \varepsilon v, \quad \text{and} \quad w \to \frac{w}{k} = \varepsilon w$$

and yields the rescaled equilibrium values

$$v_\infty = \rho_0, \quad w_\infty = \frac{1}{1+\varepsilon}(M - \varepsilon\rho_0). \tag{3.27}$$

By using (3.27), System (3.26) rescales to the following system, which we shall study subsequently:

$$\begin{cases} \frac{dv}{dt} = v(w_\infty - w) - \varepsilon v(v - v_\infty + w - w_\infty), \\ \\ \frac{dw}{dt} = w(v - v_\infty). \end{cases} \tag{3.28}$$

We point out that the rescaled system (3.28) in the limiting case $\varepsilon = 0$ constitutes the classical Lotka-Volterra system.
The following theorem proves large-time convergence to the positive equilibrium (v_∞, w_∞) by using a Lyapunov functional of System (3.28).

Theorem 16. *(Exponential convergence to positive equilibrium)*

Consider $\rho_0 \in (0, kM)$ and hence a positive equilibrium $(v_\infty, w_\infty) > 0$.
Then the functional H

$$H(v, w) = v - v_\infty \log v + (1 + \varepsilon)(w - w_\infty \log w)$$

is a Lyapunov functional for the system (3.28) *with a decay rate of order ε. More precisely,*

$$\frac{d}{dt}H(v(t), w(t)) = -\varepsilon(v(t) - v_\infty)^2. \tag{3.29}$$

Moreover, for ε sufficiently small, every solution $(v(t), w(t))$ to (3.28) *subject to positive initial data $(v_0, w_0) >$*

0 *converges exponentially to the positive equilibrium* (v_∞, w_∞)*, i.e.*

$$|v - v_\infty|^2 + |w - w_\infty|^2 \leq C(H_0 - \bar{H})e^{-\varepsilon r t}, \tag{3.30}$$

where the positive rate r and constant C depend only on the initial value of the Lyapunov $H_0 := H(v_0, w_0)$ *and the values of the positive equilibrium* (v_∞, w_∞)*.*

Proof. The decay of the functional (3.29) follows from direct calculations when evaluating H along the flow of (3.28).
In the following, we proved the exponential convergence (3.30) via a modified entropy method introduced in [54]. We note that the Lyapunov functional H has a line of degeneracy, i.e. a straight line through the equilibrium where the time derivative of the Lyapunov functional vanishes:

$$\tfrac{d}{dt}H(v, w) = 0 \quad \Longleftrightarrow \quad v = v_\infty,\ w \in (0, M). \tag{3.31}$$

In order to prove the exponential convergence to the equilibrium in such a case, we shall provide estimates which show that all solution trajectories pass through this line of degeneracy with positive speed.

We first observe from (3.28) that the null-cline $\dot{v} = 0$ is also a straight line, which passes through the equilibrium:

$$\dot{v} = 0 \quad \Longleftrightarrow \quad w - w_\infty = -\lambda_\varepsilon(v - v_\infty), \quad \lambda_\varepsilon := \tfrac{\varepsilon}{1+\varepsilon} < 1.$$

Next, we introduce a line $W_{\lambda-}$ between $\dot{v} = 0$ and $v = v_\infty$ with a slope $-\lambda$ with $\lambda > \lambda_\varepsilon$ to be chosen later:

$$W_{\lambda-}: \quad w - w_\infty = -\lambda(v - v_\infty), \qquad \lambda > \lambda_\varepsilon.$$

Similarly, on the opposite side of $v = v_\infty$ we define the line $W_{\lambda+}$:

$$W_{\lambda+}: \quad w - w_\infty = \lambda(v - v_\infty), \qquad \lambda > \lambda_\varepsilon.$$

Moreover, we denote $W_{\lambda-}(v)$ (respectively $W_{\lambda+}(v)$) the coordinate w such that $w = w_\infty - \lambda(v - v_\infty)$ (resp.$w = w_\infty + \lambda(v - v_\infty)$). In the following, we denote by $\triangle_\lambda^+$ the convex cone in the phase space $(v, w) \in \mathbb{R}^2_+$, which is defined by the interior between the lines $W_{\lambda-}$, $W_{\lambda+}$ and above the line $w = w_\infty$. Note that on $\triangle_\lambda^+$ we have $w_\infty < w$ and $\dot{v} < 0$. Analogously, the open triangle $\triangle_\lambda^-$ is defined as the interior of the lines $W_{\lambda+}$, $W_{\lambda-}$ and under the line $w = w_\infty$, i.e. we consider $0 < w < w_\infty$ and $\dot{v} > 0$.

Hence, we shall detail the estimates on the convex cone $\triangle_\lambda^+$ for $w_\infty < w$, while the estimates for $\triangle_\lambda^-$ follow analogously (e.g. by exchanging the variables v and w). We denote

$$p(t) := v(t) - v_\infty \quad \text{and} \quad \tfrac{d}{dt}H(v(t), w(t)) = -\varepsilon p^2(t).$$

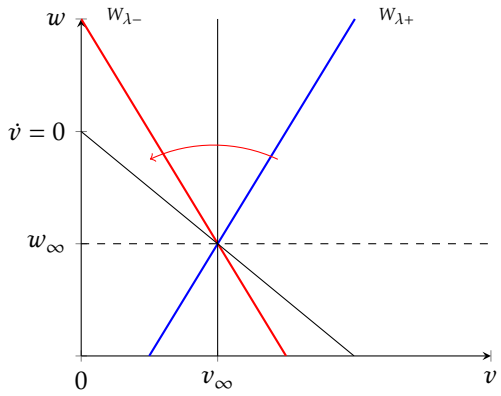

Figure 3.1 – Phase space for the system (3.28)

We first observe that

$$-\tfrac{1}{\lambda}(w-w_\infty) \le p \le \tfrac{1}{\lambda}(w-w_\infty).$$

Moreover, we point out that $\triangle_\lambda^+$ is the closed union of two convex subcones:

$$\{v > v_\infty\} \cap \triangle_\lambda^+ \quad \text{and} \quad \{v < v_\infty\} \cap \triangle_\lambda^+.$$

The sign of $\dot{w}$ is constant on the two subcones but changes in their common boundary ($\dot{w} > 0$ in $\{v > v_\infty\} \cap \triangle_\lambda^+$ and $\dot{w} < 0$ in $\{v < v_\infty\} \cap \triangle_\lambda^+$). Hence, whenever a solution trajectory enters $\triangle_\lambda^-$ at some time t_1 at a point $(v(t_1), w(t_1)) = (v_1, W_{\lambda+}(v_1))$ with $v_1 > v_\infty$ and $W_{\lambda+}(v_1) > w_\infty$ then it crosses the line $v = v_\infty$ at a time $\tilde{t} > t_1$ with $w(\tilde{t}) > W_{\lambda+}(v_1) > w_\infty$ and it must leave $\triangle_\lambda^+$ again (after a finite timespan, cf. Lemma 8) at a time t_2 at a point $(v(t_2), w(t_2)) = (v_2, W_{\lambda-}(v_2))$, for which holds that $0 < v_2 < v_1$.

In order to quantify that all solution trajectories pass through the line of degeneracy $p = 0$ where $\dot{H} = 0$, we prove that $p^2(t)$ is a strictly convex function near $p = 0$ with a positive lower bound for $\ddot{p}$ within the triangle $\triangle_\lambda^+$ (and $\triangle_\lambda^-$) for λ chosen sufficiently large $\lambda \gg 1$, i.e. that $p(t) = 0$ can only occur at discrete points in time.

We begin by calculating

$$\dot{p} = \dot{v} = v(w_\infty - w) - \varepsilon v d, \qquad \text{with } d := v - v_\infty + w - w_\infty.$$

Next,

$$\dot{d} = v w_\infty - v_\infty w - \varepsilon v d,$$

and

$$\ddot{p} = \Big[v(w-w_\infty)^2 - vw(v-v_\infty)\Big] - \varepsilon v\Big[2d(w_\infty - w) + vw_\infty - v_\infty w\Big] + \varepsilon^2\Big[v^2 d + d^2 v\Big].$$

If $p(t_0) = 0$, then

$$p^2(t) = \underbrace{p^2(t_0)}_{=0} + 2\underbrace{p(t_0)}_{=0}\dot{p}(t_0)(t-t_0) + 2\Big[(\dot{p})^2 + p\ddot{p}\Big](\theta)\frac{(t-t_0)^2}{2} = \Big[(\dot{p})^2 + p\ddot{p}\Big](\theta)(t-t_0)^2,$$

for some $\theta \in (t, t_0) \subset (t_1, t_2)$.
Hence, by using Lemma 7 and for ε sufficiently small

$$\begin{aligned}(\dot{p})^2 + p\ddot{p} &= (v(w-w_\infty))^2 + vp\Big[(w-w_\infty)^2 - w(v-v_\infty)\Big] + O(\varepsilon),\\ &\geq C(w(\theta)-w_\infty)^2 \geq C(w_1-w_\infty)^2,\end{aligned}$$

for a constant $k > 0$. Now, for any solution trajectory crossing $\triangle_\lambda^+$ in a time interval (t_1, t_2), we estimate

$$\begin{aligned}\int_{t_1}^{t_2} \dot{H}\,dt &= -\varepsilon\int_{t_1}^{t_2} p^2(t)\,dt = -\varepsilon\int_{t_1}^{t_2}\Big[(\dot{p})^2 + p\ddot{p}\Big](\theta)(t-t_0)^2\,dt\\ &\leq -\varepsilon C(w_1-w_\infty)^2\int_{t_1}^{t_2}(t-t_0)^2\,dt \leq -\varepsilon C\int_{t_1}^{t_2} C_1(w(t)-w_\infty)^2\,dt\,\frac{\int_{t_1}^{t_2}(t-t_0)^2\,dt}{t_2-t_1}\\ &\leq -\varepsilon C\,C_1 K\int_{t_1}^{t_2}(w(t)-w_\infty)^2\,dt,\end{aligned}$$

where $C_1 = \frac{(w_1-w_\infty)^2}{(w(t_0)-w_\infty)^2} \leq 1$ since $w(t) \leq w(t_0)$ for all $t \in (t_1, t_2)$ and K is a constant only depending on (the bounds of) the sojourn time $t_2 - t_1$ of all solution trajectory through $\triangle_\lambda^+$ as estimated in Lemma (8).

Next, we observe that the convexity of the Lyapunov H together with the decay of the Lyapunov $H(v(t), w(t)) \leq H^0$ for all $t \geq 0$ imply uniform-in-time positive lower and upper bounds on v and w subject to initial data with finite $H^0 = H(v^0, w^0) < +\infty$. By using this lower and upper bounds, we estimate

$$\begin{aligned}H(v,w) - H(v_\infty, w_\infty) &= v_\infty h\Big(\frac{v}{v_\infty}\Big) + (1+\varepsilon)w_\infty h\Big(\frac{w}{w_\infty}\Big)\\ &\leq C_2(v_\infty, w_\infty, H^0)\Big[(v-v_\infty)^2 + (w-w_\infty)^2\Big],\end{aligned} \tag{3.32}$$

where $h(z) = (z-1) - \ln z \geq 0$ is non-negative and convex and $h(z) \leq C_2(z_*, z^*)(z-1)^2$ for $z \in (z_*, z^*)$. Hence, on $\triangle_\lambda^+$, we have $H(v,w) - H(v_\infty, w_\infty) \leq C_3(w-w_\infty)^2$ with a constant $C_3 = C_3(C_2, \lambda)$ and conclude that

$$\int_{t_1}^{t_2}\dot{H} \leq -\varepsilon\kappa C_1 K C_3^{-1}\int_{t_1}^{t_2} H(v,w) - H(v_\infty, w_\infty)\,dt \tag{3.33}$$

Note that an analog estimate to (3.33) holds also on $\triangle_\lambda^-$.

Outside of $\triangle_\lambda = \triangle_\lambda^- \cup \triangle_\lambda^+$, there exists a constant $C_\lambda > 0$ such that the estimate $|p|^2 \geq C_\lambda\Big[(v-v_\infty)^2 + (w-w_\infty)^2\Big]$ holds. Moreover, the uniform lower and upper bounds on $v(t), w(t)$ imply that there exists a positive constant $C_4 = C_4(v_\infty, w_\infty, H^0)$

$$0 < C_4 := \min_{\{(v,w):H(v,w)\leq H^0\}\setminus\triangle_\lambda} \left\{ \frac{(v-v_\infty)^2}{v_\infty h\Big(\frac{v}{v_\infty}\Big) + (1+\varepsilon) w_\infty h\Big(\frac{w}{w_\infty}\Big)} \right\},$$

which implies $p^2 \geq C_4(H(v,w) - H(v_\infty, w_\infty)$ and

$$\dot{H} \leq -\varepsilon\, C_4(H(v,w) - H(v_\infty, w_\infty)) \qquad \text{outside of} \quad \triangle_\lambda. \tag{3.34}$$

Estimate (3.34) proves exponential convergence (of order ε) towards equilibrium first in the relative Hamiltonian distance $(H(v,w) - H(v_\infty, w_\infty))$ as long as a solution trajectory is outside the critical area $\triangle_\lambda$. Consequently, the estimate (3.32) (which holds equally true on all points with $H(v,w) \leq H^0$) implies exponential convergence to equilibrium in the Euclidian distance.

Within the critical area $\triangle_\lambda$, this exponential convergence is hampered by the line of degeneracy where $p = 0$. However, (3.33) and the lower crossing time estimates in Lemma 8 show that solutions trajectories do not get stuck (or significantly slowed down) within $\triangle_\lambda$. More precisely, since the speed of trajectories outside $\triangle_\lambda$ is bounded from above, for any fixed $\lambda > 1$ (λ large enough), all solution trajectories will remain within $\triangle_\lambda$ only a small fraction of the time spent on one rotation around (v_∞, w_∞).

Finally, this small fraction spent within $\triangle_\lambda$ per rotation can not degenerate near (v_∞, w_∞), since classical linearisation techniques shows eigenvalues of the form

$$\mu = -\varepsilon\frac{\rho_0}{2} \pm i\sqrt{(\rho_0(M - \varepsilon\rho_0) - \tfrac{\varepsilon^2\rho_0^2}{4}} \quad \xrightarrow{\varepsilon\to 0} \quad \pm i\sqrt{v_\infty w_\infty}, \tag{3.35}$$

where the right hand side values corresponds to the eigenvalues (und thus finite oscillation period) of the classical Lotka-Volterra system.

Altogether, we obtain exponential convergence to equilibrium with a rate εr as in (3.30), where r can be estimated explicitly in terms of the constants in (3.33) and (3.34) as well as the sojourn times in Lemma 8. ■

Lemma 7. *(Local convexity estimates of the Lyapunov decay)*

Consider $\triangle_\lambda^+$ to be the interior of the convex subcone above $w = w_\infty$ and between the lines

$$W_{\lambda-} : \; w - w_\infty = -\lambda(v - v_\infty) \quad \textit{and} \quad W_{\lambda+} : \; w - w_\infty = \lambda(v - v_\infty).$$

Then for $\lambda > 1$ and λ large enough, we have

$$v^2(w-w_\infty)^2 + vp\Big[(w-w_\infty)^2 - w(v-v_\infty)\Big] \geq C(w-w_\infty)^2 \tag{3.36}$$

for $C = C(\lambda, v_\infty, w_\infty, M) > 0$.

Proof. We set

$$q = (w - w_\infty)^2 - w(v - v_\infty)$$

and observe that $q < 0$ is equivalent to

$$\frac{(w - w_\infty)^2}{w} < (v - v_\infty),$$

and $q = 0$ is a curve denoted as $\mathcal{C}$ which crosses the line $W_{\lambda+}$ at the unique point

$$\Big(v_\infty + \tfrac{w_\infty}{\lambda(\lambda-1)}, \tfrac{\lambda}{\lambda-1} w_\infty\Big).$$

Moreover the line $v = v_\infty$ is the tangent line of $\mathcal{C}$ at (v_∞, w_∞).
In order to prove (3.36), we need to bound $v^2(w - w_\infty)^2 + vpq$ from below. Note that $pq < 0$ holds on two subdomains of $\triangle_\lambda^+$:

1. the domain between $\mathcal{C}$ and the line $W_{\lambda+}$ where $p > 0$ and $q < 0$. We denote this domain $\mathcal{E}_1$,

2. the domain between the lines $v = v_\infty$ and $W_{\lambda-}$ where $p < 0$ and $q > 0$. We denote this domain $\mathcal{E}_2$.

On $\mathcal{E}_1$, we estimate $0 < p < \frac{w - w_\infty}{\lambda}$. Also, we have $0 < v < M$ and $0 < w < M$ thanks to Theorem 15. This implies that

$$0 > q \geq (w - w_\infty)^2 - \frac{w(w - w_\infty)}{\lambda}$$

and

$$\begin{aligned} v^2(w - w_\infty)^2 + vpq &\geq v^2(w - w_\infty)^2 + v\frac{w - w_\infty}{\lambda}\left[(w - w_\infty)^2 - \frac{vw(w - w_\infty)}{\lambda}\right], \\ &\geq v^2(w - w_\infty)^2 - \frac{w(w - w_\infty)^2}{\lambda^2}, \\ &\geq \Big(v_\infty^2 - \tfrac{M^2}{\lambda^2}\Big)(w - w_\infty)^2. \end{aligned}$$

By choosing a λ large enough, we have

$$C_1 = \Big(v_\infty^2 - \tfrac{M^2}{\lambda^2}\Big) > 0.$$

On $\mathcal{E}_2$, we estimate $0 > p > -\frac{w-w_\infty}{\lambda}$. It implies that

$$\begin{aligned} v^2(w-w_\infty)^2 + vpq &\geq v^2(w-w_\infty)^2 - v\frac{w-w_\infty}{\lambda}\Big[(w-w_\infty)^2 - wp\Big], \\ &\geq v^2(w-w_\infty)^2 - v\frac{(w-w_\infty)^3}{\lambda} - vw\frac{(w-w_\infty)^2}{\lambda^2}, \\ &\geq \left(v_\infty^2 + 2v_\infty(v-v_\infty) - \frac{v(w-w_\infty)}{\lambda} - \frac{vw}{\lambda^2}\right)(w-w_\infty)^2, \\ &\geq \left(v_\infty^2 - \frac{(M+2v_\infty)(M-w_\infty)}{\lambda} - \frac{M^2}{\lambda^2}\right)(w-w_\infty)^2. \end{aligned}$$

By choosing a λ large enough, we have

$$C_2 = \left(v_\infty^2 - \frac{(M+2v_\infty)(M-w_\infty)}{\lambda} - \frac{M^2}{\lambda^2}\right) > 0.$$

Altogether, by choosing $C = \min(C_1, C_2)$, we obtain the estimate (3.36) on $\triangle_\lambda^+$. ∎

Lemma 8. *(Sojourn time estimates)*

Consider $\triangle_\lambda^+$ as above. Let t_1 be the time when the trajectory enters $\triangle_\lambda^+$ at a point $\left(v_1, W_{\lambda+}(v_1)\right)$ and t_2 the time when the same trajectory leaves $\triangle_\lambda^+$ at a point $\left(v_2, W_{\lambda-}(v_2)\right)$ with $v_2 < v_1$.

Then for $\varepsilon > 0$ small enough and for $\lambda > 1$ large enough and all $v_1 \in (v_\infty, M)$, we have that the crossing time is bounded below and above, i.e.

$$\frac{c_2}{2v_\infty} \leq t_2 - t_1 \leq \frac{2(c_1+1)}{\lambda v_\infty}, \tag{3.37}$$

where c_1 is a constant such that $1 \leq c_1 \leq \frac{M-w_\infty}{\min(w_1-w_\infty, w_2-w_\infty)}$ and c_2 is a constant such that $0 < c_2 < \frac{v_1-v_\infty}{M-w_\infty}$.

Proof. In the following we use the notations $W_{\lambda+}(v_1) := w_1$ and $W_{\lambda-}(v_2) := w_2$. On $\triangle_\lambda^+$, we have that $w - w_\infty > \min(w_1 - w_\infty, w_2 - w_\infty)$ and there exists a constant c_1 with $1 \leq c_1 \leq \frac{M-w_\infty}{\min(w_1-w_\infty, w_2-w_\infty)}$ such that

$$c_1 \min(w_1 - w_\infty, w_2 - w_\infty) = \max(w_1 - w_\infty, w_2 - w_\infty).$$

We get the lower bound on $w - w_\infty$:

$$w - w_\infty \geq \frac{\min(w_1 - w_\infty, w_2 - w_\infty) + \max(w_1 - w_\infty, w_2 - w_\infty)c_1^{-1}}{2}.$$

We estimate the first equation of (3.28) by using that $-\frac{w-w_\infty}{\lambda} \leq v - v_\infty \leq \frac{w-w_\infty}{\lambda}$, $w_\infty < w < M$ and the lower

bound on $w - w_\infty$:

$$\begin{aligned}
-\dot v &= v(w-w_\infty) + \varepsilon v\,[v - v_\infty + w - w_\infty],\\
&\geq (v-v_\infty)(w-w_\infty) + \varepsilon(v-v_\infty)(w-w_\infty) + v_\infty(w-w_\infty) + \varepsilon v_\infty(v-v_\infty) + \varepsilon v_\infty(w-w_\infty),\\
&\geq (w-w_\infty)\Big[\Big(1+\varepsilon\tfrac{\lambda-1}{\lambda}\Big)v_\infty - \tfrac{1+\varepsilon}{\lambda}(w-w_\infty)\Big] \geq (w-w_\infty)\Big[\Big(1+\varepsilon\tfrac{\lambda-1}{\lambda}\Big)v_\infty - \tfrac{1+\varepsilon}{\lambda}(M-w_\infty)\Big],\\
&\geq (w-w_\infty)\frac{v_\infty}{2} \geq \frac{\min(w_1-w_\infty, w_2-w_\infty) + \max(w_1-w_\infty, w_2-w_\infty)c_1^{-1}}{2}\frac{v_\infty}{2},
\end{aligned}$$

where the second last inequality holds for $\varepsilon > 0$ small enough and for sufficiently large λ, e.g. $\lambda \geq \frac{2(1+\varepsilon)(M-w_\infty)}{v_\infty}$. Hence,

$$v(t_1) - v(t_2) = \int_{t_1}^{t_2} -\dot v\,dt \geq \frac{|w_1-w_\infty| + |w_2-w_\infty|}{2}\frac{v_\infty}{2}(t_2-t_1).$$

On the other hand, we have

$$v(t_1) - v(t_2) = \frac{(w_1-w_\infty) + (w_2-w_\infty)}{\lambda} = \frac{\min(w_1-w_\infty, w_2-w_\infty) + \max(w_1-w_\infty, w_2-w_\infty)}{\lambda}$$

which yields the upper bound (3.37), i.e.

$$t_2 - t_1 \leq \frac{2(c_1+1)}{\lambda v_\infty}.$$

For the lower bound, we estimate with $v - v_\infty \leq \frac{w-w_\infty}{\lambda}$ and $w_\infty < w < M$

$$\begin{aligned}
-\dot v &= v(w-w_\infty) + \varepsilon v\,[v - v_\infty + w - w_\infty],\\
&\leq \frac{(w-w_\infty)^2}{\lambda} + v_\infty(w-w_\infty) + \varepsilon\frac{\lambda+1}{\lambda}(w-w_\infty)\left[v_\infty + \frac{(w-w_\infty)}{\lambda}\right],\\
&\leq \left[\Big(1+\varepsilon\frac{\lambda+1}{\lambda}\Big)v_\infty + \frac{1+\varepsilon(\lambda+1)}{\lambda^2}(w-w_\infty)\right],\\
&\leq (w-w_\infty)\left[\Big(1+\varepsilon\frac{\lambda+1}{\lambda}\Big)v_\infty + \frac{1+\varepsilon(\lambda+1)}{\lambda^2}(M-w_\infty)\right]\\
&\leq (M-w_\infty)2v_\infty,
\end{aligned}$$

where the last inequality holds for sufficiently large λ and ε sufficiently small.
Hence

$$v(t_1) - v(t_2) = \int_{t_1}^{t_2} -\dot v\,dt \leq (M-w_\infty)2v_\infty(t_2-t_1)$$

and we require a lower bound for $v(t_1) - v(t_2)$, which we dervie as follows. Since $v_\infty < v_1 < M$ and $w_\infty < w < M$, we estimate

$$v_1 - v_2 \geq v_1 - v_\infty \geq c_2(M - w_\infty)$$

where c_2 is a constant such that $0 < c_2 < \frac{v_1 - v_\infty}{M - w_\infty}$. We finally get the lower bound (3.37). ■

3.5.2 Results on asymptotically autonomous differential systems

In this section, we recall some results on asymptotically autonomous differential equations. The proofs of the results and further details can be found in [97, 155, 156].

Definition 6. *Let $f : \mathbb{R} \times \mathbb{R}^n \mapsto \mathbb{R}^n$ and $g : \mathbb{R}^n \mapsto \mathbb{R}^n$ be continuous and locally Lipschitz on $\mathbb{R}^n$. An ordinary differential equation in $\mathbb{R}^n$*

$$\dot{x} = f(t, x), \tag{3.38}$$

is called asymptotically autonomous with limit equation

$$\dot{y} = g(y), \tag{3.39}$$

if

$$f(t, x) \xrightarrow[t \to \infty]{} g(x), \qquad \text{locally uniformly in } x \in \mathbb{R}^n.$$

We denote the ω-limit set of ω of a forward bounded solution x to (3.38) satisfying $x(t_0) = x_0$ by $\omega(t_0, x_0)$:

$$\omega(t_0, x_0) = \bigcap_{s > t_0} \overline{\{x(t);\ t \geq s\}}.$$

We recall the main theorems established by Markus in [97].

Theorem 17. *The ω-limit set ω of a forward bounded solution x to* (3.38) *is nonempty, compact, and connected. Moreover*

$$dist(x(t), \omega) \xrightarrow[t \to \infty]{} 0.$$

Finally ω is invariant under (3.39)*, i.e. if $y(t_0) = y_0 \in \omega$ and $y(t, y_0)$ its trajectory with initial point y_0 then $y(t, y_0) \in \omega$. In particular any point in ω lies on a full orbit of* (3.39) *that is contained in ω.*

Theorem 18. *Let y_∞ be a locally asymptotically stable equilibrium of* (3.39) *and ω the ω-limit set of a forward bounded solution x to* (3.38)*. If ω contains a point y_0 such that the solution of* (3.39) *though $(0, y_0)$ converges to y_∞ for $t \to \infty$, then $\omega = \{y_\infty\}$, i.e.*

$$x(t) \xrightarrow[t \to \infty]{} y_\infty.$$

Furthermore, the Poincaré-Bendixson theorem is also extended to asymptotically autonomous planar systems.

Theorem 19. *Let $n = 2$ and ω the ω-limit set of a forward bounded solution x of* (3.38)*. Then ω either contains equilibria of* (3.39) *or is the union of periodic orbits of* (3.39)*.*

These theorems have been used in population dynamics in order to prove that asymptotically autonomous ODEs arising from the models converge to equilibrium (e.g. [32]). If $n = 2$ and the possible equilibria of (3.39) are restricted a unique equilibrium which is locally stable, then any solution of (3.38) converges to the the equilibrium of (3.39). Moreover, these theorems have been generalized in [156] to be applied for specific PDEs.

Chapter 4

Quaternary structural convergence and structural diversification of prion assemblies.

4.1 Summary and mathematical modeling.

In this chapter, we detail and explain the evidence coming from biochemical experiments which enforce the hypothesis of heterogeneity in architecture and structure of the PrP assemblies. The article containing this result is in Section 4.2. It has been accepted *Communications Biology* and is soon to appear under the title "Quaternary structural convergence and structural diversification of prion assemblies at the early replication stage". The following section contains a summary of the article and the complementary details on the mathematical model of a polymerisation/depolymerisation process with two distinct polymer assemblies.

4.1.1 Structural diversification of prion assemblies in early Prion replication stage.

In prion diseases, the prion protein PrP^C misfolds into PrP^{Sc} and auto-organizes into conformationally distinct assemblies or strains (polymers). The existence of PrP^{Sc} structural heterogeneity within prion strains is suggesting the emergence and coevolution of structurally distinct PrP^{Sc} assemblies during prion replication. Such PrP^{Sc} diversification processes remain poorly understood. Here, we characterize the evolution of the PrP^{Sc} quaternary structure during prion replication in vivo and in vitro in a cell-free system generated by PMCA. The protein quaternary structure is the number and arrangement of multiple folded protein subunits (e.g. monomers, dimers or small oligomers). The molecular mechanisms of PrP^{Sc} replication and structural diversification is observed combining Protein Misfolding Cyclic

Amplification (PMCA) and Sedimentation Velocity experiments (cf Figures 10 and 11).

Regardless of the strain studied, the early replication stage (commonly assimilated as an elongation process) results in the formation of small PrP^{Sc} oligomers, thus highlighting a quaternary structural convergence phenomenon. A bimodal behavior is observed by the formation of two peaks (P_1, P_2) in the representation of the size distribution (Figure (4.1)). The amount of assemblies in P_1 decreases over time as the amount of assemblies in P_2 increases. We also note the absence of assemblies of intermediate size between these peaks. The experiments described in Section 4.2.2 rule out the hypothesis of a condensation phenomenon in favor of an autocatalytic process as an explanation for the increase of assemblies in P_2. P_1 and P_2 contain structurally distinct subsets of assemblies, denoted respectively A_i and B_i. These subsets differ in proportion, size and architecture of their elementary bricks. Experiments suggests that B_i assemblies results from a cooperative process by the integration/conversion of PrP^C elementary bricks (monomers) and A_i assemblies. The kinetic model is detailed in the section 4.1.2.

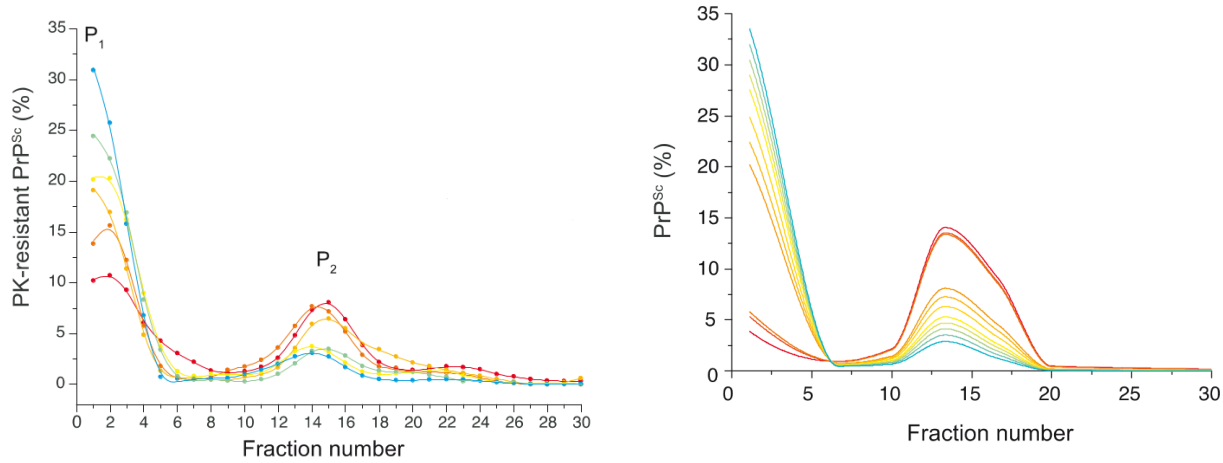

Figure 4.1 – **Size distribution evolution PrP assemblies at the early replication phase.** (Left) S.V profile describing, in vitro, the size distribution evolution of PrP assemblies obtained by PMCA from 127S-infected brain homogenates. (Right) Simulation of the size distribution of the system (4.1). The initial condition corresponds to the measures at the begining of the S.V experiments (blue curve of the graph on the left).

To validate the designed mechanism, we translated these chemical reactions into time-dependent differential equations and performed kinetic simulations using the size distribution of the PrP^{Sc} assemblies immediately after cyclic amplification as the initial condition (blue curve in Figure 4.1). The mathematical modeling and the numerical simulation give more insights about the kinetics between A_i and B_i. These oligomers undergo structural rearrangements, by a PrP^C-dependent, secondary templating pathway. This pathway provides mechanistic insights into prion structural diversification, a key determinant for prion toxicity and inter-species transmission. The uncovered processes are also key for a better understanding of misfolded assemblies propagating by a prion-like process in other neurodegenerative

diseases.

4.1.2 Mathematical modeling of the kinetics and numerical simulations

As explained in the previous section, we consider two different kinds of oligomers: on the one hand, A_i, of size $2i$, are formed by the aggregation of i SuPrP formed of two monomers, and denoted A_1. Due to the fact that $i_A < 5$, as A_i assemblies are eluded in the first Sedimentation Velocity (S.V) fractions, we neglect here the oligomers A_i with $i > 1$ for the sake of clarity and simplicity. On the second hand, oligomers B_i, of size $3i$, able to aggregate by B_1- addition, where B_1 is another SuPrP formed of three monomers. However, A_1 may react with monomers to give rise to B_1. Let us also note that the size of A_1 and B_1, respectively formed of two and three monomers, is somewhat arbitrary: all we know is that this is their order of magnitude, in coherence with [74]. As explained in the following article, a convenient reaction scheme should also be such that without monomers, almost nothing happens (Figure 4.4).

1. A_1 and B_1 can form a complex C in a reversible way:

$$A_1 + B_1 \underset{k_C^-}{\overset{k_C^+}{\rightleftharpoons}} C.$$

2. The complex C can then react with the monomer M to form two B_1:

$$M + C \xrightarrow{k_+} 2B_1.$$

3. The oligomers B_i follow a classical polymerisation/depolymerisation chain reaction, by B_1- addition:

$$B_1 + B_i \underset{k_{dep}^{i+1}}{\overset{k_{on}^i}{\rightleftharpoons}} B_{i+1}, \qquad 1 \leq i \leq n-1.$$

Ordinary differential equations

The data obtained by S.V are interpreted as a dilatation of a size distribution density, normalized at 100%, so that if u_i denotes the concentration of polymers formed of i monomers, the data represent $\frac{iu_i}{\sum_k ku_k}$.

We translate this reaction scheme into the following system of differential equations, denoting a_1, b_1,

c and b_i respectively the concentrations of A_1, B_1, C and B_i :

$$\begin{cases} \frac{dm}{dt} = -k_+ m(t)c(t), & m(0) = m^0, \\ \frac{dc}{dt} = k_C^+ a_1(t)b_1(t) - k_C^- c(t) - k_+ m(t)c(t), & c(0) = c^0, \\ \frac{da_1}{dt} = -k_C^+ a_1(t)b_1(t) + k_C^- c(t), & a_1(0) = a_1^0, \\ \frac{db_1}{dt} = -k_C^+ a_1(t)b_1(t) + k_C^- c(t) + 2k_+ m(t)c(t) - J_1 - \sum_{i=1}^{n-1} J_i, & \\ \frac{db_i}{dt} = J_{i-1} - J_i, & 2 \le i \le n-1, \\ \frac{db_n}{dt} = J_{n-1}, & b_i(0) = b_i^0 \ 1 \le i \le n, \end{cases} \tag{4.1}$$

where J_i is the net rate at which a polymer of size $3i$ grows into a polymer of size $3(i+1)$, hence:

$$J_i = k_{on}^i b_1 b_i - k_{dep}^{i+1} b_{i+1}.$$

The parameters to estimate are: m^0, c^0, a_1^0, b_i^0, k_+, k_C^+, k_C^-, k_{on}^i and k_{dep}^{i+1} - total of $2(n-1)+n+6 = 3n+4$ parameters if there are n different sizes of polymers.

We can however use the properties of the model to determine part of the parameters.

Interpretation of the S.V data

In the absence of an exactly reliable relation between the fraction number and the sizes of the oligomers, we assume (a choice which is qualitatively acceptable rather than exactly quantitative) that if $O_j(t)$ denotes the measured proportion of the fraction number j at time t, it measures the proportion of polymerised mass present in oligomers containing roughly $j-$ monomers.

In the following, we denote the total polymerised mass as

$$\mathcal{M}(t) := 2a_1(t) + 3b_1(t) + 5c(t) + 3\sum_{i=2}^{n} i b_i(t).$$

We thus interpret the fraction number measured as follows:

$$\frac{2a_1(t) + 3b_1(t) + 5c(t)}{\mathcal{M}(t)} \approx \sum_{j=1}^{5} O_j(t) := \mathcal{O}_1(t), \qquad \frac{3ib_i(t)}{\mathcal{M}(t)} \approx \sum_{j=3i}^{3i+2} O_j(t) := \mathcal{O}_i(t), \quad i \ge 2,$$

and we use the quantities $\mathcal{O}_i(t)$, measured at several time points, to compare the model with the experimental data. We have a maximal fraction number equal to 30, so that we define $\mathcal{O}_j$ for $j \le 9$ and add the value of O_{30} to compute $\mathcal{O}_9$ in the above definition.

Let us recall here that the size of three monomers for suPrP-B constitutes itself an approximation, so that the fit of our model to the experimental data is meant as a qualitative rather than quantitative insight.

Analysis and calibration of the model

Conserved quantities The system has two conserved quantities: first, the total mass:

$$\frac{d}{dt}\left(m + 2a_1 + 5c + 3\sum_{i=1}^{n} ib_i\right) = 0 = \frac{d}{dt}\left(m(t) + \mathcal{M}(t)\right),$$

and second, what can be viewed as the excess of monomers which will not be consumed to form suPrP-B:

$$\frac{d}{dt}\left(m - a_1 - c\right) = 0.$$

We denote these conserved quantities respectively $\mathcal{M}_{tot} = m^0 + 2a_1^0 + 5c^0 + 3\sum_{i=1}^{n} ib_i^0$ and $\rho^0 = m^0 - a_1^0 - c^0$. These two quantities depend on the parameters to be estimated.

A quantity directly measured experimentally is the so-called *centroid*, defined as the average size:

$$centroid(t) := \frac{\mathcal{M}_2(t)}{\mathcal{M}(t)} = \frac{4a_1(t) + 9b_1(t) + 9\sum_{i=1}^{9} i^2 b_i(t)}{2a_1(t) + 3b_1(t) + 3\sum_{i=1}^{9} ib_i(t)} = \frac{\sum_{j=1}^{30} jO_j(t)}{\sum_{j=1}^{30} O_j(t)}.$$

Asymptotic and initial behaviour of the model We consider that at the final time measurement, an equilibrium has been reached, that we denote with $^\infty$ superscripts. The equilibrium fulfills the following equations:

$$\begin{cases} -k_+ m^\infty c^\infty &= 0, \\ k_C^+ a_1^\infty b_1^\infty - k_C^- c^\infty &= 0, \\ J_1^\infty = \ldots = J_9^\infty &= 0. \end{cases} \tag{4.2}$$

Asymptotically, if the monomers are in excess, the system converges towards the following state:

$$c^\infty = a_1^\infty = 0, \qquad m^\infty = \rho^0, \qquad b_i^\infty = \frac{k_{on}^{i-1}}{k_{dep}^i} b_1^\infty b_{i-1}^\infty, \quad i \geq 2.$$

The last equality allows us to define recursively b_i from b_1, and b_1 is given by the following mass equality:

$$\mathcal{M}^\infty = 3\sum_{i=1}^{9} ib_i^\infty.$$

Since $\mathcal{O}_1^\infty = \frac{3b_1^\infty}{\mathcal{M}^\infty}$, we have

$$\frac{k_{on}^{i-1}}{k_{dep}^{i}}\mathcal{M}^\infty = \frac{3b_i^\infty}{b_{i-1}^\infty \mathcal{O}_1^\infty} = 3\frac{\mathcal{O}_i^\infty}{\mathcal{O}_{i-1}^\infty \mathcal{O}_1^\infty}\frac{i-1}{i}$$

which can be experimentally measured: this gives us $n-1$ relations, thus we now have $2n+5$ parameters to estimate (here $n=9$).

We also assume that initially, before adding monomers, the system was in equilibrium, which means:

$$k_C^- c^0 = k_C^+ a_1^0 b_1^0, \qquad \frac{b_i^0}{b_{i-1}^0 b_1^0} = \frac{k_{on}^{i-1}}{k_{dep}^{i}} = \frac{\mathcal{O}_i^0}{b_1^0 \mathcal{O}_{i-1}^0}\frac{i-1}{i}, \qquad i \geq 3,$$

so that we have $n-1$ new relations, and the number of parameters to estimate is reduced to $n+6$.

Numerical simulations We run the simulations with Matlab, and used the ode solver ode45 (cf Figure 4.1). The parameters which were not given by the analysis have been adjusted qualitatively. The time scale is in hours, the concentrations are in arbitrary units.

k_{on}^1	k_{on}^2	k_{on}^3	k_{on}^4	k_{on}^5	k_{on}^6	k_{on}^7	k_{on}^8
8.4	52.6	166	4.4	0.35	5.4	5.6	4.8
k_{dep}^2	k_{dep}^3	k_{dep}^4	k_{dep}^5	k_{dep}^6	k_{dep}^7	k_{dep}^8	k_{dep}^9
100	100	100	25	25	25	25	25
$b_2(0)$	$b_3(0)$	$b_4(0)$	$b_5(0)$	$b_6(0)$	$b_7(0)$	$b_8(0)$	$b_9(0)$
0.42	0.32	0.65	0.27	0.1	0.07	0.046	0.03
k_+^C	k_-^C	k_+	$m(0)$	$c(0)$	$a_1(0)$	$b_1(0)$	
0.15	3000	5	300	7.10^{-4}	38.2	0.39	

4.2 Article

Quaternary structural convergence and structural diversification of prion assemblies at the early replication stage. *Communications Biology, to appear.*

Authors Angélique Igel-Egalon[1], Florent Laferrière[1], Mohammed Moudjou[1], Jan Bohl[1], Mathieu Mezache[2], Tina Knäpple[1], Laetitia Herzog[1], Fabienne Reine[1], Marie Doumic[2], Human Rezaei[1], Vincent Béringue[1]

Author contributions AIE, FL, MMo, JB, MD, HR and VB conceived and designed the experiments. AIE, FL, MMo, JB, MMe, TK, LH, FR, CJD, MD, HR and VB performed the experiments and analyzed the data. AIE, HR and VB wrote the manuscript. All authors reviewed and edited the manuscript.

[1]VIM, INRA, Université Paris-Saclay, 78350 Jouy-en-Josas, France.
[2]MAMBA, Inria Paris, Laboratoire Jacques-Louis Lions, Sorbonne Université Paris VI, 75005 Paris, France.

Acknowledgments We thank the staff of the Animal facility (INRA-UEAR, Jouy-en-Josas) for animal care. This work was supported by grants from the Fondation pour la Recherche Médicale (Equipe FRM DEQ20150331689), the European Research Council (ERC Starting Grant SKIPPERAD, number 306321), and the Ile de France region (DIM MALINF).

4.2.1 Introduction

In terms of pathogenic mechanisms, the prion paradigm unifies a number of neurodegenerative disorders that are caused by protein misfolding and aggregation [43, 79, 80, 24]. These disorders include prion diseases, Alzheimer's disease, Parkinson's disease and Huntington's disease. In principle, host-encoded monomeric proteins are converted into misfolded and aggregated assemblies, which serve as templates for further autocatalytic conversion. In prion diseases, the prion protein PrP^C is converted into a misfolded, β-sheet-rich conformer termed PrP^{Sc} [130]. In susceptible host species and in laboratory rodents, PrP^{Sc} assemblies form stable, structurally distinct PrP^{Sc} conformers [12, 23, 42], known as prion strains, which encode stereotypical biological phenotypes [148, 151, 152, 15]. The strain-specific structural differences can be observed at the secondary and tertiary structural level in terms of local structural variation but also at the quaternary level with strain-specific size distribution signature [151, 147, 157]. A large body of evidence supports the view for structural diversity within specific prion populations and strains:

(i) prion substrains can be preferentially selected during prion transmission [34, 90, 4, 94] with a species/transmission barrier,

(ii) size- or density-fractionation studies support the existence of a heterogeneous spectrum of PrP^{Sc} assemblies with distinct tertiary/quaternary structures [147, 157, 84, 81, 159, 16, 17, 138] and biological activity (templating activity and infectivity),

(iii) kinetic studies of prion pathogenesis suggest that the formation of neurotoxic PrP^{Sc} species [149] occurs at the late stage of prion infection when replicative PrP^{Sc} assemblies are formed at earlier stages [140, 139].

The prion replication process thus intrinsically allows the structural diversification of PrP^{Sc} assemblies. While the kinetic aspects of prion replication 'as a whole' have been comprehensively described by measuring infectivity or PrP^{Sc} levels in the brain (see [85, 107] as examples), the processes by which PrP^{Sc} structural diversification and the formation of different subpopulations occur within a given strain remain unknown and are not mechanistically supported in the actual framework of the prion paradigm. The autocatalytic conversion model proposed by Griffith in 1967 [66], the nucleated-polymerization model described by Lansbury and Caughey in 1995 [86] and other derived models (e.g. [99]) merely assume the existence of structurally homogeneous assemblies that have absolutely identical propensity to replicate throughout disease progression. These mechanisms intrinsically reduce PrP^{Sc} heterogeneity due to the best replicator selection process [105, 114]. A recent high-resolution structural analysis of the N-terminal domain of the yeast prion SuP35 suggests that conformational fluctuations in natively disordered monomeric Sup35 are responsible for the stochastic, structural diversification of Sup35

aggregates [113]. This idea can be extrapolated to mammalian prion PrP to explain intrastrain structural diversification and strain mutation [42]. However, based on the best replicator selection concept [105, 114, 108], the aforementioned idea does not explain the coevolution of at least two structurally distinct PrP^{Sc} subassemblies within the same environment [34, 91].

To examine the molecular mechanisms of PrP^{Sc} replication and structural diversification in depth, we explore, by sedimentation velocity (SV)-based methods, the quaternary structure evolution of PrP^{Sc} assemblies during the early stage of prion conversion in vivo and in a cell-free system by protein misfolding cyclic amplification [137] (PMCA). By using several prion strains as templates, we demonstrate that the early stage of prion replication invariably generates two subsets of assemblies, termed A_i and B_i, which differ in proportion, size, the architecture of their elementary bricks and structure. The analysis of their kinetics of formation during PMCA combined with kinetic data assimilation reveals the existence of two sequential processes of formation. The first process corresponds to a quaternary structural convergence, as it tends to reduce the parental quaternary structure polydispersity to generate mostly small-sized assemblies, namely A_i. The second process transforms the A_i into structurally different assemblies, namely, B_i, according to a secondary auto-catalytic pathway requiring PrP^C, whereby B_i facilitates its own formation. Our findings provide, for the first time, mechanistic insights into prion structural diversification.

4.2.2 Results

Small PrP^{Sc} oligomers are formed at early replication stage

The early phases of prion replication are commonly thought to consist of an elongation process [61], with the PrP^{Sc} template serving as a base. We studied the size distribution of proteinase K (PK)-resistant PrP^{Sc} (PrP^{res}) assemblies at the early step of prion replication in the brain by SV in an iodixanol gradient using a previously published methodology [157, 84, 74]. The PrP^{res} size distribution at the disease end-stage served as control. Three different host-PrP/strain combinations were studied:

- the 127S cloned scrapie prion strain in ovine PrP tg338 transgenic mice [85],
- the 139A cloned mouse prion strain in mouse PrP tga20 mice [60],
- the vCJD cloned human prion strain in human PrP tg650 mice [13, 67].

Details on Figure 4.2. *The size distribution of proteinase K (PK)-resistant PrP^{Sc} assemblies present in the brain in vivo (a-c) and in PMCA products (d-e) was examined by sedimentation velocity (SV). (a-c) For the in vivo sedimentograms, brains from ovine (tg338), murine (tga20) and human (tg650) transgenic mice inoculated with 127S scrapie prions (a), 139A mouse prions (b) and vCJD human prions (c) were collected (in triplicate) at the early stage (15 days postinfection (127S), 11 days postinfection (139A) and 120 days postinfection (vCJD), blue curves) and at the end stage of the disease (60 days postinfection (127S), 55 days postinfection (139A), 495 days postinfection (vCJD), red curves). The brains were solubilized and*

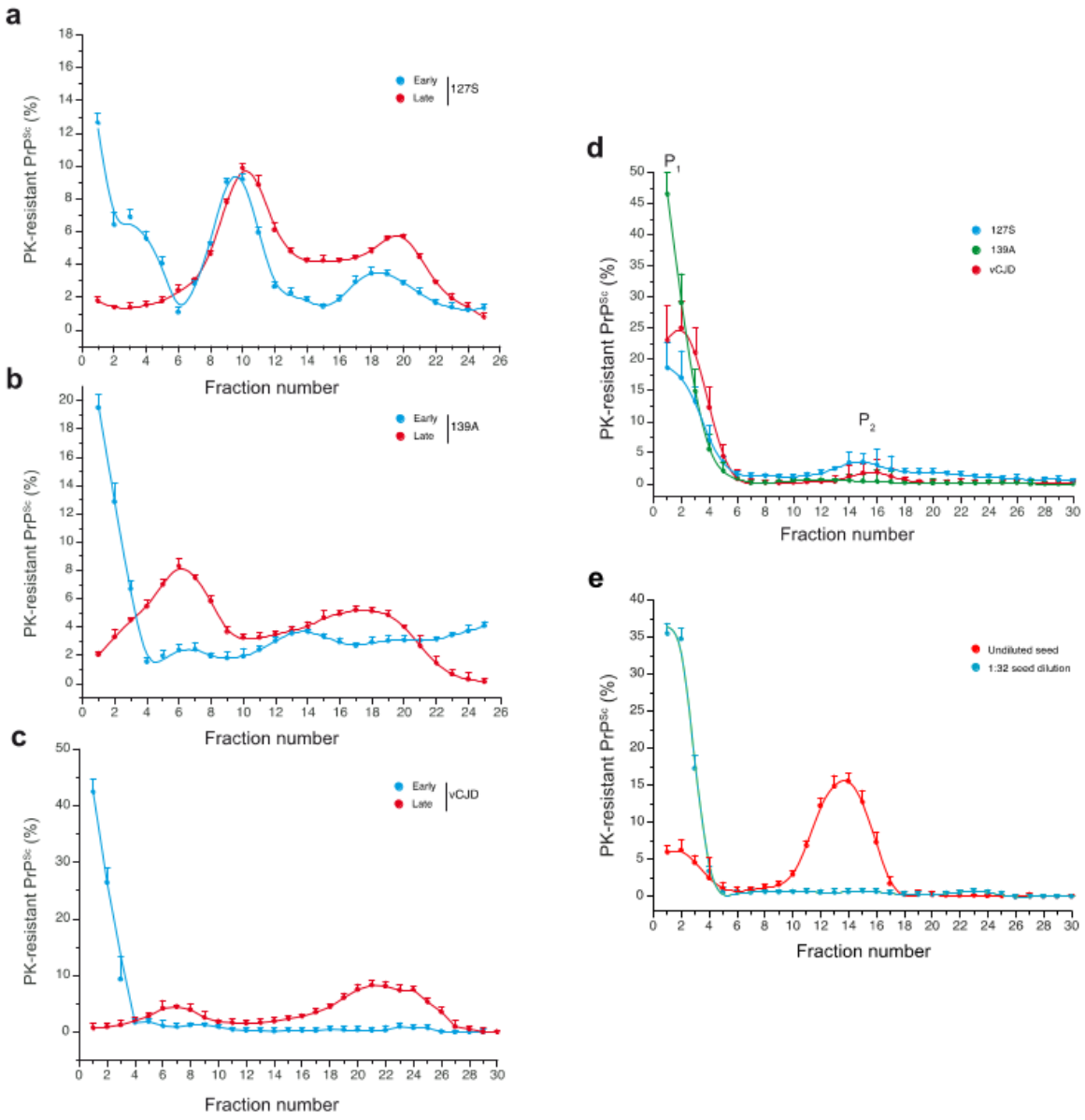

Figure 4.2 – **Size distribution of PrP^{Sc} assemblies from different prion strains at the early and late stages of pathogenesis in vivo and after the PMCA reaction.**

SV-fractionated. The collected fractions (numbered from top to bottom) were analyzed for PK-resistant PrP^{Sc} content by immunoblotting. (d-e) For the sedimentograms from the PMCA products with PrP^{C} substrate (d), the same prion strains were subjected to a single round of mb-PMCA by using 10-5 (139A) or 10-6 (vCJD, 127S) diluted brain homogenates as seed for the reaction. Thirty minutes after the last sonication, the amplified products were solubilized and SV-fractionated. The mean ± SEM levels of PK-resistant PrPSc per fraction were

obtained from the immunoblot analysis of n=4 independent fractionations of PMCA reactions. The peaks containing PrP^{Sc} assemblies sedimentating in the top and middle fractions are denoted P_1 and P_2, respectively. For the sedimentograms from the PMCA products without PrPC substrate (e), undiluted 127S-infected tg338 brain (20% w/v, red curve) or a 1:32 dilution in PMCA buffer (blue curve) was used as seed, mixed with equal volume of brain homogenate from $PrP^{0/0}$ mice as substrate and subjected to a single round of mb-PMCA before SV fractionation.

As shown in Figure 4.2 a–c, small oligomers sedimenting between fractions 1 and 4 were preferentially detected at the early stage of pathogenesis, regardless of the strain considered. A second population of oligomers with a larger size distribution and peaking in fractions 8–10 and 18 was observed for the 127S prion strain. The contribution of incompletely digested PrP^{C} or remnant input PrP^{Sc} inoculum to the PrP signal detected in the top fractions was discarded. Indeed, no PrP^{C} signal was detected after PK treatment of uninfected tg338 brain and no PrP^{res} was detected in the brain of PrP knock-out mice (PrP-/-) inoculated with vCJD prions and analyzed for PrP^{Sc} content at early time points.
At the disease end stage and for the 3 strains, larger assemblies were observed (Figure 4.2 a–c). These observations suggest that prion replication in the brain proceeds through distinct mechanistic phases that are common to the three prion strains studied here:

- a phase that generates mainly small and similar oligomers with respect to quaternary structure (at the SV resolution) at the early stage of the replication process;
- a phase that generates a quaternary structural diversification of PrP assemblies during the disease evolution.

We next determined whether these phases can be reproduced by an in vitro bona fide amplification method. We used a high-throughput variant of PMCA (termed mb-PMCA [74, 103, 104]), which generates in one unique round of 48 h as much infectivity as in the brain at the terminal stage of the disease, with high reproducibility in terms of limiting dilution and the amplification yield [103, 104]. When the size distribution of the amplified products was analyzed by SV after one mb-PMCA round, two discrete distributions were observed for the three strains (Figure 4.2 d), a major set of small PrP^{res} assemblies sedimenting between fractions 1 and 3 (named peak P_1) and a minor set of larger assemblies with a well-defined Gaussian distribution centered on fraction 15 (named peak P_2). The relative proportions of P_1 and P_2 varied among the three strains; P_2 was barely detected in the 139A amplicons. When the mb-PMCA reaction was seeded with healthy brain homogenate, there was no evidence of spontaneously formed P_1 and P_2 PrP^{res} in the amplified products. These data indicate that during mb-PMCA amplification, two populations of PrP^{Sc} assemblies are generated that differ according to their quaternary structures, with a predominance of small assemblies.

The bimodal (i.e., generation of two peaks) and discrete behavior of the size distribution as well as the formation of predominantly small assemblies in P_1 may originate from the mb-PMCA conditions (i.e. shearing forces during the sonication step [1, 115, 163]) rather than from the replication process

itself. To discriminate between these two possibilities, undiluted 127S seeds (i.e., 20% brain homogenate) were incubated and sonicated in identical mb-PMCA conditions but without the PrP^C substrate (i.e., 1:1 dilution in $PrP^{0/0}$ brain lysate). The samples were then SV-fractionated and analyzed for PrP^{res} content by western blot. For comparison, the same brain was diluted in the PMCA buffer before the mb-PMCA reaction, as we reported previously that a simple dilution affects the size distribution of PrP^{Sc} assemblies, by displacing the equilibrium between PrP^{Sc} assemblies and their suPrP elementary subunit ($PrP_i^{Sc} \rightleftharpoons PrP_{i-1}^{Sc} + suPrP$) [74, 73].
While the dilution of 127S seed indeed drastically affected the size distribution of 127S PrP^{Sc} assemblies, sonication of concentrated 127S seeds in the $PrP^{0/0}$ substrate revealed mostly the presence of large-sized assemblies (Figure 4.2 e), peaking in fraction 12–16, as for 127S fractionated brain material solubilized at 37°C [84]. The absence of sonication effect on PrP^{Sc} assemblies size distribution rules out a fragmentation process during the mb-PMCA being at the origin of the formation of small-size assemblies.

Altogether, these observations suggest that:

- in vivo, the early phase of replication generates mainly small-sized assemblies, which diversify with respect to quaternary structure during the disease pathogenesis.
- Similar to in vivo replication, the mb-PMCA amplification condition generates two sets of PrP assemblies that differ in their quaternary structures.

The formation of these two groups of assemblies is common to the 127S, 139A and vCJD prion strains used here.

Bimodal and autocatalytic evolution of PrP^{res} from P_1 to P_2

We next asked whether P_2 formation resulted from a simple condensation of P_1 peak assemblies (coagulation process [106, 143]) or from an alternative templating pathway. We first examined the influence of the amplification rate on the formation of these two species by varying the concentration of the seed used as the template for the mb-PMCA reaction. We generated mb-PMCA products seeded with 10-3 to 10-10 diluted 127S brain homogenate. The amounts of PrP^{res} amongst the amplified products were similar, whatever the seed dilution, as previously observed [104]. The SV-sedimentograms of the mb-PMCA products are shown in Figure 4.3 a. The relative amounts of assemblies in P_1 decreased as the amounts of those from P_2 increased as a function of the seed concentration. The variation in the P_1 and P_2 peak maximum as a function of the logarithm of the dilution factor revealed a quasi-linear decrease in P_1 when the P_2 peak maximum followed a sigmoidal increase (Figure 4.3 b). Such uncorrelated variations in P_1 and P_2 indicate that:

- P_2 peak formation does not result from the simple condensation of assemblies present in P_1,
- the formation of PrP^{res} assemblies in P_2 follows a seed concentration-dependent cooperative process.

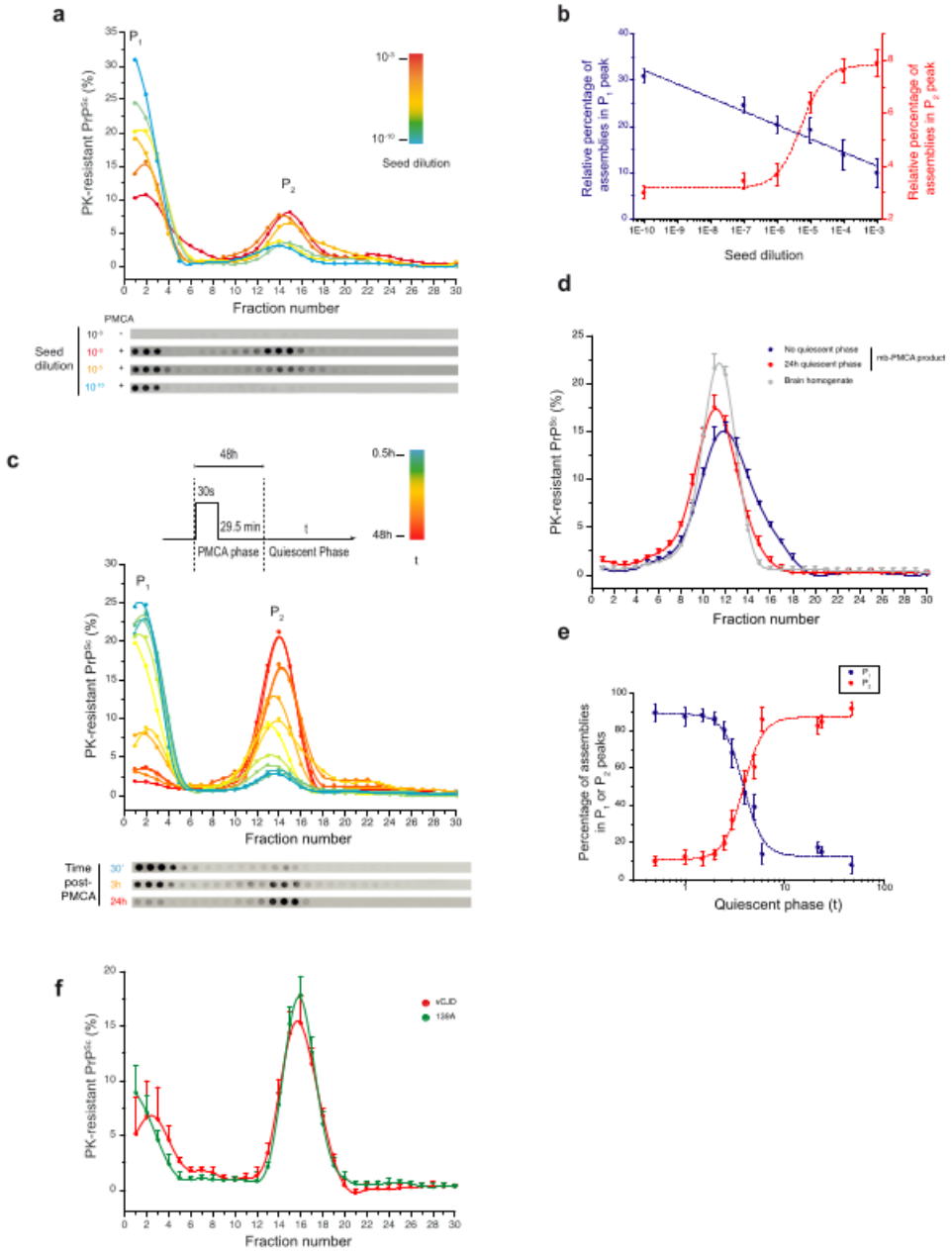

Figure 4.3 – **Seed concentration- and time-dependent dynamic evolution of the PMCA-generated PrP^{Sc} assemblies.**

This observation strongly suggests that the assemblies forming the P_1 and P_2 peaks result from distinct polymerization pathways and should therefore be structurally distinct.

Details on Figure 4.3 *(a–b) SV profiles of mb-PMCA products seeded with serial ten-fold dilutions*

from 127S-infected brain homogenates. Thirty minutes after the last sonication, the amplified products were solubilized and SV-fractionated. The mean relative levels of PK-resistant PrP^{Sc} per fraction (a) were obtained from the immunoblot analysis of n = 4 independent fractionations of PMCA reactions (representative dot-blot shown). Variation in the P_1 and P_2 peak maximum (mean ± SEM values) as a function of the logarithm of the seed dilution factor (b). (c) PK-resistant PrP^{Sc} sedimentograms from the PMCA products generated with 127S prions (10-5 dilution) and further incubated at 37°C during the indicated quiescent phase (t), i.e., without sonication. At each time point, the collected products were frozen prior SV analysis. All collected samples were then thawed, fractionated in parallel by SV and analyzed by immunoblot (c, n = 3 independent experiments, representative dot-blot shown). (d) PK-resistant PrP^{Sc} isopycnic sedimentograms from PMCA products generated with 127S prions (10-5 dilution) and immediately fractionated at the end of the PMCA reaction (blue line and symbol) or after a 24h-quiecent incubation at 37°C (red line and symbol). At each time point, the collected samples were frozen. All collected samples were then thawed, fractionated in parallel by sedimentation at the equilibrium [84] and analyzed by immunoblot (the mean ± SEM levels of PK-resistant PrP^{Sc} per fraction were obtained from the immunoblot analysis of n = 3 independent fractionations of PMCA reactions). As control, the density profile of PK-resistant PrP^{Sc} assemblies from the brain of terminally sick tg338 mice infected with 127S prions (solubilization at 37°C to mimic the PMCA conditions) is shown (gray line and symbol). (e) Evolution of the percentage of P_1 and P_2 peak surface areas (under the curve) as a function of the quiescent phase post-PMCA reaction (C). (f) PK-resistant PrP^{Sc} sedimentograms from the PMCA products generated with 139A and vCJD prion seeds (10-5 dilution) and further incubated for a quiescent period of 48 h at 37°C (mean ± SEM values from n = 3 independent experiments).

To further explore the entanglement between the assemblies forming P_1 and P_2, we set the mb-PMCA regime to favor the formation of the P_1 peak by using high dilutions of the inoculum seed, followed by quiescent incubations (i.e., without sonication) at 37°C for increasing periods. As shown with 127S prions, the SV analysis at defined incubation time points post-PMCA reaction revealed a decrease in the population of P_1 in favor of P_2 (Figure 4.3 c). At 3 h post-incubation, there were equal proportions of assemblies forming P_1 and P_2. At 24 h, most of the PrP^{res} assemblies were located in the P_2 peak.
Comparing the distribution in isopycnic gradients [84] of the PrP^{res} populations at 0h and 24h of quiescent incubation revealed a quasi-similar density for PrP^{res} assemblies composing the P_1 and the P_2 peaks (Figure 4.3 d). This observation implies that the low sedimentation velocity of the assemblies forming P_1 does not result from an interaction with lipids or other low-density molecules and that the sedimentation velocity increase of P_2 compared to P_1 results strictly from a quaternary structure rearrangement through size increase.
As shown in Figure 4.3 c, the formation of assemblies sedimenting in P_2 exhibited a bimodal behavior (i.e., absence of assemblies of intermediate size), without any significant shift in the P_2 peak position. This suggests that the formation of these assemblies resulted from the association with a specific number of assemblies present in P_1. Drawing the time-dependent surface variation in P_1 and P_2 showed that the formation of P_2 assemblies proceeded slowly at the start, increased steadily from 2–3h up to 7h where it slowed down again. This sigmoidal variation is typical of an autocatalytic reaction [102]. This indicates

that the assemblies present in P_2 enhance their own formation according to an autocatalytic process. Similarly, the 139A and vCJD prions showed a bimodal evolution of P_1 to P_2 during a 24-h quiescent phase (Figure 4.3 f), arguing in favor of a generic process of transformation.
To determine whether the P_2 peak assemblies could further evolve, we extended the quiescent phase up to 30 days. For the 127S, 139A and vCJD prion strains, the sedimentogram curves at 7 and 30 days showed a translational shift in the P_2 peak to higher fractions, indicative of an isokinetic increase in their mean average sizes (Figure 4.4 a, left curves). This size translation deeply contrasts with the bimodal phase (transformation of P_1 to P_2) observed during the 0 to 7-day quiescent incubation and highlights a change in the kinetic regime. This new regime would be compatible with a coalescence process [168, 106, 143], whereby assemblies would grow by end-to-end or lateral association of assemblies rather than by incorporation of monomers.

Details on Figure 4.4. *(a) PMCA products from 127S, 139A and vCJD prions (105, 104 and 104 diluted seeds, respectively) were treated with or without PK to eliminate PrP^C before quiescent incubation at 37°C for 2 days, 7 days or 30 days, as indicated. At each time point, the collected products were frozen. All collected samples were then thawed, SV-fractionated in parallel and analyzed by immunoblotting (mean ± SEM values from n = 3 independent experiments). (b-c) Relative percentage of P_1 versus P_2 peaks in SV-sedimentograms from ± PK-treated PMCA products reconstituted in $PrP^{0/0}$ or PrP^C containing tg338 mouse brain homogenates, and incubated in quiescent conditions for 2 or 7 days. (b) PMCA products were generated with a 105-diluted 127S prion seed. At the end of the PMCA reaction (t0), the products were mixed, and eventually treated with high concentration of PK to remove residual PrP^C. After PK inhibition, the products were then diluted 1:1 in either $PrP^{0/0}$ brain homogenate or in tg338 brain homogenate and incubated for 2 days or 7 days at 37°C in quiescent conditions. (c) The PMCA products were then fractionated by sedimentation velocity and analysed for PrP^{Sc} content by immunoblot. The amount of PrP^{Sc} in the fractions corresponding to P_1 and P_2 populations was quantified. The results shown are the mean ± SEM values of three independent experiments.*

Altogether, the quaternary structure variation of PrP^{res} assemblies as a function of seed-concentration or time followed two distinct kinetic regimes. The first regime, occurring during the early steps of the conversion process, leads to a bimodal and cooperative size increase, which indicates the existence of an autocatalytic transformation of PrP^{res} assemblies present in P_1 to P_2. The bimodal aspect of the size distribution tends to indicate that the PrP^{res} assemblies forming P_1 structurally differ from those forming P_2. The second regime, occurring on long-term quiescence is more compatible with a coalescence process.

Quasi-irreversible transformation of PrP^{res} from P_1 to P_2

The bimodal and cooperative transformation of P_1 to P_2 reported in Figure 4.3 c-e is incompatible with the existence of an equilibrium between the assemblies populating these peaks and a coalescence or coagulation process. To further disprove the existence of an equilibrium process (or detailed-balance) governing the P_1 to P_2 transformation, we first set the mb-PMCA regime favoring the formation of

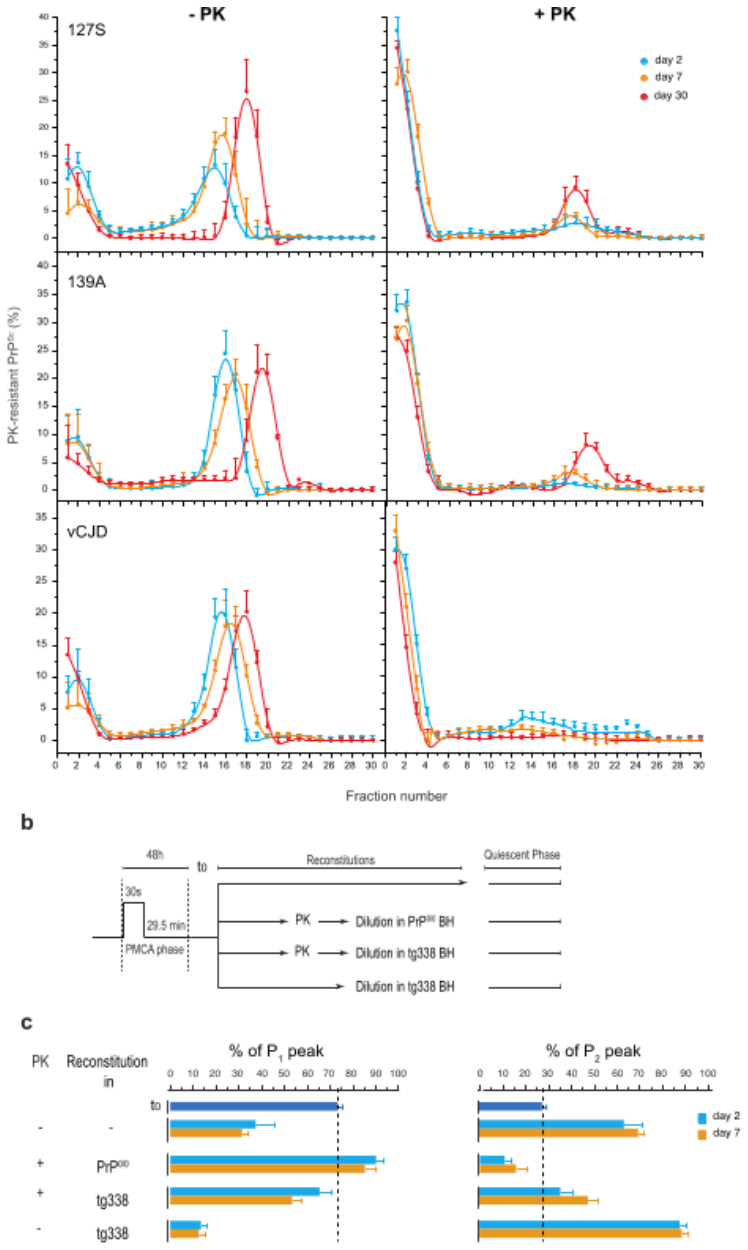

Figure 4.4 – **PrP-dependent generation of Bi assemblies from Ai assemblies.**

the P_1 peak together with the P_2 peak (low dilution of the inoculum seed, Figure 4.5 a, isolated by SV the assemblies forming P_1 (fraction 1 to 3) and P_2 (fraction 14 to 18) and studied their quaternary structural evolution on isolation during quiescent incubation for 7 days at $37°C$. As shown in Figure 4.5 b, almost all P_1 was transformed into P_2, which reflects an irreversible transformation process rather than an equilibrium displacement or a simple condensation or coagulation. In sharp

contrast, the P_2 peak in isolation did not lead to the retro-formation of the P_1 peak by depolymerization (Figure 4.5 c), underlying the absence of an equilibrium or detailed-balance between P_2 and P_1 as expected for a simple condensation or coagulation process. The irreversible nature of the transformation of P_1 to P_2 argues in favour of the existence of a thermodynamically-driven "locking" process. This implies structural rearrangements of P_1 assemblies and formation of higher stable P_2 objects.

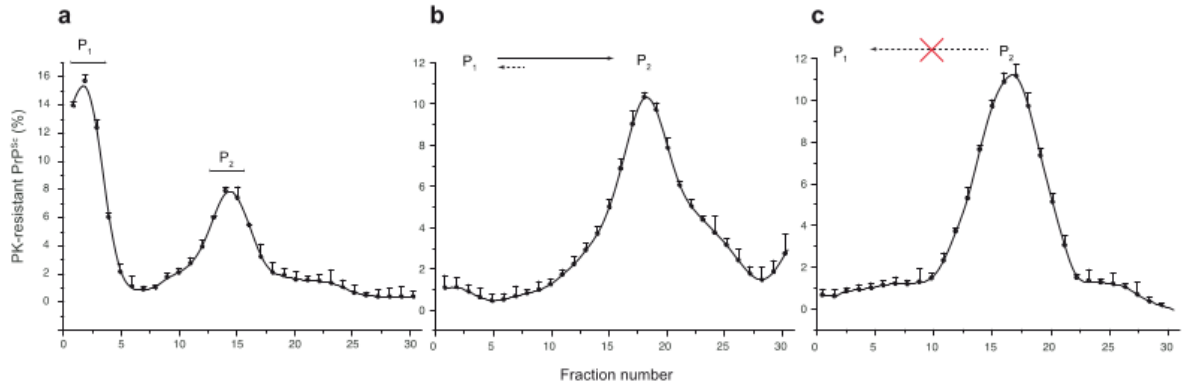

Figure 4.5 – **Quaternary structural evolution of isolated PrP^{Sc} assemblies in P_1 and P_2 peaks on quiescent incubation.** (a) SV profile of PMCA products seeded with 106-diluted 127S brain homogenate, leading to the formation of P_1 and P_2 assemblies (as in Figure 4.3 a). The fractions corresponding to P_1 and P_2 peaks were pooled as indicated, and further incubated for 7 days at $37°C$ in quiescent conditions, prior SV analysis. (b) On quiescent incubation, most of the assemblies present in the pooled P_1 fractions evolved and formed P_2. (c) On quiescent incubation, the pool of P_2 fractions did not evolve, underlying the irreversible character of the P_1 to P_2 transformation and the absence of an equilibrium between P_1 and P_2. The results shown are the mean ± SEM values from $n = 3$ independent fractionations.

P_1 and P_2 contain structurally distinct PrP^{res} assemblies

To further confirm the structural rearrangement in the PrP^{Sc} assemblies accompanying the transformation of P_1 to P_2, we determined the specific infectivity of the P_1 and P_2 assemblies. A 127S-PMCA product was fractionated at the end of the reaction or after 48 h of quiescent incubation. Pools of fractions corresponding to the P_1 and P_2 peaks were inoculated into reporter tg338 mice. The specific infectivity (infectivity per PrP molecule), which is mostly associated to PrP^{res} assemblies (i.e. negligible contribution of PK-sensitive PrP^{Sc} species to 127S infectivity [157, 84]), was calculated from the mean survival time using 127S dose-response curves [157]. As shown in Figure 4.6, the specific infectivity of the P_1 peak assemblies was 50-100-fold higher than that of the P_2 peak assemblies. These observations indicate that the P_1 and P_2 peaks contain structurally distinct sets of PrP^{res} assemblies, named A_i and B_i (the i index referring to the number of monomer/subunit in the assembly). The specific infectivity of P_2 did not change over a longer period of quiescent incubation (7 days), suggesting that the transformation of the assemblies present in the P_2 peak into larger assemblies was not associated with a structural change measurable by their specific activity.

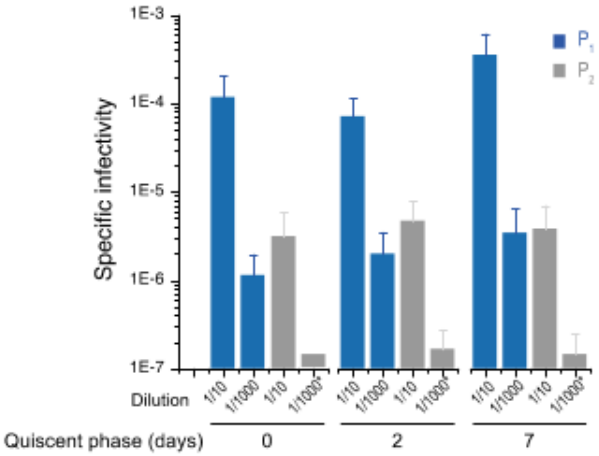

Figure 4.6 – **Specific infectivity of the P_1 and P_2 peaks post-PMCA reaction and after quiescent incubation.** Fractions corresponding to P_1 (fractions 1-3) and P_2 (fractions 14-16 (days 0 and 2) or 16-18 (day 7)) from PMCA products seeded with 106-diluted 127S brain homogenate were pooled and inoculated into groups of reporter tg338 mice at two different dilutions (1:10 and 1:1000) for better accuracy. The specific infectivity of the assemblies was calculated from the mean survival time of the mice using a 127S dose-response curve.

Architectural characterization of A_i and B_i assemblies

To characterize the structural difference between A_i and B_i assemblies at the level of their elementary subunit [74], we used a size exclusion chromatography (SEC) method in native condition, allowing hydrodynamic radius-based analyses. To determine if the hydrodynamic radius from B_i elementary subunit (suPrPB) differ from that of A_i (suPrPA), 127S-PMCA products generated at high-seed dilution (10-8) were analysed by SEC immediately at the end of the reaction (defined at t0) or after a 7-day quiescent incubation. At t0, the SEC profile showed the existence of a unique peak eluting at 14.7ml (Figure 4.7 a). As PMCA products generated at 10-8 seed dilution mostly contain A_i assemblies in the P_1 peak (Figure 4.7 b), one can attribute the SEC peak at t0 to suPrPA. After the 7-day quiescence, the chromatogram revealed the emergence of an additional peak eluting at 15.5ml (Figure 4.7 a), which correlates with the transformation of A_i to B_i observed by SV (Figure 4.7 b). This new peak was thus attributed to suPrPB. The low difference observed in the elution volume between suPrPA and suPrPB suggests a difference in their hydrodynamic radius (suPrPB assemblies being more compact than suPrPA assemblies), and therefore a difference in their structure.

To gain further insight into the mechanism of suPrPB formation, 127S-PMCA products generated with different seed concentrations ,as in Figure 4.3 a, were analysed by SEC. At high seed dilution (10-8 dilution factor), the chromatogram revealed the existence of suPrPA (Figure 4.7 c). Lower seed dilutions led to the emergence of a new peak with an elution volume of 15.50ml corresponding to the emergence of suPrPB, and a shift toward lower elution volume of suPrPA (Figure 4.7 c). This last phenomenon could be the consequence of dissociation /association equilibrium displacement between different species during the separation on the SEC column [8, 78].

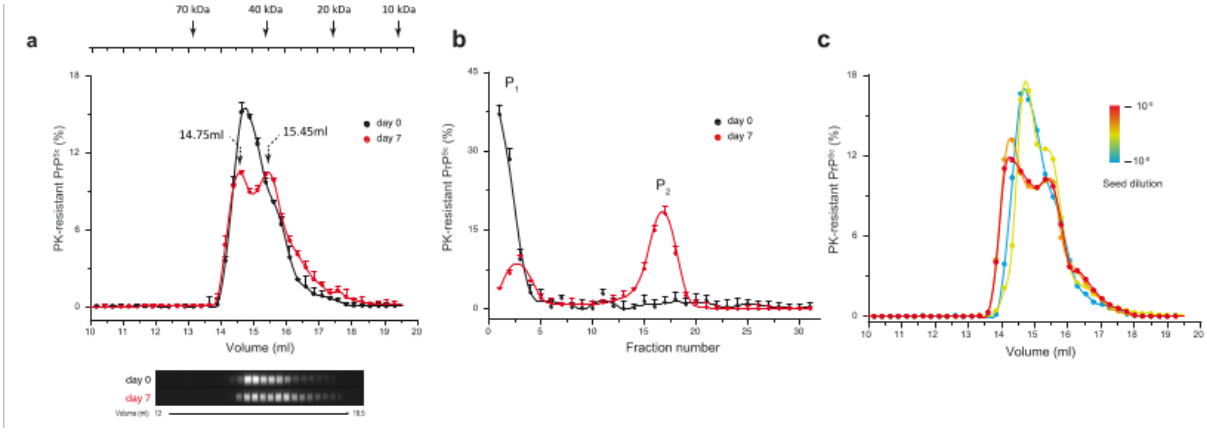

Figure 4.7 – **Characterization of the elementary subunit of PMCA-generated PrP^{Sc} assemblies by size exclusion chromatography (SEC) under native conditions.** (a) SEC analysis ($n \geq 3$) of mb-PMCA products generated with 127S prions (10-8 dilution) immediately after the PMCA phase (day 0) or after 7 days of quiescent incubation (day 7). A representative immunoblot corresponding to elution volumes 12ml to 18ml is shown. The column calibration was performed using standard MW calibrants under identical conditions as for PMCA products analysis. (b) Representative sedimentogram of mb-PMCA products generated with 127S prions (10-8 dilution) post-PMCA reaction (day 0) and after a 7-day quiescent incubation, highlighting the P_1 to P_2 evolution of PrP^{Sc} assemblies.(c) SEC profiles of mb-PMCA products generated with 127S seeds at different dilution factors, as indicated. Thirty minutes after the last sonication, the amplified products were solubilized and SEC-fractionated. The mean relative levels of PK-resistant PrP^{Sc} per fraction were obtained from the immunoblot analysis of $n = 3$ independent fractionations of PMCA reactions. Note the formation of at least two distinct set of assemblies as function of seed concentration.

Collectively, the SEC analysis of the P_1 to P_2 transformation demonstrates that the formation of B_i species is concerted with the emergence of a new elementary subunit (suPrPB). suPrPB differs from suPrPA by its hydrodynamic radius and therefore its structure. The structural difference between suPrPA and suPrPB is at the origin of their physicochemical properties and their aggregation propensity. The existence of conformationally distinct suPrP further demonstrates that A_i and B_i are fundamentally different in terms of ultrastructure and further exclude a simple coalescence or coagulation process at the origin of the A_i to B_i transformation.

The formation of B_i from A_i assemblies requires PrP^C

Our previous studies revealed that only ~ 30% of the PrP^C substrate was converted into PrP^{Sc} after a complete round of mb-PMCA [103, 104]. To determine whether the remaining 70% still participated in the transformation of A_i to B_i assemblies during the quiescent phase, PMCA products from the 139A, 127S and vCJD prions were treated with PK to eliminate PrP^C before quiescent incubation at 37°C. As shown in Figure 4.4 a, the amount of B_i assemblies generated during the 48-h quiescent incubation was drastically decreased for the three prion strains. Further quiescent incubation for 7 and 30 days in the absence of PrP^C allowed the formation of comparatively low amounts of B_i assemblies for the 127S and 139A prion strains.

To determine if the drastic decrease of A_i to B_i transformation after PK treatment was specific to

depletion of PrP^C or of cofactors, we performed reconstitution experiments of ± PK-treated 127S-PMCA products (e.g. without potential, PK-susceptible co-factors) with either $PrP^{0/0}$ brain homogenate (e.g. media containing all brain cofactors except PrP^C) or tg338 brain homogenate (e.g. media containing all cofactors and PrP^C) before 48 h or 7 days of quiescent incubation (Figure 4.4 b). The quiescent products were then SV-fractionated and the amount of PrP^{Sc} in the fractions corresponding to P_1 and P_2 peaks was quantified. As shown in Figure 4.4 c, reconstitution of the PK-treated PMCA amplicons with $PrP^{0/0}$ brain homogenate did not allow B_i neoformation as compared with reconstitution in tg338 media. A depolymerization of B_i assemblies was even observed when the reconstitution was done in $PrP^{0/0}$ brain homogenate. Thus, at the resolution of this experiment, the contribution of PK-sensitive PrP conformers and protein cofactors appeared negligible. The formation of B_i assemblies upon reconstitution of PK-treated mb-PMCA product with tg338 brain homogenate also indicated that the N-terminal segment of A_i had a low contribution to the process.

Finally, the importance of PrP^C in the A_i to B_i transformation was further strengthened when comparing the quiescent evolution of non-PK-treated mb-PMCA products freshly reconstituted with tg338 brain homogenate with that of mb-PMCA products alone. As can be seen, the amount B_i assemblies formed was 1.4-fold increased upon fresh reconstitution (Figure 4.4 c).

Collectively, this set of reconstitution experiments indicates that the A_i to B_i transformation can be qualified as a pure PrP^C-dependent process without significant contribution of PK-susceptible cofactors. PrP^C requirement suggests that B_i assemblies result from the integration/conversion of PrP^C into A_i assemblies during the quiescent phase. The appearance of a low amount of B_i after a long incubation period without PrP^C may result from the leakage of monomers from a conformer cosedimenting with A_i.

Kinetic scheme describing the transformation of A_i to B_i

To establish a kinetic mechanism and provide a molecular interpretation of the assemblies dynamics during the quiescent phase, a number of elementary steps were identified based on experimental observations and were used as unavoidable constraints [56].
The first constraint was the existence of two structurally distinct PrP^{Sc} subassemblies, namely, A_i and B_i, with distinct dynamics. Indeed, structurally equivalent assemblies would fail to present a bimodal size distribution, cooperative seed concentration and kinetic evolution or distinct specific infectivity.
The second constraint was the existence of a detailed balance relation between the PrP^{Sc} assemblies and their elementary subunit (suPrP), as previously shown [74], making the size distribution of the PrP^{Sc} assemblies highly dynamic and dependent on the assembly concentration, as shown in Figure 4.2 e. Indeed, SV analysis of the $PrP^{0/0}$ brain lysates seeded with 30-fold-diluted 127S-infected brains and submitted to PMCA revealed a quaternary structure rearrangement with a shift in lower molecular

weight assemblies according to the detailed balance:

$$PrP_i^{Sc} \rightleftharpoons PrP_{i-1}^{Sc} + suPrP$$

where PrP_i^{Sc} and PrP_{i-1}^{Sc} are the sizes i and i-1 of suPrP^{Sc}, respectively.

The 3rd constraint is that the A_i and B_i assemblies are in detailed balance with their respective suPrPs (Figure 4.7, denoted $suPrP^A$ and $suPrP^B$) but with distinct equilibrium constants K_{eq}^A and K_{eq}^B. Thus, at any moment of the process of assembly transformation of A_i to B_i, the following equilibrium should be respected:

$$A_i \rightleftharpoons A_{i-1} + suPrP^A, B_i \rightleftharpoons B_{i-1} + suPrP^B. \tag{4.3}$$

The equilibrium constant $K_{eq}^{A_i}$ and $K_{eq}^{B_i}$ governs the respective size distribution of the A_i and B_i assemblies and, thus, the bimodal aspect of the curve. According to our previous SV calibrations with PrP oligomers and globular mass markers [157], the size distribution of the A_i and B_i subassemblies were fixed: $i_A < 5$ and i_B centered around 20 PrP-mers. Due to the limited resolution of SV fractionation for small assemblies, we assumed that A_i and suPrPB cosedimented. The fourth constraint relies on the fact that the transformation of A to B requires PrP^C and that the kinetic is cooperative, as shown in Figures 4.2 e and **??**. This cooperativity implies that B subassemblies facilitate their own formation according to an autocatalytic process. This can be resumed by the following minimalistic autocatalytic process:

$$C \rightleftharpoons suPrP^B + suPrP^A, C + PrP^C \rightarrow 2suPrP^B, \tag{4.4}$$

where C is an active complex reacting with PrP^C that generates B assemblies. Considering that $suPrP^B$ can condense into B_2 [74] and according to detailed balance (2), one can establish the reaction model describing the formation of B_i assemblies from the neo-formed $suPrP^B$:

$$2suPrP^B \rightleftharpoons B_2. \tag{4.5}$$

Altogether, these five elementary steps constitute the reaction mechanism that describes the transformation of A_i into B_i subassembly species. To validate the designed mechanism, we translated these elementary reactions into time-dependent differential equations and performed kinetic simulations using the size distribution of the PrP^{Sc} assemblies immediately after cyclic amplification as the initial condition (blue curve in Figure 4.3 a).

According to the model, the simulated size distribution variation as a function of time showed bimodal behavior, as was experimentally observed (Figure 4.8 a). Furthermore, the theoretical size distribution centroid presented similar sigmoidal patterns to those of the experimental data (Figure 4.8 b), arguing in favour of an autocatalytic kinetic model describing the overall quaternary structure evolution of PrP^{Sc} assemblies during the quiescent phase. The numerical analysis of the model revealed that the autocatalytic formation of B_i species occurs at the expense of A_i species and with PrP^C

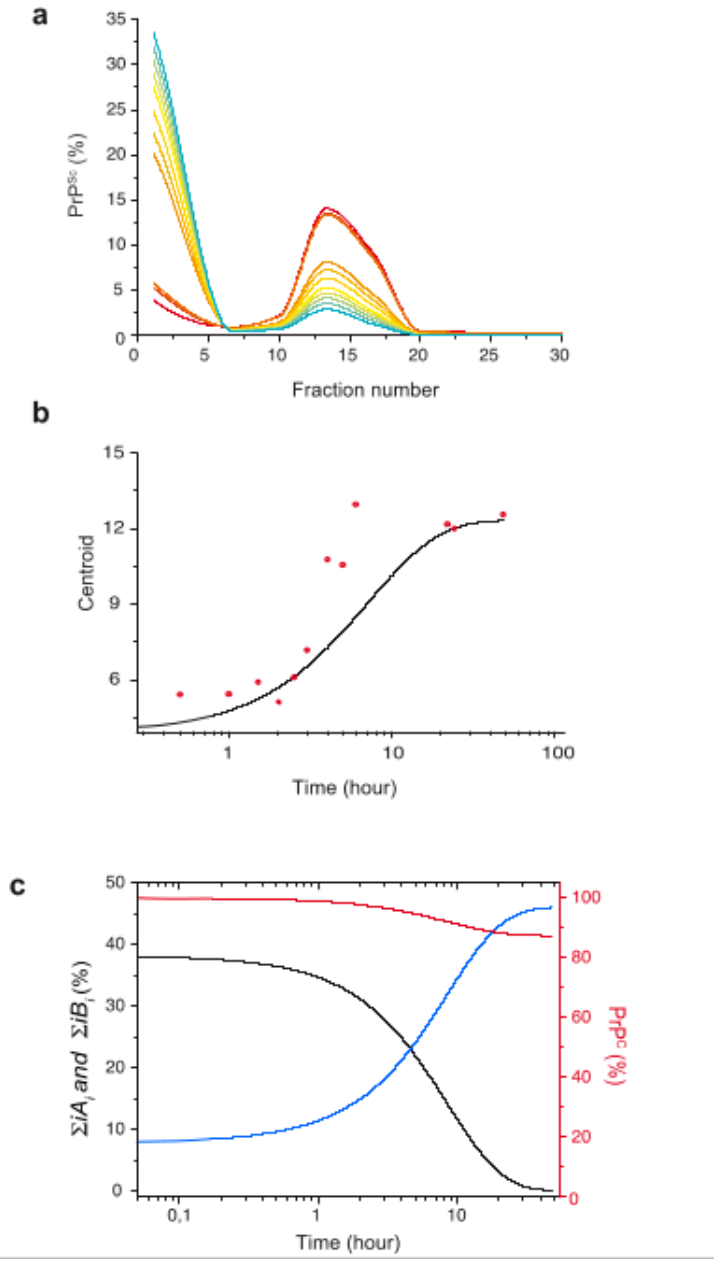

Figure 4.8 – **Mathematical modeling of the time-dependent dynamic evolution of the PMCA-generated PrP^{Sc} assemblies.** (a) The size distribution evolution of a structurally distinct set of assemblies A_i and B_i dimensioned on gradient fraction numbers was simulated based on the kinetic scheme described in the results section (equations (4.3) to (4.5)). (b) The time dependency evolution of the simulated centroid (black line) and centroid calculated from experimental sedimentograms of Figure 4.3 d (red circle) show a similar shape, supporting the cooperativity hypothesis of the transformation of A_i into B_i. (c) The simulation of time dependency evolution of the total amount of A_i assemblies ($\sum iA_i$ in black), B_i assemblies ($\sum iB_i$ in blue) and the monomer (in red) revealed that A_i assemblies constitute the limiting species for the conversion of PrP^C during the quiescent phase. In the present simulation framework, only 14% of PrP^C is consumed.

consumption (Figure 4.8 c). According to this model, when PrP^C is in large excess, A_i constitutes the limiting compound for the formation of B_i assemblies. Therefore, during the quiescent phase, the PrP^C

to PrP^{Sc} conversion rate is directly proportional to the amount of A_i assemblies (Figure 4.8 c).

4.2.3 Discussion

The mechanisms of prion replication and the dynamics responsible for prion structural diversification in the infected host remain unclear and rarely addressed. In the actual framework of the prion paradigm, the templating process is admitted to occur at the prion assembly interface, leading to an increased size of the complex formed by the template: substrate, out of the fragmentation/depolymerization context. The atypical size distribution observed here at the early stage of the replication process for three distinct prion strains, where accumulation of small-size assemblies dominates, contrasts with this canonical templating model and requires an additional process that considers the dynamics of replication.

As shown in vivo for the vCJD, 127S and 139A prion strains, the early stage of the replication process in the brain is dominated by the accumulation of small assemblies, whereas higher-size subsets are detected at the terminal stage of pathogenesis. Such quaternary structural diversity, - and beyond the existence of structurally distinct types of assemblies, as defined by their specific infectivity ([157, 84]), can be exclusively explained by the existence of a balance between at least two kinetic modes taking place at different stage of the pathogenesis. Both can be governed by evolution or a fluctuation in the replication micro-environment due to the physio-pathological state of the infected animal and/or to the sequential involvement of specific prion-replicating cell types.
However, another possibility can lie in the intrinsic and deterministic properties of the PrP replication process to generate structurally distinct types of assemblies. Discriminating between these two non-mutually exclusive hypotheses is technically difficult in vivo. The mb-PMCA as a bona fide amplification method in a more simplified and kinetically controlled context constitutes a relevant method for investigating the intrinsic propensity of the replication process to generate structurally distinct assemblies. Interestingly, and against common belief, the size distribution of the PrP^{Sc} assemblies used as seeds was relatively insensitive to mb-PMCA sonication cycles when a simple dilution displaced the assemblies towards a smaller size (Figure 4.3 e), as previously reported[74].
These two observations exclude the contribution of the fragmentation process during the mb-PMCA sonication cycles to the size distribution pattern of PrP^{Sc} assemblies and emphasize the existence of a constitutional dynamic between the PrP^{Sc} subpopulation [74], which should be considered during the replication process. We showed that two sets of PrP^{Sc} assemblies, A_i and B_i, were generated during the mb-PMCA reaction. The A_i and B_i assemblies constitute two structurally distinct PrP^{Sc} subpopulations. Beside the fact that the bimodal size distribution instead of a continuum constitutes an indirect but solid argument for structural differences in the PrP assemblies populating the P_1 and P_2 peaks, the best arguments are undoubtedly their distinct specific infectivity and the existence of two distinct elementary subunits as shown by SEC. The irreversibility of the P_1 to P_2 transformation (Figure **??**) physically demonstrates a PrP structural rearrangement associated to the $A_i \rightarrow B_i$ transformation process. Indeed, as evocated in the results section, the irreversible transformation of $A_i \rightarrow B_i$ can only be explained if

the process is thermodynamically favored through a structural rearrangement and the formation of higher stable object rendering the process irreversible. Therefore, the prion replication process per se intrinsically generates structurally diverse PrP^{Sc} subassemblies in a deterministic process.

According to our SV experiments, small-sized PrP^{Sc} assemblies were mainly formed at the early stage of prion replication in the brain and during the mb-PMCA reaction. This was observed with three distinct prion strains (127S, 139A, vCJD) on 3 different PrP genetic backgrounds. Considering that the PrP^{Sc} assemblies that constitute each strain are structurally distinct, one can ask how distinct PrP^{Sc} assemblies all can generate A_i assemblies that harbor strain structural information while showing the same quaternary structure (at the SV resolution). The first explanation can be the existence of a common narrow subpopulation of PrP^{Sc} (with respect to their quaternary structure) within the three strains that serves as the best replicator and participates in the formation of A_i assemblies.
However, the PrP^{Sc} quaternary structure subset that exhibits the highest specific infectivity in vivo (i.e., the best replicator) can be associated with either small-size assemblies (i.e., 127S and 139A in [157, 84]) or high-molecular-weight assemblies (i.e., vCJD) and is therefore strain-dependent. The existence of a structurally common PrP^{Sc} subpopulation is thus unlikely to be at the origin of the generic formation of a small-size subset in the brain or A_i assemblies in the mb-PMCA condition. Intrinsically, the early steps of the replication process favor the emergence of mainly one subspecies A_i with a highly narrowed size distribution, arguing in favor of a quaternary structural convergence phenomenon during these steps. This structural convergence concerns the PrP domain that governs polymerization (the size of assemblies). However, as the A assemblies harbor the strain structural determinant, one can conclude that A_i assemblies present a certain degree of structural variability, allowing strain structural information encoding.

All along the quiescent phase and for the three prion strains studied, the A_i assemblies constitute the precursor species in the formation of B_i assemblies. Furthermore, there is compelling evidence that the presence of PrP^{C} is required for the evolution of A_i into B_i assemblies. The set of reconstituted media experiments (Figure 4.4) led us to firmly exclude the contribution of PK-susceptible cofactors and highlighted the existence of a secondary templating pathway. In addition, the N-terminal part of PrP^{Sc} (at least for 127S seeds) is dispensable for $A_i \rightarrow B_i$ transformation, even if the yield of the process is significantly decreased when 127S PMCA products were PK-treated (i.e. removal of their N-terminal domain) before reconstitution and quiescent incubation with tg338 normal brain homogenate. This decrease could clearly be attributed to the kinetic effect of 2-fold dilution factor of both PrP^{C} and PMCA product occurring during the reconstitution process.

According to the kinetic model describing the autocatalytic formation of B_i during the quiescent phase, A_i is the limiting species for conversion when large amounts of PrP^{C} are present (Figure 4.8 c). Even if the first event conducing to the formation of B_i assemblies remains undetermined, we can assume that A_i can have the intrinsic propensity to spontaneously evolve into B_i assemblies in the presence of

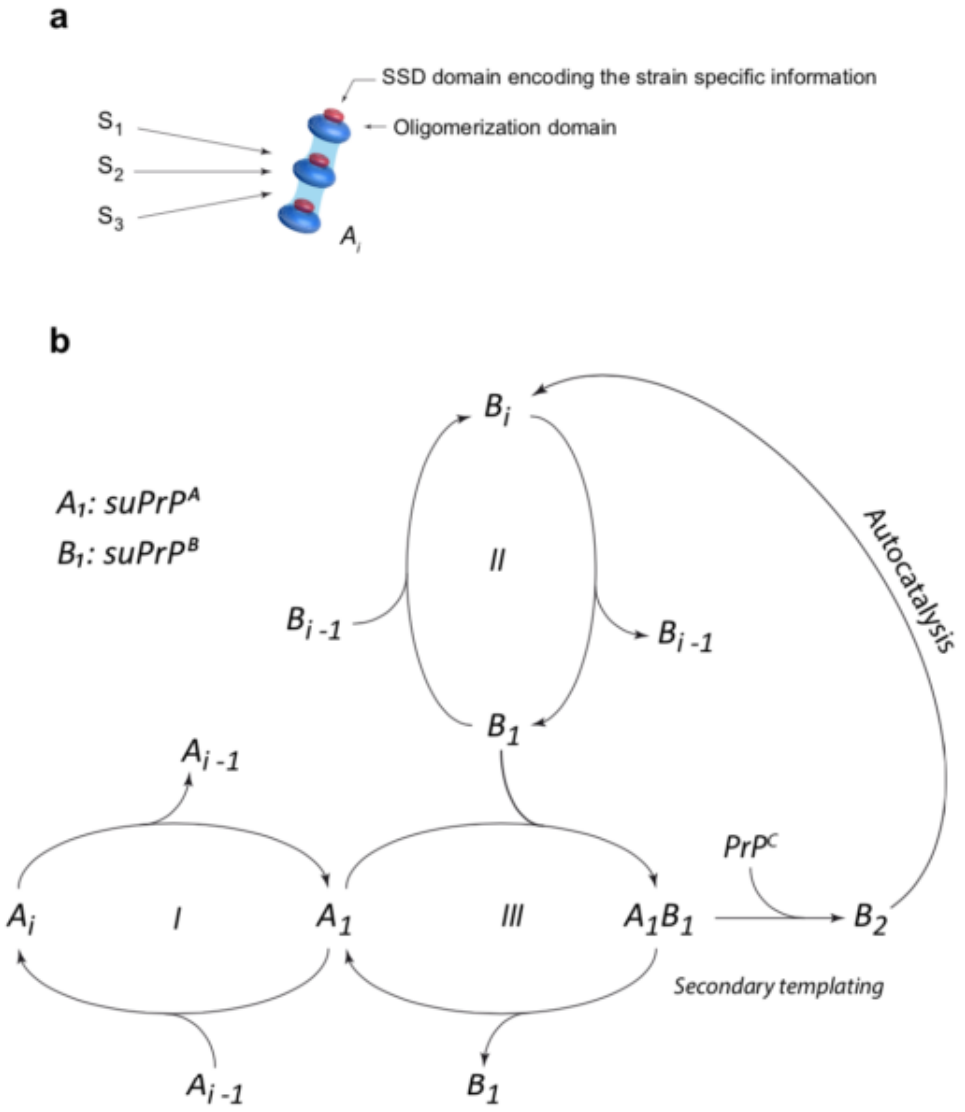

Figure 4.9 – **Quaternary structural convergence and secondary autocatalytic pathway at the root of the formation of B_i assemblies.** (a) Different prion strains (S_1, S_2 and S_3) give rise to the formation of common oligomeric assemblies, termed A_i, with a narrowed size distribution during mb-PMCA reactions. This common quaternary structural convergence at the early stage of the replication process suggests the existence of a common conversion pathway and a common oligomerization domain that is independent of the strain structural determinant (SSD, i.e., the PrP domain(s) harboring the replicative and strain information [74, 73], represented in red). (b) A_i and B_i assemblies are in an equilibrium/detailed balanced with their respective suPrP (step I and II) as was previously showed [74] and also demonstrated by the dilution experiment (see Figure 4.3 e). Based on the constraints imposed by the experimental observations, the best model to account for the cooperative and PrP^C dependency transformation of A_i into B_i assemblies implicates the formation of complex between $suPrP^A$ and $suPrP^B$ (step III). The formation of this complex is at the origin of a secondary templating pathway where the transformation of $suPrP^A$ (A_1) to $suPrP^B$ (B_1) is assisted by $suPrP^B$, making the process autocatalytic.

PrP^C (Figure 4.9). The cooperative disappearance of P_1 in favor of P_2 strongly suggests an autocatalytic process for the transformation of A_i to B_i (4.4)-(**??**). This last phenomenon shows the existence of a

secondary autocatalytic process, undescribed until now, in the canonical prion replication process [86]. It can be reasonably envisaged that A_i have the intrinsic propensity to generate B_i assemblies in the presence of PrP^C assemblies with a very low efficiency. This parallel pathway to the autocatalytic process can then explain how the first set of B_i assemblies is generated (Figure 4.9).
The existence of a secondary autocatalytic process can be a way to maintain PrP^{Sc} structural diversity throughout the evolution of the pathology. In the absence of this secondary autocatalytic process, the system only selects the best replicator assembly. In the present case, the best replicator is A_i assembly according to its specific infectivity (Figure 4.6). The secondary templating pathway allows the system to escape this rule, leading the accumulation of the autocatalytic pathway product (here, the B_i assemblies). This phenomenon can explain why, for certain prion strains, the most infectious assemblies represent a minor population, while those with the lowest specific infectivity mostly accumulate [157, 84].

4.2.4 Conclusion

The early step of prion replication for at least three distinct prion strains leads to the formation of small assemblies. The mb-PMCA approach clearly demonstrates the intrinsic properties of the bona fide replication process to generate at least two structurally distinct PrP^{Sc} subassemblies. The deterministic aspect of the replication process to generate a structurally diverse set of assemblies contrasts with the widespread idea that considers the prion diversification process within a given strain (often referred to as the creation of prion quasi-species) as a stochastic event and as a process that is governed by environmental fluctuations9. The secondary autocatalytic pathway leading to the formation of B_i subassemblies can participate in prion adaptation during transmission events with species barriers. Considering that the transmitted inoculum initially contains A_i and B_i assemblies, the autocatalytic conversion process of B_i can kinetically drive the adjustment and integration of the new-host PrP^C to generate host-adapted B_i assemblies. This hypothesis is supported by our recent observations in which complementation between A_i and B_i subassemblies is required to cross existing species barriers.

4.2.5 Methods

Ethics

Animal experiments were conducted in strict accordance with ECC and EU directives 86/009 and 2010/63 and were approved by the local ethics committee of the author's institution (Comethea; permit numbers 12/034 and 15/045).

Transgenic mouse lines and prion strains

The ovine (tg338 line; Val136-Arg154-Gln171 VRQ allele), human (tg650 line; Met129 allele) and mouse (tga20) PrP transgenic lines have been described previously[85, 60, 13]. The mouse lines were homozygous and overexpressed approximately 8-, 6-, and 10-fold amounts of heterologous PrP^C on a mouse PrP-null background. $PrP^{0/0}$ mice were Zürich-I mice [26]. Cloned 127S scrapie, human vCJD and

mouse 139A prion strains were serially passaged in tg338, tg650 and tga20 mice, respectively [103, 104]. These strains were used as pools of mouse-infected brains and prepared as 20% wt/vol homogenates in 5% glucose by use of a tissue homogenizer (Precellys 24 Ribolyzer; Ozyme, France).

Time course analysis of prion accumulation

Eight-week-old female tg338, tg650 and tga20 mice were inoculated intracerebrally in the right cerebral hemisphere with 127S, vCJD or 139A prions (20μl of a 10% brain homogenate dose). Infected animals were euthanized by cervical column disruption in triplicate at regular time points and at the terminal stage of disease. Brains were removed and kept for PrP^{Sc} size fractionation.

Miniaturized bead-PMCA assay

The miniaturized bead-PMCA (mb-PMCA) assay [34, 74, 104] was used to amplify prions. Briefly, serial ten-fold dilutions of 127S, vCJD and 139A prions (mouse brain homogenates diluted in PMCA buffer) were mixed with brain lysates (10% wt/vol) from healthy tg338, tg650 and tga20 mice as respective substrates and subjected to one round of 96 cycles of 30-s sonications (220-240 Watts) followed by 29.5 min of incubation at 37°C. With $a > 104$ dilution of the seeds, input PrP^{Sc} is not detected in the mb-PMCA products. PMCA was performed in a 96-well microplate format using a Q700 sonicator (QSonica, USA, Delta Labo, Colombelles, France). For quiescent incubation, the samples were left in the incubator at 37°C for the indicated period of time, without any sonication. To eliminate residual PrP^{C} present in the PMCA products before quiescent incubation, the samples were treated with PK (80 μg/ml final concentration). The treatment was stopped by adding 2 mM Pefabloc and 1x EDTA-free protease inhibitor cocktail. All final products were kept for PrP^{Sc} size fractionation, and aliquots were PK-digested (115 μg/ml final concentration, 0.6% SDS, 1 h, 37°C) prior to immunoblot analyses, as described below.
For reconstitution experiments, mb-PMCA products were generated with a 105-diluted 127S prion seed. At the end of the mb-PMCA reaction, the products were mixed, eventually treated with PK (150 μg/ml final concentration, 1h, 37°C). PK activity was inactivated by the combined addition of 4mM Pefabloc and 2x EDTA-free protease inhibitor cocktail. The products were then diluted 1:1 in either $PrP^{0/0}$ or in tg338 brain homogenate and incubated for 48h or 7 days at 37°C in quiescent conditions. The PMCA products were then fractionated by sedimentation velocity and analyzed for PrP^{Sc} content by immunoblot.

Sedimentation velocity (SV) fractionation

SV experiments were performed as described previously [157, 84, 74]. Mouse brain homogenates or PMCA products were solubilized by adding an equal volume of solubilization buffer (50 mM HEPES pH 7.4, 300 mM NaCl, 10 mM EDTA, 4% wt/vol dodecyl-β-D-maltoside (Sigma)) and incubated for 45 min on ice. Sarkosyl (N-lauryl sarcosine; Fluka) was added to a final concentration of 2% wt/vol, and the incubation continued for an additional 30 min on ice. A total of 150 μl of solubilized samples was loaded atop a 4.8-ml continuous 10-25% iodixanol gradient (Optiprep, Axys-Shield), with a final concentration

of 25 mM HEPES pH 7.4, 150 mM NaCl, 2 mM EDTA, 0.5% Sarkosyl. The gradients were centrifuged at 285,000 g for 45 min in a swinging-bucket SW-55 rotor using an Optima LE-80K ultracentrifuge (Beckman Coulter). Gradients were then manually segregated into 30 equal fractions of 165 μl from the bottom using a peristaltic pump and analyzed by immunoblotting or bioassay for PrP^{Sc} or infectivity, respectively. To avoid any cross-contamination, each piece of equipment was thoroughly decontaminated with 5 N NaOH followed by several rinses in deionized water after each gradient collection [84].

Isopycnic sedimentation

The entire procedure was performed as described previously [84]. Mouse brain homogenates or PMCA products were solubilized as described above. For mouse brain homogenates, solubilization was performed at 37°C to mimic PMCA conditions. A total of 220 μl of solubilized material was mixed to reach 40% iodixanol, 25 mM HEPES pH 7.4, 150 mM NaCl, 2 mM EDTA, 0.5% Sarkosyl final concentration and loaded within a 4.8 ml of 10-60% discontinuous iodixanol gradient with a final concentration of 25 mM HEPES pH 7.4, 150 mM NaCl, 2 mM EDTA, 0.5% Sarkosyl. The gradients were centrifuged at 115 000 g for 17 hours in a swinging-bucket SW-55 rotor using an Optima LE-80K ultracentrifuge (Beckman Coulter). Gradients were then manually segregated into 30 equal fractions of 165 μl from the bottom using a peristaltic pump and analyzed for PrP^{Sc} content by immunoblotting.

Size exclusion chromatography

SEC analysis was performed using an ÄKTA-100 purifier FPLC. 200 μl of the PMCA products were mixed with an equal volume of 2X-buffer to reach 25 mM HEPES pH 7.4, 150 mM NaCl, 10 mM EDTA, 35 mM n-Dodecyl β-D-Maltoside, 2 % w/w Sarkosyl and 0.5% Triton-X100 final concentration. After centrifugation at 10 000g for 3 min (no visible pellet), the solution was loaded on Superdex 200 10/300 GL column (24 ml, GE healthcare). The chromatography running buffer was HEPES 25 mM pH7.2, 200 mM NaCl, without detergents to avoid the formation of micellar structure. The flow rate was fixed at 0.35ml/min. After sample injection, the flow-through of the column was fractionated every 250 μl. The PrP levels per fraction were estimated by western blotting, as for SV. For molecular weight estimation, the Superdex 200 was calibrated with blue dextran molecules with varying molecular weight.

Analysis of PrP^{Sc} content by immunoblotting

Aliquots of the SV-fractionated PMCA samples were treated with PK (50 μg/ml final concentration, 1 h, 37°C) before mixing in Laemmli buffer and denaturation at 100°C for 5 min. The samples were run on 12% Bis-Tris Criterion gels (Bio-Rad, Marne la Vallée, France) and electrotransferred onto nitrocellulose membranes. In some instances, denatured samples were spotted onto nitrocellulose membranes using a dot-blot apparatus (Schleicher and Schuell BioScience (Whatman)). Nitrocellulose membranes were probed for PrP with 0.1 μg/ml biotinylated anti-PrP monoclonal antibody Sha31. Immunoreactivity was visualized by chemiluminescence (GE Healthcare). The protein levels were quantified with ImageLab software after acquisition of chemiluminescent signals with a Chemidoc digital imager (Bio-Rad,

Marnes-la-Coquette, France). For all SDS-PAGE analyses, a fixed quantity of human recombinant PrP was employed for consistent calibration of the PrP signals in different gels.

To improve the sensitivity of the western blot detection method for the samples containing low levels of PrP^{res} (e.g., early samples and SEC fractions) a double-deposit was made to electro-concentrate the sample. Typically, after a first round of sample loading in SDS-PAGE wells, a short migration time was performed to allow running within the acrylamide gel for 2mm. Then, a second round of sample loading was done identically to the first one and the migration was continued until the front reached 3cm within the gel. The electrotransfer and detection was then identical as above.

Bioassays

The pool of fractions of interest was extemporarily diluted ten-fold in 5% glucose and immediately inoculated via the intracerebral route into reporter tg338 mice (20 μl per pool of fraction, $n = 5$ mice per pool). Mice showing prion-specific neurological signs were euthanized at the end stage. To confirm prion disease, brains were removed and analyzed for PrP^{Sc} content using the Bio-Rad TsSeE detection kit [90] prior to immunoblotting, as described above. The survival time was defined as the number of days from inoculation to euthanasia. To estimate what the difference in mean survival times means in terms of infectivity, strain-specific curves correlating the relative infectious dose to survival times were used, as previously described [157].

Bibliography

[1] Masayuki Adachi et al. "Supersaturation-limited and unlimited phase transitions compete to produce the pathway complexity in amyloid fibrillation". In: *Journal of Biological Chemistry* 290.29 (2015), pp. 18134–18145.

[2] Myles R Allen and Leonard A Smith. "Monte Carlo SSA: Detecting irregular oscillations in the presence of colored noise". In: *Journal of climate* 9.12 (1996), pp. 3373–3404.

[3] Tikvah Alper et al. "Does the agent of scrapie replicate without nucleic acid?" In: *Nature* 214.5090 (1967), p. 764.

[4] Rachel C Angers et al. "Prion strain mutation determined by prion protein conformational compatibility and primary structure". In: *Science* 328.5982 (2010), pp. 1154–1158.

[5] Aurora Armiento et al. "Estimation from Moments Measurements for Amyloid Depolymerisation". In: *Journal of Theoretical Biology* (2016). URL: https://hal.archives-ouvertes.fr/hal-01248255.

[6] Aurora Armiento et al. "The mechanism of monomer transfer between two structurally distinct PrP oligomers". In: *PLoS ONE* 12.7 (2017). DOI: 10.1371/journal.pone.0180538. URL: https://hal.archives-ouvertes.fr/hal-01574346.

[7] John M Ball, Jack Carr, and Oliver Penrose. "The Becker-Döring cluster equations: basic properties and asymptotic behaviour of solutions". In: *Communications in mathematical physics* 104.4 (1986), pp. 657–692.

[8] Jiayin Bao et al. "Pre-equilibration kinetic size-exclusion chromatography with mass spectrometry detection (peKSEC-MS) for label-free solution-based kinetic analysis of protein–small molecule interactions". In: *Analyst* 140.4 (2015), pp. 990–994.

[9] R. Becker and W. Döring. "Kinetische Behandlung der Keimbildung in übersättigten Dämpfen". In: *Annalen der Physik* 416.8 (1935), pp. 719–752. ISSN: 1521-3889. DOI: 10.1002/andp.19354160806. URL: http://dx.doi.org/10.1002/andp.19354160806.

[10] Ermias D Belay. "Transmissible spongiform encephalopathies in humans". In: *Annual Reviews in Microbiology* 53.1 (1999), pp. 283–314.

[11] Ermias D Belay and Lawrence B Schonberger. "The public health impact of prion diseases". In: *Annu. Rev. Public Health* 26 (2005), pp. 191–212.

[12] Vincent Béringue, Jean-Luc Vilotte, and Hubert Laude. "Prion agent diversity and species barrier". In: *Veterinary research* 39.4 (2008), pp. 1–30.

[13] Vincent Béringue et al. "Prominent and persistent extraneural infection in human PrP transgenic mice infected with variant CJD". In: *PloS one* 3.1 (2008), e1419.

[14] Etienne Bernard, Marie Doumic, and Pierre Gabriel. "Cyclic asymptotic behaviour of a population reproducing by fission into two equal parts". In: *arXiv preprint arXiv:1609.03846* (2016).

[15] Richard A Bessen and Richard F Marsh. "Distinct PrP properties suggest the molecular basis of strain variation in transmissible mink encephalopathy." In: *Journal of virology* 68.12 (1994), pp. 7859–7868.

[16] Cyrus Bett et al. "Biochemical properties of highly neuroinvasive prion strains". In: *PLoS pathogens* 8.2 (2012), e1002522.

[17] Cyrus Bett et al. "Enhanced neuroinvasion by smaller, soluble prions". In: *Acta neuropathologica communications* 5.1 (2017), p. 32.

[18] M.F. Bishop and F.A. Ferrone. "Kinetics of nucleation-controlled polymerization. A perturbation treatment for use with a secondary pathway". In: *Biophysical Journal* 46.5 (1984), pp. 631–644. ISSN: 0006-3495. DOI: 10.1016/S0006-3495(84)84062-X.

[19] David C Bolton, Michael P McKinley, and Stanley B Prusiner. "Identification of a protein that purifies with the scrapie prion". In: *Science* 218.4579 (1982), pp. 1309–1311.

[20] Immanuel M. Bomze. "Lotka-Volterra equation and replicator dynamics: A two-dimensional classification". In: *Biological Cybernetics* 48.3 (1983), pp. 201–211. URL: https://doi.org/10.1007/BF00318088.

[21] Leonid Breydo, Natallia Makarava, and Ilia V Baskakov. "Methods for conversion of prion protein into amyloid fibrils". In: *Prion Protein Protocols*. Springer, 2008, pp. 105–115.

[22] David S Broomhead and Roger Jones. "Time-series analysis". In: *Proc. R. Soc. Lond. A* 423.1864 (1989), pp. 103–121.

[23] Moira E Bruce. "TSE strain variation: An investigation into prion disease diversity". In: *British medical bulletin* 66.1 (2003), pp. 99–108.

[24] Patrik Brundin, Ronald Melki, and Ron Kopito. "Prion-like transmission of protein aggregates in neurodegenerative diseases". In: *Nature reviews Molecular cell biology* 11.4 (2010), p. 301.

[25] Jonathan Buckheit et al. "Wavelab reference manual". In: *Version 0.700, December* (1995).

[26] Hansruedi Büeler et al. "Normal development and behaviour of mice lacking the neuronal cell-surface PrP protein". In: *Nature* 356.6370 (1992), p. 577.

[27] Juan Calvo, Marie Doumic, and Benoît Perthame. "Long-time asymptotics for polymerization models". In: *Communications in Mathematical Physics* 363.1 (2018), pp. 111–137.

[28] José Cañizo, Amit Einav, and Bertrand Lods. "Trend to equilibrium for the Becker–Döring equations: An analogue of Cercignani's conjecture". In: *Analysis & PDE* 10.7 (2017), pp. 1663–1708.

[29] José A Canizo, Amit Einav, and Bertrand Lods. "Uniform moment propagation for the Becker–Döring equations". In: *Proceedings of the Royal Society of Edinburgh Section A: Mathematics* 149.4 (2019), pp. 995–1015.

[30] José A Canizo and Bertrand Lods. "Exponential convergence to equilibrium for subcritical solutions of the Becker–Döring equations". In: *Journal of Differential Equations* 255.5 (2013), pp. 905–950.

[31] José A Carrillo and Thierry Goudon. "A numerical study on large-time asymptotics of the Lifshitz–Slyozov system". In: *Journal of Scientific Computing* 20.1 (2004), pp. 69–113.

[32] Carlos Castillo-Chavez, Horst Thieme, et al. "Asymptotically autonomous epidemic models". In: (1994).

[33] Byron Caughey and Peter T Lansbury Jr. "Protofibrils, pores, fibrils, and neurodegeneration: separating the responsible protein aggregates from the innocent bystanders". In: *Annual review of neuroscience* 26.1 (2003), pp. 267–298.

[34] Jérôme Chapuis et al. “Emergence of two prion subtypes in ovine PrP transgenic mice infected with human MM2-cortical Creutzfeldt-Jakob disease prions”. In: *Acta neuropathologica communications* 4.1 (2016), p. 10.

[35] Tapan K Chaudhuri and Subhankar Paul. “Protein-misfolding diseases and chaperone-based therapeutic approaches”. In: *The FEBS journal* 273.7 (2006), pp. 1331–1349.

[36] James L Cole et al. “Analytical ultracentrifugation: sedimentation velocity and sedimentation equilibrium”. In: *Methods in cell biology* 84 (2008), pp. 143–179.

[37] Jean-François Collet and Thierry Goudon. “On solutions of the Lifshitz-Slyozov model”. In: *Nonlinearity* 13.4 (2000), p. 1239.

[38] Jean-François Collet et al. “Some modelling issues in the theory of fragmentation-coagulation systems”. In: *Communications in Mathematical Sciences* 2.Supplemental Issue (2004), pp. 35–54.

[39] Jean-Francois Collet et al. “The Becker–Döring System and Its Lifshitz–Slyozov Limit”. In: *SIAM Journal on Applied Mathematics* 62.5 (2002), pp. 1488–1500.

[40] John Collinge. “Prion diseases of humans and animals: their causes and molecular basis”. In: *Annual review of neuroscience* 24.1 (2001), pp. 519–550.

[41] John Collinge and Anthony R. Clarke. “A General Model of Prion Strains and Their Pathogenicity”. In: *Science* 318.5852 (2007), pp. 930–936. ISSN: 0036-8075. DOI: 10.1126/science.1138718. eprint: http://science.sciencemag.org/content/318/5852/930.full.pdf. URL: http://science.sciencemag.org/content/318/5852/930.

[42] John Collinge and Anthony R Clarke. “A general model of prion strains and their pathogenicity”. In: *Science* 318.5852 (2007), pp. 930–936.

[43] Carlo Condello and Jan Stöehr. “Aβ propagation and strains: implications for the phenotypic diversity in Alzheimer’s disease”. In: *Neurobiology of disease* 109 (2018), pp. 191–200.

[44] Joseph G Conlon, Michael Dabkowski, and Jingchen Wu. “On Large Time Behavior and Selection Principle for a Diffusive Carr–Penrose Model”. In: *Journal of Nonlinear Science* 26.2 (2016), pp. 453–518.

[45] Peter Debye. “Light scattering in solutions”. In: *Journal of Applied Physics* 15.4 (1944), pp. 338–342.

[46] Borries Demeler and Kensal E van Holde. “Sedimentation velocity analysis of highly heterogeneous systems”. In: *Analytical biochemistry* 335.2 (2004), pp. 279–288.

[47] Laurent Desvillettes and Klemens Fellner. “ Exponential decay toward equilibrium via entropy methods for reaction–diffusion equations”. In: *J. Math. Anal. Appl.* 319 (2006), pp. 157–176.

[48] Laurent Desvillettes, Klemens Fellner, and Bao Quoc Tang. “Trend to equilibrium for reaction-diffusion systems arising from complex balanced chemical reaction networks”. In: *SIAM Journal on Math. Analysis* 49.4 (2017), pp. 2666–2709.

[49] David L Donoho and Iain M Johnstone. “Threshold selection for wavelet shrinkage of noisy data”. In: *Engineering in Medicine and Biology Society, 1994. Engineering Advances: New Opportunities for Biomedical Engineers. Proceedings of the 16th Annual International Conference of the IEEE*. Vol. 1. IEEE. 1994, A24–A25.

[50] David L Donoho, Iain M Johnstone, et al. “Minimax estimation via wavelet shrinkage”. In: *The annals of Statistics* 26.3 (1998), pp. 879–921.

[51] David L Donoho and Jain M Johnstone. “Ideal spatial adaptation by wavelet shrinkage”. In: *biometrika* 81.3 (1994), pp. 425–455.

[52] David L Donoho et al. “Wavelet shrinkage: asymptopia?” In: *Journal of the Royal Statistical Society. Series B (Methodological)* (1995), pp. 301–369.

[53] Marie Doumic, Thierry Goudon, Thomas Lepoutre, et al. "Scaling limit of a discrete prion dynamics model". In: *Communications in Mathematical Sciences* 7.4 (2009), pp. 839–865.

[54] Marie Doumic et al. "A bi-monomeric, nonlinear Becker-Döring-type system to capture oscillatory aggregation kinetics in prion dynamics". preprint. 2018. URL: https://hal.archives-ouvertes.fr/hal-01863748.

[55] Marie Doumic et al. "A bi-monomeric, nonlinear Becker-Döring-type system to capture oscillatory aggregation kinetics in prion dynamics". In: *Journal of theoretical biology* (2019).

[56] Irving R Epstein and John A Pojman. *An introduction to nonlinear chemical dynamics: oscillations, waves, patterns, and chaos*. Oxford University Press, 1998.

[57] Klemens Fellner and Bao Quoc Tang. "Convergence to equilibrium of renormalised solutions to nonlinear chemical reaction-diffusion systems". In: *ZAMP* 69:54 (2018).

[58] Klemens Fellner and Bao Quoc Tang. "Explicit exponential convergence to equilibrium for nonlinear reaction-diffusion systems with detailed balance condition". In: *Nonlinear Analysis* 159 (2017), pp. 145–180.

[59] Francis Filbet and Philippe Laurençot. "Numerical Approximation of the Lifshitz–Slyozov–Wagner Equation". In: *SIAM journal on numerical analysis* 41.2 (2003), pp. 563–588.

[60] Marek Fischer et al. "Prion protein (PrP) with amino-proximal deletions restoring susceptibility of PrP knockout mice to scrapie." In: *The EMBO journal* 15.6 (1996), pp. 1255–1264.

[61] Ricardo Gaspar et al. "Secondary nucleation of monomers on fibril surface dominates α-synuclein aggregation and provides autocatalytic amyloid amplification". In: *Quarterly reviews of biophysics* 50 (2017).

[62] Nina Golyandina, Vladimir Nekrutkin, and Anatoly A Zhigljavsky. *Analysis of time series structure: SSA and related techniques*. Chapman and Hall/CRC, 2001.

[63] Thierry Goudon, Frédéric Lagoutiere, and Léon M Tine. "The Lifschitz-Slyozov equation with space-diffusion of monomers". In: *Kinetic and Related Models* 5.2 (2012), pp. 325–355.

[64] John Graham. "Formation of self-generated gradients of iodixanol". In: *The Scientific World Journal* 2 (2002), pp. 1356–1360.

[65] John Graham. "Preparation of preformed iodixanol gradients". In: *The Scientific World Journal* 2 (2002), pp. 1351–1355.

[66] John S Griffith. "Nature of the scrapie agent: Self-replication and scrapie". In: *Nature* 215.5105 (1967), p. 1043.

[67] Sophie Halliez et al. "Accelerated, spleen-based titration of variant Creutzfeldt-Jakob disease infectivity in transgenic mice expressing human prion protein with sensitivity comparable to that of survival time bioassay". In: *Journal of virology* 88.15 (2014), pp. 8678–8686.

[68] Pentti Haukkanen and Timo Tossavainen. "A generalization of Descartes' rule of signs and fundamental theorem of algebra". In: *Applied Mathematics and Computation* 218.4 (2011), pp. 1203–1207.

[69] Erwan Hingant and Romain Yvinec. "Deterministic and stochastic Becker–Döring equations: Past and recent mathematical developments". In: *Stochastic processes, multiscale modeling, and numerical methods for computational cellular biology*. Springer, 2017, pp. 175–204.

[70] Josef Hofbauer and Karl Sigmund. *Evolutionary games and population dynamics*. Cambridge university press, 1998.

[71] Fritz Horn. "Necessary and sufficient conditions for complex balancing in chemical kinetics". In: *Archive for Rational Mechanics and Analysis* 49.3 (1972), pp. 172–186.

[72] Geoffrey J Howlett, Allen P Minton, and Germán Rivas. "Analytical ultracentrifugation for the study of protein association and assembly". In: *Current opinion in chemical biology* 10.5 (2006), pp. 430–436.

[73] Angélique Igel-Egalon et al. "Heterogeneity and Architecture of Pathological Prion Protein Assemblies: Time to Revisit the Molecular Basis of the Prion Replication Process?" In: *Viruses* 11.5 (2019), p. 429.

[74] Angélique Igel-Egalon et al. "Reversible unfolding of infectious prion assemblies reveals the existence of an oligomeric elementary brick". In: *PLoS pathogens* 13.9 (2017), e1006557.

[75] Pierre-Emmanuel Jabin and Barbara Niethammer. "On the rate of convergence to equilibrium in the Becker–Döring equations". In: *Journal of Differential Equations* 191.2 (2003), pp. 518–543.

[76] Joseph T Jarrett and Peter T Lansbury Jr. "Seeding "one-dimensional crystallization" of amyloid: a pathogenic mechanism in Alzheimer's disease and scrapie?" In: *Cell* 73.6 (1993), pp. 1055–1058.

[77] John Edward Jones. "On the determination of molecular fields.—II. From the equation of state of a gas". In: *Proceedings of the Royal Society of London. Series A, Containing Papers of a Mathematical and Physical Character* 106.738 (1924), pp. 463–477.

[78] Niels Jonker et al. "Recent developments in protein–ligand affinity mass spectrometry". In: *Analytical and bioanalytical chemistry* 399.8 (2011), pp. 2669–2681.

[79] Mathias Jucker and Lary C Walker. "Pathogenic protein seeding in Alzheimer disease and other neurodegenerative disorders". In: *Annals of neurology* 70.4 (2011), pp. 532–540.

[80] Mathias Jucker and Lary C Walker. "Self-propagation of pathogenic protein aggregates in neurodegenerative diseases". In: *Nature* 501.7465 (2013), p. 45.

[81] Chae Kim et al. "Small protease sensitive oligomers of PrPSc in distinct human prions determine conversion rate of PrPC". In: *PLoS pathogens* 8.8 (2012), e1002835.

[82] Seung-Jean Kim et al. "ℓ_1 Trend Filtering". In: *SIAM review* 51.2 (2009), pp. 339–360.

[83] John R King and Jonathan AD Wattis. "Asymptotic solutions of the Becker–Döring equations with size-dependent rate constants". In: *Journal of Physics A: Mathematical and General* 35.6 (2002), p. 1357.

[84] Florent Laferrière et al. "Quaternary structure of pathological prion protein as a determining factor of strain-specific prion replication dynamics". In: *PLoS pathogens* 9.10 (2013), e1003702.

[85] Christelle Langevin et al. "Marked influence of the route of infection on prion strain apparent phenotype in a scrapie transgenic mouse model". In: *Neurobiology of disease* 41.1 (2011), pp. 219–225.

[86] Peter T Lansbury Jr and Byron Caughey. "The chemistry of scrapie infection: implications of the 'ice 9'metaphor". In: *Chemistry & biology* 2.1 (1995), pp. 1–5.

[87] Philippe Laurençot. "Weak Solutions to the Lifshitz-Slyozov-Wagner Equation". In: *Indiana University Mathematics Journal* 50.3 (2001), pp. 1319–1346. URL: http://www.jstor.org/stable/24901638.

[88] Philippe Laurençot and Stéphane Mischler. "From the Becker–Döring to the Lifshitz–Slyozov–Wagner equations". In: *Journal of statistical physics* 106.5-6 (2002), pp. 957–991.

[89] Philippe Laurençot and Stéphane Mischler. "From the discrete to the continuous coagulation–fragmentation equations". In: *Proceedings of the Royal Society of Edinburgh Section A: Mathematics* 132.5 (2002), pp. 1219–1248.

[90] Annick Le Dur et al. "A newly identified type of scrapie agent can naturally infect sheep with resistant PrP genotypes". In: *Proceedings of the National Academy of Sciences* 102.44 (2005), pp. 16031–16036.

[91] Annick Le Dur et al. "Divergent prion strain evolution driven by PrP C expression level in transgenic mice". In: *Nature communications* 8 (2017), p. 14170.

[92] Jacob Lebowitz, Marc S Lewis, and Peter Schuck. "Modern analytical ultracentrifugation in protein science: a tutorial review". In: *Protein science* 11.9 (2002), pp. 2067–2079.

[93] Giuseppe Legname et al. "Synthetic mammalian prions". In: *Science* 305.5684 (2004), pp. 673–676.

[94] Jiali Li et al. "Darwinian evolution of prions in cell culture". In: *Science* 327.5967 (2010), pp. 869–872.

[95] Ilya M Lifshitz and Vitaly V Slyozov. "The kinetics of precipitation from supersaturated solid solutions". In: *Journal of physics and chemistry of solids* 19.1-2 (1961), pp. 35–50.

[96] Stéphane Mallat. *A wavelet tour of signal processing*. Elsevier, 1999.

[97] L Markus. "Ii. asymptotically autonomous differential systems". In: *Contributions to the Theory of Nonlinear Oscillations (AM-36)* 3 (2016), p. 17.

[98] J. Masel, V. A. Jansen, and M. A. Nowak. "Quantifying the kinetic parameters of prion replication." In: *Biophys. Chem.* 77 (1999), pp. 139–152.

[99] Joanna Masel, Vincent AA Jansen, and Martin A Nowak. "Quantifying the kinetic parameters of prion replication". In: *Biophysical chemistry* 77.2-3 (1999), pp. 139–152.

[100] Mathieu Mezache et al. "Structural polydispersity of Prion assemblies governs their constitutional dynamics". submitted.

[101] Richard G Miller and RA Phillips. "Separation of cells by velocity sedimentation". In: *Journal of cellular physiology* 73.3 (1969), pp. 191–201.

[102] John W Moore and Ralph G Pearson. *Kinetics and mechanism*. John Wiley & Sons, 1981.

[103] Mohammed Moudjou et al. "Glycoform-independent prion conversion by highly efficient, cell-based, protein misfolding cyclic amplification". In: *Scientific reports* 6 (2016), p. 29116.

[104] Mohammed Moudjou et al. "Highly infectious prions generated by a single round of microplate-based protein misfolding cyclic amplification". In: *MBio* 5.1 (2014), e00829–13.

[105] Emilie Moulin and Nicolas Giuseppone. "Dynamic combinatorial self-replicating systems". In: *Constitutional Dynamic Chemistry*. Springer, 2011, pp. 87–105.

[106] Victor Munoz et al. "Folding and aggregation kinetics of a β-hairpin". In: *Biochemistry* 45.23 (2006), pp. 7023–7035.

[107] Ryota Nakaoke et al. "Early appearance but lagged accumulation of detergent-insoluble prion protein in the brains of mice inoculated with a mouse-adapted Creutzfeldt–Jakob disease agent". In: *Cellular and molecular neurobiology* 20.6 (2000), pp. 717–730.

[108] Sean Nee. "The evolutionary ecology of molecular replicators". In: *Royal Society Open Science* 3.8 (2016), p. 160235.

[109] Barbara Niethammer. "Derivation of the LSW-Theory for Ostwald Ripening by Homogenization Methods". In: *Archive for rational mechanics and analysis* 147.2 (1999), pp. 119–178.

[110] Barbara Niethammer. "On the Evolution of Large Clusters in the Becker-Döring Model." In: *Journal of Nonlinear Science* 13.1 (2003), pp. 115–122.

[111] Barbara Niethammer and Robert L. Pego. "Non-Self-Similar Behavior in the LSW Theory of Ostwald Ripening". In: *Journal of Statistical Physics* 95.5 (1999), pp. 867–902. DOI: 10.1023/A:1004546215920. URL: https://doi.org/10.1023/A:1004546215920.

[112] Barbara Niethammer and Robert L Pego. "On the Initial-Value Problem in the Lifshitz–Slyozov–Wagner Theory of Ostwald Ripening". In: *SIAM Journal on Mathematical Analysis* 31.3 (2000), pp. 467–485.

[113] Yumiko Ohhashi et al. "Molecular basis for diversification of yeast prion strain conformation". In: *Proceedings of the National Academy of Sciences* 115.10 (2018), pp. 2389–2394.

[114] Samuel Ojosnegros et al. "Quasispecies as a matter of fact: viruses and beyond". In: *Virus research* 162.1-2 (2011), pp. 203–215.

[115] Hisashi Okumura and Satoru G Itoh. "Amyloid fibril disruption by ultrasonic cavitation: nonequilibrium molecular dynamics simulations". In: *Journal of the American Chemical Society* 136.30 (2014), pp. 10549–10552.

[116] Milan Palus and Dagmar Novotná. "Detecting modes with nontrivial dynamics embedded in colored noise: Enhanced Monte Carlo SSA and the case of climate oscillations". In: *Physics Letters A* 248.2-4 (1998), pp. 191–202.

[117] Milan Paluš and Dagmar Novotná. "Detecting oscillations hidden in noise: Common cycles in atmospheric, geomagnetic and solar data". In: *Nonlinear Time Series Analysis in the Geosciences*. Springer, 2008, pp. 327–353.

[118] Keh-Ming Pan et al. "Conversion of alpha-helices into beta-sheets features in the formation of the scrapie prion proteins". In: *Proceedings of the National Academy of Sciences* 90.23 (1993), pp. 10962–10966.

[119] Iain H Pattison et al. "Resistance of the scrapie agent to formalin." In: *Journal of comparative pathology* 75 (1965), pp. 159–164.

[120] Robert L Pego and Juan JL Velázquez. "Temporal oscillations in Becker-Döring equations with atomization". In: *arXiv preprint arXiv:1905.02605* (2019).

[121] O Penrose. "The Becker-Döring equations for the kinetics of phase transitions". In: *Math. Proc. Camb. Phil. Soc*. Vol. 96. 2001.

[122] O Penrose et al. "Growth of clusters in a first-order phase transition". In: *Journal of Statistical Physics* 19.3 (1978), pp. 243–267.

[123] Oliver Penrose. "Metastable states for the Becker-Döring cluster equations". In: *Communications in Mathematical Physics* 124.4 (1989), pp. 515–541.

[124] Oliver Penrose and Joel L Lebowitz. "Towards a rigorous molecular theory of metastability". In: *Fluctuation Phenomena* 7 (1987), pp. 293–340.

[125] Benoît Perthame. "Parabolic equations in biology". In: *Parabolic Equations in Biology*. Springer, 2015, pp. 1–21.

[126] S. Prigent et al. "An Efficient Kinetic Model for Assemblies of Amyloid Fibrils and Its Application to Polyglutamine Aggregation". In: *PLoS ONE* 7.11 (Nov. 2012), e43273. DOI: 10.1371/journal.pone.0043273.

[127] Stéphanie Prigent and Human Rezaei. "PrP assemblies: spotting the responsible regions in prion propagation". In: *Prion* 5.2 (2011), pp. 69–75.

[128] Stéphanie Prigent et al. "An efficient kinetic model for assemblies of amyloid fibrils and its application to polyglutamine aggregation". In: *PLoS One* 7.11 (2012), e43273.

[129] Stanley B Prusiner. "Molecular biology of prion diseases". In: *Science* 252.5012 (1991), pp. 1515–1522.

[130] Stanley B Prusiner. "Novel proteinaceous infectious particles cause scrapie". In: *Science* 216.4542 (1982), pp. 136–144.

[131] Stanley B Prusiner. "Prions". In: *Proceedings of the National Academy of Sciences* 95.23 (1998), pp. 13363–13383.

[132] Stanley B Prusiner and Michael R Scott. "Genetics of prions". In: *Annual review of genetics* 31.1 (1997), pp. 139–175.

[133] Stanley B Prusiner et al. "Ablation of the prion protein (PrP) gene in mice prevents scrapie and facilitates production of anti-PrP antibodies". In: *Proceedings of the National Academy of Sciences* 90.22 (1993), pp. 10608–10612.

[134] Morten O Ravn and Harald Uhlig. "On adjusting the Hodrick-Prescott filter for the frequency of observations". In: *Review of economics and statistics* 84.2 (2002), pp. 371–376.

[135] Joseph B Rayman and Eric R Kandel. "Functional prions in the brain". In: *Cold Spring Harbor perspectives in biology* 9.1 (2017), a023671.

[136] Christian H Reinsch. "Smoothing by spline functions". In: *Numerische mathematik* 10.3 (1967), pp. 177–183.

[137] Gabriela P Saborio, Bruno Permanne, and Claudio Soto. "Sensitive detection of pathological prion protein by cyclic amplification of protein misfolding". In: *Nature* 411.6839 (2001), p. 810.

[138] Gustavo Sajnani et al. "PK-sensitive PrPSc is infectious and shares basic structural features with PK-resistant PrPSc". In: *PLoS pathogens* 8.3 (2012), e1002547.

[139] Malin K Sandberg et al. "Prion neuropathology follows the accumulation of alternate prion protein isoforms after infective titre has peaked". In: *Nature communications* 5 (2014), p. 4347.

[140] Malin K Sandberg et al. "Prion propagation and toxicity in vivo occur in two distinct mechanistic phases". In: *Nature* 470.7335 (2011), p. 540.

[141] Howard K Schachman. *Ultracentrifugation in biochemistry*. Elsevier, 2013.

[142] André Schlichting. "Macroscopic limit of the Becker–Döring equation via gradient flows". In: *ESAIM: Control, Optimisation and Calculus of Variations* 25 (2019), p. 22.

[143] John S Schreck and Jian-Min Yuan. "A kinetic study of amyloid formation: fibril growth and length distributions". In: *The Journal of Physical Chemistry B* 117.21 (2013), pp. 6574–6583.

[144] Peter Schuck. "Size-distribution analysis of macromolecules by sedimentation velocity ultracentrifugation and lamm equation modeling". In: *Biophysical journal* 78.3 (2000), pp. 1606–1619.

[145] David J Scott and PETER Schuck. "A brief introduction to the analytical ultracentrifugation of proteins for beginners". In: *Analytical Ultracentrifugation: Techniques and Methods*. Royal Society of Chemistry Cambridge, England, 2005.

[146] Björn Sigurdsson. "Rida, a chronic encephalitis of sheep: with general remarks on infections which develop slowly and some of their special characteristics". In: *Br. vet. J.* 110 (1954), pp. 341–354.

[147] Jay R Silveira et al. "The most infectious prion protein particles". In: *Nature* 437.7056 (2005), p. 257.

[148] Valerie L Sim and Byron Caughey. "Ultrastructures and strain comparison of under-glycosylated scrapie prion fibrils". In: *Neurobiology of aging* 30.12 (2009), pp. 2031–2042.

[149] Steve Simoneau et al. "In vitro and in vivo neurotoxicity of prion protein oligomers". In: *PLoS pathogens* 3.8 (2007), e125.

[150] Marshall Slemrod. "Trend to equilibrium in the Becker-Doring cluster equations". In: *Nonlinearity* 2.3 (1989), p. 429.

[151] Sashko Spassov, Michael Beekes, and Dieter Naumann. "Structural differences between TSEs strains investigated by FT-IR spectroscopy". In: *Biochimica et Biophysica Acta (BBA)-General Subjects* 1760.7 (2006), pp. 1138–1149.

[152] Glenn C Telling et al. "Evidence for the conformation of the pathologic isoform of the prion protein enciphering and propagating prion diversity". In: *Science* 274.5295 (1996), pp. 2079–2082.

[153] Gerald Teschl. *Ordinary Differential Equations and Dynamical Systems*. Vol. 140. Graduate Studies in Mathematics. American Mathematical Society, 2012.

[154] Peter M Tessier and Susan Lindquist. "Unraveling infectious structures, strain variants and species barriers for the yeast prion [PSI+]". In: *Nature Structural and Molecular Biology* 16.6 (2009), p. 598.

[155] Horst R Thieme. "Asymptotically autonomous differential equations in the plane". In: *The Rocky Mountain Journal of Mathematics* (1994), pp. 351–380.

[156] Horst R Thieme. "Convergence results and a Poincaré-Bendixson trichotomy for asymptotically autonomous differential equations". In: *Journal of mathematical biology* 30.7 (1992), pp. 755–763.

[157] Philippe Tixador et al. "The physical relationship between infectivity and prion protein aggregates is strain-dependent". In: *PLoS pathogens* 6.4 (2010), e1000859.

[158] Alasdair Turner. "A simple model of the Belousov-Zhabotinsky reaction from first principles". In: *Bartlett School of Graduate Studies, UCL* (2009).

[159] Salit Tzaban et al. "Protease-sensitive scrapie prion protein in aggregates of heterogeneous sizes". In: *Biochemistry* 41.42 (2002), pp. 12868–12875.

[160] Robert Vautard, Pascal Yiou, and Michael Ghil. "Singular-spectrum analysis: A toolkit for short, noisy chaotic signals". In: *Physica D: Nonlinear Phenomena* 58.1-4 (1992), pp. 95–126.

[161] JJL Velázquez. "The Becker–Döring equations and the Lifshitz–Slyozov theory of coarsening". In: *Journal of statistical physics* 92.1-2 (1998), pp. 195–236.

[162] Aizik Isaakovich Volpert and Sergei Ivanovich Khudiaev. "Analysis in classes of discontinuous functions and the equations of mathematical physics". In: *Moscow Izdatel Nauka* (1975).

[163] Grant T Webster et al. "Detecting the early onset of shear-induced fibril formation of insulin in situ". In: *The Journal of Physical Chemistry B* 115.11 (2011), pp. 2617–2626.

[164] Limei Xu et al. "Quantifying signals with power-law correlations: A comparative study of detrended fluctuation analysis and detrended moving average techniques". In: *Physical Review E* 71.5 (2005), p. 051101.

[165] W-F Xue, S W Homans, and S E Radford. "Systematic analysis of nucleation-dependent polymerization reveals new insights into the mechanism of amyloid self-assembly". In: *PNAS* 105 (2008), pp. 8926–8931.

[166] Andrew T Young. "Rayleigh scattering". In: *Phys. Today* 35.1 (1982), pp. 42–48.

[167] Mark D Zabel and Crystal Reid. "A brief history of prions". In: *Pathogens and disease* 73.9 (2015).

[168] Jianing Zhang and M Muthukumar. "Simulations of nucleation and elongation of amyloid fibrils". In: *The Journal of chemical physics* 130.3 (2009), 01B610.

[169] Antoni Zygmund. *Trigonometric series*. Vol. 1. Cambridge university press, 2002.

Contents